

University of Strathclyde
Department of Pure and Applied Chemistry

Optical spectroscopic techniques for in-situ characterisation of
the milling of concentrated pigment dispersions.

David Wilsdon

A thesis submitted to the Department of Pure and Applied
Chemistry, University of Strathclyde, Glasgow, in part
fulfilment of the regulations for the degree of Doctor of
Philosophy.

March 2013

Copyright

This thesis is the result of the author's original research. It has been composed by the author and has not been previously submitted for examination which has led to the award of a degree.

The copyright of this thesis belongs to the author under the terms of the United Kingdom Copyright Acts as qualified by University of Strathclyde Regulation 3.50. Due acknowledgement must always be made of the use of any material contained in, or derived from, this thesis.

Signed:

Date:

For my family

Aut inveniam viam aut faciam

Acknowledgements

Firstly, to my supervisor, Dr Alison Nordon. Thank you! Who would have known that short text from Nicci and an e-mail from you a few years ago could have changed the direction of my career and life thereafter. Looking back on it all I'd make the same decision to do it all over again and I feel privileged to have worked under your guidance.

To my second supervisor Dr Suresh Thennadil, thank you for your enlightening discussions throughout my studies and your efforts developing several Matlab scripts. I'd also like to acknowledge Claudia Chen for her help when getting to grips with the Cary spectrometer. Without either I would not have been able to probe the optical properties of the pigment dispersions

I'd like to thank John Andrews and Paul Dallin from Clairet Scientific for the use of the Raman PhAT probe instrument and the analysis of some pigment dispersions using the long wavelength excitation Raman spectrometer.

I would like to acknowledge the outstanding support from Fujifilm Imaging Colorants (Grangemouth) throughout my entire project. Their support in materials, equipment and expertise was above and beyond what was expected of them. I'd specifically like to mention my primary contact, Jill Johnson, and Rupert McIntyre for special thanks. I want to add a special acknowledgement to Ewan Polwart from Fujifilm Imaging Colorants who sadly passed away when the project was just beginning. It is a source of sadness that I never had the opportunity to work alongside you more.

Throughout my project I have been fortunate enough to work with some outstanding undergraduates who have made valuable contributions. I'd like to extend my thanks to you all (Siobhan Kerr, Joanna Lothian and Joshua Barron). Special thanks go to Jamie McIntyre for his invaluable help during the small scale DoE milling experiments.

The project was part funded by the SPIRIT scheme, Fujifilm Imaging Colourants and the University of Strathclyde. Thanks for providing such an amazing opportunity.

I feel lucky to have met so many interesting people in the analytical group at Strathclyde and I am very lucky to count many of you as good friends. Thanks for all the tea! Lastly, I'd like to thank my friends and family for putting up with me throughout this whole process.

Abstract

The use of UV-visible, mid infrared, near infrared (NIR) and Raman spectrometries for monitoring the milling of polymer-pigment dispersions was investigated. Experiments showed that both NIR and Raman showed possibility for in-situ monitoring of particle size reduction and were both investigated further.

A fundamental investigation of the information content of NIR spectra was completed, showing the influence of particle size on the scattering properties of the pigment dispersions. This was used to rationalise observations made from spectra collected in-situ during particle size reduction experiments on different scales. Cyan, magenta and yellow pigment dispersion NIR spectra, collected in-situ, during milling, showed an increase in baseline offset as pigment size was reduced. Experimentation was performed on < 1 kg scale to develop and assess the technique before applying to larger scale 10 kg and 200 kg milling experiments. Qualitative and quantitative, univariate and multivariate, modelling approaches were explored for monitoring experiments performed on different scales. < 1 kg scale milling experiments showed errors in prediction of between 0.90 – 7.96 % for samples at the end point of milling (with particle sizes ranging from 100 to 114 nm). A calibration model derived from < 1 kg experiments was applied to 10 kg milling experiments with an error of prediction of 4.14 % for particles of 110 nm. Qualitative univariate modelling of 200 kg pigment dispersion milling experiments was able to show where faults occurred and where particle size reduction was no longer progressing. The work has demonstrated that in situ NIR measurements could potentially replace the current off-line particle size method. Raman spectroscopy also showed potential for following particle size reduction processes (< 1 kg scale) for cyan and yellow pigment dispersions using a wide area illumination Raman probe. Issues with fluorescence were encountered for magenta pigments and alternatives were explored to remove this.

Table of Contents

1.	Introduction	1
	1.1 Process analytical technology	3
	1.2 Pigment dispersions	5
	1.3 Particle sizing in industry	9
	1.4 Aims	13
	1.5 Summary	13
	1.6 References	14
2.	Theory	18
	2.1 Spectroscopy	18
	2.1.1 UV-visible attenuated total reflection	20
	2.1.2 Infrared spectroscopy	21
	2.1.3 Raman spectroscopy	27
	2.2 Particle sizing	30
	2.2.1 Dynamic light scattering theory	30
	2.2.2 Laser diffraction	36
	2.3 Data Analysis	37
	2.3.1 Multivariate techniques	38
	2.3.2 Derivatives	40
	2.4 Summary	41
	2.5 References	42
3.	Experimental	44
	3.1 Materials	44
	3.1.1 Pigment powders	44
	3.1.2 Polymer	46
	3.2 Pigment dispersion preparation	47
	3.3 Milling	48
	3.3.1 Netzsch Labstar mill	51
	3.4 Spectroscopic measurements	52
	3.4.1 UV-visible spectroscopy	52

3.4.2	FOSS on-line 6500	54
3.4.3	Cary 5000 off-line NIR spectrometer	59
3.4.4	Raman Spectrometer and PhAT probe for on-line monitoring	61
3.4.5	Optical probes for in-situ analysis	64
3.4.6	Off-line Visible-Near infrared measurements	66
3.5	Particle size analysis	67
3.5.1	DLS	67
3.5.2	Laser diffraction	70
3.6	Data analysis tools	71
3.7	Summary	71
3.8	References	72
4.	Investigation of techniques	73
4.1	Literature	73
4.1.1	UV-visible spectroscopy process monitoring	73
4.1.2	Mid infrared ATR for process monitoring	76
4.1.3	NIR	78
4.1.4	Raman	83
4.1.5	Summary	87
4.2	Sample Stability	88
4.2.1	Experimental	88
4.2.2	Result and Discussion	88
4.3	UV-visible ATR	91
4.3.1	Results and discussion	91
4.4	MIR ATR	96
4.4.1	Additional equipment	96
4.4.2	Results and discussion	96
4.5	NIR	99
4.5.1	Results and Discussion	99
4.6	Raman	102
4.6.1	Experimental	102

4.6.2	Results and discussion	103
4.7	Conclusions	105
4.8	References	106
5.	Off-line visible-NIR spectroscopy	111
5.1	Experimental	117
5.2	Results and Discussion	120
5.2.1	Magenta pigment dispersions	120
5.2.2	Yellow pigment	131
5.2.3	Cyan pigment	134
5.2.4	Particle size and number density	137
5.3	Summary	139
5.4	References	140
6.	On-line NIR measurements	142
6.1	Penetration Depth	143
6.1.1	Experimental	144
6.1.2	Results and Discussion	145
6.2	Small scale milling experiments (~ 1 kg)	148
6.2.1	Magenta	148
6.2.2	Summary	150
6.3	Milling Reservoir Temperature	151
6.3.1	Experimental	151
6.3.2	Results and Discussion	151
6.4	DoE matrix of milling experiments for magenta pigment PR122	153
6.4.1	Experimental	153
6.4.2	Results and Discussion	154
6.5	PLS	163
6.6	Chemical Information	166
6.6.1	Data selection and processing	166
6.6.2	Results and discussion	166
6.7	Larger scale milling experiments (10 kg)	169

6.7.1	Experimental	169
6.7.2	Cyan pigment dispersion milling - Results and Discussion.	171
6.7.3	Yellow pigment dispersion milling- Results and Discussion	172
6.7.4	Transferability of a PLS model developed on < 1 kg magenta milling experiments	174
6.8	Summary	179
6.9	References	181
7.	NIR for 200 kg scale milling experiments	182
7.1	Experimental	183
7.2	Results and discussion	185
7.2.1	Sample volume	185
7.2.2	Milling temperature	189
7.2.3	200 kg scale milling data	190
7.3	Conclusions	220
8.	Raman spectroscopy	222
8.1	Individual component spectra	223
8.1.1	785 nm Excitation	223
8.1.2	998 nm Excitation	228
8.2	Penetration depth at 785 nm	231
8.2.1	Experimental	231
8.2.2	Results and discussion	232
8.3	Interfering effects	235
8.3.1	Stirring	235
8.3.2	Sample distance	239
8.4	Milling of yellow pigment dispersion	239
8.4.1	Experimental	239
8.4.2	Results and discussion	240
8.5	Summary	245
8.6	References	247

9.	Conclusions and Future Work	248
10.	Appendices	253
10.1	Spectrometer specifications	253
10.2	Absorption and scattering coefficients	255

1. Introduction

Both pigments and dyes have been used as inks for inkjet printing and it is useful to understand the differences between the two. Both contain chromophores and conjugated systems but dyes have weaker intermolecular forces and as a result the molecules can be dispersed in aqueous or organic media. Pigments have stronger intermolecular bonding and are difficult to dissolve. These pigments usually exist as small particles containing tens to thousands of molecules and require the use of a polymer to attach to the pigment surface; without which, the small particles of pigment would aggregate and sediment. The use of pigment dispersions as a replacement for traditional soluble dye based inks is increasing as pigment dispersions typically display better light fastness as only the exposed surface of the pigment is able to be broken down by prolonged exposure to sunlight.

Dispersion of pigments using stabilising polymers is an important area of development for Fujifilm Imaging Colorants (FFIC) at Grangemouth. A number of factors determine the final properties of nanoscale polymer-stabilised pigment dispersions in aqueous media. These include the concentration, size and size distribution of the pigment particles, and the distribution of the stabilising polymer. Therefore, it is important to be able to measure such properties during the development and manufacture of new pigment-based ink products. Traditionally, this has involved taking a sub-sample of the process for analysis. However, such off-line characterisation of nanoscale polymer-stabilised pigment dispersions is particularly challenging and very time-consuming. The particle size of the dispersed pigment has a direct effect on the product quality as the colour and hue observed from the pigment is a combination of the chemical and physical properties of the system (the absorption and scattering properties). Additionally, the particle size impacts the stability and, hence, the shelf life of the product. If the particles flocculate and sediment in the final product the large particles will block the narrow nozzles of inkjet printers.

Particle size, shape and the distribution of particle size in a dispersion can be reduced by milling, grinding or application of high energy ultrasound, all of which are designed to break down large agglomerate particles. Grinding is used to remove agglomerates in dry powders. This can be achieved by passing the powder through

steel rollers that are separated by a distance that will be the maximum particle size diameter (for spherical particles). The technology is derived from basic wind or water powered mill stones which were used to mill flour¹. Primitive flour milling was a one step process however the production process changed to incorporate multiple stone milling steps where the stones became closer and closer together. This allowed different fractions of flour to be produced with different physical and chemical properties. Horizontal rotating drums are used in place of mill stones for modern high throughput flour production and essentially operate by the same mechanism – breaking the larger particles by friction.

More commonly in the pharmaceutical industry, wet milling (or ball milling) is used to reduce the particle size of particulate dispersions from the micron to the nano range². This is especially useful in affecting an increase in bioavailability and altering the dissolution profiles of newly discovered drugs which are poorly soluble in water³⁻⁶. Nanosizing a particulate dispersion of drug product produces a huge increase in the surface area of active pharmaceutical ingredients which enhances the solubility. Wet milling utilises small metal, plastic or ceramic beads contained within a chamber with very high agitation. The kinetic energy of the milling media is transferred through collisions to the surrounding dispersion causing the breakup of the larger particles.

There are several other methods of altering particle^{7, 8} size such as hammer mills, jet mills and ultrasonic mills, in addition to those already mentioned, which are used in industry to alter and control the particle size of food products, cosmetic dispersions (such as nail varnish and toothpaste) and pharmaceutical actives and excipients. The method of particle size reduction can vary but all require a method of quantifying the particle size of the product to check that the desired product has been produced. This typically involves sampling the process and performing particle size analysis such as sieving (for dried powder samples with larger particle sizes), microscopy (optical or scanning electron microscopy for samples in the nano domain), laser diffraction or dynamic light scattering. The methodology of off-line analysis is time consuming, often messy and can be prohibitively dangerous when dealing with highly volatile or harmful samples. Therefore, the work presented herein aims to present an optical spectroscopic method for measuring the particle size reduction manufacturing step of

highly concentrated pigment dispersion using on-line optical spectroscopic techniques.

1.1 Process analytical technology⁹⁻¹⁴

The use of process analytical technology (PAT) has great potential benefits when applied to the pharmaceutical and consumer product industries, offering a source of savings as manufacturers strive to reduce operating and production costs while still producing a high quality product that is “best in class” cost. Non-impact printing is a growing multi-million pound industry and there is increasing commercial interest in printing in more technical demanding applications with aqueous pigment-based inks. The possibility of applying process analytical technology to the production of pigment dispersions may provide process and cost improvements. Recently there has been an emphasis in the pharmaceutical industry, instigated in part by the regulatory authorities (US Food and Drug Administration (FDA) and the Medicine and Health care product Regulatory Agency (MHRA)), to incorporate quality by design so that the quality is built in to the product rather than testing the quality in at the end of production¹⁵. This approach can also be applied to the production of high performance pigment based inks.

A variety of sampling strategies are employed when controlling plant processes. Conventional off-line analysis involves the extraction of a sample from the process and testing being undertaken in a centralised laboratory. Centralised testing has the advantages that complex analysis can be performed by trained personnel and that equipment is not necessarily dedicated to a specific product in the way it would be if the analyser is deployed on plant. FFIC currently monitor the production stages of the dispersion manufacture using this methodology but a significant advantage of using PAT would be that the physical handling of the concentrated colourants could be minimised. Samples frequently have to be diluted or manipulated for off-line analysis and hence, they no longer exhibit the same properties as the original process sample and the application of PAT would enable monitoring of the products in their natural state. This testing regime does not allow rapid feedback to plant processes and can be time consuming and costly.

Situating an analyser close to a process can reduce analysis times but this requires that operators are trained to use and possibly maintain the analytical equipment. This “at-line” situation has similar disadvantages to off-line testing as extraction of a potentially hazardous substance adds a safety risk to the operator and sometimes the extraction of a sample can require a temporary shutdown of the process, adding energy and production time costs to the product.

Diverting sample from the reactor or process stream to a parallel stream is described as “on-line” analysis. The sample may undergo pre-treatment such as a filtration step before being presented to an analyser such as process gas chromatography¹⁶ (GC) or high performance liquid chromatography¹⁷ (HPLC) instruments. On-line analysis can provide real time measurements and allows rapid feedback control of the process. However, the removal of a stream for sampling will make the pipework and fittings more complex and require a more difficult cleaning regime to prevent cross contamination between batches in situations where the loop containing the analyser is removed and fed back in to the process stream or vessel in a continuous loop. The elimination of cross product contamination is an important factor to consider when designing a plant for the production of pigment based inks.

In-line analysers involve measuring the process directly and can be achieved using a variety of techniques such as classical sensors in contact with the sample like pH or dissolved oxygen sensors. Modern analytical equipment such as UV-visible, near infrared (NIR), mid infrared (MIR) and Raman spectrometers can be coupled to probes or sample interfaces using optical fibres which allows the analyser to be situated some distance away from the actual process, in a safe environment. Inserting probes directly into a process can result in additional complications such as fouling and can require the shutdown of a process to allow servicing but the advantage is that real time measurements can be obtained which allow rapid feedback and control of a process and can lead to significant efficiency improvements.

One method of overcoming fouling or harsh conditions is to use non-contact spectroscopic measurements such as NIR and Raman. However, difficulties can arise when attempting to retrofit existing plant equipment with windows or openings to

situate the source and collection optics of the spectrometer. Table 1.1 details some common PAT applications of optical spectroscopic techniques.

Table 1.1 – Typical examples of PAT techniques and their applications in industry.

Technique	PAT applications
UV-Visible	Reaction monitoring ¹⁸ Assay of API content in liquids ¹⁹ Colour measurement ²⁰ Automated dissolution testing ²¹
NIR	Mixing/blending ²²⁻²⁵ Particle size ²⁶⁻³⁰ API assay ³¹ Content uniformity ³² Drying - solvents ³³ Water content ^{34, 35}
MIR	Reaction monitoring ³⁶⁻³⁸ Crystallisation ³⁹
Raman	Polymorph formation ^{40, 41} Reaction monitoring ⁴² Crystallisation ^{39, 43} Polymerisation ^{44, 45} Particle size ^{44, 46}

The measurement of particle size is an important subject in the area of process analytical chemistry as many everyday items are formulated as dispersions. Examples range from toothpastes, shower gels and cosmetics, right through to the food products we consume and beyond to applications in paints and printing media such as the aqueous pigment dispersions being developed by FFIC.

1.2 Pigment dispersions

As described from IUPAC definitions, a colloidal dispersion can be defined by two factors. The term "colloidal" refers to the state of subdivision whereby molecules or polymers dispersed in a medium must have at least one dimension between 1 nm and 1 µm and the term colloidal dispersion refers to the situation where particles of colloidal size (which can be either solid, liquid or gas) are dispersed in a continuous phase of a different composition (or state)^{47, 48}. In the case of aqueous based pigment dispersions for inkjet printing, polymers are used to stabilise the nanoscale pigment

particles. The polymer forms a layer on the pigment surface which prevents flocculation, aggregation and sedimentation via contributions from steric hindrance and charge stabilisation. Floccules⁴⁹ are small aggregates of particulates loosely held together and can be removed by mechanical agitation. The polymer can incorporate carboxylic acid groups that are not fully neutralised which provides some charge stabilisation by repelling the surrounding polymer coated pigment particles. The total free energy difference (ΔG) of the colloid when it interacts with another nearby particle can be described by the general formula:

$$\Delta G = \Delta G^{att} + \Delta G^{rep} + \Delta G^{other} \quad \text{Equation 1.1}$$

where ΔG^{att} is a result of the van der Waals forces, ΔG^{rep} accounts for repulsive forces where the contributions will be from short range forces, electrostatic and steric effects. Figure 1.1 shows the mechanisms of stability for polymer-colloid dispersions and it is likely that the most significant contributions in aqueous dispersions are from charge repulsion and steric stabilisation.

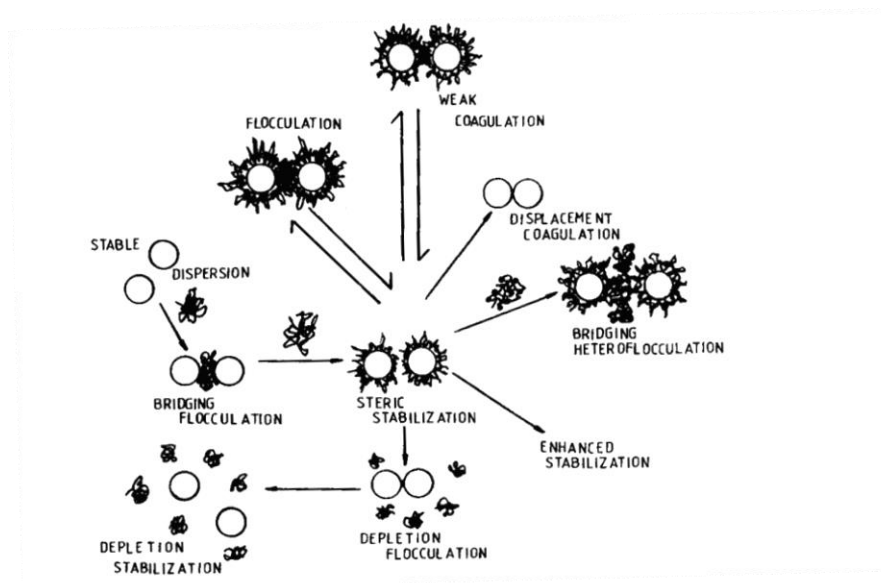


Figure 1.1 – Mechanisms of stability⁵⁰.

Steric repulsion⁵⁰⁻⁵² will occur when the two polymer layers adsorbed on to the pigment particle come close together and the polymer layers begin to merge with each other. This mixing will result in a localised osmotic pressure increase and when the polymer chains are forced closely together as is the case in the concentrated pigment dispersion, the effect of mixing of the outer layers is overridden by the effect that reducing the available space has on the chain conformation of the polymer. Several theories exist in order to explain the osmotic effects such as Fischer's theory, which accounts for an enthalpy contribution to osmotic pressure. To best describe the system when the particles are closer and the osmotic pressure contribution has less of an input, the following need to be considered:

- 1) The number of chains per unit area surface,
- 2) The thickness of the adsorbed layer, δ ,
- 3) The solvent quality, and
- 4) The strength of the "anchor" of the adsorbed chains.

It is proposed that the affinity of the hydrophobic part of the polymer is strong for the pigment particle. The number of chains per unit area, n_p on the surface can be related to:

$$n_p = \frac{\Gamma N_A}{M_n A} \quad \text{Equation 1.2}$$

where A is the specific surface area, N_A is Avogadro's number, M_n is the molecular weight average of the polymer and Γ is the adsorbed weight of polymer. The polymer used for the pigment-polymer dispersions contains sections that are hydrophobic in nature, which orientate to the pigment particle, and hence can be considered to be anchored to the pigment (see Figure 1.2).

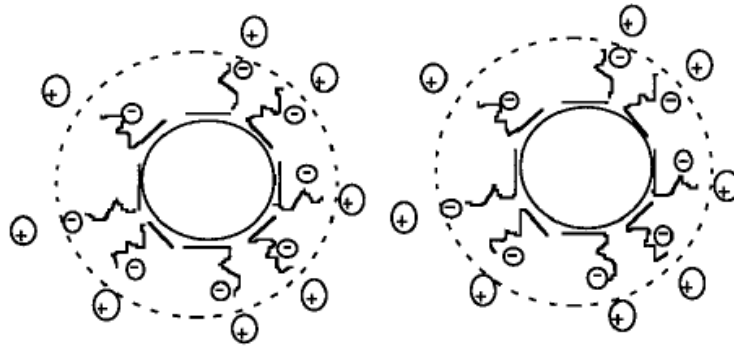


Figure 1.2 – Polymeric dispersants surrounding a pigment particle. The flat section of the polymer represents the hydrophobic portion which orientates itself towards the pigment surface and the wavy charged line represents the hydrophilic portion of the dispersing polymer which extends out in the aqueous medium⁵³.

Charge repulsion of the pigment-polymer dispersion also plays a large part in stabilisation of the aqueous dispersion and this relationship has been described by the Derjaguin-Verwey-Landau-Overbeek (DVLO) theory. This describes the stability in terms of a balance between the van der Waals forces (attractive forces) and the electrostatic repulsive forces.

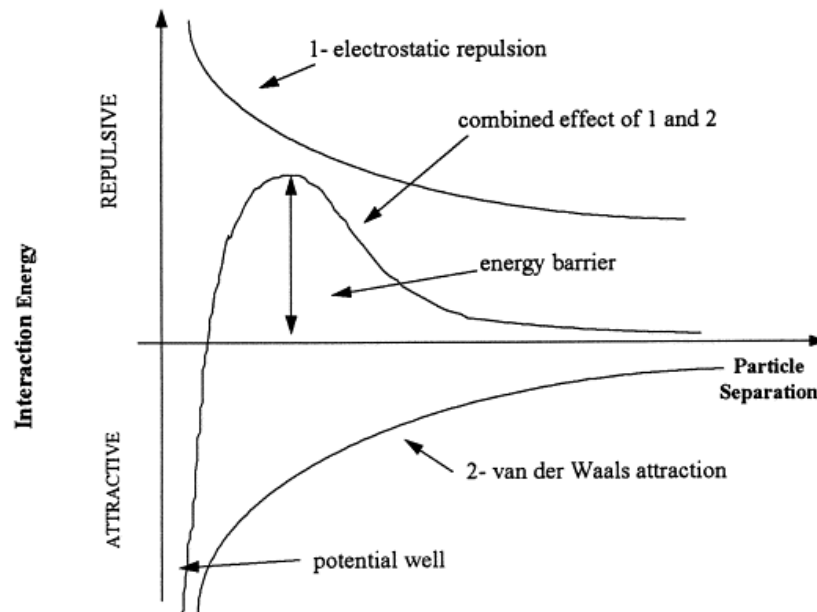


Figure 1.3 – DVLO energy diagram⁵⁴.

The repulsive forces (V_R) from charge repulsion can be described by the equation:

$$V_R = \left(\frac{\epsilon r \psi_0^2}{R} \right) \{ \exp[-k[R - 2r]] \} \quad \text{Equation 1.3}$$

and, where ϵ the dielectric constant of the solvent, ψ_0 is the surface potential, R is the distance between the centres of two particles, r is the radius of the charged particle, k is the Boltzmann constant. The attractive forces (V_A) can be described by

$$V_A = \frac{-A}{12\pi H^2} \quad \text{Equation 1.4}$$

where A is the Hamaker constant (in the range of 10^{-12} to 10^{-13}) and H is the particle separation. When the particles collide with enough energy to overcome the repulsive forces flocculation and aggregation will occur, however, in some situations the net energy of the repulsive and attractive forces can result in there being a second energy minimum where floccules will form that cannot be broken by Brownian motion. During manufacture these floccules can be broken by mechanical agitation but in the final product the pigment dispersion has to be free of floccules and sedimenting particles. This is achieved by the combination of the correct stabilising polymer and controlling the particle size of the pigment particles in the dispersion.

1.3 Particle sizing in industry

The particle size of a powder or dispersion will affect how a product or medicine performs⁵⁵ and there are a number of techniques used to measure this important property. For powders, for example, the particle size of an excipient or active pharmaceutical ingredient (API) used in a tablet can influence the mixing properties and flow properties as the blended material is moved through different unit operations. When the powder is then pressing to a tablet the particle size of each constituent of the powder mix can affect how much or little pressure is required by the tableting press to create a tablet free from deformations and cracks. The next important step is dissolution where the release of the drug from the tablet has to meet a consistent specification. Differences in the particle sizes of actives or excipients,

which can occur from using different batches or suppliers, can dramatically alter how the tablet disintegrates to release the API. There are other examples in the pharmaceutical industry where APIs have been coated to prevent the patient from tasting a bitter antibiotic or where the coating is designed to aid passage of an API through the harsh acidity of the stomach in to the intestinal tract. In these instances an increase in the particle size from the coatings can be measured and compared to the distribution of particle sizes from the uncoated particulates.

The control of the particle size in pigment dispersions is crucial for the stability of the product and the performance (colour and hue). The presence of larger particles can block the fine nozzles used in inkjet printers and it can cause the dispersion to sediment. Whilst this is not too serious during manufacturing where the particles can be re-dispersed by rapid agitation, sedimentation in the final product that is delivered to customers has to be avoided completely.

There are a number of techniques used in industry to analyse dry powders or liquid colloidal dispersions, some of which can be used to analyse both types of samples. The choice of technique is determined by not only the presentation of the sample (i.e. solid or liquid) but the range of the size and shape of the particles⁵⁶.

For particulate powders in the μm domain the simplest particle sizing technique involves sieving and gravimetric analysis of the retained particulates. Samples are placed on to sieves constructed of a fine mesh with small holes which allow particles smaller than the gaps in the sieve to pass through. Optical microscopy and particle counting is another common method of measuring particle size. Images obtained can be manually investigated by an analyst which can be time consuming and tedious. Alternatively, a number of image analysis software packages are available to automate and speed up analysis of the microscope pictures.

Other methods of particle size measurement for particles in the μm domain include laser diffraction measurements^{57, 58} which is suitable for powders or dispersions or scanning electron microscopy⁵⁶ (SEM). SEM measurements are not typically used for liquids as the sample chamber operates under vacuum, however, there are sample accessories which allow the sample to be stored at atmospheric pressure, allowing

the analysis of dispersed samples such as biological tissue samples or pigment dispersions.

An important PAT tool for monitoring the particle size in the μm domain for wet powders and slurries is focussed beam reflectance measurements⁵⁹ (FBRM). FBRM measurements can determine particle sizes in the range of 1 – 4000 μm and operate using a tightly focused laser beam. The beam is emitted from the end of the probe and the position of the beam is continuously changed so that the beam is emitted in a circular profile. This rapid beam travelling in a circular motion then interacts with the sample. When the light hits the sample there is an increase in the reflected light collected by the probe and the discrimination between the light and dark areas (where no particle was struck by the laser beam) allows the determination of size (commonly referred to as chord length) to be made.

Both laser diffraction and dynamic light scattering (DLS) measurements are two of the most commonly used techniques in industry and academia. Laser diffraction measurements have the capacity to measure both dry powder and dispersion samples within the range of 20 nm to 2000 μm whereas DLS measurements can determine the particle size of dispersion samples between 0.1 and 1000 nm. Laser diffraction operates by scattering of laser light by the particles as they pass through the beam and the amount of scattering is inversely proportional to the size of the scattering particle. DLS measurements operate by a different principle whereby particles which move under Brownian motion cause the scattered light to produce an interference pattern. The rate of change of the interference pattern produced is linked to the speed of the particles which is, in turn, related to the size.

Grating light reflection spectroscopy^{60, 61} (GLRS) can be exploited for analytical measurements of dispersions and colloids in-situ as optical scattering in heterogeneous mixtures is influenced by the characteristics of the particles such as shape, size, morphology and the distribution in the matrix. GLRS exploits the change in intensity and phase of light reflected from a transmission grating, which is in contact with the sample⁶². Hamad et al⁶³ describe the basic principles by which grating light spectroscopy works and have also shown an example of how the technique can be used to monitor attrition milling of an API.

There are a number of alternative additional techniques available as described in the review paper by Haskell⁶⁴ such as centrifugation, particle counting and electrozone sensing. However, the main advantage of using in-situ optical spectroscopy is the sample can be measured in real time without the need for sample dilution before being presented to one of the many different types of particle size analysers available on the market today.

1.4 Aims

The aims of the work presented are to investigate the use of optical spectroscopic techniques capable of measuring the particle size reduction of pigment dispersions through in-situ measurements. UV-visible, mid infrared, near infrared (NIR) and Raman spectrometry are investigated as potential techniques. To do this, the key steps that must be achieved are to:

- Show that the reference measurement is robust.
- Select the most promising optical spectroscopic technique(s).
- Show how the fundamental optical properties contribute to the observations in-situ.
- Apply spectroscopic measurements across different scales and conditions to show that the spectroscopic measurement is robust.

1.5 Summary

The work presented herein is split into distinct sections. Chapter 1 has set the scene for process analytical technologies and given an overview of pigment dispersions, detailing the current state of analytical techniques used to characterise them. Chapter 2 describes the theory of techniques used (both on-line optical spectroscopic and off-line particle size) and chapter 3 contains the experimental information. Chapter 4 details the preliminary investigation of techniques (UV-visible, mid-infrared, near infrared and Raman), showing that NIR and Raman were the most promising. Chapter 5 contains the results of a fundamental investigation in to the information encoded in to the NIR spectra which is then used to rationalise the results of NIR spectra collected in-situ during monitoring of small scale (chapter 6) and large scale (chapter 7) pigment dispersion milling. Chapter 8 then examines the use of Raman spectroscopy.

1.6 References

1. J. Tann and R. G. Jones, *Technology and Culture*, 1996, **37**, 36-69.
2. L. Dintenfass, *Colloid & polymer science*, 1960, **170**, 1-19.
3. E. Merisko-Liversidge and G. G. Liversidge, *Advanced Drug Delivery Reviews*, 2011, **63**, 427-440.
4. T. Niwa, Y. Nakanishi and K. Danjo, *European Journal of Pharmaceutical Sciences*, 2010, **41**, 78-85.
5. E. L. Parrott, *Journal of Pharmaceutical Sciences*, 1974, **63**, 813-829.
6. J. P. Higgins, S. M. Arrivo, G. Thurau, R. L. Green, W. Bowen, A. Lange, A. C. Templeton, D. L. Thomas and R. A. Reed, *Analytical Chemistry*, 2003, **75**, 1777-1785.
7. <http://www.netzsch-grinding.com/en/industries-applications.html> (accessed 12 Dec 2012).
8. E. M. Hansuld, L. Briens, A. Sayani and J. A. B. McCann, *Powder Technology*, 2012, **215–216**, 117-123.
9. J. Workman, B. Lavine, R. Chrisman and M. Koch, *Analytical Chemistry*, 2011, **83**, 4557-4578.
10. J. Workman, M. Koch, B. Lavine and R. Chrisman, *Analytical Chemistry*, 2009, **81**, 4623-4643.
11. J. Workman, D. J. Veltkamp, S. Doherty, B. B. Anderson, K. E. Creasy, M. Koch, J. F. Tatera, A. L. Robinson, L. Bond, L. W. Burgess, G. N. Bokerman, A. H. Ullman, G. P. Darsey, F. Mozayeni, J. A. Bamberger and M. S. Greenwood, *Analytical Chemistry*, 1999, **71**, 121R-180R.
12. D. Hinz, *Analytical and Bioanalytical Chemistry*, 2006, **384**, 1036-1042.
13. F. Sistare, L. St. Pierre Berry and C. A. Mojica, *Organic Process Research & Development*, 2005, **9**, 332-336.
14. J. Munson, C. F. Stanfield and B. Gujral, *Current Pharmaceutical Analysis*, 2006, **2**, 405-414.
15. <http://www.fda.gov/Cder/OPS/PAT.htm> (accessed 07 Nov 08).
16. E. Pocurull, C. Aguilar, F. Borrull and R. Marce, *Journal of chromatography A*, 1998, **818**, 85-93.
17. A. Rathore, M. Yu, S. Yeboah and A. Sharma, *Biotechnology and bioengineering*, 2008, **100**, 306-316.

18. A. C. Quinn, P. J. Gemperline, B. Baker, M. Zhu and D. S. Walker, *Chemometrics and Intelligent Laboratory Systems*, 1999, **45**, 199-214.
19. H. Schlemmer and J. Katzer, *Fresenius' Journal of Analytical Chemistry*, 1987, **329**, 435-439.
20. A. S. Nateri and E. Ekrami, *Pigment & Resin Technology*, 2009, **38**, 43-48.
21. J. Johansson, M. Cauchi and M. Sundgren, *Journal of Pharmaceutical and Biomedical Analysis*, 2002, **29**, 469-476.
22. L. J. Bellamy, A. Nordon and D. Littlejohn, *Analyst*, 2008, **133**, 58-64.
23. O. Berntsson, L. G. Danielsson, B. Lagerholm and S. Folestad, *Powder Technology*, 2002, **123**, 185-193.
24. T. R. M. De Beer, C. Bodson, B. Dejaegher, B. Walczak, P. Vercruyse, A. Burggraeve, A. Lemos, L. Delattre, Y. V. Heyden, J. P. Remon, C. Vervaet and W. R. G. Baeyens, *Journal of Pharmaceutical and Biomedical Analysis*, 2008, **48**, 772-779.
25. Z. Q. Shi, R. P. Cogdill, S. M. Short and C. A. Anderson, *Journal of Pharmaceutical and Biomedical Analysis*, 2008, **47**, 738-745.
26. L. K. H. Bittner, N. Heigl, C. H. Petter, M. F. Noisternig, U. J. Griesser, G. K. Bonn and C. W. Huck, *Journal of Pharmaceutical and Biomedical Analysis*, 2011, **54**, 1059-1064.
27. P. Frake, I. Gill, C. N. Luscombe, D. R. Rudd, J. Waterhouse and U. A. Jayasorriya, *Analyst*, 1998, **123**, 2043-2046.
28. A. J. O'Neil, R. D. Jee and A. C. Moffat, *Analyst*, 1998, **123**, 2297-2302.
29. A. J. O'Neil, R. D. Jee and A. C. Moffat, *Analyst*, 2003, **128**, 1326-1330.
30. A. Szalay, I. Antal, Z. Zsigmond, S. Marton, I. Er, odblac, G. R. jr. and K. Pintye-Hódi, *Particle & Particle Systems Characterization*, 2005, **22**, 219-222.
31. M. R. Smith, R. D. Jee and A. C. Moffat, *Analyst*, 2002, **127**, 1682-1692.
32. M. Blanco, M. Alcalá, J. M. Gonzalez and E. Torrasz, *Journal of Pharmaceutical Sciences*, 2006, **95**, 2137-2144.
33. J. Märk, M. Karner, M. Andre, J. Rueland and C. W. Huck, *Analytical Chemistry*, 2010, **82**, 4209-4215.
34. W. Cao, C. Mao, W. Chen, H. Lin, S. Krishnan and N. Cauchon, *Journal of Pharmaceutical Sciences*, 2006, **95**, 2077-2086.

35. H. W. Ward and F. E. Sistare, *Analytica Chimica Acta*, 2007, **595**, 319-322.
36. I. M. Clegg, A. M. Daly, C. Donnelly, R. Hardy, D. Harris, H. Jackman, R. Jones, A. Luan, D. McAndrew, P. McGauley, J. Pearce, G. Scotney and M. L. Yeow, *Applied Spectroscopy*, 2012, **66**, 574-579.
37. E. N. M. van Sprang, H. J. Ramaker, H. F. M. Boelens, J. A. Westerhuis, D. Whiteman, D. Baines and I. Weaver, *Analyst*, 2003, **128**, 98-102.
38. R. Foley, S. Hennessy and I. W. Marison, *Appl. Spectrosc.*, 2012, **66**, 33-39.
39. J. Cornel, C. Lindenberg and M. Mazzotti, *Industrial & Engineering Chemistry Research*, 2008, **47**, 4870-4882.
40. *Pharmaceutical applications of Raman spectroscopy*, Hoboken, N.J. : Wiley-Interscience, 2008.
41. T. Vankeirsbilck, A. Vercauteren, W. Baeyens, G. Van der Weken, F. Verpoort, G. Vergote and J. P. Remon, *TrAC Trends in Analytical Chemistry*, 2002, **21**, 869-877.
42. S. Mozharov, A. Nordon, J. M. Girkin and D. Littlejohn, *Lab on a Chip*, 2010, **10**, 2101-2107.
43. G. Févotte, *Chemical Engineering Research and Design*, 2007, **85**, 906-920.
44. J. C. Santos, C. N. Lopes, M. M. Reis, R. Giudici, C. Sayer, R. A. F. Machado and P. H. H. Araujo, *Brazilian Journal of Chemical Engineering*, 2008, **25**, 399-407.
45. J. C. Santos, M. M. Reis, R. A. F. Machado, A. Bolzan, C. Sayer, R. Giudici and P. H. H. Araujo, *Industrial & Engineering Chemistry Research*, 2004, **43**, 7282-7289.
46. M. M. Reis, P. H. H. Araujo, C. Sayer and R. Giudici, *Polymer*, 2003, **44**, 6123-6128.
47. <http://goldbook.iupac.org/C01172.html> (Accessed 09 Jan 12).
48. <http://goldbook.iupac.org/C01174.html> (Accessed 09 Jan 12).
49. D. B. Genovese, J. E. Lozano and M. A. Rao, *J. Food Sci.*, 2007, **72**, R11-R20.
50. Napper D.H, *Polymeric stabilization of colloidal dispersions*, Academic press, 1983.
51. H. R. W. Goodwin J.W, *Rheology for chemists, an introduction 2nd edition*, RSC publishing, 2008.

52. R. R. Sato T, *Stabilization of colloidal by polymer adsorption*, 1980.
53. H. J. Spinelli, *Advanced Materials*, 1998, **10**, 1215-1218.
54. D. N. Thomas, S. J. Judd and N. Fawcett, *Water Research*, 1999, **33**, 1579-1592.
55. B. E. Rabinow, *Nature Reviews Drug Discovery*, 2004, **3**, 785-796.
56. B. Shekunov, P. Chattopadhyay, H. Tong and A. Chow, *Pharmaceutical Research*, 2007, **24**, 203-227.
57. M. McGarvey, D. McGregor and R. B. McKay, *Progress in Organic Coatings*, 1997, **31**, 223-228.
58. H. G. Merkus, *Laser Diffraction Particle Size Measurements*, Springer Netherlands, 2009.
59. K. Vay, W. Frieß and S. Scheler, *International Journal of Pharmaceutics*, 2012, **437**, 1-10.
60. A. M. Brodsky, L. W. Burgess and S. Smith, *Appl. Spectrosc.*, 1998, **52**, 332A-343A.
61. B. B. Anderson, A. M. Brodsky and L. W. Burgess, *Analytical Chemistry*, 1996, **68**, 1081-1088.
62. B. B. Anderson, A. M. Brodsky and L. W. Burgess, *Langmuir*, 1997, **13**, 4273-4279.
63. M. L. Hamad, S. Kailasam, A. M. Brodsky, R. Han, J. P. Higgins, D. Thomas, R. A. Reed and L. W. Burgess, *Applied Spectroscopy*, 2005, **59**, 16-25.
64. R. J. Haskell, *Journal of Pharmaceutical Sciences*, 1998, **87**, 125-129.

2. Theory

UV-visible, near-infrared (NIR), mid-infrared (MIR) and Raman spectroscopic measurements were investigated as potential techniques for measuring the change in particle size of pigment dispersions and most of the work presented herein will focus on NIR and Raman spectroscopy. The reference techniques dynamic light scattering and laser diffraction were used for off-line analysis of the diluted pigment dispersions. Multivariate data analysis was then used to explore the correlations between the spectroscopic data and the particle size data and to build quantitative models to predict particle size

2.1 Spectroscopy

Both Raman and near infrared spectroscopies have been used for on and offline monitoring of pigment dispersion milling. Figure 2.1 represents the various energy level transitions associated with vibrational and electronic spectroscopic techniques.

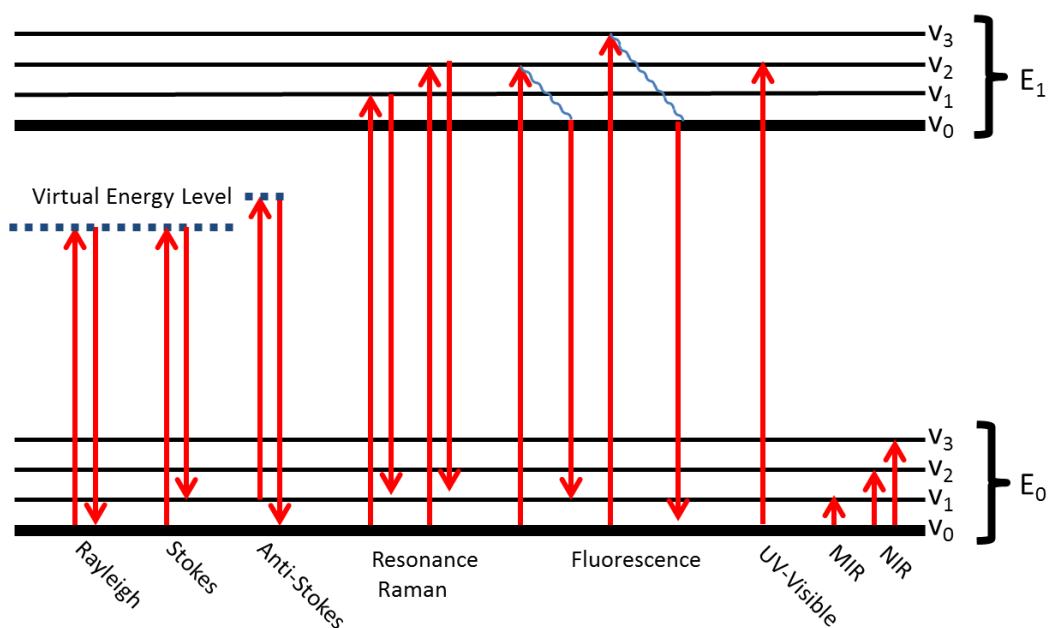


Figure 2.1 – Energy level diagram representing the various transitions in vibrational and electronic spectroscopic techniques.

Working from left to right, the first three events (Rayleigh, Stokes and anti-Stokes scattering) show the processes where a molecule interacts with photons of a wavelength less than that required to promote an electron from the highest occupied molecular orbital to the lowest unoccupied molecular orbital (HOMO to LUMO). Rayleigh scattering is an elastic process where the scattered light is not changed from the original frequency of the incoming photon and this is what occurs with most photons. However, every 1 in 10^6 - 10^8 photons undergo inelastic scattering events whereby the released photon is shifted to a lower or higher frequency by an amount of energy equal to the difference in energy levels $v_0 \rightarrow v_1$ (Stokes and anti-Stokes Raman scattering respectively).

The following two processes represent resonance Raman which is where the incoming photons of light have an energy greater than the energy of the first electronic transition. Resonance Raman provides selective band enhancements which facilitate detection at lower levels than that of conventional Raman scattering.

The next two events, labeled fluorescence in Figure 2.1, are a cause of interference in Raman spectroscopy as it is a much more efficient process than Raman scattering. When a photon has been resonantly absorbed it decays through the vibrational bands of the excited state which loses energy. If the energy gap between the HOMO and LUMO is in the visible range, a photon of light will be emitted and the number of photons produced by this process will dwarf the Raman scattered photons. Kerr gating^{1, 2} can be used to remove fluorescence as the Raman effect occurs on the picosecond scale whereas fluorescence is on the nanosecond scale so by using an optical shutter the fluorescence can be excluded.

The final 3 processes (UV-visible, MIR and NIR) represent absorption spectroscopy. The absorbance of a sample is given by Beer-Lambert law:

$$A = \log_{10} \frac{I_0}{I} = \epsilon cl$$

Equation 2.1

where A is the absorbance, I_0 is the intensity of light before entering the sample, I is the intensity of light on leaving the sample, ε is the absorption coefficient, c is the concentration of the analyte and l is the path length.

For the UV-visible process, absorption of light by a chromophore is frequently observed as a broad band and to explain this, the Franck-Condon principle needs to be considered. Promotion of an electron from a bonding to a non-bonding orbital reduces the strength of the bond. However the process of absorption of a photon ($\sim 10^{-15}$ s) is much quicker than the process of bond stretching ($\sim 10^{-13}$ s) hence absorptions will not result in a change in the position of the two nuclei. Most electrons in the ground state will occupy the lowest vibrational state but on absorption to the excited state will occupy one of a number of vibrational energy levels in the excited state and hence a distribution of wavelengths of radiation are absorbed.

The final two scenarios in Figure 2.1 represent mid infrared and near infrared spectroscopy which are described in more detail in the following section.

2.1.1 UV-visible attenuated total reflection

UV-visible spectroscopy (often called electronic spectroscopy) is a much used and well understood technique utilised in the chemical, pharmaceutical and food production industries as a tool for both research and development and quality control. The technique has been established for some time and advances in electronics and the low cost of instrumentation enhance the attractiveness of the technique for PAT applications. Integration of UV-visible spectrometers to plant processes can be done by using transmission, transmittance, attenuated total reflectance (ATR) probes or flow cells. Transmission and transmittance probes are suitable when there is a low concentration of a highly absorbing sample present whereas ATR is more suitable at higher concentrations due to the small penetration depth (d_p) of the evanescent wave produced at the interface of the crystal.

Small penetration depths are ideal when analysing highly concentrated samples or samples that have large absorption coefficients (ε). When light hits the boundary between two materials at an angle higher than the critical angle (θ_c) an evanescent wave is produced (Equation 2.2)

$$\theta_c = \sin^{-1} \frac{n_2}{n_1} \quad \text{Equation 2.2}$$

where (n_1) is the refractive index of the waveguide (in the case of ATR UV-visible probes this is sapphire) and (n_2) is the refractive index of the sample and is lower than that of the waveguide.

The evanescent wave is produced at the point of reflection as the interference from the incident and reflected waves produces a standing wave which extends in to the sample perpendicularly and decays exponentially with the depth. The penetration depth (d_p) of the evanescent wave in to the sample is given by:

$$d_p = \frac{\lambda}{2\pi n_1 \sqrt{\left[\sin^2 \theta - \left(\frac{n_2}{n_1}\right)^2\right]}} \quad \text{Equation 2.3}$$

Physical phenomena such as diffusion, refraction, diffraction as well as chemical absorption will all contribute to the spectra of suspensions^{3, 4}. Hence, the measurement of suspensions using ATR UV-visible spectroscopy and correct interpretation of the results can be difficult

2.1.2 Infrared spectroscopy⁵⁻⁸

Electromagnetic radiation can be described as an electronic and magnetic field oscillating at the same frequency and perpendicular to each other. Photons of light are quantised (meaning that they can be described as discrete bundles of light) and the energy of each quanta is described by the Planck-Einstein equation (Equation 2.4)

$$E = h \frac{c}{\lambda} = hv; \quad \text{Equation 2.4}$$

where the energy (E) of a photon is equal to Planck's constant ($h = 6.626 \times 10^{-34} \text{ Js}^{-1}$) multiplied by the speed of light in vacuo (c) divided by the wavelength (λ) which is the frequency (ν).

The interaction of the electronic field with matter is used to understand the process of vibrational spectroscopy. Infrared spectroscopy depends on there being an energy transfer between the incoming light photon and the molecular groups in the substance. If the incoming energy matches the energy required to induce a vibration in a group which has a permanent dipole the light will be absorbed. A permanent dipole is when two bonded atoms have different electro negativities from each other such as C-O or C-H bonds. The different electronegativities forces one of the atoms to be more positively charged and one more negatively charged resulting in a dipole moment vector. The absorption of mid infrared radiation produces movement which will alter the dipole moment with the frequency of the wave, creating an electric field. The absorbed photon is then lost to kinetic transitions or re-emitted as a photon which can be absorbed in the same way as the original photon multiple times. This drastically reduces the likelihood of the photon re-emerging in the direction of the original path.

The infrared region covers the wavelength range 780 – 1,000,000 nm and the region between 2500 to 25,000 nm (*c.f.* 4000 to 400 cm^{-1}) is called the mid infrared region. The energy of the photons in this region corresponds to the energy required to produce an oscillation in most permanent dipoles in a molecule.

For instance, considering the case for a simple diatomic molecule; to shift the molecule from equilibrium will cause an exponential rise in the potential energy of the molecule. Firstly, the case of the harmonic oscillator model (blue parabola in Figure 2.2) is considered. The vibrational frequency (ν_0) required to shift the dipole moment is given by Equation 2.5 where k is the bonding force constant and μ is the reduced mass of the atoms making up the diatomic molecule (masses m_1 and m_2) and c is the speed of light.

$$\nu_0 = \frac{1}{2\pi} \sqrt{\frac{k}{\mu}} \text{ where } \mu = \frac{m_1 \cdot m_2}{m_1 + m_2} \quad \text{Equation 2.5}$$

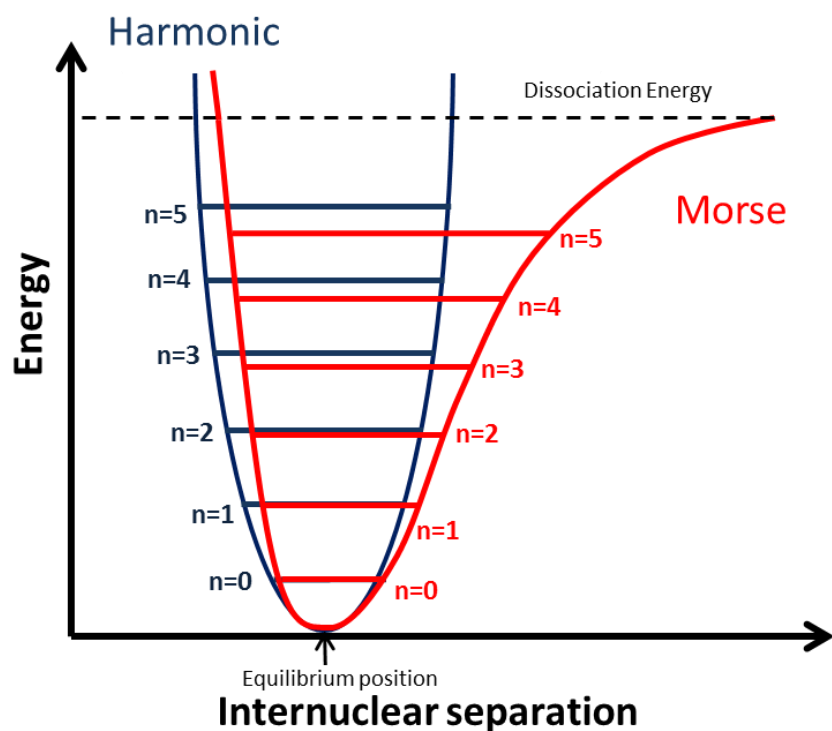


Figure 2.2 – Harmonic and anharmonic oscillator models for a diatomic molecule.

In the harmonic model the vibrational energy levels (n) are discrete and evenly spaced and their energy is given by:

$$E_n = h\bar{\nu}_0(n + 1/2) \quad \text{Equation 2.6}$$

where n is the vibrational quantum number and $\bar{\nu}_0$ is;

$$\bar{\nu}_0 = \frac{1}{2\pi c} \sqrt{\frac{k}{\mu}} \quad \text{Equation 2.7}$$

and c is the speed of light.

In the harmonic oscillator model the vibrational quantum number can only change by 1. The transition between $n = 0$ to $n = 1$ is known as the fundamental vibration as at room

temperature most of the molecules are in the ground vibrational state as described by the Boltzmann distribution (Equation 2.8).

$$\frac{N_1}{N_0} = \exp\left(\frac{-(E_1 - E_0)}{kT}\right) \quad \text{Equation 2.8}$$

The ratio of the number of molecules in the ground vibrational state to the excited state (N_0 and N_1 respectively) is the exponential product of the difference in energy between the two energy levels (E_0 and E_1) divided by the Boltzmann constant k ($1.3806 \times 10^{-23} \text{ JK}^{-1}$) and temperature (T). The energy of the fundamental vibration generally falls in the mid infrared region ($400 \rightarrow 4000 \text{ cm}^{-1}$ *cf.* $25,000 \rightarrow 2500 \text{ nm}$). The typical modes of vibration are described by bending and stretching (symmetric or asymmetric), rocking, wagging, and twisting.

Real life molecules are not ideal harmonic oscillators as the molecules are affected by properties of the surrounding groups in the molecule which may be electron withdrawing or electron donating. The Morse curve in Figure 2.2 is used to approximate the anharmonic model. The Morse curve incorporates bond breaking as the two nuclei are moved further apart and vibrational energy levels are no longer equally spaced. At lower energy levels the difference between $n_0 \rightarrow n_1$ and $n_1 \rightarrow n_2$ is small but the difference increases with increasing energy. To describe this mathematically an anharmonicity constant is introduced when $n \geq 2$

$$G_n = \frac{E_n}{hc} = \bar{\nu}_0 \left[\left(n + \frac{1}{2} \right) - x \left(n + \frac{1}{2} \right)^2 \right] \quad \text{Equation 2.9}$$

where the energy levels (G_n) are described by the anharmonicity constant, x , which leads to the uneven distribution of energy levels with increasing vibrational quantum number n . As a consequence, the transitions with $n > 1$ are allowed, and $n_0 \rightarrow n_2$ and $n_0 \rightarrow n_3$ are observed as overtones in the infrared region. The intensity of the transition is much lower than the fundamental vibration as the square root of the intensity of a

transition is inversely proportional to the probability of a transition. Heating a substance above room temperature can produce "hot bands" where there is a transition from an already excited vibrational state to the higher state but these are generally less intense.

Not all samples are simple diatomic oscillators and for polyatomic molecules the harmonic model states that the number of vibrations possible for a molecule consisting of n atoms is $3n-5$ for linear molecules and $3n-6$ for non-linear molecules. These are not the only bands observed in practical spectroscopy and as a result of the anharmonic model allowing higher transitions there are additional bands observed as a result of combinations and overtones of the fundamental vibration.

Combination bands arise from linear combinations of the fundamental vibrations and are typically weaker than the fundamental vibration. For example, light with an energy equal to the sum of the energy of two fundamental vibrations can be absorbed. These appear in the spectrum at the summed total of the wavenumber of the fundamental vibrations.

NIR spectra (780 – 2500 nm) exhibit peaks arising from combinations and overtones of fundamental vibrations of C-H, O-H, N-H and S-H functional groups. The absence of C-Cl, C-C, C=O etc is mainly due to the fact that the fundamental vibrations of each occur at low frequencies and the overtones are observed within the mid infrared region. Overtones occur at multiples of the fundamental vibration wavenumber but in reality the anharmonic models vibrational levels decrease with increasing number although this effect is small in the range of vibrational transitions observed in the NIR range.

In mid infrared spectroscopy the convention is to display the wavelength scale in the reciprocal form of wavenumbers (cm^{-1}) whereas near infrared spectra are nearly always produced with a nanometer scale (10^{-9} m). The range 2500 – 2000 nm features the strongest absorptions in the NIR region where the combinations and overtones appear. First, second and third overtones appear in the regions 2000-1500 nm, 1500 – 1100 nm, and 1100 – 780 nm respectively. The regions are a guide and overlap with the adjoining regions. The molecular absorption coefficients in the NIR wavelength range are low (ranging from 0.01 to $0.1 \text{ dm}^3 \text{ mol}^{-1} \text{ cm}^{-1}$) and decrease with wavelength as the probability of the transitions is reduced. The lower molecular absorptivity provides

another advantage as relatively thick samples can be probed using reflectance or transmission NIR measurements.

The Kubelka-Munk theory for diffuse reflection (Figure 2.3) can be represented by Figure 2.3. This equation represents the case when only diffuse reflection is measured and it assumes that the particles under analysis are much smaller than the depth of sample and that they are randomly distributed.

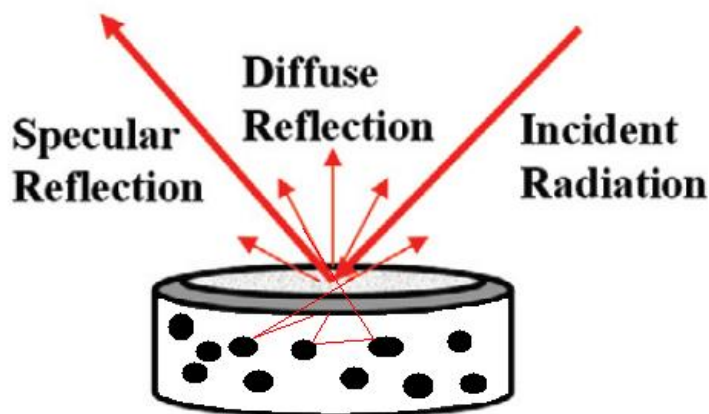


Figure 2.3 – Schematic of diffuse and specular reflection⁹.

$$\frac{K}{S} = \frac{(1 - R)^2}{2R} = f(R) \quad \text{Equation 2.10}$$

The Kubelka-Munk function, $f(R)$, is represented as the ratio between the coefficient of absorption K and the coefficient of scattering S , and R is the diffuse reflectance of the sample. The percentage reflectance of the sample is:

$$\%R = \left(\frac{I_R}{I_0} \right) \times 100 \quad \text{Equation 2.11}$$

where I_0 is the intensity of the incident light on the sample and I_R is the intensity of the diffusely scattered light collected by the integrating sphere. The absorbance of the sample is given by:

$$A = \log\left(\frac{1}{R}\right) \quad \text{Equation 2.12}$$

Kubelka-Munk adequately describes the interaction of NIR light with larger particle sizes in the μm domain but breaks down when the particle size is in the nm domain, such as the pigment dispersions analysed herein. In this case Mie theory is used to rationalise the interaction of NIR light with concentrated pigment dispersions and is discussed in more details in section 4.1.3.

2.1.3 Raman spectroscopy¹⁰⁻¹²

Unlike infrared vibrational spectroscopy, Raman spectroscopy does not require a permanent dipole and instead relies on a weaker effect where an induced dipole is created by an incoming light source. This allows vibrational spectroscopic information to be obtained for homonuclear systems such as S_8 or carbon to carbon double and single bonds. The electronic vector of the incoming wave distorts the electron cloud in a molecule, temporarily creating a dipole. A high intensity laser light source is required to produce enough Raman scattered photons. The classical theory of Raman spectroscopy states that when the electric field (E) is low enough the magnitude of the induced dipole (P) is proportional to the polarisability (Equation 2.13). The polarisability (P) is a measure of how easily the electron cloud can be distorted to produce a dipole.

$$P = \alpha E \quad \text{Equation 2.13}$$

The oscillating electric field (E) supplied by the laser is described by

$$E = E_0 \cos 2\pi\nu_0 t \quad \text{Equation 2.14}$$

where ν_0 is the frequency of the laser, E_0 is the intensity of the laser and t is time. By substituting Equation 2.14 in to Equation 2.13 we get:

$$P = \alpha E_0 \cos 2\pi\nu_0 t \quad \text{Equation 2.15}$$

For Raman active bonds, Q is the magnitude of displacement of the molecular vibration where Q_0 is the maximum vibration

$$Q = Q_0 \cos 2\pi\nu t \quad \text{Equation 2.16}$$

where ν is the vibrational quantum number. If the distortion causes a change in the polarisability that is small and linear, the polarisability of the molecules is described by:

$$\alpha = \alpha_0 + \left(\frac{\delta\alpha}{\delta Q}\right)_0 Q \quad \text{Equation 2.17}$$

where α_0 is the polarisability of the molecule at equilibrium and the rate of change of change of polarisability is described by $\left(\frac{\delta\alpha}{\delta Q}\right)_0$. Hence, the polarisability can now be described as:

$$\alpha = \alpha_0 + \left(\frac{\delta\alpha}{\delta Q}\right)_0 Q_0 \cos 2\pi\nu t \quad \text{Equation 2.18}$$

Substituting Equation 2.18 in to Equation 2.15 gives:

$$P = \left\{ \alpha_0 + \left(\frac{\delta\alpha}{\delta Q}\right)_0 Q_0 \cos 2\pi\nu t \right\} E_0 \cos 2\pi\nu_0 t \quad \text{Equation 2.19}$$

By using the product of two cosine rules, Equation 2.19 can be rewritten as:

$$P = \alpha_0 E_0 \cos 2\pi\nu_0 t + \frac{1}{2} \left(\frac{\delta\alpha}{\delta Q} \right)_0 Q_0 E_0 \{ \cos 2\pi(\nu_0 + \nu_n)t + \cos 2\pi(\nu_0 - \nu_n)t \} \quad \text{Equation 2.20}$$

where $(\nu_0 + \nu_n)$ and $(\nu_0 - \nu_n)$ represent the contributions from anti-Stokes and Stokes scattering, respectively and n is the vibrational quantum number. The first term shows the contribution from Rayleigh scattering which will produce a peak at the laser excitation frequency.

Stokes scattering occurs when the molecule is excited from the ground vibrational state to a virtual excited state and relaxes to the vibrational state above the ground state ($\Delta n = 1$). Stokes scattering is measured in conventional Raman spectroscopy as at room temperature the vast majority of molecules are in the lowest vibrational energy level (which was already discussed in reference to NIR spectroscopy, Equation 2.8). Anti-Stokes scattering gives rise to a mirror image of the bands observed in Stokes scattered light but the intensities are much reduced as there is a lower probability of the molecules already inhabiting the higher vibrational energy levels.

The intensity (I) of Raman active bands is described by

$$I = \frac{k I_{excitation} \alpha^2}{\lambda^4} \quad \text{Equation 2.21}$$

where I is directly proportional to the intensity of the laser ($I_{excitation}$) and inversely proportional to the 4th power of the wavelength of the laser (λ). The other terms represent a constant (k) and the polarisability (α). This has practical implications as there is a trade-off between moving to a higher wavelength to reduce fluorescence and the intensity of Raman scattering. At lower wavelengths the scattering is strongest but so is the likelihood of sample fluorescence.

2.2 Particle sizing

There are a variety of techniques by which particle size can be measured ranging from the use of microscopy to automated techniques which take advantage of the way laser light interacts with particles of different size such as laser diffraction or dynamic light scattering (DLS, also known as or quasi-elastic light scattering). Many commercial instruments are available that are designed to analyse dry powders, slurries and droplets (as are used in aerosol drug delivery) from manufacturers such as Malvern¹³, Sympatec¹⁴ and Brookhaven instruments¹⁵ which are specialised for each application and some instruments can be used on-plant to provide real time data for industrial processes. The milled dispersions generated throughout this project were analysed using dynamic light scattering. Some of the particle size analysis provided by FFIC on the larger scale laboratory and plant experimentation used a combination of dynamic light scattering and laser diffraction particle size analysis.

2.2.1 Dynamic light scattering theory¹⁶⁻¹⁸

For any DLS it is essential that there be a difference between the refractive indices of the dispersed and dispersing medium for scattering to occur. If the refractive indices were identical, the dispersion would appear homogeneous and no scattering would occur as the laser light travelled through the sample.

When laser light is directed at a heterogeneous solution, it is absorbed and re-emitted if the wavelength of light used does not coincide with an absorption band of the sample. This re-emitted light is scattered light. Rayleigh scattering describes when smaller particles are illuminated by the laser in the DLS instrument. When the diameter of the particle is below one tenth of the excitation source wavelength ($d < \lambda_{source}/10$) the particle scatters light isotropically (light is scattered equally in all directions). The Rayleigh scattering phenomenon can be characterised by Equation 2.22 and Equation 2.23.

$$I \propto d^6$$

Equation 2.22

and

$$I \propto \frac{1}{\lambda^4}$$

Equation 2.23

where the intensity of scattered light (I) is directly proportional to the 6th power of the particle diameter (d) and inversely proportional to the fourth power of the wavelength of the source (λ). This illustrates that the intensity of scattered light will be one million times greater than that of a particle of one tenth of its size. This will add complications when measuring dispersions where the signal from the larger particles may swamp the contribution from the smaller particles in the sample.

Mie theory^{19, 20} can best describe the scattering system when the particle sizes under analysis are similar in size to the wavelength of the laser source used in the instrument. The intensity of scattered light is highly dependent on the angle at which the light is collected and the particle size. The intensity of scattered light observed at the 90° and 173° position is different and Mie theory is used to account for the difference in scattering distribution with angle and particle size. Key limitations to Mie theory include cases where the particles analysed are not completely spherical although it is noted that literature is available²¹ where this problem is addressed. The advantages of the 173° scattering collection is that the collection area is larger in the cuvette and that the scattering is less affected by larger particles such as dust which may have contaminated the sample.

The process of scattering arises as the laser light (which is an electromagnetic wave) interacts with the charges in the molecules suspended in the dispersion causing them to oscillate and as a result of this oscillation the particles can be seen to emit radiation in all directions. This electromagnetic radiation is the scattered light.

As the laser is directed toward the heterogeneous solution and the light is scattered by particles which are moving randomly by Brownian motion a speckle pattern is observed at the detector which is a result of constructive and destructive interference of the scattered light. The dispersed particles under analysis undergoing random Brownian motion are moving in all directions and this means that the frequency of the scattered light will be Doppler shifted. Where particles are moving towards the detector there will

be an increase in frequency and where the particle is moving away from the detector there will be a decrease in frequency.

$$\Delta f = -\frac{v_{rel}}{\lambda_0} \quad \text{Equation 2.24}$$

where v_{rel} is the velocity of the particle relative to the detector and negative when the particle is moving away from the detector. Conversely, v_{rel} is positive when moving away from the detector. λ_0 is the wavelength of the light. When the dispersed particles are undergoing random movement, the resulting distribution will appear as a Lorentzian distribution and the width at half height of the distribution is related to the translational diffusion coefficient of the particle in dispersion. For a result to be representative of the sample it is important to accurately maintain the temperature of the dispersion in the cuvette as thermal currents within the sample will remove the randomness of motion of the particles resulting in a change in the speckle pattern.

The result obtained from the instrument is given as the diameter of a sphere with an equivalent diffusion rate, the hydrodynamic diameter (d_H). This is determined from the Stokes-Einstein equation:

$$d_H = \frac{kT}{3\pi\eta D} \quad \text{Equation 2.25}$$

where k is Boltzmann's constant, T is the temperature, η is the viscosity and D is the translational diffusion coefficient which is related to the width of shifted frequencies of light created by the Doppler shifted scattered light from the particles. The width at half height of the distribution of frequencies (Γ) is given by Equation 2.26

$$\Gamma = Dq^2 \quad \text{Equation 2.26}$$

and

$$q = \frac{4\pi n}{\lambda} \sin \theta/2 \quad \text{Equation 2.27}$$

where q is the magnitude of the scattering vector, n is the refractive index of the medium, λ is the wavelength of the light and θ is the detection angle of the scattered light.

Smaller particles will move faster causing the speckle pattern to change more quickly whereas the larger particles will move more slowly and hence the speckle pattern intensity will change as the dispersed particles move. Particle size is determined by using a correlation function to compare the signals at the detector. Particles which are larger and therefore move more slowly will exhibit a higher correlation of signal at the detector for a longer time as opposed to smaller particles which will change very rapidly (see Figure 2.4).

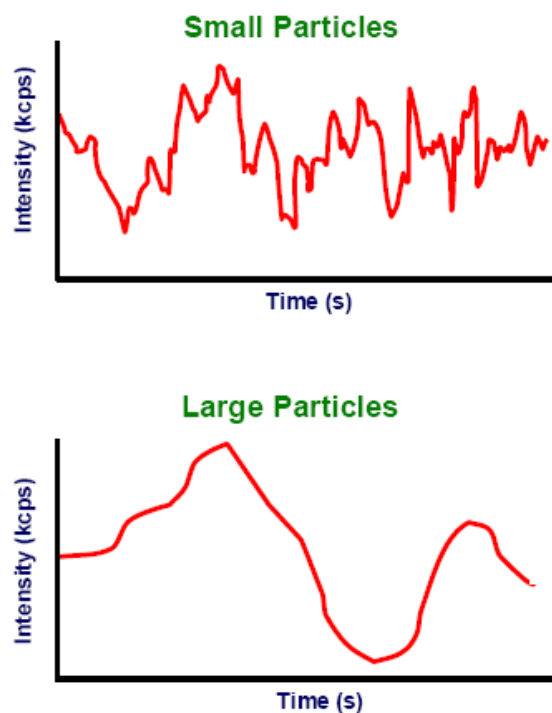


Figure 2.4 – Illustration of the observed intensity of scattered light for small and large particles²² .

The correlator function is used to compare differences in the intensity of a signal at very short time intervals, if a signal has not changed after a small time delay the correlation

would be high (close to 1) whereas if the intensity has changed and shows no resemblance to the original intensity the correlation will be low (close to 0). By following the loss in correlation of the scattered signal intensity, particle size can be inferred. Figure 2.5 shows the decaying correlation for intensity signals as time progresses and highlights the key properties of the shape of the correlogram that are indicative of the particle size in the sample.

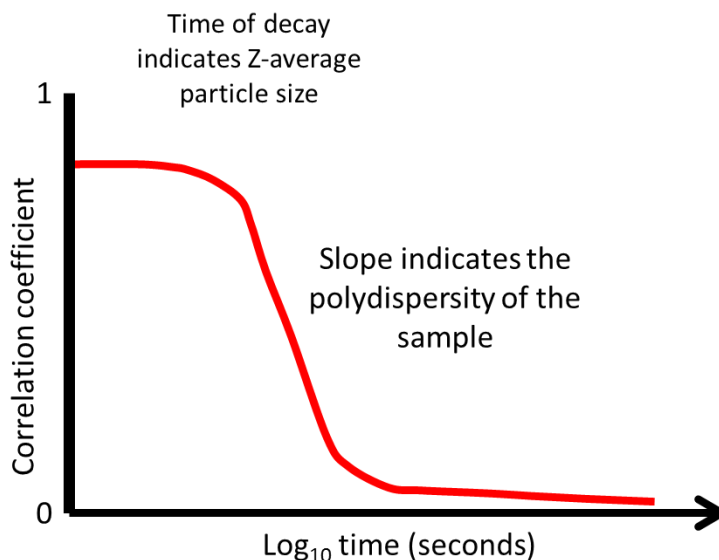


Figure 2.5 – Correlogram showing the decaying correlation of intensity signals over time

If the correlation coefficient remains high for a longer time (i.e. the observed intensity of scattered light does not change quickly) this is indicative of larger particle sizes. The gradient of the correlation coefficient decay is related to the polydispersity of the sample and the base line will not reach zero if there are a large number of oversize sedimenting particles.

To extract information from the correlogram a third order fit of a polynomial to a semi-log plot of the correlation is performed (see Figure 2.6).

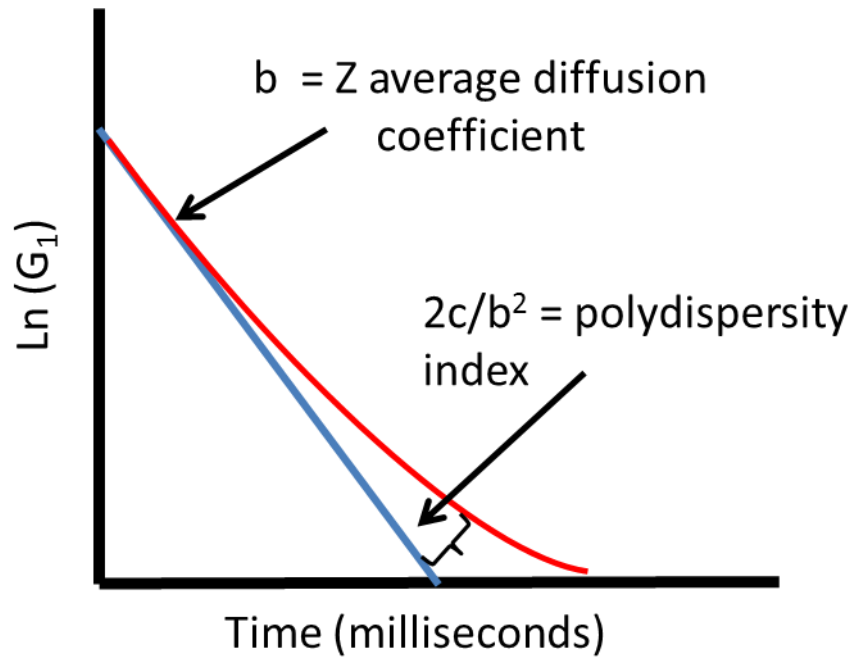


Figure 2.6 – Cumulants fit to the semi log plot of the correlation function.

$\ln(G_1)$ is the natural log of the correlation function G_1 . The initial gradient of the slope (b) is used as the average diffusion coefficient of the sample for the determination of particle size using Equation 2.25 and the polydispersity is a measure of the deviation of the slope b from the 3rd order polynomial fitted to the data. This polydispersity value is between 0 and 1 and describes the distribution of particle sizes present in the sample. When the sample is monodisperse, as in the case for latex standards, the value will be <0.05 . Most samples will fall in the region between 0.05 to 0.7. In this region the intensity distribution, generated by analysing the correlation function by non-negative least squares (NNLS), is used.

For completeness, the equation of the curve from the experimental data in Figure 2.6 is represented as

$$\ln[G_1] = a + b\tau + c\tau^2 \quad \text{Equation 2.28}$$

where $b\tau$ is the first cumulant and $c\tau^2$ is the second cumulant at time interval τ .

2.2.2 Laser diffraction^{23,24}

Laser diffraction works on the principle that larger particles scatter more light than smaller particles. Figure 2.7 shows a basic schematic of a typical laser diffraction set up.

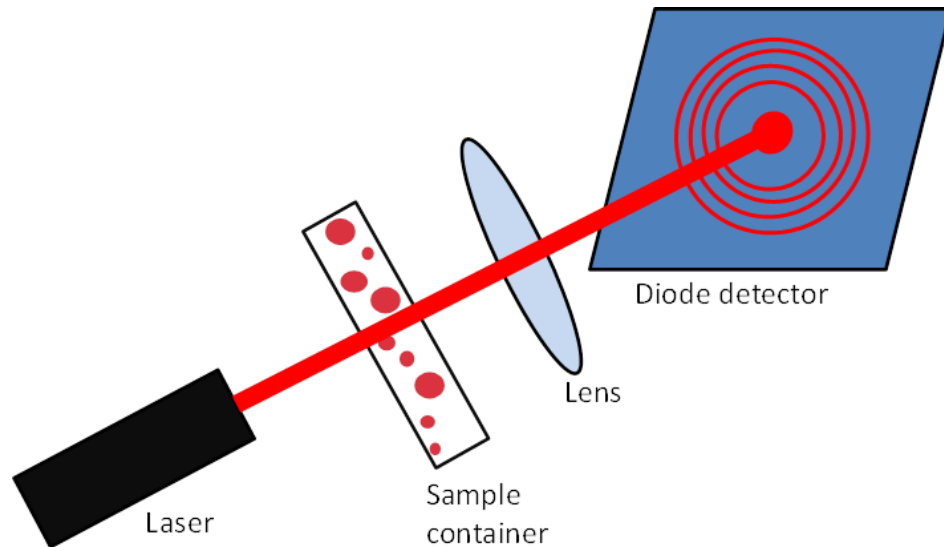


Figure 2.7 – Basic laser diffraction apparatus schematic showing a diffraction pattern for a single spherical particle.

The laser light is diffracted on interaction with the particulate sample before being focused on to a set of ring diodes where an interference pattern is produced. Multiple scattering effects create different interference patterns for single particles, and hence, samples are introduced to the laser at a low concentration. The basis of the technique is that the scattering pattern from a single particle is a function of the particle size. Two main mathematical theories are used to generate a particle size from the laser diffraction pattern. Fraunhofer is used to predict particle size when the particles are much larger than the wavelength of the illuminating laser and Mie theory is used to cover the complete range of particle sizes (nm to μm). Both theories are computationally intense but Fraunhofer theory requires less information on the optical properties of the sample. Fraunhofer theory makes the assumptions that the particles are 2 dimensional circular opaque discs and that light only interacts with the surface of the particle. Only low angle light scattering is considered for Fraunhofer scattering calculations although most new particle size instruments come with a number of detectors capable of measuring the

low angle scattered light (from larger particles) and the wide angle scattered light from smaller particles.

Like Fraunhofer theory, Mie theory assumes that all particles are spherical and requires the analysis of dilute particles to remove multiple scattering effects. Unlike Fraunhofer theory, the optical properties of the sample and the dispersing media have to be used in the calculation describing absorption and scattering. Light which impinges on a sample can undergo one of several processes (as shown in Figure 2.8) and Mie scattering accounts for all of these phenomena using the interference patterns at low and wide angle detectors.

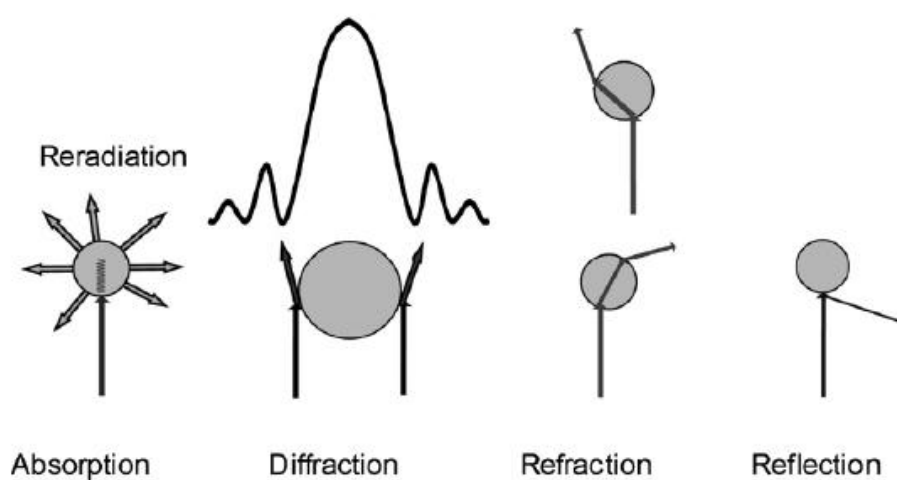


Figure 2.8 – Physical phenomena of light scattering when interacting with suspended colloidal particles⁴.

2.3 Data Analysis

In addition to univariate methods of data analysis, multivariate techniques such as principal component analysis (PCA) and partial least squares (PLS) regression have been used to interpret vast numbers of complex spectra obtained using NIR and Raman spectroscopy instruments. The advantage of using such techniques is that they can compress large numbers of complex spectra, each containing many data points, into just a few variables which are easier to visualise and identify trends in the data. PCA is used primarily as an investigative tool for visualising trends and groupings in the spectral

data whereas PLS is used quantitatively to model and predict a measured parameter such as particle size from input spectra.

2.3.1 Multivariate techniques^{25,26}

PCA is represented by Figure 2.9 and Equation 2.29 where a matrix of spectra are decomposed into scores and loadings plus a residual matrix which represents the data not captured by the scores and loadings.

$$\boxed{X} = \boxed{T} \boxed{P} + \boxed{E}$$

X = Data set $i \times j$ (samples \times data points)

T = Scores Matrix $i \times A$ (samples \times number of principal components)

P = Loadings matrix $A \times j$ (number of principal components \times data points)

E = Residual matrix $i \times j$ (samples \times data points)

Figure 2.9 – PCA.

$$X = T.P + E$$

Equation 2.29

Firstly, the input dataset is mean centred whereby a mean is calculated for each column and this mean subtracted from every value in the column. The mean centering step is important as if it is omitted the first principal component will represent an average spectra and not the variance in the data set. As the following components are orthogonal to the first they are effectively constrained by the first principal component and more principal components will be required to capture the variation in the data set.

Each scores value represents a sample (in this case, a spectrum) and shows how similar or different the samples are from each other. The loadings values show the correlation between the individual data points (j). In reality there are often several sets of scores and loadings used to characterise large datasets with the first PC capturing the largest variation in the data. Is it desirable to select a number of components that does not over fit the data, hence, when selecting the number of principal components the user should

bear in mind the number of elements causing the change (i.e. to model a 3 solvent system with different concentrations, the number of principal components should be 3).

PLS is used to build quantitative models which can predict the properties of a sample provided it is in the range of the data used in the calibration data. In this instance the X block represents multivariate measurement such as spectra and the y block contains some quality attribute or property which has been measured in the laboratory. PLS1 is used in situations where the Y block represents only one measured property such as particle size or concentration. When the Y block contains more than one measured property (i.e. is multivariate) PLS2 is used.

PLS is similar to PCA whereby scores and loadings are calculated for the data matrices X and Y (see Figure 2.10 and Equation 2.30) but although the models are structurally similar to PCA models there are differences in the way the scores and loadings are calculated.

$$\begin{array}{rcc}
 \boxed{X} & = & \boxed{T} \boxed{P} + \boxed{E} \\
 \boxed{y} & = & \boxed{R} \boxed{q} + \boxed{f}
 \end{array}$$

- X = Data set i x j (samples x data points)
- T = Scores Matrix i x A (samples x number of latent variables)
- R = Scores Matrix i x A (samples x number of latent variables)
- P = Loadings matrix A x j (number of latent variables x data points)
- E = Residual matrix i x j (samples x data points)
- y = Reference data (i x 1 for 1 reference value e.g. particle size)
- q = Loadings vector (i x A samples x number of latent variables)
- f = Residuals vector (i x 1)

Figure 2.10 – Partial least squares regression example for PLS1.

$$\begin{aligned} X &= T \cdot P + E \\ y &= R \cdot q + f \end{aligned}$$

Equation 2.30

Instead of independently calculating the scores and loadings for each of the data matrices X and y, PLS calculates score values which have the maximum covariance between T and R. Maximising the covariance between T and R, and hence the correlation between both, enables the model to use the scores from the X block to predict the scores value of the y block. From this predicted score value for the y block, R, the prediction of y can be calculated simply as the predicted scores value multiplied by the loadings plus the residuals.

2.3.2 Derivatives

Sometimes it is necessary to apply derivatives to spectra prior to univariate or multivariate analysis. Transforming data to the first or second derivative is done using the Savitzky-Golay function which includes a smoothing parameter. Derivatives can be particularly useful for removing baseline offsets (1st derivatives) or sloping baseline offsets (2nd derivatives). Figure 2.11 shows the basic transform of a data set with a baseline off-set. The 1st derivative basically shows the rate of change of a tangent drawn at each point of the untreated data. When the slope is increasing most, the value is high and positive, when the slope is flat, such at the top of the peak in the untreated data, the value of the 1st derivative is zero and when the untreated data decreases quickest, the gradient of the tangent is negative and large. The second derivative shows the rate of change of the first derivative in the same way the first derivative represents the rate of change in the untreated data.

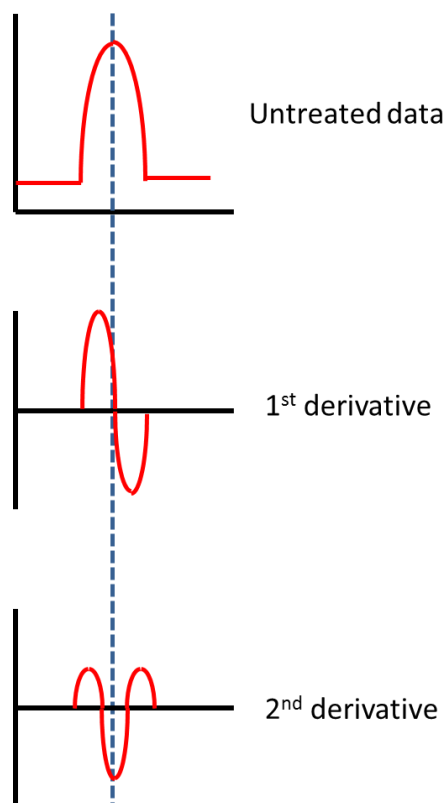


Figure 2.11 – Exemplar first and second derivative transforms.

2.4 Summary

Chapter 2 has detailed the theory behind each the main on-line/off-line optical spectroscopic techniques, particle characterisation and data interpretation tools (multivariate analysis and basic data pre-processing by calculating derivatives). All of which are used to explore UV-visible, NIR, MIR and Raman as potential methods of measuring the particle size of concentrated pigment dispersions on-line.

2.5 References

1. P. Matousek, M. Towrie, A. Stanley and A. W. Parker, *Appl. Spectrosc.*, 1999, **53**, 1485-1489.
2. R. E. Littleford, P. Matousek, M. Towrie, A. W. Parker, G. Dent, R. J. Lacey and W. E. Smith, *Analyst*, 2004, **129**, 505-506.
3. C. Berho, M. F. Pouet, S. Bayle, N. Azema and O. Thomas, *Colloids and Surfaces A: Physicochemical and Engineering Aspects*, 2004, **248**, 9-16.
4. C. M. Keck and R. H. Muller, *International Journal of Pharmaceutics*, 2008, **355**, 150-163.
5. *Near-infrared spectroscopy : principles, instruments, applications*, Weinheim : Wiley-VCH, 2002.
6. J. Maas, *Basic infrared spectroscopy*, Heyden, 1972.
7. B. G. Osborne, *Practical NIR spectroscopy with applications in food and beverage analysis*, Harlow, Essex, England : Longman Scientific & Technical ; New York : Wiley, 1993.
8. M. Blanco, J. Coello, H. Iturriaga, S. Maspoch and C. de la Pezuela, *Analyst*, 1998, **123**, 135R-150R.
9. http://www.hunterlab.com/appnotes/an07_06.pdf (Accessed 01 Jun 09).
10. *Pharmaceutical applications of Raman spectroscopy*, Hoboken, N.J. : Wiley-Interscience, 2008.
11. E. Smith & G. Dent, *Modern Raman spectroscopy : a practical approach*, Hoboken, NJ : J. Wiley, 2005.
12. I. Lewis, *Handbook of Raman spectroscopy : from the research laboratory to the process line*, New York : Marcel Dekker, 2001.
13. http://www.malvern.com/LabEng/products/iwtm/particle_size.htm (accessed 26 Nov 09).
14. <http://www.sympatec.com/Index/Portfolio.html> (accessed 26 Nov 09).
15. http://www.bic.com/Particle_Sizers_overview.html (accessed 26 Nov 09).
16. R. Finsy, *Advances in Colloid and Interface Science*, 1994, **52**, 79-143.
17. *Malvern instruments - Nanometrics training course*, Training manual.
18. M. L. McConnell, *Analytical Chemistry*, 1981, **53**, 1007A-1018A.

19. C. F. Bohren and D. R. Huffman, *Absorption and light scattering by small particles*, Wiley-Interscience, 1998.
20. J. A. Lock and G. Gouesbet, *Journal of Quantitative Spectroscopy and Radiative Transfer*, 2009, **110**, 800-807.
21. A. Doicu, F. Ebert and S. Schabel, *Particle and Particle Systems Characterization*, 1996, **13**, 79-88.
22. *ZS90 DLS instrument brochure*, Malvern Instruments.
23. M. McGarvey, D. McGregor and R. B. McKay, *Progress in Organic Coatings*, 1997, **31**, 223-228.
24. H. G. Merkus, *Laser Diffraction Particle Size Measurements*, Springer Netherlands, 2009.
25. J. N. Miller, *Statistics and chemometrics for analytical chemistry*, Harlow, England ; New York : Pearson/Prentice Hall, 2005.
26. R. G. Brereton, *Chemometrics: Data analysis for the laboratory and chemical plant*, Wiley, 2003.

3. Experimental

Pigment dispersions were prepared from materials provided by FFIC and milled to reduce their particle size. The milling experiments were monitored using NIR or Raman spectroscopy and off-line particle size analysis was performed on diluted pigment dispersions collected at different stages of the milling process.

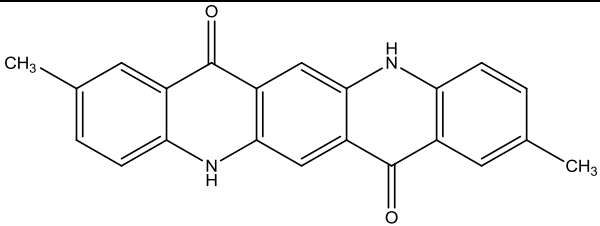
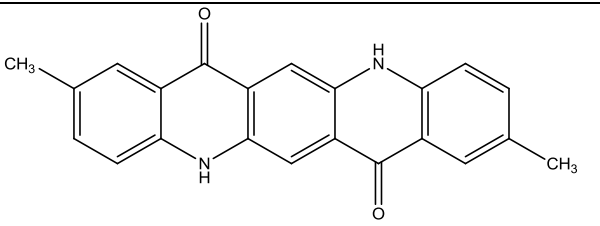
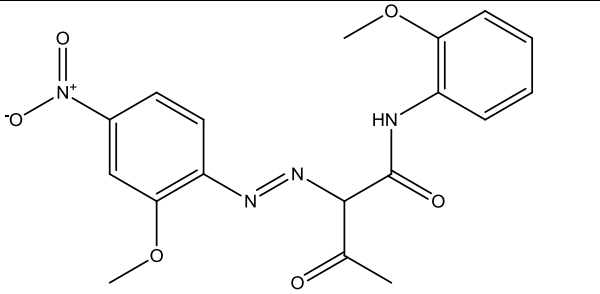
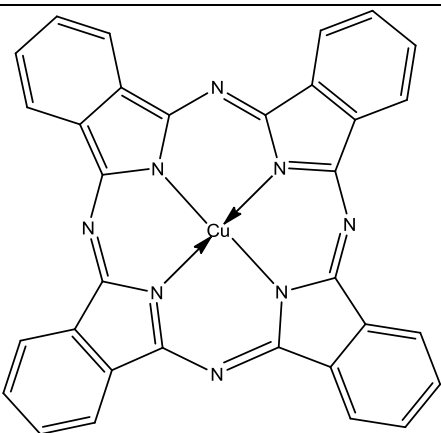
Samples were also diluted for off-line NIR transmission and reflectance measurements and these results were used to determine the fundamental optical properties of the diluted pigment dispersion samples.

3.1 Materials

3.1.1 Pigment powders

The following pigment powders were provided by FFIC, Grangemouth (Table 3.1).

Table 3.1 – Pigment materials provided by FFIC.

	<p>Clariant IJ E5B02 VP2984 Pigment Violet 19, quinacridone CAS 1047-16-1</p>
	<p>Sunfast red 122 220-8828 Pigment Red 122, 2,9-Dimethyl quinacridone, CAS 980-26-7</p>
	<p>Irgallite yellow GS Pigment yellow 74 (PY74) 2-[(2-Methoxy-4-nitrophenyl)azo]- N-(2-methoxyphenyl)-3- oxobutylamide CAS 6358-31-2</p>
	<p>Sunfast Cyan 249-8450, Pigment blue. 15:4 Copper (II) phthalocyanine CAS 147-14-8</p>

3.1.2 Polymer

The polymers used in all experimental work were sourced or manufactured by FFIC, Grangemouth. The three that were used are called: Acid 10, Acid 45 and Acid 46.

All 3 polymers are acid functional methacrylate copolymers, prepared in a glycol solvent. Hydrophobic moieties in the polymer encapsulate the pigment surface whilst hydrophilic carboxylic acid groups extend out in to the surrounding water. The size of the polymer and the resulting charge from the acidic groups stabilise the pigment dispersions by ionic and steric stabilisation. Table 3.2 contains the polymer concentrations.

Table 3.2 – Polymer concentrations

Polymer	Strength (%)
Acid 10	35.0
Acid 46	31.5
Acid 45	31.0

3.2 Pigment dispersion preparation

Several pigment dispersions were prepared for experimentation. An exemplar procedure is presented for a 600 g dispersion of 20 % w/w PR122 with 40 % loading of polymer Acid 46. Explanations of the terminology are provided. To prepare 600 g of 20% w/w pigment dispersion, the required weight of pigment (assuming 100 % purity) is:

$$\underline{20\% \text{ of } 600 \text{ g} = 120 \text{ g Pigment PR122}}$$

Secondly, the required polymer weight is calculated. Polymer loading refers to the weight of polymer present relative to the pigment.

$$\underline{40\% \text{ of } 120 \text{ g Pigment PR122} = 48 \text{ g Polymer Acid 46}}$$

The polymer solution is not 100 % polymer. In the case of Acid 46 it is only 31.5 % (Table 3.2) polymer, hence;

$$\underline{\text{Total Acid 46 required} = 48 \times (100 \div 31.5) = 152.38 \text{ g Polymer Acid 46}}$$

To make the total weight up to 600 g water is added,

$$\underline{\text{Water required} = 600.00 - 120.00 - 152.38 = 327.62 \text{ g}}$$

To prepare pigment dispersions; the following procedure was followed:

- The required weights of polymer and water were weighed into a large beaker and tared on a 2 figure top pan balance situated within a dust cabinet.
- The mixture was then blended using a Kenwood hand blender until the contents of the beaker displayed a smooth consistency.
- The required charge of pigment powder was dispensed in the dust cabinet and weighed in to the water/polymer solution.
- The dispersion was first mixed by hand using a large spatula whilst in the dust cabinet. Once the pigment was wet, the possibility of dust release is eliminated, and the materials may now be used on the open bench.
- The contents of the beaker were then further blended using the Kenwood hand blender for between 5 to 10 minutes to produce a smooth dispersion.

3.3 Milling

The Netzsch minizeta mill (Figure 3.1) is a lab scale bead mill used for the reduction of particle size of dispersions in the pharmaceutical and consumer product industries. The high energy milling chamber houses a high speed stainless steel agitator, which operates at 3080 rpm, and a 200 ml charge of ceramic beads of 0.6 to 0.8 mm in diameter. The rapid movement of the beads results in the dispersing of loosely held floccules and the fracture of larger pigment particles as the milling progresses.

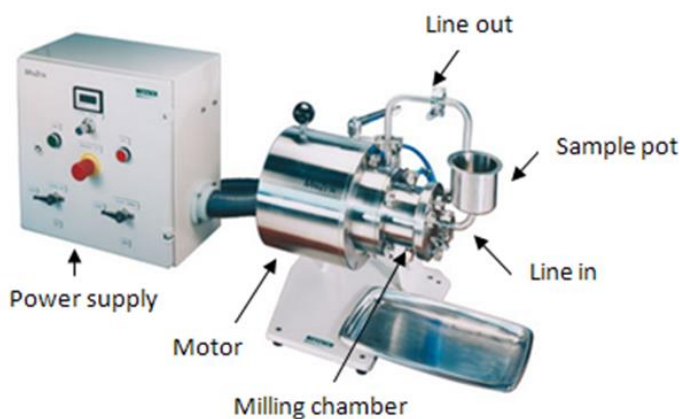


Figure 3.1 - Netzsch Minizeta mill.¹

The milling chamber is water jacketed to remove the heat produced from the frictional forces generated and millings typically take between 4 to 5 hours until the pigment dispersion particles have a Z average particle size between 100 and 130 nm. The efficiency of a milling experiment and the rate at which the particle size is reduced not only depend on the rate of the agitator speed in the chamber but the viscosity of the mill base. Milling at lower viscosity reduces the rate at which the milling proceeds. When less energy is absorbed by the dispersed particles, the energy is dissipated on collision of the beads with the internal surfaces of the mill chamber. This can result in excessive wear to the agitator, mill chamber and screen that are in contact with the fast moving ceramic beads. As the milling progresses the amount of energy required to reduce the size of the particles increases and the profiles obtained from experimental data show that the greatest change occurs early in the process. Figure 3.2 shows a typical particle size reduction profile obtained during a milling experiment.

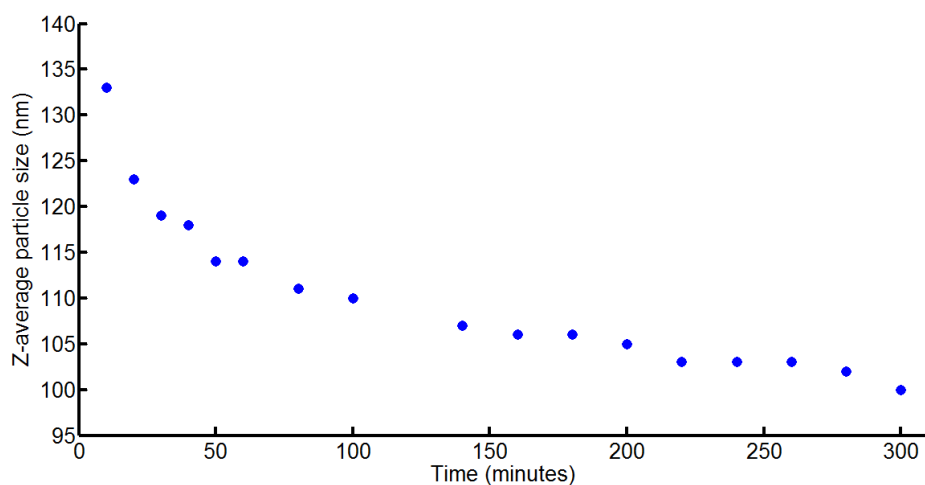


Figure 3.2 - Typical particle size reduction profile for 20 % w/w PR122 pigment dispersion containing 40% polymer acid 46 milled for 5 hours using the Netzsch minizeta lab mill.

The trend observed in the reducing Z-average particle size is typical of all the milling experiments performed herein and is similar for all colours of pigment (cyan, magenta and yellow).

200 mL milling media (ceramic beads 0.6 to 0.8 mm) were placed in the centre of the milling chamber containing the agitator by careful decantation whilst the mill was locked in the upright position. A section of 90° L-shaped pipework was secured to the outlet of the milling chamber by triclover fittings. This prevented accidental release of the pigment when the milling chamber was loaded with liquid in the upright position. Milling media which escaped was immediately collected by using adhesive tape. The pigment dispersion was then added to the chamber by careful decantation. When the milling chamber was full the chamber endplate was attached by three bolts, followed by attaching the sample reservoir and the chamber draining hole plug to the end plate. At this point the mill and motor were rotated and locked in the horizontal position. Further sample was then added to the mill pot and a second 90° bend attached to the outlet of the milling chamber to provide a return loop to the

sample pot. An agitator was then placed in the sample pot to stir the pigment dispersion.

The mill requires a water flow to prevent a dangerous build-up of heat in the milling chamber and to prevent excessive wear to the lip seal unit which prevents sample washing back from the milling chamber to the motor. Water was provided to the lip seal unit by a gravitational feed and to the milling chamber jacket by regulating the mains pressure at the tap. The purpose of the gravitational feed system for the lip seal unit was to prevent excessive pressure which may have caused the seals to invert and fail.

Temperature trips are incorporated in to the design of the mill to prevent dangerous operating conditions. High viscosity samples may cause heat to be generated in the mill, however, trips in the power unit (when the mill draws too much current) or temperature trips will prevent the mill continuing under unsafe operating conditions. The power unit contains a red emergency stop button on the centre of the panel for rapid shutdown in case of emergency or to make the equipment safe in the event of a building evacuation.

To start up a milling experiment, the agitator in the milling chamber was gradually increased to 3080 rpm and the outflow of the recirculation line was observed to ensure that there were no blockages in the system. If an unusually low flow was observed the flow rate and agitation speed in the chamber (both controlled by the same function in the control panel) were cycled several times between low and high rpm. This procedure was able to remove most blockages and air locks in the milling system. For the first few minutes of milling, the outflow of the pigment dispersion was collected in to the plastic beaker that the pigment dispersion was prepared in and the contents mixed and added back to the mill sample reservoir. This ensured a representative sample was added to the mill.

Post experimentation, preliminary cleaning of the mill was performed by switching the mill chamber agitator and pump unit down to low rpm and collecting the return feed in to a plastic bottle. The process was repeated, filling the sample reservoir with warm water until the collected wash water was no longer strongly coloured. The waste liquid was collected in 5 L jerry cans for disposal.

After isolation from the power supply, the mill was dismantled as per manufacturer instructions for cleaning with 5% decon 90 solution. Collection of the milling media was done by placing a metal tray under the mill which was tipped at a downward angle of 15° and removing the end plate. Media which remained in the chamber was washed in to the tray using a water bottle. Strongly contaminated water washings from cleaning the mill components were collected for waste disposal.

3.3.1 Netzsch Labstar mill

The Netzsch labstar mill (Figure 3.3) is the same basic configuration of the minizeta mill but accommodates larger batch sizes up to approximately 13 kg. The main difference is that the peristaltic pump controlling the recirculation of the pigment dispersion from the sample reservoir to the milling chamber can be independently controlled.

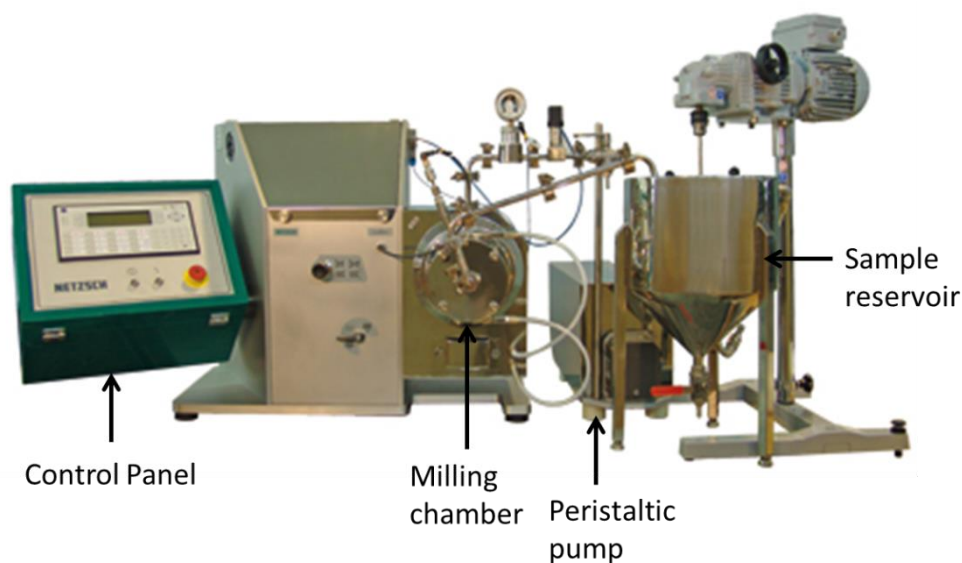


Figure 3.3 – Netzsch Labstar mill. 2

Plastic beads were used in the milling chamber in place of the spherical ceramic beads. Typical milling times for magenta and cyan pigments were between 10 and 20 hours. Milling of yellow dispersions can take substantially longer (> 30 hours). Operation of the mill was comparable to that described in for the Netzsch minizeta mill.

3.4 Spectroscopic measurements

During the course of the experimental work 3 spectroscopic techniques have been employed using different spectrometer systems. UV-visible ATR, NIR reflectance and non-contact Raman spectroscopy have used to obtain in-process measurements. Diluted pigment samples were analysed off-line using a bench top visible-NIR instrument and some additional work was performed on small scale milling experiments using Raman spectroscopy. The following sections detail the spectrometers used. Appendix 10.1 contains five tables of additional specification information for the Zeiss MCS 522 UV-Visible (Table 10.1), ABB MB3000 FTIR (Table 10.2), Foss on-line 6500 NIR (Table 10.3), Cary 5000 UV-Visible-NIR (Table 10.4) and the Kaiser RXN 1 PhAT probe system (Table 10.5)

3.4.1 UV-visible spectroscopy

UV-visible ATR spectra were collected using a Carl Zeiss MCS 522 UV-visible spectrometer (Figure 3.4). The spectrometer has a xenon flash lamp source and two 256 channel photodiode detectors (Figure 3.5) which allow the rapid collection of UV-visible spectra.



Figure 3.4 – MCS 522 UV-Visible spectrometer.

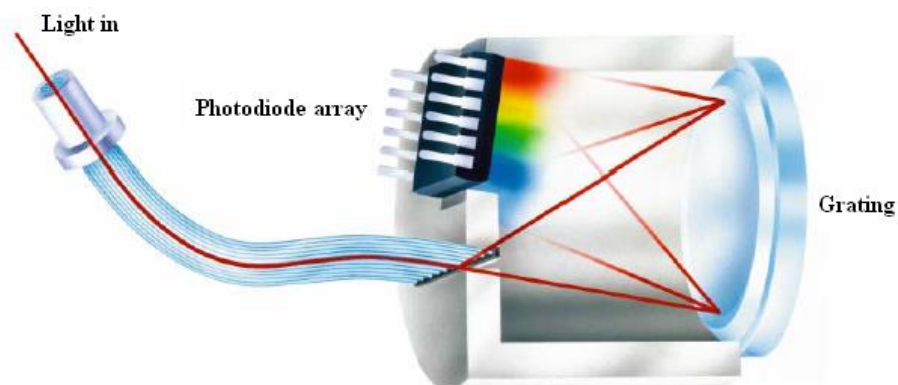


Figure 3.5 – Monolithic miniature spectrometer (MMS) detector for Zeiss UV-Visible MCS 522³.

A beam splitter (200 μm core diameter, Ocean Optics) was connected to the source port to provide two light sources, one of which was connected to the reference detector module via single strand silica fibres connected in series. The second fibre from the beam splitter was connected to the ATR probe. The output from the probe was connected to the sample detector module.

To ensure optimal performance of the spectrometer, a combination of fibres with different core diameters and attenuators were used so that the intensity of the light reaching the detector from the reference line was similar to the signal from the clean probe. For all experimental data the number of source flashes was 36 and the detector integration time was 1800 ms. An air reference was collected prior to each experiment.

3.4.1.1 ATR probe

A 6 inch long, Hastelloy body, Hellma 3 bounce ATR probe (see Figure 3.6) was used to collect UV-visible spectra. The interface at the end of the probe was an angular sapphire with 3 smooth faces and 2 opaque faces. The probe was 12.7 mm in diameter.

The ATR probe was used in 2 configurations. For some experiments the probe was placed in a custom made probe port which allowed the measurement under flow

conditions and for some experiments the probe was placed within the sample reservoir of the Netzsch minizeta mill.



Figure 3.6 – Hellma 3 bounce UV-visible ATR probe.

3.4.2 FOSS on-line 6500

In-situ NIR measurements were achieved using a FOSS on-line 6500 spectrometer (Figure 3.7) manufactured by FOSS NIRSystems, Silver Spring, Maryland. The FOSS on-line 6500 is a post dispersive scanning grating spectrometer, whereby, all the light (provided by a tungsten halogen lamp) is transmitted from the source to illuminate the sample and a holographic grating is used to separate different wavelengths of light returned before they are focussed on the detector.

The spectrometer is complete with low hydroxy silica fibres (3 m in length) coupled to a multipurpose probe head which can utilise either reflectance or transmittance probe sleeves. The fibre bundle contains 210 collection and 210 illumination fibres. Figure 3.7 shows a close up of the probe head revealing a solid centre ring of collection fibres at the centre and a concentric ring of illumination fibres surrounding it. A relatively high number of fibres are required as reflectance measurements require a high light throughput. The outer body of the NIR reflectance probe is constructed of hastelloy and is 17.6 mm in diameter. The sapphire end window is 8.0 mm in diameter.



Figure 3.7 – The trolley mounted FOSS on-line 6500 (left) and the reflectance probe head (right).

The wavelength region scanned was 600 – 1760 nm and detection was achieved using a thermoelectrically cooled semiconductor photodiode detector - InGaAs. Photodiode detectors operate by creating a current or voltage across a p – n type junction diode on the absorption of a photon in the intrinsic region (the lightly doped middle semiconductor layer between the p-layer and n-layer). Figure 3.8 shows a simplified schematic of the FOSS on-line 6500.

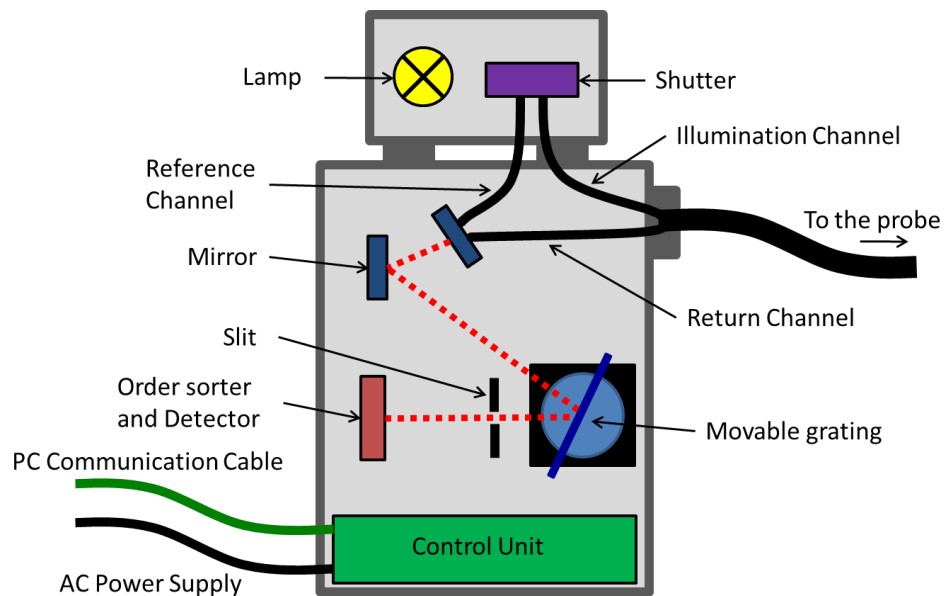


Figure 3.8 - FOSS on-line 6500 schematic.

NIR measurements were obtained at 2 nm intervals and in total 32 scans were collected per spectrum. Sample measurements were collected every 120 seconds and the data collected using Vision software (FOSS NIRSystems, ver. 3.1). Each scan begins with the NIR source blocked while the photometric zero is acquired for the detector. The system then collects 32 scans from the internal reference fibre before directing the light to the sample fibres for a further 32 scans. The purpose of collecting a reference using the reference fibre is to correct for the temperature and flux of the lamp which occurs through normal operation.

The other major components of the spectrometer are the movable holographic grating and the order sorter and detector module. The holographic grating separates the light in to different wavelengths, allowing the first order diffracted light to strike the detector. The order sorter component comprises of a series of narrow band filters which are controlled in coordination with the diffraction grating stepper motor. This order sorter prevents overlapping 2nd order and third order diffracted reaching the detector. For example when analysing 2000 nm 1st order light there will be overlapping second order 1000 nm and third order 500 nm light diffracted from the holographic grating towards the detector.

An external reference was used for each experiment. A white spectralon disc was placed in direct contact with the NIR reflectance probe window and measured and saved. The Vision software parameters were altered to use this scan as an external reference and a reference check performed with the NIR probe and Spectralon disc in the same position. The resulting reference check scan has absorption of zero across the wavelength range. The absorbance, A , is calculated from the scan of the white disc where light travelling through the reference fibre is I_o and the light returned from the probe is I . Likewise, when analysing samples an absorbance is calculated using the light directed through the reference fibre and the probe. Applying the external reference means subtracts the absorbance from the white disc is subtracted from the absorbance of the sample. The data was exported from the Vision software as excel files for smaller files and as comma separated variable ASCII files for larger numbers of spectra.

3.4.2.1 < 1 and 10 kg milling experiments

Lab scale experiments conducted in the Netzsch minizeta (< 1kg) and Labstar mills (10kg) were monitored in situ by NIR reflectance measurements. In each case the NIR reflectance probe was positioned in the stirred sample reservoir (Figure 3.9). For the minizeta mill, the sample vessel was agitated by a small PTFE turbine style agitator controlled at 250 rpm. For the Labstar, the mixing was achieved using a large helical agitator which had 2 inch clearance at each side where the NIR probe was positioned. The stir rate of the labstar vessel varied slightly from experiment to experiment. The stir rate was set at a value where the surface of the pigment in the large sample reservoir was moving.

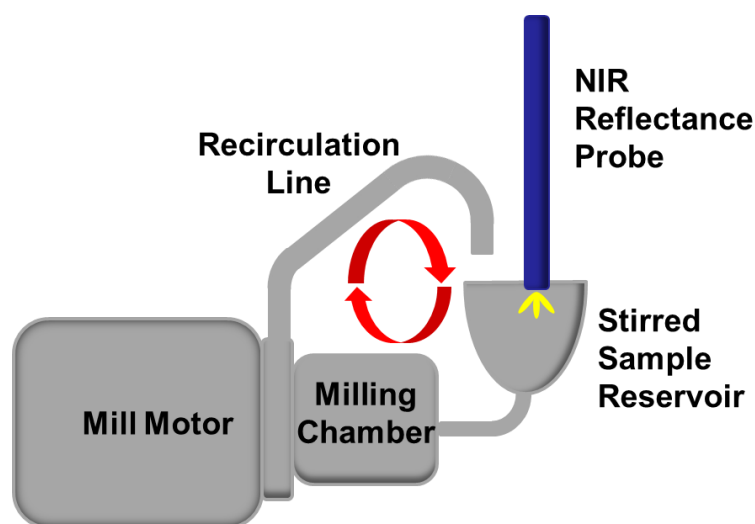


Figure 3.9 – Schematic showing the NIR reflectance probe positioning for milling experiments performed using the Netzsch minizeta mill.

3.4.2.2 Large Scale Monitoring

NIR monitoring of 200 kg scale dispersion milling was achieved by integrating the NIR probe in to the return line of a large scale mill which processed approximately 200 kg of concentrated pigment dispersion per run. The machinery is a much larger version of those used in the laboratory with larger milling chambers and recirculation rates but the particle size is reduced in the same way – by energetic collisions with ceramic or plastic milling media.

The sampling location was an important factor to consider as small scale experimentation monitored the change in the particle size in the vessel. In small scale experiments the particle size changed relatively quickly in the sample reservoir but the change in the overall particle size in a large pigment reservoir is much slower. Additionally, retrofitting the existing equipment to allow a probe port to be attached to the reservoir was not possible. Hence, the NIR reflectance probe was integrated in to the return line after a heat exchanger (Figure 3.10) using a custom designed section of pipework to accommodate the probe (Figure 3.11).

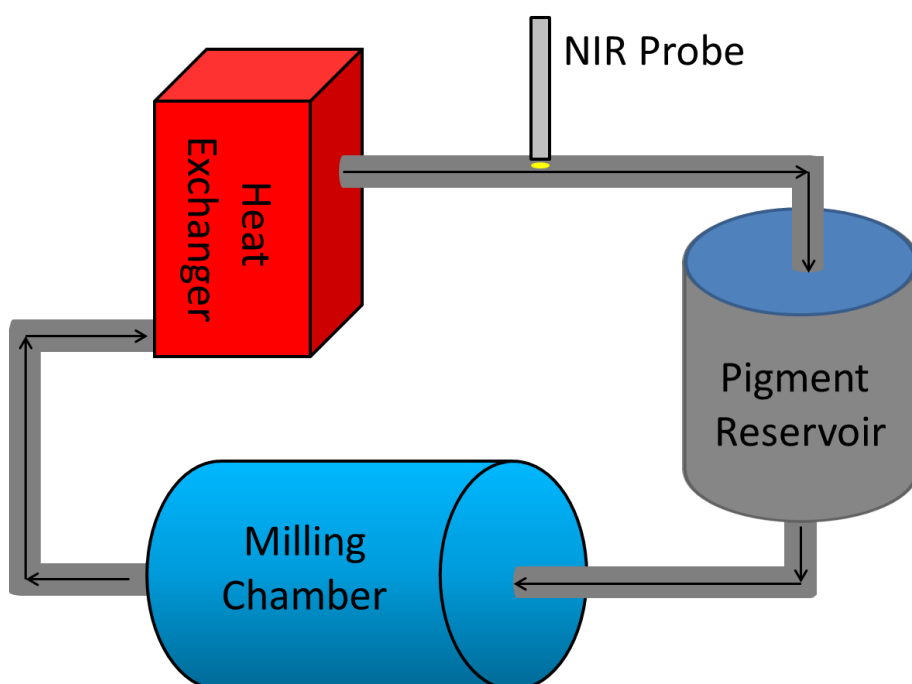


Figure 3.10 – Simplified schematic diagram showing the approximate location of the NIR probe for in-situ monitoring experiments.

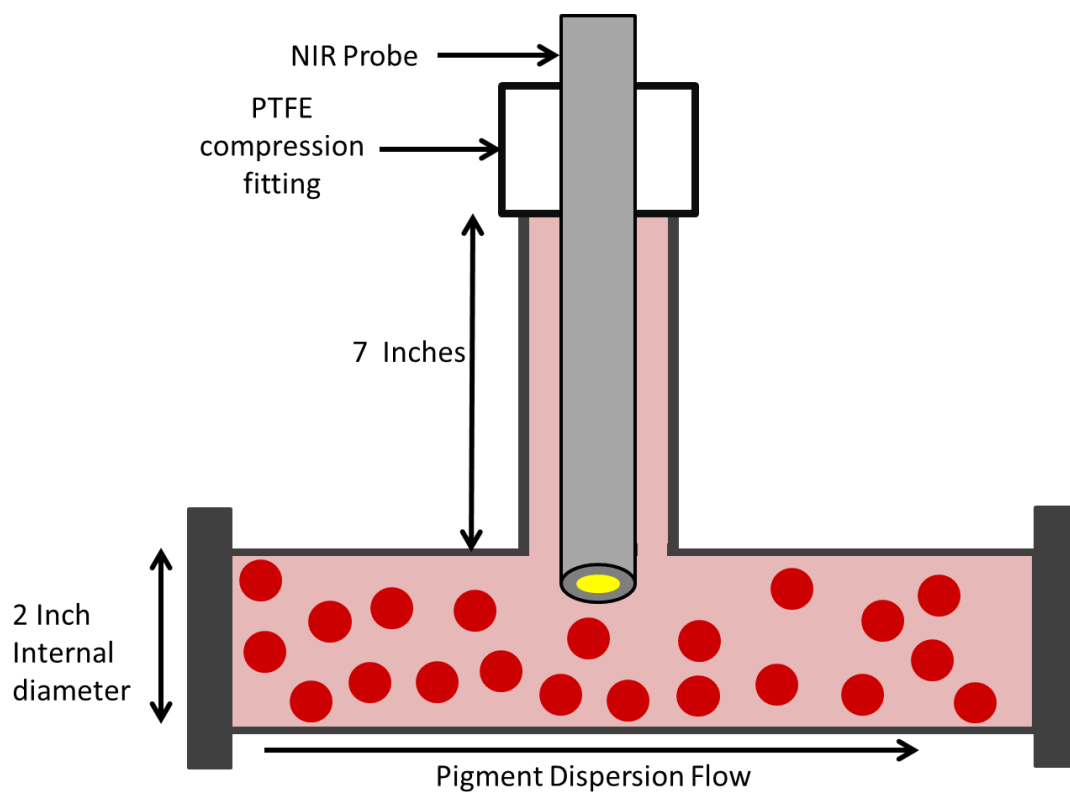


Figure 3.11 – NIR probe port for 200 kg scale milling experiments.

Integration of the probe post heat exchanger allowed a limited degree of temperature control. More viscous pigment dispersions reside in the high energy milling chamber for longer, and hence the temperature of the dispersion is warmer. Differences in the milling temperature between different batches (of different viscosity) can vary but the temperature profile throughout a single batch remains stable throughout milling, typically only varying by one or two degrees on account of the environmental conditions.

3.4.3 Cary 5000 off-line NIR spectrometer

Off-line measurements of diluted pigment samples were obtained using the Cary 5000 UV-visible-NIR spectrometer complete with a diffuse reflectance accessory (DRA-2500). Figure 3.12 shows the spectrometer and reflectance accessory and Figure 3.13 shows the schematic diagram of the reflectance accessory.



Figure 3.12 – Cary 5000 UV-Visible-NIR (left) spectrometer and external diffuse reflectance accessory DRA 2500 (right)⁴.

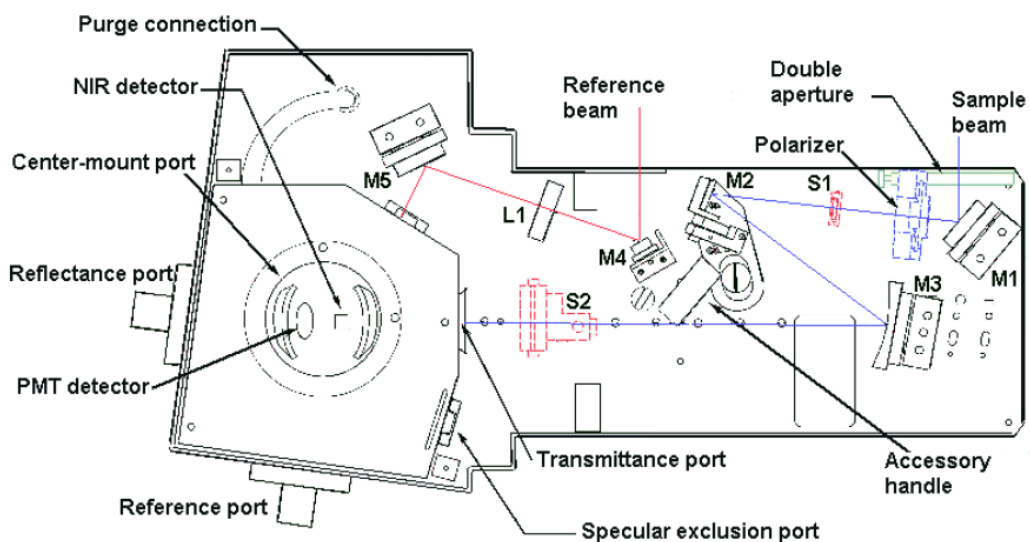


Figure 3.13 – External diffuse reflectance accessory 2500 schematic. M = mirror, S = lens.⁴

The DRA 2500 features a photomultiplier UV-visible detector and a thermoelectrically cooled PbS detector for NIR wavelengths. The lead sulphide detector works on the same principle of the InGaAs detector and it is sensitive to light in the wavelength region 800 to 2500 nm. The photomultiplier tube is sensitive from 200 to 800 nm and is able to amplify the relatively weak signal from a photocathode. When high energy photons strike the cathode, photoelectrons are released and these are focussed towards a series of dynodes. A dynode is a device

between the cathode and anode which is responsible for amplification. The surface is coated with a substance such as beryllium oxide which can emit several electrons after the impact of one high energy electron. This process repeats, amplifying the signal, as the electrons travel through several dynodes before reaching the anode.

3.4.4 Raman Spectrometer and PhAT probe for on-line monitoring

A Kaiser Rxn 1 Raman spectrometer with PhAT probe (Kaiser Optical systems, Ann Arbor, USA) was used to monitor the milling of yellow and cyan pigment dispersions. Daily diagnostic tests were performed with a cyclohexane standard using the external sample compartment accessory for the instrument. Raman spectra were recorded using IC Raman software (Metler-Toledo, Columbus, USA) and exported as .SPC files for use in Matlab. Unlike the FOSS reflectance NIR spectrometer, the instrument parameters such as acquisition time and number of accumulations were varied for different pigments. The acquisition time and number of accumulations are detailed in the experimental details section for each subset of experiments. The PhAT probe spot size was 6 mm in diameter. In-situ monitoring of milling experiments was achieved by placing the sample probe directly above the sample reservoir with an 8 inch spacer tube fixed onto the PhAT probe. To exclude external light, the sample reservoir and PhAT probe were surrounded by tinfoil.

The Kaiser Rxn 1 spectrometer uses a 400 mW power, 785 nm wavelength laser to induce Raman excitation. The measured power at the sample was 220 mW. Figure 3.14 shows a simplified schematic diagram of the key components of the spectrometer. The signal measured by the probe (discussed later) contains both Rayleigh (elastically) scattered and Raman (inelastically) scattered light. As the Raman effect is relatively weak, the Rayleigh light needs to be excluded; this is done by using a notch filter which blocks light of a specific wavelength. A notch filter allows light of all other frequencies to pass whilst reflecting a very narrow range of specific frequencies with a very high efficiency. When the light from the excitation source is removed, only the Raman shifted photons remain and are passed to the transmission grating. The performance of notch filters is improving, allowing the collection of Raman scattered photons very close to the excitation wavelength of the

laser source. This is very useful as this region contains what is called the phonon vibration of molecules where the scattering here is influenced by the chemical and physical structure of the sample. Better collection in this region can be used for polymorph identification and monitoring.

The transmission grating is a holographic grating which disperses the incident radiation into component frequencies such that the first order diffraction pattern is focussed on the detector. The holographic grating contains no moving parts, allowing increased data collection rates and improving accuracy.

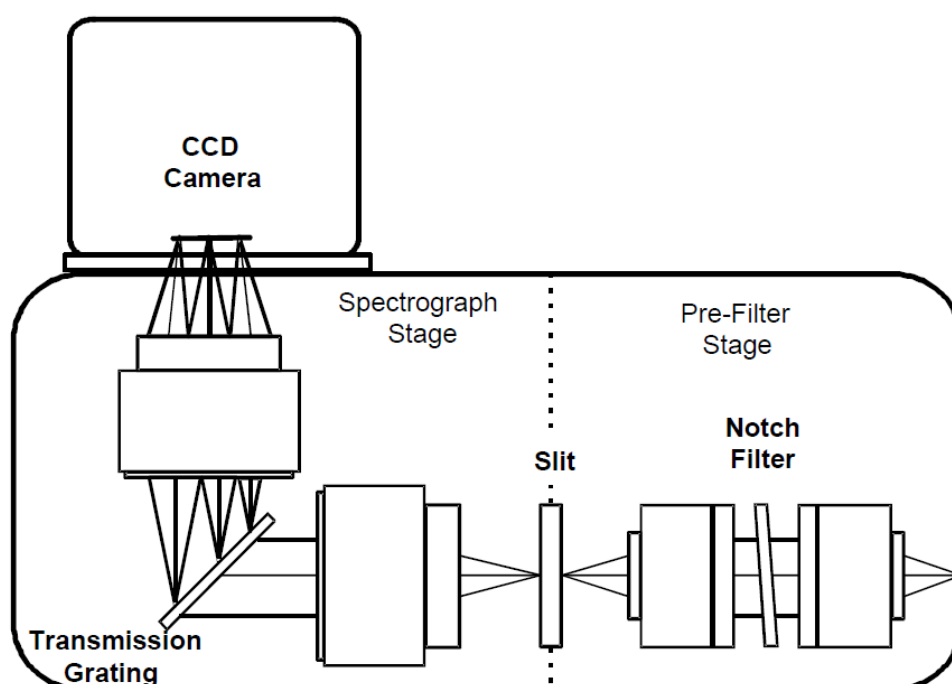


Figure 3.14 – Schematic diagram of the Kaiser Rxn 1 spectrophotometer⁵.

The charge coupled device (CCD) detector is an array detector which is thermoelectrically cooled to $-40\text{ }^{\circ}\text{C}$ to reduce the dark current. The detector consists of an array of pixels $26\text{ }\mu\text{m}$ length and breadth; arranged 256×256 pixels. The fibre bundle is randomised and no spatial information is provided in the Raman spectra. In this instance, the x axis of the detector provides the wavelength information and the signals from each of the columns (the y axis) is summed to provide the spectra. The

detector operates based on the photoelectric effect whereby an incoming photon is absorbed by the silicon layer, promoting an electron from the valence band to the conduction band. This creates a positive hole in the pixel which would normally recombine with the promoted electron but it is prevented from doing this by applying an electric field. The electrons are then gated in to a potential well which accumulates charge. The charge generated is proportional to the intensity of light and the duration of exposure of the light hitting the pixel.

The PhAT probe (Figure 3.15) is a non-contact, wide area illumination Raman probe, specifically designed for analysis of powders and slurries. The advantage of the Raman probe is that it is easy to apply to pre-existing plant and laboratory equipment and can be focussed through glass windows for applications in harsh or inaccessible environments. Another advantage of the PhAT probe is the large laser spot diameter which allows a larger area of a sample to be interrogated per measurement.

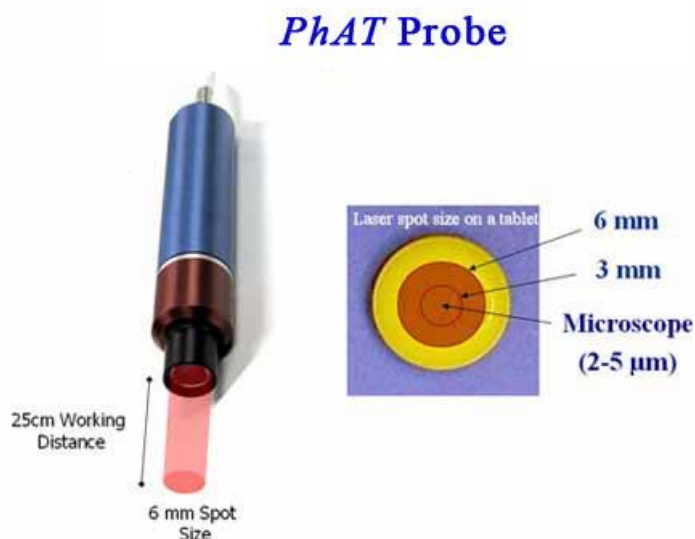


Figure 3.15 – Raman PhAT probe and typical spot sizes⁶.

A limited number of pigment dispersion samples were analysed using a 998 nm excitation Kaiser RXN2 spectrometer which had a non-contact probe head to produce a confocal spot around 80 to 100 μm in diameter. The exciting source was a diode laser. The probe was designed with a single fibre for collection and one for illumination and the power at the sample spot was around 300 mW from the

technical specifications. The detector was a thermoelectrically cooled single track InGaAs array.

3.4.5 Optical probes for in-situ analysis

Figure 3.16 details the different probe types typically used in PAT applications. Although probes, such as ATR probes, are used in the UV-Visible and MIR region, the materials used to construct the probes are different to maximise the light throughput for each wavelength region. UV-visible probes use silica fibres which have good transmission characteristics over the UV and visible range. Low solarisation silica fibres can be used in place of regular silica fibres as they are damaged by repeated exposure to low wavelength UV around 190 nm. MIR ATR probes use either chalcogenide or silver halide fibres but are limited to just a few metres. The ATR probe heads also differ. Sapphire is commonly used for ATR probes in the UV-visible region whereas ZnSe or diamond is used in the MIR region. Table 3.3 details the typical materials used to construct probes for in-situ applications.

Table 3.3 – Probe types and typical constriction materials.

Probe	Region	Fibres	Probe head/window
ATR	UV-visible	Silica	Sapphire
	MIR	AgX, Chalcogenide	Diamond or Silicon film
Transmission & Transflection	UV-visible	Silica	Sapphire
	NIR	Low hydroxy silica	Sapphire
Reflectance	NIR	Low hydroxyl silica	Sapphire

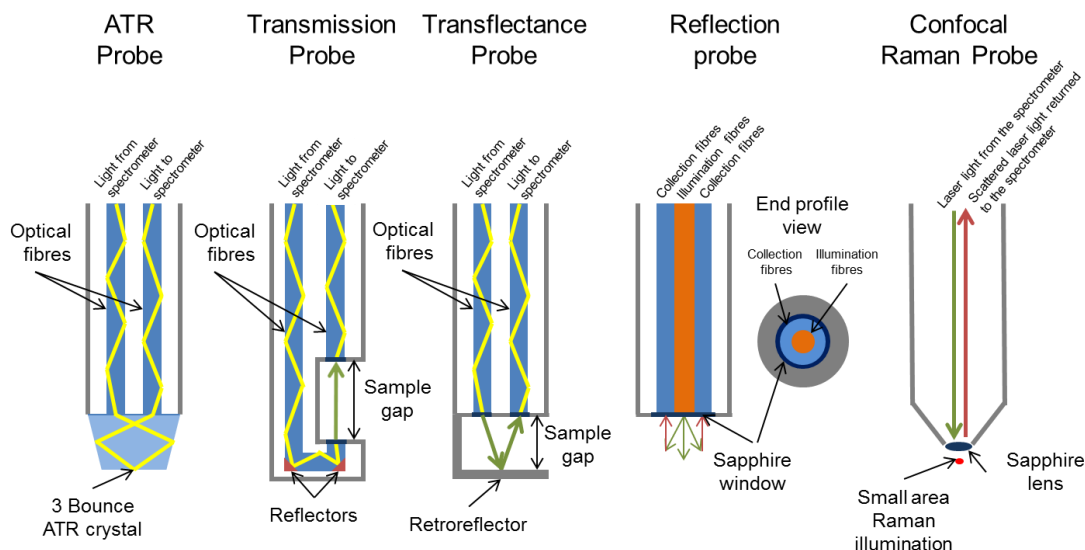


Figure 3.16 – ATR, transmission, transflectance, reflectance and confocal Raman probe schematics.

Transmission and transflection probes can be used in both the UV-visible and NIR region. The main difference in the two probe configurations is the path length of the light where it is exposed to the sample. The pathlength of the transmission probe is the distance of the sample gap whereas the transflectance probe is approximately double the sample gap. The reason it is not exactly double the pathlength is that the angle of the light striking the retroreflector has to be taken in to consideration. When dealing with very short pathlengths, in the order of a few mm, this difference will be negligible. Reflectance probes are primarily used in the NIR region and immersion Raman probes can be used in-situ for industrial applications. Confocal Raman probes have a small field of illumination which is typically focused close to the end of the immersion probe. These probes are not discussed further for the in-situ analysis of pigment dispersions. The previous section, chapter 3.4.4, describes the Raman PhAT probe system that was utilised in this work.

3.4.6 Off-line Visible-Near infrared measurements

Pigment dispersion samples were collected at defined time points during the milling of pigment dispersions. The samples were diluted by a factor of 250 immediately after collection to prevent flocculation of the milled pigment particles. The samples were then measured in transmission and reflectance mode in a 1 mm path length quartz cuvette (30 mm external width). Measurements were taken using a CARY 5000 UV-visible-NIR spectrophotometer (Agilent Technologies, California, USA) complete with a 150 mm diffuse reflectance accessory DRA-2500. Scans were collected at 2 nm intervals over the wavelength range 400 – 1800 nm. To reference the instrument scans were performed at 0 % transmission (by blocking the source beam path to the DRA) and 100 % transmission using 2 white Spectralon® discs at the reference and reflectance ports on the DRA. Measurements in transmission and reflectance mode required different optical configurations in the DRA, hence, the 0% and 100 % reference procedure was performed for each. The energy level of the source was set to 1.00 for 400 – 800 nm and 3.00 for the range 800 – 1800 nm. Spectra were saved as CSV files.

3.5 Particle size analysis

Pigment dispersion samples, collected throughout various stages of small and large scale experimentation were analysed using two different methodologies, dynamic light scattering (DLS) and laser diffraction (LD). The following section details the instrumentation used and the operating parameters.

3.5.1 DLS

3.5.1.1 HPPS5001 NIBS particle sizer

Two instruments with slightly different configurations were used to analyse diluted pigment dispersion samples.

The Malvern HPPS5001 (Figure 3.17) is a dynamic light scattering instrument capable of measuring samples with a particle size of between 0.6 nm and 6 μm and particle concentrations from 0.1 ppm to 20 vol %. The source is a HeNe laser with a wavelength of 632 nm and a power of 3.0 mW, and the detector is an avalanche photodiode. The cuvette compartment temperature is maintained by thermoelectric heating/cooling. Scattered light is collected at 173° relative to the path of the illuminating source. Before each day's analysis, the performance of the instrument was assessed by measuring certified latex sphere standards (20 and 40 nm).



Figure 3.17 – Malvern HPPS 5001 non invasive back scatter particle sizer.⁷

3.5.1.2 ZS90 Zetasizer

The Malvern ZS90 Zetasizer (Figure 3.18) is the most recent model (as of March 2013) of Malvern's DLS particle size analysis equipment . It is a multipurpose instrument, capable of measuring zeta potential (the electrokinetic potential in dispersed systems), molecular weight and particle size.



Figure 3.18 – Malvern ZS90 Zetasizer⁸.

The instrument is capable of measuring particle sizes between 0.3 nm and 5 μm . Again, the quality of the particle size measurements depends on the physical properties of the analyte and dispersant. The source is a HeNe laser with a wavelength of 632 nm and a power of 3.0 mW and the detector is an avalanche photodiode. The cuvette compartment temperature is maintained by thermoelectric heating/cooling.

Dynamic light scattering measurements of diluted pigment samples were used as the primary reference technique for following the particle size reduction of pigment dispersions. The main instrumentation used was a HPPS5001 NIBS (non-invasive back scatter) particle sizer (Malvern, UK) owned by Centre for Nanometrology at the University of Strathclyde. Some experimentation was performed on site with the project industrial partners, FFIC, utilising a ZS90 Zetasizer (Malvern, UK). There are

distinct differences in the optical configuration of the two instruments but the results obtained are equivalent.

3.5.1.3 Procedure

Aliquots of extracted samples were diluted ($\times 4000$) in double distilled de-ionised water for particle size analysis by dynamic light scattering (DLS). Samples were measured in a 1 cm path length polymethylmethacrylate (PMMA) cuvette at a compartment temperature of 25 °C. The required inputs for the operating method were; refractive indices of the pigment (Table 3.4) and water (1.330), absorption of pigment (Table 3.4) and viscosity of sample media (0.8872 cP).

Table 3.4 – Refractive indices and absorption values for pigments characterised using the Malvern HPPS50001 DLS particle sizer.

	PV19	PR122	PY74	PB15:4
Refractive index	2.52	2.04	1.65	1.63
Absorption	0.10	0.03	0.01	0.30

The measurement duration and number of replicate measurements was set to automatic. The Z-average particle size (mean weighted hydrodynamic diameter) of the dispersion was taken as the result. The measurement was performed once for each sample when using the Malvern HPPS5001 NIBS and three times for the Malvern ZS90 Zetasizer. When three replicates were performed the average is reported. The reason that three measurements were collected was to comply with the FFIC standard operating procedure. Typically, very little change was observed between the three replicate measurements of the Z-average so experiments where the HPPS5001 particle sizer was used were performed only once to save time when analysing a large number of samples.

3.5.2 Laser diffraction

Several pigment dispersion samples, collected during large scale experimentation (200 kg scale), were analysed using the Mastersizer 2000 (Malvern, UK) stationed in the quality control laboratory at FFIC, Grangemouth.



Figure 3.19 – Malvern Mastersizer 2000 with HydroG sample dispersing unit.⁹

To measure the particle size of a pigment dispersion sample, the sampling unit was drained of washing water and replaced with ultra-high quality (UHQ) water (prepared in-house). The software inputs were then adjusted, such that the sample chamber was stirred at 1250 rpm, the recirculation rate set to 50% and the sonication set to 100%. A background scan was collected before pigment dispersion was added to the sample unit. Sample was added by pipette until the obscuration was between 10 and 12 %. Background and sample measurements were set to 20 seconds duration in the software. The number of measurement cycles was 3, with a 3 second gap between each measurement. The model used to calculate the sample properties was the general purpose model contained within the Malvern instrument operating software. The instrument contains both a red light source (HeNe laser, 632 nm wavelength) and a blue diode source (470 nm) and the required parameters for each different pigment are detailed in Table 3.5.

Table 3.5 – Refractive index and absorption value inputs for cyan, yellow and magenta pigment dispersion laser diffraction particle size measurement.

Colour	Laser	Refractive Index	Absorption
Cyan PB15:4	Red	1.63	0.30
	Blue	1.55	0.00
Yellow PY 74	Red	1.65	0.01
	Blue	Off	Off
Magenta PV 19	Red	2.52	0.10
	Blue	Off	Off
Magenta PR 122	Red	2.04	0.03
	Blue	Off	Off

The blue light source was not used for sample measurement where the refractive index and absorption value is denoted as "off".

3.6 Data analysis tools

The spectroscopic and particle size data were analysed using Matlab version 2010b (The Mathworks, Natick, USA) and the optimisation toolbox add-in (The Mathworks, Natick, USA). Additionally, PLS_toolbox version 4.1 (Eigenvector research Inc., Wenatchee, USA) was used for chemometrics.

3.7 Summary

Chapter 3 has detailed the equipment and materials necessary to perform pigment dispersion milling experiments and the particle characterisation techniques used as the reference method throughout all of the following experimental work. Additionally, the details of the optical spectroscopic equipment, used in the subsequent 4 chapters are included. The experimental work included in chapter 5 describes how each of the techniques, equipment and materials detailed in this chapter were used to investigate which technique(s) showed most promise for monitoring pigment dispersion particle size reduction.

3.8 References

1. <http://www.netzsch-grinding.com/products-solutions/laboratory-machines/wet-mills/minizeta.html> (Accessed 13 Mar 2011).
2. <http://www.netzsch-grinding.com/products-solutions/laboratory-machines/wet-mills/labstar.html>, Accessed 02 April 2012.
3. P. Dallin, *E-mail communication - MCS 522 UV-Vis system overview*.
4. *Instruction manual - Varian 4000/5000/6000i external diffuse reflectance accessory*, Varian Inc (2004).
5. *Raman Rxn2 Operations Manual 2007410 R2 (Kaiser optical systems Inc)*, 2007.
6. http://www.kosi.com/Raman_Spectroscopy/phat-probehead.php?ss=300, Accessed 19 Jan 2012.
7. *High performance particle sizer (HPPS) instrument brochure, Malvern instruments* (2002).
8. *ZS90 DLS instrument brochure*, Malvern Instruments (2012).
9. *Mastersizer 2000 instrument brochure*, Malvern Instruments (2005).

4. Investigation of techniques

The first investigation assessed the pigment dispersion stability and determined the standard operating procedure used throughout the rest of the work for the reference technique (DLS). UV-visible, near infrared, mid infrared and Raman spectrometries were then assessed for the potential to measure particle size in highly concentrated pigment dispersions throughout a milling process. Section 4.1 contains a review of how the aforementioned optical spectroscopic techniques have been used in industry, focusing on examples where they have been used to monitor changes in particle size

4.1 Literature

Milling to reduce particle size is an important step in producing high performance pigments and the effect of milling on the absorption and scattering properties of the pigments may be observed using spectroscopic measurements. The appearance and performance of the pigment is affected by the physical parameters such as the geometry of the unit cell, crystal lattice modification and crystal shape modification. In addition the physical characteristics of particles such as size, distribution of size, shape, surface area, surface structure and crystallinity will all effect the diffuse reflection of the pigment and hence, the appearance of the pigment which is a result of the way the pigment absorbs and scatters incident light^{1,2}.

UV-visible, NIR, MIR and Raman spectrometries can all provide information on the physical and chemical properties of a sample. The following literature review highlights some pertinent optical spectroscopic methods which have been used to measure chemical and/or physical properties.

4.1.1 UV-visible spectroscopy process monitoring

The effect that particle size has on UV-visible spectra has been investigated for colloidal C₆₀ particles in water³ and it was noted that the UV-visible spectra were red shifted (the wavelength increased) for fractions with a larger average particle size. Changes in the λ_{\max} for normalised C₆₀ UV-visible spectra could be correlated with the changes in particle size and a ratio between two absorption peaks showed a relationship with particle size from around 100 to 200 nm. The change in the observed spectra can be explained by a combination of effects such as a change in

the size/structure, and/or interactions between the C₆₀ particles and the surrounding water molecules and shows the potential application of PAT to determine the particle size in an in-line/on-line process.

Analysis of pigment dispersions using off-line transmission visible spectroscopy (400 to 800 nm) has been investigated by Fu et al² where the Beer-Lambert law can be expressed as:

$$A = (a_1 + \tau_1)bc \quad \text{Equation 4.1}$$

where a_1 and τ_1 and are the contributions of absorption and scattering coefficients ($L g^{-1} cm^{-1}$) respectively at a wavelength λ_1 , b is the pathlength of the cell used (cm) and c is the concentration of the pigment in the dispersion ($g L^{-1}$).

The change in off-line visible spectra was monitored throughout a milling process. It was shown that a change in the absorption and scattering coefficients was observable as the particle size of the pigment in the dispersion was reduced. As the milling progressed the particles became smaller and the contribution from scattering decreased. The absorption increased as the surface area of the exposed pigment increased with smaller particle size for showing the potential to use UV-visible spectroscopy to monitor a milling process.

Using spectroscopic techniques such as UV- visible it may be possible to obtain information on the particle size without the need for conventional particle sizing techniques such as laser diffraction or dynamic light scattering. One major disadvantage of the technique is that it requires a dilution step as is the case for both the conventional particle sizing techniques mentioned beforehand and this will fundamentally change the nature of the sample.

As a sample is illuminated light is refracted, reflected and diffracted and this is known as the diffusion phenomena. To simplify the picture a size parameter, a , is used to identify where these effects are dominant taking account of the wavelength of the incident light, λ , and the particle diameter, d . The relationship is given by

$$a = \frac{\pi d}{\lambda} \quad \text{Equation 4.2}$$

where the wavelength of the source is in the ultraviolet (200 – 400 nm), visible (400 – 800 nm) and near infrared (800 – 2500 nm) and Figure 4.1 shows which optical model is used to describe each regime.

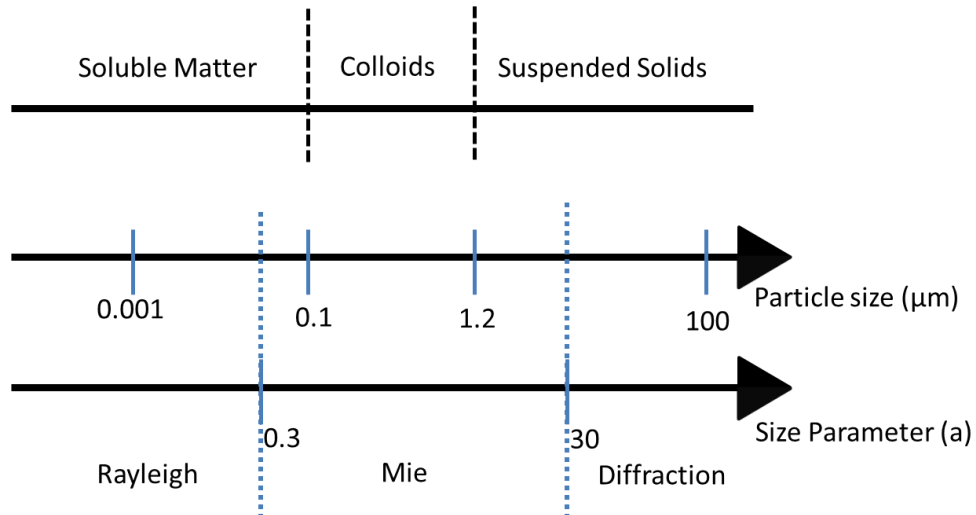


Figure 4.1 – Diffusion domain for changing particle sizes⁴

Rayleigh scattering occurs when the particles are smaller than the wavelength of the incident radiation and light is scattered in all directions. Diffraction occurs where the particle size is much larger than the incident wavelength and the light is mainly scattered in the forward direction and Mie theory is used to describe the scattering in the mid-range where the particles are approximately the same size of the incident wavelength and requires the knowledge of the optical properties of the sample.

Berho et al⁴ have investigated the effect of particle size on transmission UV-visible spectra for a non-absorbing species such as talc, kaolin and carbonate suspensions. Using non-absorbing species allows a simpler investigation of the effect that the physical properties have on the UV-visible spectra and it was shown that the physical absorbance of samples containing particles larger than 1 μm showed little dependence on the wavelength whereas when the particles were smaller than 1 μm the absorbance was approximately inversely proportional to the wavelength. The aim of this was to improve the treatment of waste water by developing a technique that

could rapidly identify whether the particles present in the system were colloidal or larger particles.

Flow through UV-visible cells with path lengths of 200 to 2000 μm are commercially available⁵ but are not suitable for the rapid process analysis of pigment dispersions due to the strong possibility of blocking and fouling of the cells and tubing by oversized particles present in pigment dispersions. Problems associated with transmission measurements make ATR UV-visible spectroscopy an attractive technique for monitoring highly concentrated pigment dispersions. One pertinent observation from searching the available literature is that the application of on-line UV-visible ATR spectroscopy has not been fully investigated for determination of particle size and distribution. Such measurements have significant advantages over dynamic light scattering or off-line UV-visible.

Data gathered in real time without the requirements of sub-sampling and extensive sample preparation would provide a significant step forward for process analysis of concentrated dispersions and laboratory scale experiments were performed to assess whether UV-visible ATR measurements could be used as a means of monitoring the particle size of pigment dispersion. Previous scoping experiments performed by FFIC identified that UV-visible spectroscopy may yield information on the pigment particle size and concentration⁶. Several milling experiments were performed to assess whether UV-visible spectroscopy would be a suitable technique for monitoring the milling process and are not presented herein. Instead, three experiments are described which show the difficulty in using UV-visible ATR spectroscopy for consistent measurements in highly concentrated pigment dispersions.

4.1.2 Mid infrared ATR for process monitoring

Mid infrared spectroscopy is a well-established laboratory technique, often used to confirm the identity of chemical entities by comparison of the spectrum with that of a known reference material. The mid infrared spectrum (between 4000 and 500 cm^{-1}) consists of the fundamental vibrations of most organic functional groups as well as strong absorptions from O-H and N-H groups. The region between 1500 – 500 cm^{-1} is known as the fingerprint region which can be used for

identification. This region contains numerous absorptions which are more difficult to assign to one specific vibration of a group within a molecule.

The increase in the uptake of the MIR as a valuable tool in the PAT spectroscopy toolbox is in part due to the development of rugged high performance spectrometers from vendors such as ABB, Bruker and Mettler Toledo which can be used in process environments. Additionally, advances in probe and fibre manufacturing have provided robust silver halide fibre coupled probes for use in chemically harsh environments.

Probes are not the only means of obtaining process measurements and Trevisan et al⁷ have published an example where an ATR flow cell was used to quantify the amount of ephedrine intermediate present in a biotransformation reaction. Unfortunately, it is not always safe or convenient to incorporate the additional pipes and tubing for in-line measurements as they often complicate cleaning or can be difficult to retrofit to existing equipment. Also, removing sample from the process which then has to be discarded will reduce the yield. When dealing with expensive or toxic compounds MIR ATR probes can be employed in the vessel for in-situ analysis.

Clegg et al⁸ have published an example showing the use of MIR ATR probe measurements for the development and manufacture of an API. The spectroscopic measurements were used to monitor a two-step reaction process, providing valuable process understanding, and enabling the reaction to be monitored without operators having to remove samples which contained a potentially genotoxic intermediate. The measurements were also used on different scales from lab to commercial manufacture between two different sites which aided the technology transfer of the product.

MIR ATR spectroscopy has also been used to monitor crystallisation. ATR probes are ideal for monitoring solvent and active concentrations in the solution phase but have some notable limitations. The main one is that the ATR probe can become an effective surface for the crystals to form. This may change the particle size and distribution of particles that could have been achieved without the probe present and can often lead to probe fouling. Additionally, the short penetration depth of the ATR evanescent wave will not be able to monitor the solid phase particles as they form,

hence, monitoring the particles requires another technique such as focused beam reflectance measurements (FBRM), laser diffraction, Raman or NIR spectroscopy. However, there are interesting examples in the available literature which detail the use of MIR ATR spectroscopy for use in crystallisations. Yu et al⁹ maintained supersaturation conditions in a crystallisation vessel using FTIR measurements and feedback control for real time control of the process. Cornel et al¹⁰ have compared in situ Raman and MIR measurements in crystallisations and demonstrated that MIR measurements are a useful means of following the solute concentration whereas Raman was a good means of monitoring the particulates formed.

Other pharmaceutical applications of MIR ATR measurements include monitoring the biologics such as fermentation monitoring¹¹ and cell cultures growth¹². Other novel applications have detailed the usefulness of the technique for detection of counterfeit whiskies by examining the alcohol content or the colourings present¹³.

4.1.3 NIR

In 1800 William Herschel, a German born astronomer and musician, first introduced the concept of an extended electromagnetic spectrum beyond the visible region by separating light through a prism^{14, 15}. The separated light was shone on to three thermometers with carbon black coated bulbs and it was found that heating was observed as the colour of the light tended towards red and the greatest heating occurred just beyond the red light visible region. Indeed, this region from 700 – 1100 nm is often referred to as the "Herschel region" although at the time Herschel described this as another type of radiation not like light. The realisation that this was a region of invisible light (or what we now refer to as the near infrared region of the electromagnetic spectrum) and this behaved in the same way as visible light was not achieved until some years later in 1835 by André-Marie Ampère. The near infrared region of the electromagnetic spectrum spans from ~780 to 2500 nm.

The advent of modern NIR spectroscopy began in the 1960s where novel applications were being developed by Karl Norris of the Agricultural Research Service, part of the US Department of Agriculture. Since then the use of NIR has increased dramatically. The attractiveness of the technique to industry is, in part, due to the vast amount of information that is encoded in each spectrum as both the

chemical and physical properties of the sample have an effect which is measurable in the near infrared region¹⁶. This versatility is exploited by a wide range of industries. NIR spectroscopy is used as both a qualitative and a quantitative tool for food production, petrochemicals, pharmaceuticals and agrochemicals^{15, 17-19}. The pharmaceutical industry has, in general, been reluctant to embrace process analytical technologies. Especially when compared to the number of applications of NIR used in food production but adoption is increasing, aided by clarification from the US Food and Drug Administration (FDA) "Guidance for Industry, PAT – a framework for innovative pharmaceutical development"²⁰.

NIR spectra can be collected by transmittance, transreflectance or diffuse reflectance and the latter method has been used extensively to collect spectra with information relating to the chemical and physical properties of the sample. Kubelka-Munk theory^{21, 22} (Equation 4.3) has been used to rationalise the effect of absorption and scattering effect on the NIR spectra. Information from the chemical makeup of the sample is accounted for by the absorption coefficient, K , and the scattering coefficient, S , contains information related to the physical properties of the sample (e.g. particle size). The absorbance, A , is a property of the ratio of the absorption and scattering coefficients (K and S) and R is the diffuse reflectance of the sample.

$$A_{\infty} = \frac{(1 - R_{\infty})^2}{2R_{\infty}} = \frac{K}{S} \quad \text{Equation 4.3}$$

For Kubelka-Munk theory, three assumptions are made:

- 1) The scattered radiation is isotropically distributed.
- 2) The particles in the layer are randomly distributed and smaller than the layer thickness.
- 3) The layer is subject only to diffuse reflection.

For this relationship, reflectance increases as particle size decreases. This causes a decrease in the apparent absorption of the sample.

The food industry has employed NIR measurements from the 1960s onwards. Some examples include monitoring the fermentation of yogurt²³, diffuse reflectance for analysis of meat²⁴ and monitoring wheat agglomeration²⁵. Monitoring the production of wheat flour is particularly interesting because the samples are undergoing a chemical and physical change and by using NIR reflectance measurements both can be observed. With particle sizes in the millimeter domain, the size of the flour particulates had a direct effect on the NIR spectra, showing an increase in baseline offset as the particle size increased. The increase of particle size in the millimeter domain resulted in the scattering decreasing and the NIR light penetrating deeper in to the sample. It was noted that the effect became larger at higher wavelengths and this concurred with previous analysis of wheat flour²². PCA on the untreated data showed that most of particle size variation was well characterized in the first principal component whereas the changes in the hydration of the flour particles were captured in the second principal component. Further interrogation of the NIR data showed that preprocessing to remove the particle size effects could yield information which could be related to the hydration changes and the level of sodium dodecyl sulfate (SDS) insoluble glutenins. Continuing in that vein, the food industry continues to develop new and interesting applications for NIR spectroscopy. Increasingly, it is used to discriminate between transgenic foods aka genetically modified organisms (GMO)²⁶. Current techniques employing DNA analysis such as polymerase chain reaction (PCR) and enzyme linked immunosorbent assay (ELISA) can be replaced, removing the requirement for time consuming, destructive and costly analysis of foodstuffs such as grains, barley and tomatoes. NIR reflectance measurements have also been used to classify different types of meat which are used as feeds for livestock and the possibility of rapid results and a high throughput is very attractive to industry.

Often, the effect of particle size is considered a hindrance when attempting to build robust calibration models, for instance when using NIR spectroscopy as the identification method when excipients are received that are of different grades or from different manufacturers²⁷. Several mathematical pre-treatments have been developed to minimise the effect of particle size on NIR spectra^{15, 28-30} such as multiplicative scatter correction³¹ (MSC), standard normal variate³² (SNV),

orthogonal signal correction³³ (OSC) and derivatives³⁴. Luypaert et al evaluated different pre-processing techniques such as offset correction, detrending, derivatives and SNV for the analysis of creams with different constituent concentrations³⁵.

The effect of particle size on NIR spectra can be exploited for useful means. Such as, the identification of particular grades of excipients³⁶ received from suppliers that will then go on to be used in the formulation of drug products. Excipients such as sorbitol³⁷, microcrystalline cellulose³⁸ and lactose monohydrate³⁹ have all been analysed by NIR spectroscopy to verify the chemical signature and the particle size fraction (often referred to as the grade). The particle size of excipients and active pharmaceutical ingredients is crucial in the formulation step for solid dose products. Variations in the grade of excipient can lead to different compaction properties which will, in turn, cause difficulties when tableting. Moreover, subtle differences in the particle size of excipients and active pharmaceutical ingredients will change the dissolution profile and possibly even the bioavailability of the drug⁴⁰.

All of the examples above focus on examples where the particle size is above 100 μm whereas few publications have dealt with particle sizes smaller than this region. Bittner et al⁴¹ have used near infrared reflectance measurements for the identification and monitoring of particle size of a β -lactam antibiotic with D90 particle size diameters ranging 6.5 to 21.7 μm . For particle sizes of $\geq 100 \mu\text{m}$ there is an increase in the absorption (A) at any wavelength (λ) which is negatively proportional to the inverse of the particle diameter (d) (Equation 4.4),

$$A_{\lambda} \propto -\frac{1}{d} \qquad \text{Equation 4.4}$$

However, it was shown for smaller particles that this trend is reversed. As the particle size decreased the Kubelka-Munk theory broke down and the absorption increased with decreasing particle size. When the wavelength of light is much smaller than the particles under investigation the number of re-reflections decreases which leads to a reduction in the light reflected back towards the collection fibres.

This is shown in the spectra as an increase in baseline offset and this effect is dependent on wavelength.

Another example where the particle size is much smaller than the wavelengths of light was reported by Higgins et al,⁴² whereby, 2nd derivative NIR spectroscopy was successfully used to follow the production of nanoparticle active pharmaceutical ingredient. Milling of the concentrated API suspension was monitored on-line using in-situ diffuse reflectance NIR measurements. Prior to milling, larger particles in the dispersion resulted in more light being back scattered towards the detector leading to a smaller non-specific absorption. As the milling proceeded, and the number density of the smaller particles increased, less NIR light was non-resonantly scattered back to the detector. This led to a larger baseline offset which increased with wavelength as the particle size was reduced. In addition, the larger number of smaller particles increased multiple scattering, hence, increasing the path length of the NIR photons and increasing the absorption. In such a concentrated system multiple scattering effects dominate the spectra. The sloping baseline was removed using the second derivative transformation and the particle size was inferred from the increase in the water absorbance as a result of the increase in effective path length as the milling progressed.

Aside from quality control type testing, NIR is used extensively as a tool for process development and real-time process monitoring of the various unit operations involved in the manufacture of pharmaceuticals^{43, 44}. NIR process measurements can be made using either contact or non-contact systems in challenging production processes such as crystallisation^{45, 46} (where the particle is formed), drying^{47, 48} (removal of solvents), grinding^{22, 49}, milling⁵⁰ (where the particle size is reduced) and powder blending⁵¹ (where homogeneous mixtures need to be prepared). NIR spectroscopy can also be used to screen between different polymorphs⁵² as differences in the lattice conformation and the resultant hydrogen bonding will alter the molecular vibrations observed in near infrared spectra. Although it is possible to monitor polymorphism using NIR spectroscopy there are more examples in the literature which focus on Raman spectrometry for the purpose of polymorphism monitoring⁵³. Raman spectra typically consist of sharp and well defined bands whereas near

infrared spectra are broad. This often makes univariate modeling of processes difficult and requires multivariate techniques such as PCA and PLS.

4.1.4 Raman

Raman spectroscopy is increasingly used for process measurements and the increased uptake in this technique has been as a result of the need in the pharmaceutical industry for increased process control^{54, 55} and the availability and relatively low capital costs of robust spectrometers. Industries increased exposure to this technique and the rise in the number of people trained and knowledgeable about Raman spectrometry means that the number of applications will only increase in the future. Raman is an attractive tool for process monitoring because of the complex information that is included in the Raman spectrum, revealing not only the molecular structure, but also the surrounding media and even polymorphic state. All of which can be used to control manufacturing and processing steps in products ranging from pharmaceuticals to food. A significant advantage of Raman spectrometry is that, unlike NIR spectroscopy it is not sensitive to water.

Leaps in the development of compact and robust CCD detectors, miniaturisation of electronics and spectrometers with few or no moving parts make small Raman spectrometers an attractive tool for rapid identification in non laboratory settings. Suppliers such as ThermoScientific (Massachusetts, USA), Bayspec (California USA), Ocean optics (Florida, USA) and Analytik (Cambridge, UK) already supply a wide range of hand held Raman spectrometers for industrial applications.

Typical Raman spectra contain sharp, well defined features that are proportional to the number of scattering molecules present, allowing it to be used as a qualitative and/or a quantitative technique as required. Depending on the contributions of each component analyte it is sometimes possible to build simple univariate models following the reduction or increase in the intensity of Raman shifted light at a particular frequency. When Raman bands overlap in complex mixtures multivariate analysis techniques such as PCA and PLS can be used for modeling.

The Raman process is an inherently weak process with only 1 in 10^6 to 10^8 molecules producing Raman scattered photons and the signal can be masked by sample fluorescence (described in more detail in the theory section) which is a much more

efficient process. The intensity of Raman scattered photons is inversely proportional to the fourth power of the excitation wavelength which means that at lower wavelengths, the intensity of scattered photons is high and at higher wavelengths the intensity is reduced. The selection of excitation wavelength has to balance the intensity of Raman scattering with fluorescence which is more of a problem at lower wavelengths. Even a small amount of a fluorescing impurity can overwhelm the Raman scattered photon signal. As a result, a large number of pharmaceutical applications have been compromised by using 785 nm wavelength Raman spectrometers to reduce the impact of fluorescence. The advent of tunable lasers means that robust, high performance lasers are available over the UV through to visible and in to the low near infrared red region. The Nd:YAG laser operates at a wavelength of 1064 nm which is well in to the NIR region and is a good alternative for the pharmaceutical industry when samples fluoresce at 785 nm. Moving to a higher wavelength is not the only option to avoid fluorescence in samples. Instead Kerr gating can be used where the Raman signal is allowed to pass through an optical gate which quickly closes to reject the majority of the fluorescence signal. This has been used successfully to identify samples of illicit drug which often contain impurities that fluoresce⁵⁶ and to provide depth profiling information in tissue samples⁵⁷.

Raman spectrometry offers a lot of flexibility when integrating probes in to hazardous or messy applications. Raman measurements can be obtained through water jackets or glass windows (providing the glass has not been doped with a fluorophore) which means the Raman probe can be kept in a safe environment. Additionally, Raman probes can be coupled by over 1 km long silica fibre runs which allow expensive and sensitive spectrometers to be situated in a safe room with only the probe and fibre run exposed to the harsh manufacturing environment. Multiple probes can be run from a single spectrometer which can reduce the initial capital cost of an installation.

There are a huge number of published examples in literature where Raman has been used to control manufacturing processes in the pharmaceutical industry⁵⁸ such as;

1) Synthesis

Raman spectrometry can be used to monitor the synthesis of various pharmaceutical actives⁵⁹. Clegg et al⁶⁰ have published the first industrial example of a comparison of 785 and 998 nm Raman spectrometry for a de-protection reaction. Samples fluoresced at 785 nm and the spectra obtained at 998 nm showed that the reaction was over much sooner than expected. This is an example of lab scale development leading to decreased reaction times on plant scale manufacturing. Mozharov et al⁶¹ have shown an example of Raman spectrometry which followed an esterification reaction in micro channel reactors.

2) Crystallisation

APIs are removed and purified from the solution phase to a solid by crystallisation which is a poorly understood and often poorly controlled step in the manufacturing process^{10, 45, 46, 62}. The crystallisation step determines the physical properties of the isolated material (particle size, shape, distribution of particle sizes and polymorph form) and the information is used to determine the next manufacturing steps required for downstream processing such as milling or powder blending. Different particle sizes and polymorph forms of the same API can have a drastic effect on the bioavailability and efficaciousness of the drug. Raman spectroscopy is particularly useful for monitoring the formation of different polymorphs. The advent of better notch filters allows collection of Raman scattered photons closer to the laser excitation wavelength where the phonon (crystal lattice) vibration bands can be observed for a crystalline material.

3) Granulation or milling

The physical properties of APIs can be altered by either milling^{50, 63}, which reduces the particle size, or granulation^{64, 65}, where the particles are agglomerated to form larger particles by either wet or dry granulation. Typical methods of analysis involve particle sizing by laser diffraction,

dynamic light scattering or focused beam reflectance measurements but there are advantages of using on-line spectroscopic techniques which may be able to characterise more than just the particle size. Raman spectroscopy can be used to follow the granulation process and Jørgensen et al⁶⁶ have compared NIR and Raman spectroscopies to follow the hydrate formation in a granulation process. It was shown that NIR and Raman provide complementary information as Raman spectroscopy is capable of monitoring the hydrate formation on the drug itself whereas the NIR was capable of differentiating between the free and hydrate water present in the granulation.

4) Blending

Mixtures of API and excipients are blended to a homogeneous mixture before preparing the form of the drug that will be delivered to the patient such as a tablet. It is important that the material is homogeneous as this will determine the content uniformity of the drug. Good control of this step in the manufacturing can reduce the likelihood of tablets being produced with too much or too little API. Additionally, on-line monitoring by Raman spectroscopy allows the end point of the blending to be determined in real time, freeing up valuable plant time and reducing the likelihood of over blending where the homogeneity of the mix is reduced⁶⁷.

Raman spectroscopy is not exclusively used by the pharmaceutical industry. Examples are published in the literature where Raman spectroscopy has been used to identify meat spoilage by bacteria⁶⁸. One of the main advantages of the technique over conventional lab based testing is that the measurement is non-destructive. Various reviews are published showing the wide and varied applications in the food and agriculture area⁶⁹. For example, Raman spectroscopy has been used to quantify the level of unsaturated fats contained within fat containing food stuffs⁷⁰. Raman has also been used to monitor the production of titanium dioxide⁷¹ which is a white pigment powder used in paint and as a whitening agent in paper amongst other things.

However, the applications where Raman spectroscopy is employed to follow a change in particle size are of most interest. Like NIR spectroscopy, there are a number of mathematical pre-treatments which can be used to minimise the effect of particle size on Raman spectra such as multiplicative scatter correction³¹ (MSC), standard normal variate³² (SNV), orthogonal signal correction³³ (OSC) and derivatives³⁴. However, there are a very limited number of applications which use the Raman spectra to infer some useful properties of particle size.

Reis⁷² and Santos⁷³ have published papers in collaboration which have described a correlation between particle size and Raman scattering during polymerisation reactions. Reis was able to show that a prediction of particle size could be made using the region $400 - 500 \text{ cm}^{-1}$ which correlated with particle size between $40 - 300 \text{ nm}$. Good quality predictions of particle size were made using PLS models which were independent of monomer concentrations. Santos expanded on this to use the whole Raman spectrum and chemometrics to build a model for particle size and distribution during a suspension polymerisation reaction which produced particles in the micrometre region.

4.1.5 Summary

All the optical spectroscopic techniques selected show some promise for monitoring changes in particle size but very few published examples exist for analysis of high concentration nanoparticle dispersions. Indeed, the particle size regime poses a challenge for optical spectroscopic techniques as diameter of the particles manufactured during milling is similar to/smaller than the wavelengths of light in the ultraviolet to near infrared region. Hence, UV-visible ATR, MIR ATR, NIR reflectance and Raman were all used to investigate their potential for monitoring milling of pigment dispersions.

4.2 Sample Stability

Experimental work performed with high concentration pigment dispersions is time consuming because of the amount of cleaning involved to remove the pigment from the equipment, especially important when performing successive experiments with different colours. It was also easier to clean down the contaminated equipment immediately after the experiment was performed to prevent it drying on to surfaces. As a result it was easier to analyse the diluted pigment dispersion samples for particle size the day after the milling experiment was performed. Discussions with experts at FFIC indicated that the particle size of a highly diluted sample should be stable for a few days and show no significant change in particle size when measured by DLS. To test this hypothesis the sample stability was assessed for diluted and concentrated samples over a five day period to provide confidence in the reference technique for subsequent experimentation.

4.2.1 Experimental

Samples of 20 % w/w PV19 magenta dispersion (acid 10, 30% polymer loading) were extracted at 10, 20, 30, 60, 120 and 240 minutes during a small scale milling experiment using the Netzsch minizeta mill. The total charge of pigment dispersion was 600 g. For each time point a sample was diluted by a factor of around 4000 and 1 cm³ stored in sealed cuvettes shortly after extraction. These samples were analysed by DLS using the instrument Malvern HPPS5001 NIBS particle sizer. Samples were diluted each day from the concentrated sample collected from the experiment and analysed by DLS and the results compared to those from the samples which were prepared immediately, excluding the 20 minute sample which was lost. Each sample was analysed over a period of 5 days with the samples collected on day 0 analysed immediately after the sample was extracted from the mill reservoir and diluted.

4.2.2 Result and Discussion

Figure 4.2 shows the mean and the standard deviation particle size data for samples stored when in dilute and the concentrated form. Both sets of samples show a large standard deviation for the sample collected after milling for 10 minutes as the

pigment dispersion still contained some larger particles. These particles are not stable and tend to sediment in the cuvette. The data shows that, for samples that are diluted immediately after extraction, there is very little change in the Z-average particle size after 10 minutes of milling. Samples stored in their concentrated form show an increase in particle size and an increase in the spread of the Z-average. It can therefore be assumed that samples which are diluted immediately and stored can be analysed within 5 days of the extraction with little effect on the quality of the particle size data.

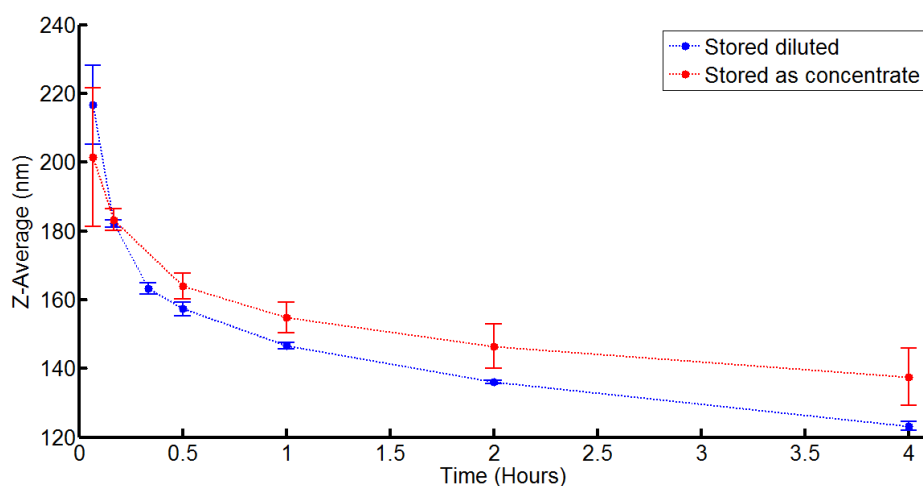


Figure 4.2 – Average particle size (n=5) of samples extracted during milling and analysed by DLS over 5 consecutive days. The blue data set are samples stored after dilution and the red data set were stored at 20 % w/w concentration and diluted from stock each day. The error bars represent ± one standard deviation (n=5)

As a result, the decision was made to dilute all pigment dispersion samples immediately when extracted for milling process. The cuvettes were sealed using Parafilm and analysed within 5 days. In almost all cases the samples were analysed within 24 hours but the additional stability made it easier to plan experiments around demand for the particle size instrument which was used by several groups at the university.

4.3 UV-visible ATR

Previous scoping experiments performed by Jonathan Coulter at FFIC showed that cyan, magenta and yellow pigment dispersions could be measured using UV-visible ATR probes and there was a measurable change in the spectra as the particle size was reduced⁶. Therefore, significant experimental work was undertaken to examine whether this technique was robust enough to provide a means of following the particle size reduction of pigment particles throughout laboratory and plant milling processes.

4.3.1 Results and discussion

Good quality UV-visible spectra can be obtained for the magenta, cyan and yellow pigment dispersions. Figure 4.3 shows three typical spectra collected near the end of milling experiments using an ATR submerged under the level of the pigment dispersion in the stirred sample reservoir of the Netzsch minizeta mill.

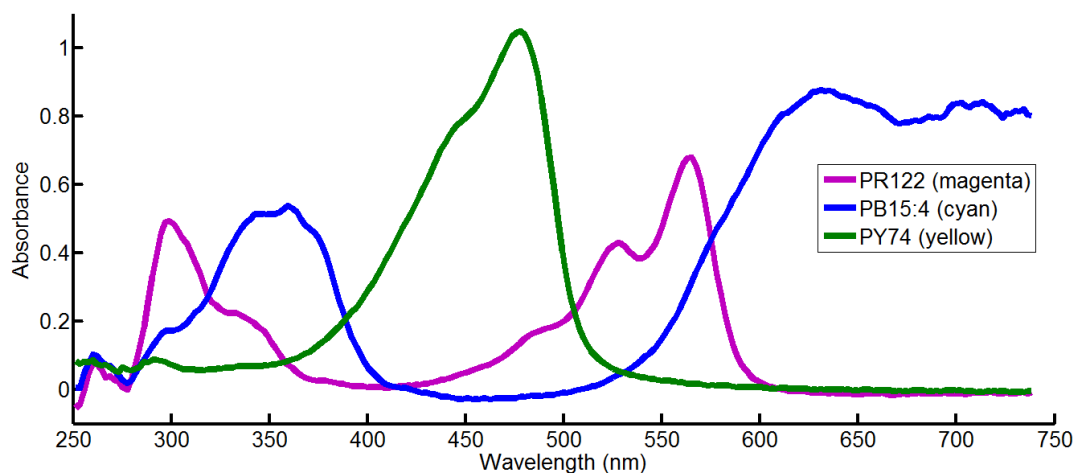


Figure 4.3– UV-visible ATR spectra of 20% w/w pigment dispersions which were milled for 5 hours using the Netzsch minizeta lab mill. The spectra were collected using the Zeiss MCS522 UV-visible spectrometer and 3 bounce Hellma ATR probe.

Several milling experiments were monitored using the UV-visible ATR probe placed within the stirred sample reservoir of the Netzsch minizeta mill and initially encouraging results were obtained. Figure 4.4 shows selected spectra collected in-

situ throughout a milling experiment. The spectra show an increase in absorption as the particle size of the pigment dispersion was reduced

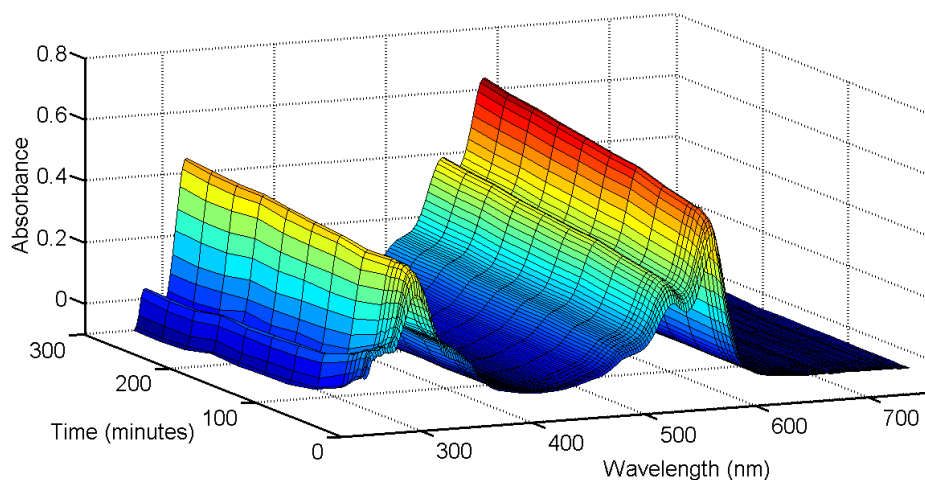


Figure 4.4 – UV-visible spectra collected during a milling experiment of a 20 % w/w dispersion of PR122 with 50 % loading of the acid 10 polymer. The dispersion was milled for approximately five hours using the Netzsch minizeta mill. The spectra shown correspond to sampling times.

From the reference measurements it can be seen that the greatest change in particle size occurs within the first hour of the milling experiment and the UV-visible spectra show similar trends. Figure 4.5 shows the absorbance at 565 nm (the largest feature in the process spectra) and the off-line DLS particle size measurements obtained using the Malvern HPPS5001 DLS instrument. There appears to be an obvious relationship between the particle size and absorbance. The calculated correlation coefficient for the particle size versus absorbance at 565 nm is 0.97.

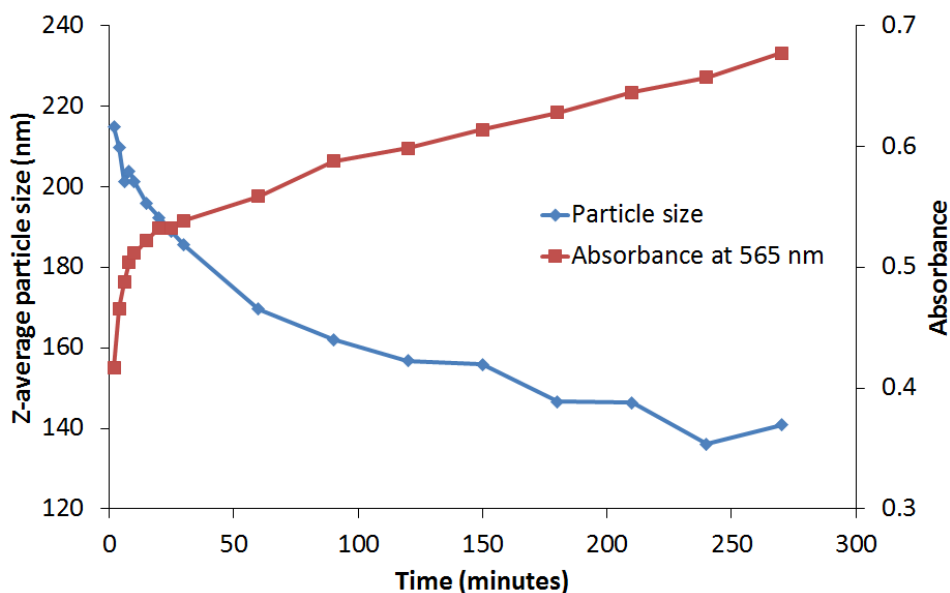


Figure 4.5 – Particle size and absorbance at 565 nm during a milling experiment of 20 % w/w dispersion of PR122 with 50 % loading of the acid 10 polymer.

Several pigment dispersion milling experiments were performed and the main observation was that although the spectra changed with particle size, the change was not consistent. Spectra collected during magenta pigment dispersion milling showed a dramatic rise in the absorption bands present in the spectra and a much more subtle increase in baseline off-set in the non-absorbing regions. Off-line particle size measurements showed consistent trends in the particle size reduction throughout milling experiments of the same constitution and under the same experimental conditions. Ultimately, the UV-visible ATR set up and spectrometers were verified as working correctly and the probe and fibre issues were investigated. The MCS522 UV-visible spectrometer is a process instrument which uses various external optical fibres to connect the source to the probe and reference lines to the detector. As a result the fibres are easily disturbed during and between experiments. However, systematically disturbing the fibres during repeated measurements of a static pigment dispersion sample showed that the fibre movement had a very small effect on the UV-visible spectra that were produced. This then left the possibility that there were potential interface and flow issues that were affecting the quality and reproducibility of the UV-visible spectra. The possibility of probe fouling was investigated. Experiments performed by undergraduate student Joshua Baron estimated that the

penetration depth of the evanescent wave into the sample was approximately 530 nm at a wavelength of 565 nm⁷⁴. Hence, any probe fouling would affect whether the spectra represented the sample in the sample reservoir.

The ATR probe was removed from the sample reservoir at several time points throughout a milling experiment and cleaned using a diluted Decon 90 solution. The effectiveness of the cleaning procedure was verified by collecting a scan of the cleaned, dried probe in air in another experiment.

Figure 4.6 shows the change in the three λ_{max} values during the milling of a PR122 pigment dispersion. The three absorbance values show a large variation after each cleaning which cannot be accounted for as an effect of moving the optical probe and fibres. Additionally, the step changes are not consistent over the whole wavelength range as different λ_{max} seem to be affected by different amounts each time.

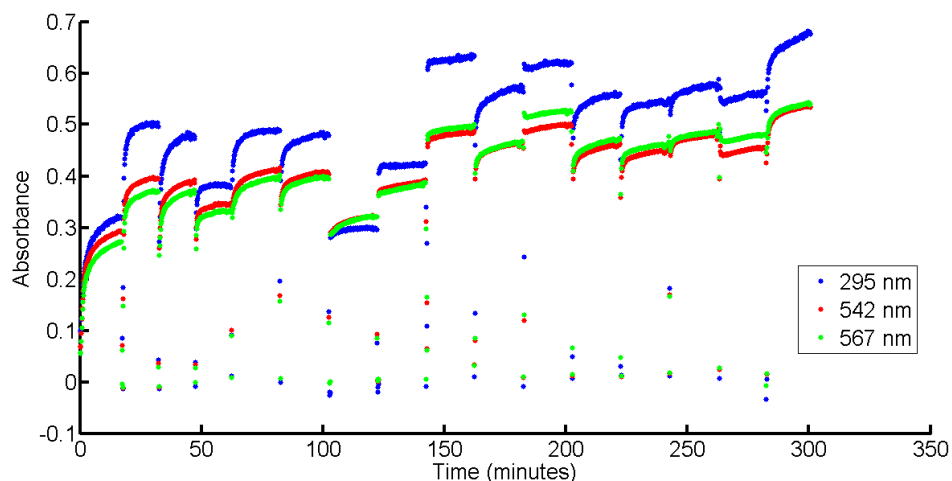


Figure 4.6 – Three λ_{max} absorption values tracked throughout the milling of a 20 % PR122 milling experiment with 40 % loading of polymer "Acid 10". The UV-visible ATR spectra were collected using an ATR probe placed into a stirred sample reservoir. The probe was removed and cleaned every 15 minutes to eliminate any possible probe fouling.

Visual inspection of the probe head showed that there was no obvious probe fouling. The stirring in the sample reservoir ensured that the sample was continually moved to and from the ATR crystal interface.

The large variations observed between cleaning steps was a result of the changing flow of the sample in the reservoir as the probe is effectively a large baffle – forcing

the flow around the body of the probe and the ATR crystal. To confirm that the flow rate did affect the absorption spectra, the probe was placed in the return pipeline of the mill and the recirculation rate run at different levels while spectra were collected. The agitation rate in the milling chamber and the recirculation speed are controlled by the mill motor spin speed. To estimate the effect of flow rate, previously milled pigment dispersion was recirculated through the mill with no milling media present in the chamber. Figure 4.7 shows the response of absorption versus the mill motor speed (analogous to the speed of the pigment through the recirculation loop). The three λ_{max} values differ slightly from those reported in Figure 4.6 as the pigment used was different. Each of the three maximum absorptions show a linear relationship between the speed of the pigment dispersion passing the ATR crystal and the absorption value.

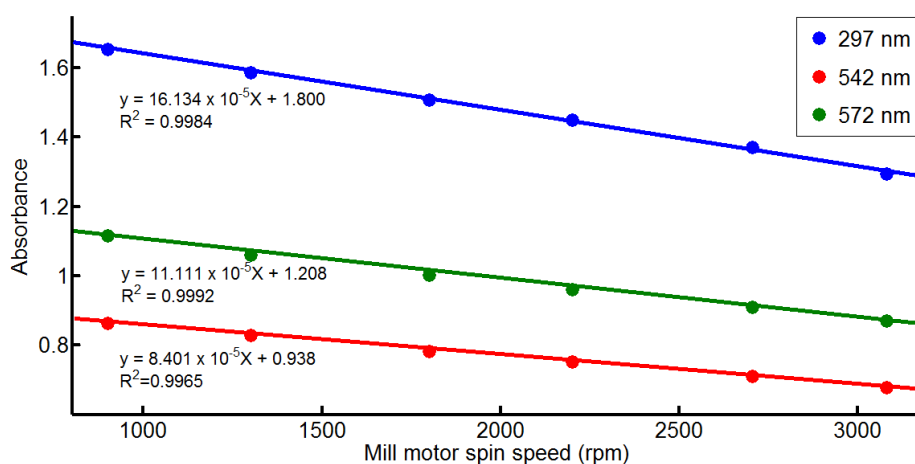


Figure 4.7 – Changing absorption at three λ_{max} absorptions for a 20 % w/w PV19 dispersion with 40 % loading of polymer "Acid 10".

Whether this was unique to dispersions or not was investigated by another undergraduate. Joshua Barron measured the UV-visible spectra of an aqueous solution of Rhodamine B and found that the spectra were not affected by the speed at which the sample was moving⁷⁴.

This further indicates that the speed of the sample is an important parameter to consider when measuring a sample and this makes the creation of a model which can

predict particle size difficult. This also helps to explain the previous experiments results where the probe was removed from the sample reservoir and cleaned. After each replacement the position of the probe changed the way the pigment moved in the sample reservoir. A simple way of avoiding flow problems was to analyse the sample under stop-flow conditions but this provided an additional layer of complications. Incorporation of a bypass loop in to existing plant equipment would be problematic because of the additional cleaning required to maintain such a system. Laboratory experiments where static pigment dispersion samples were analysed were difficult to replicate. This indicated that there are unknown surface effects between the ATR sapphire and the pigment dispersion. Further work performed by FFIC has shown that the surface of the ATR sapphire is not necessarily inert and can be susceptible to coating by methacrylates which are present in the polymer used to stabilise the pigment⁷⁵.

It was concluded that, due to the difficulty in obtaining reproducible UV-visible spectra from milling experiments that UV-visible spectroscopy was not a suitable method for measuring the particle size reduction of high concentration pigment dispersions. The main reasons for this were the effect of sample speed and the comparatively small penetration depth of the evanescent wave in comparison to the particle sizes of the pigments being analysed.

4.4 MIR ATR

The following experiment was performed by Siobhan Kerr as part of her final year thesis project⁷⁶. A 20 % w/w dispersion of PR122 with 50 % loading of the acid 10 polymer was milled for approximately five hours using the Netzsch minizeta mill. Samples were removed from the mill at 30 minute intervals (except the final sample at 285 minutes) and stored in 4 dram vials. Particle size measurements were obtained by DLS at each of the sample extraction time points. The ATR probe was immobilised in a vertical position with the diamond probe head pointing downwards. Vials of sample were raised to submerge the probe head to remove the effect of fibre movements.

4.4.1 Additional equipment

An ABB MB3000 FTIR spectrometer was coupled by 1.5 m polycrystalline silver halide fibres to a 30 cm long by 12 mm diameter hastelloy bodied probe with a diamond ATR. Spectra were collected using a resolution of 16 cm^{-1} over the range $400 - 4000\text{ cm}^{-1}$ and recorded using Horizon MB FTIR software. The number of scans was set to 50 and the detector gain was 243.

4.4.2 Results and discussion

Off-line particle size data showed the Z-average particle size decreased as the pigment was milled. Figure 4.8 shows the MIR spectra between 585 and 1900 cm^{-1} . The diamond ATR showed a strong absorption between $1900 - 2200\text{ cm}^{-1}$ and the region above 2200 cm^{-1} showed a very noisy signal due to the low light throughput of the silver halide fibres in this region. The region is removed from all of the spectra presented herein.

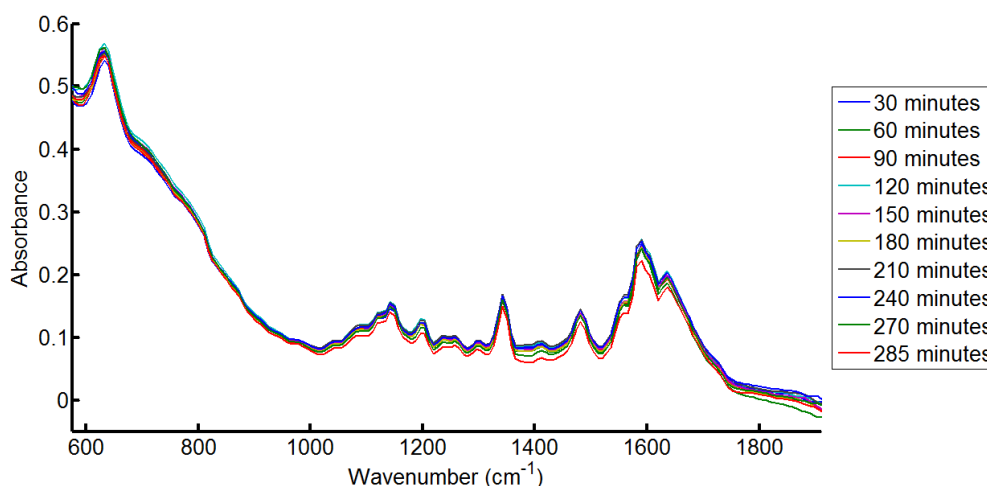


Figure 4.8 – MIR ATR spectra of freshly milled pigment dispersion containing 20 % w/w PR122 with 50 % loading of acid 10 polymer.

There were no clear trends in the data which correlated with the particle size reduction during milling. Figure 4.9 shows the absorbance at 1589 cm^{-1} for the various samples collected throughout the milling experiment. This wavenumber region displayed the highest absorbance between 1000 – 1800 cm^{-1} and the absorption at 1589 cm^{-1} corresponds to C=C double bonds stretching vibration and/or an aromatic skeletal vibration, both of which are present in the PR122 molecule.

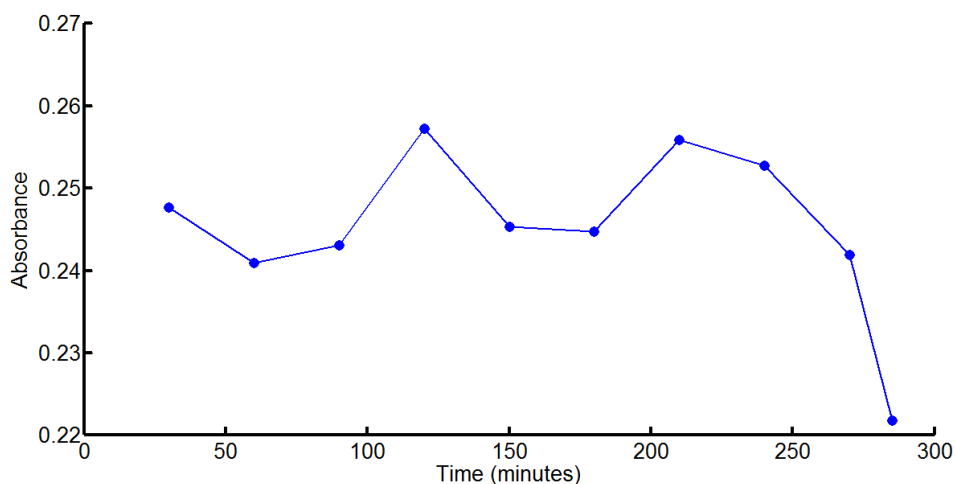


Figure 4.9 – MIR absorption at 1589 cm^{-1} for pigment dispersion samples collected at different stages during a milling experiment.

A number of data treatment methods were applied to the spectra (standard normal variate, multiplicative scatter correction, 1st and 2nd derivatives) but provided no enhancement of the data. Additionally, the spectra were analysed using PCA but no clear trends in the data were identified that could be related to the change in particle size.

It was surmised that the longer wavelengths of radiation used in the MIR range (>2500 nm) result in larger penetration depth which is much larger than the dispersed pigment particles. Allyson McIntyre estimated that the effective pathlength of the evanescent wave was around 6.7 μm at 1095 cm^{-1} for acetone⁷⁷. This penetration depth is significantly larger than the particle size of the nanoscale pigment dispersions. Hence, the technique is not suitable for following the particle size reduction of pigment dispersions.

4.5 NIR

A 20 % w/w dispersion of PY74 with 50 % loading of the acid 10 polymer was milled for approximately five hours using the Netzsch minizeta mill and near infrared spectra collected using the FOSS 6500 probe placed in the sample pot. Each spectrum was an average of 32 scans and spectra were collected at 2 minute intervals.

4.5.1 Results and Discussion

The region from 600 to 1800 nm increases in baseline offset as the particle size is decreased (Figure 4.10). Some detector artifacts appear in the region of 700 to 900 nm but contribute little to the overall spectra. The absorptions in the spectra are typically wide and are therefore difficult to assign to one specific source in the complex matrix of the pigment dispersion apart from water which is the largest constituent of the pigment dispersion. Carboxylic acid groups from the polymer and dipropylene glycol will contribute to the spectra at around 1400 and 1000 nm from the first and second overtones respectively. The third overtone is much weaker but may contribute to the spectra around 750 nm. The water absorption at 1440 nm will arise from the first overtone of the OH stretch for water. The unusually well-defined peak at 1500 nm that appears with the broad water band seems to originate from a reflection from the probes quartz window. The NIR fibre assembly can be placed in to several different sleeves to allow either reflectance or transreflectance measurements. It was observed that by altering the distance the fibre tip was from the quartz window, the prominence of the band could be altered. An optimum position for the probe was selected and kept consistent throughout all the experimentation and as a result the contribution from the quartz window was ignored.

Both the pigment and polymer acid 10 in dipropylene glycol will contain substantial amounts of C-H groups that will contribute to the NIR spectrum of the pigment dispersion. The 1st overtone of which will contribute in the 1600 – 1800 nm region of the spectra. The second overtone occurs between 1000 - 1200 nm and the 1st overtone of the C-H combination bands are contributing between 1350 – 1450 nm.

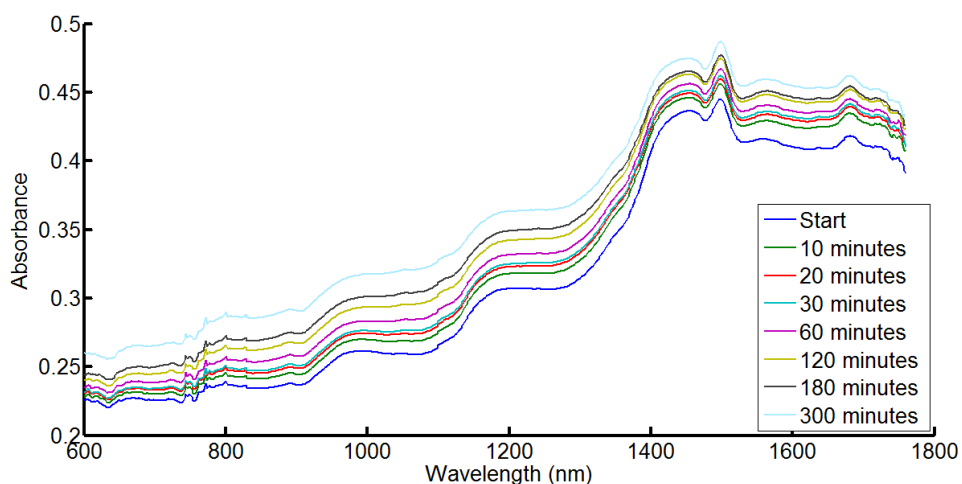


Figure 4.10 – NIR spectra collected during a milling experiment of 20 % w/w PY74 with polymer acid 10 at 50 % polymer loading. 600g pigment dispersion was milled using the Netzsch minizeta mill for 5 hours.

For univariate interrogation of the data, a single wavelength, 1220 nm was selected. This region exhibits a large baseline off-set throughout the experiment whilst remaining relatively flat. Figure 4.11 shows the increase in absorption at 1220 nm and the reduction in particle size as measured by dynamic light scattering (DLS). The discontinuities in the absorption trend are a result of the experimental setup whereby the probe was knocked when samples were removed for characterisation by DLS. The larger discontinuity at 4 hours was a result of the process being restarted after the milling process was suspended overnight. At high concentrations it would be expected that the sample would flocculate overnight and the loosely bound flocculates would be separated shortly after the milling was resumed.

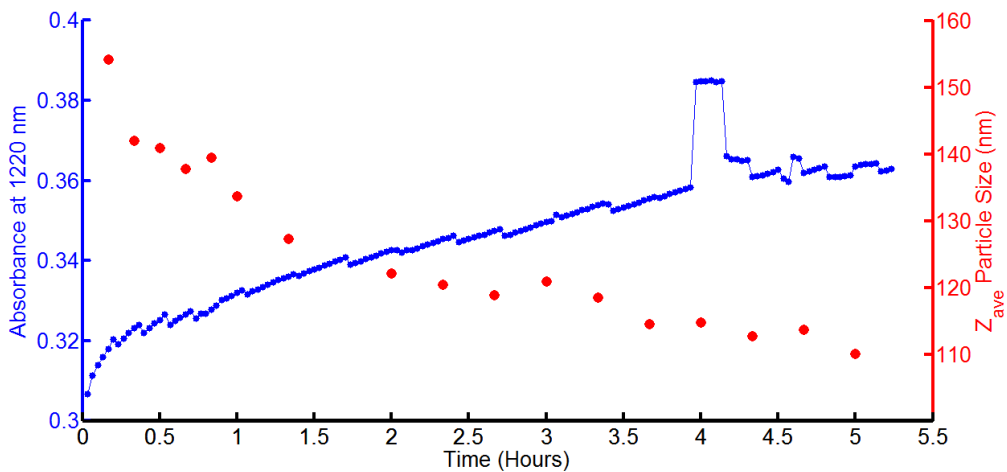


Figure 4.11 – NIR absorbance at 1220 nm and Z-average particle size data measured by DLS for a milling experiment of 20 % PY74 50% polymer loading of acid 10. Conditions as per Figure 4.10.

Although the experimental set up required adjustment to avoid the probe being moved it was clear that there was a measurable effect on the NIR spectra obtained during the milling of a high concentration of yellow pigment dispersion. This observation was extended to spectra collected during milling for cyan and magenta pigment dispersions.

4.6 Raman

Two cyan pigment dispersion milling experiments were monitored using on-line Raman spectrometry to evaluate whether Raman was suitable for monitoring changes in the particle size. Raman spectroscopy offers an advantage over NIR spectroscopy as Raman spectra display a greater molecular specificity with sharp, well defined features which can be assigned to specific parts of a molecule in a sample.

4.6.1 Experimental

Two 800 g 20% w/w cyan pigment dispersions with 60 % loading polymer of polymer "Acid 46" were milled using the Netzsch minizeta mill. The first experiment was milled for approximately 10 hours minizeta mill and the second milled for approximately 12 hours. The sample reservoir was stirred at 240 rpm using an overhead stirrer. The agitator was a small 4 cm diameter turbine type stirrer shaft.

Raman spectra were acquired using the Kaiser Rxn 1 Raman spectrometer with PhAT probe (Kaiser Optical systems, Ann Arbor, USA) and recorded using IC Raman software (Mettler-Toledo, Columbus, USA). Each spectrum was the product of 3 acquisitions of 20 seconds and repeated every 75 seconds. The Raman PhAT probe spacer was situated 30 mm from the level of the pigment dispersion in the stirred sample reservoir.

Experiment 1 was sampled at 30 minutes, 1 hour and every subsequent hour until 5 hours. The experiment was then paused overnight before resuming milling the following day. Samples were then extracted from 6.5 to 9.5 hours at 1 hour intervals. Experiment 2 was sampled at 30 minutes, 1 hour, and then every hour until 6 hours. The experiment was then stored overnight before resuming the next day. On resumption of milling the pigment dispersion was sampled at 6.5 hours and 7 hours then every hour until 12 hours elapsed. Each sample was diluted immediately for analysis by DLS using the Malvern HPPS5001 NIBS particle sizer.

4.6.2 Results and discussion

Figure 4.12 shows the Raman spectra collected at each sampling time point. The intensity of the Raman active bands and the baseline decrease as the milling experiments progress.

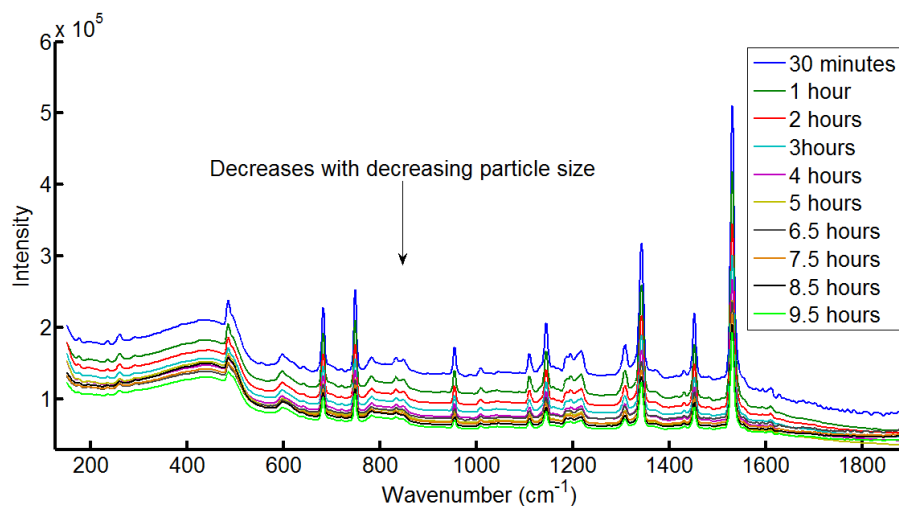


Figure 4.12 - Raman PhAT probe spectra collected during the milling of cyan pigment dispersion Experiment 1.

Figure 4.13 shows the Z-average particle size data for the two milling experiments. The particle size information was examined and samples which showed a bimodal distribution were omitted from the reference data.

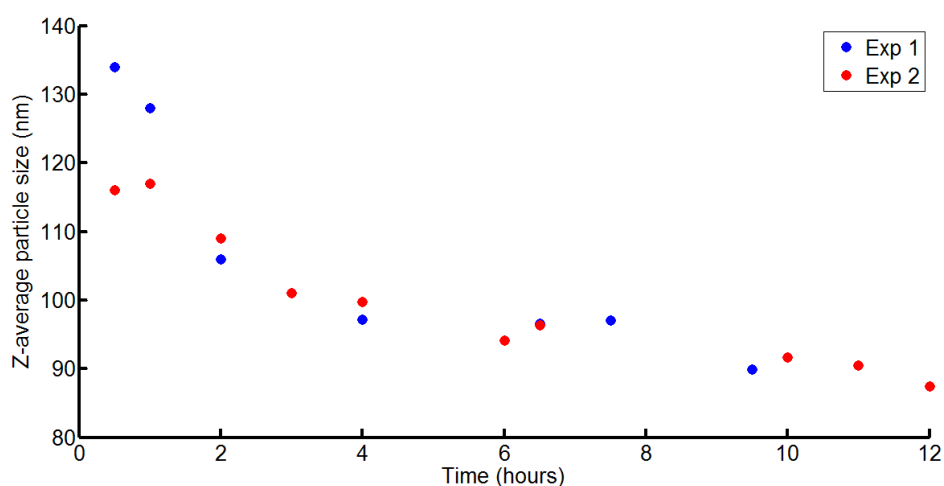


Figure 4.13 - Z-average particle size for two cyan pigment dispersion milling experiments.

The Raman spectra baseline and bands both decrease as the particle size of the pigment dispersion decreases. Figure 4.14 shows the change in intensity of the strongest Raman band in the spectrum at 1530 cm^{-1} . For experiment 1 the intensity of the band decreases to 24% of the starting value after 10 hours of milling. The spectra show a steady change with particle size.

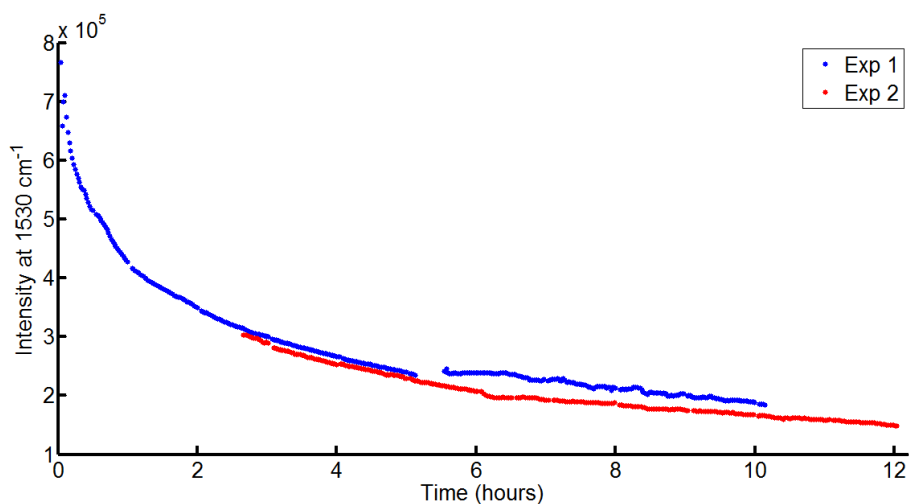


Figure 4.14 - Raman intensity at 1530 cm^{-1} for two cyan pigment dispersion milling experiments.

Experiment 1 has a gap in the spectral data for approximately 30 minutes at 6 hours in to the milling where the software was not recording the spectra. Experiment 2 has spectral data before 2.5 hours into the milling experiment. At the start of experiment 2 the detector was saturated and the scan time was reduced to 15 seconds from 20 seconds. After 2.5 hours the acquisition time was increased back to 20 seconds to allow a direct comparison of the data with the first experiment.

The Raman spectra collected during the milling of cyan pigment dispersion showed that there was an observable change in the spectra as the particle size was reduced. Following this promising work, further investigation was done to examine the applicability of Raman spectroscopy to yellow and magenta pigment dispersions.

4.7 Conclusions

For the reference technique (DLS), it was demonstrated that the pigment samples are stable when diluted immediately for particle size analysis which allows more flexibility when planning and executing lab experiments.

UV-visible and ATR-MIR were not explored further. NIR and Raman were the most promising techniques. The information content of NIR spectra is examined in chapter 5 before using on-line NIR to monitor small and large scale milling experiments in chapters 6 and 7. In chapter 8 the challenges and suitability of Raman spectroscopy for monitoring milling experiments was further explored.

4.8 References

1. K. I. R. Naumenko E.K *Journal of Applied Spectroscopy*, 1981, **34**, 696-700.
2. J. M. Fu, Y. Li and J. L. Guo, *Journal of Colloid and Interface Science*, 1998, **202**, 450-455.
3. H. Kato, A. Nakamura, K. Takahashi and S. Kinugasa, *Physical Chemistry Chemical Physics*, 2009, **11**, 4946-4948.
4. C. Berho, M. F. Pouet, S. Bayle, N. Azema and O. Thomas, *Colloids and Surfaces A: Physicochemical and Engineering Aspects*, 2004, **248**, 9-16.
5. <http://www.oceanoptics.com/Products/fiausp.asp> (Accessed 02 Feb 09).
6. J. Coulter, *Reactive dispersants and ATR spectroscopy*, Fujifilm imaging colorants, Grangemouth (2008).
7. M. G. Trevisan and R. J. Poppi, *Talanta*, 2008, **75**, 1021-1027.
8. I. M. Clegg, A. M. Daly, C. Donnelly, R. Hardy, D. Harris, H. Jackman, R. Jones, A. Luan, D. McAndrew, P. McGauley, J. Pearce, G. Scotney and M. L. Yeow, *Applied Spectroscopy*, 2012, **66**, 574-579.
9. Z. Q. Yu, P. S. Chow and R. B. H. Tan, *Industrial & Engineering Chemistry Research*, 2006, **45**, 438-444.
10. J. Cornel, C. Lindenberg and M. Mazzotti, *Industrial & Engineering Chemistry Research*, 2008, **47**, 4870-4882.
11. J. Schnoller and B. Lendl, *Proceedings of the IEEE Sensors 2004, Vols 1-3*, 2004, 742-745.
12. R. Foley, S. Hennessy and I. W. Marison, *Appl. Spectrosc.*, 2012, **66**, 33-39.
13. A. C. McIntyre, M. L. Bilyk, A. Nordon, G. Colquhoun and D. Littlejohn, *Analytica Chimica Acta*, 2011, **690**, 228-233.
14. W. Clark, *Photography by infrared : its principles and applications*, Wiley u.a., New York u.a., 1947.
15. M. Blanco, J. Coello, H. Iturriaga, S. MasPOCH and C. de la Pezuela, *Analyst*, 1998, **123**, 135R-150R.
16. D. R. Ely, M. Thommes and M. T. Carvajal, *Colloids and Surfaces A: Physicochemical and Engineering Aspects*, 2008, **331**, 63-67.
17. E. Stark, K. Luchter and M. Margoshes, *Applied Spectroscopy Reviews*, 1986, **22**, 335 - 399.

18. W. F. McClure, *Analytical Chemistry*, 1994, **66**, A43-A53.
19. G. Reich, *Advanced Drug Delivery Reviews*, 2005, **57**, 1109-1143.
20. *Guidance for Industry: PAT - a framework for innovative pharmaceutical development, manufacturing and quality assurance*, 2004.
21. R. McDonald, ed., *Colour physics for industry*, 1987.
22. M. C. Pasikatan, J. L. Steele, C. K. Spillman and E. Haque, *Journal of near Infrared Spectroscopy*, 2001, **9**, 153-164.
23. M. Navrátil, C. Cimander and C.-F. Mandenius, *Journal of Agricultural and Food Chemistry*, 2004, **52**, 415-420.
24. N. Prieto, R. Roehle, P. Lavín, G. Batten and S. Andrés, *Meat Science*, 2009, **83**, 175-186.
25. A. Ait Kaddour and B. Cuq, *Powder Technology*, 2009, **190**, 10-18.
26. A. Alishahi, H. Farahmand, N. Prieto and D. Cozzolino, *Spectrochimica Acta Part A: Molecular and Biomolecular Spectroscopy*, 2010, **75**, 1-7.
27. M. Blanco and A. Peguero, *Journal of Pharmaceutical and Biomedical Analysis*, 2010, **52**, 59-65.
28. L. S. Aucott, P. H. Garthwaite and S. T. Buckland, *Analyst*, 1988, **113**, 1849-1854.
29. M. Blanco, J. Coello, H. Iturriaga, S. Maspoch and C. delaPezuela, *Applied Spectroscopy*, 1997, **51**, 240-246.
30. L. Stordrange, F. O. Libnau, D. Malthe-Sørensen and O. M. Kvalheim, *Journal of Chemometrics*, 2002, **16**, 529-541.
31. J. L. Ilari, H. Martens and T. Isaksson, *Applied Spectroscopy*, 1988, **42**, 722-728.
32. R. J. Barnes, M. S. Dhanoa and S. J. Lister, *Applied Spectroscopy*, 1989, **43**, 772-777.
33. S. Wold, H. Antti, F. Lindgren and J. Ohman, *Chemometrics and Intelligent Laboratory Systems*, 1998, **44**, 175-185.
34. A. Savitzky and M. J. E. Golay, *Analytical Chemistry*, 1964, **36**, 1627-1639.
35. J. Luypaert, S. Heuerding, Y. Vander Heyden and D. L. Massart, *Journal of Pharmaceutical and Biomedical Analysis*, 2004, **36**, 495-503.
36. A. J. O'Neil, R. D. Jee and A. C. Moffat, *Analyst*, 1998, **123**, 2297-2302.

37. A. Szalay, I. Antal, Z. Zsigmond, S. Marton, I. Er, odblac, G. R. jr. and K. Pintye-Hódi, *Particle & Particle Systems Characterization*, 2005, **22**, 219-222.
38. A. J. O'Neil, R. D. Jee and A. C. Moffat, *Analyst*, 2003, **128**, 1326-1330.
39. P. Frake, I. Gill, C. N. Luscombe, D. R. Rudd, J. Waterhouse and U. A. Jayasorriya, *Analyst*, 1998, **123**, 2043-2046.
40. F. Kesisoglou, S. Panmai and Y. Wu, *Advanced Drug Delivery Reviews*, 2007, **59**, 631-644.
41. L. K. H. Bittner, N. Heigl, C. H. Petter, M. F. Noisternig, U. J. Griesser, G. K. Bonn and C. W. Huck, *Journal of Pharmaceutical and Biomedical Analysis*, 2011, **54**, 1059-1064.
42. J. P. Higgins, S. M. Arrivo, G. Thurau, R. L. Green, W. Bowen, A. Lange, A. C. Templeton, D. L. Thomas and R. A. Reed, *Analytical Chemistry*, 2003, **75**, 1777-1785.
43. J. Luybaert, D. L. Massart and Y. Vander Heyden, *Talanta*, 2007, **72**, 865-883.
44. A. Rathore, R. Bhambure and V. Ghare, *Analytical and Bioanalytical Chemistry*, 2010, **398**, 137-154.
45. P. Barrett, B. Smith, J. Worlitschek, V. Bracken, B. O'Sullivan and D. O'Grady, *Organic process research & development*, 2005, **9**, 348-355.
46. L. Yu, R. Lionberger, A. Raw, R. D'Costa, H. Wu and A. Hussain, *Advanced Drug Delivery Reviews*, 2004, **56**, 349-369.
47. J. Ma□rk, M. Karner, M. Andre, J. Rueland and C. W. Huck, *Analytical Chemistry*, 2010, **82**, 4209-4215.
48. A. Peinado, J. Hammond and A. Scott, *Journal of Pharmaceutical and Biomedical Analysis*, 2011, **54**, 13-20.
49. J. Rantanen, H. Wikström, R. Turner and L. S. Taylor, *Analytical Chemistry*, 2004, **77**, 556-563.
50. E. L. Parrott, *Journal of Pharmaceutical Sciences*, 1974, **63**, 813-829.
51. S. S. Sekulic, J. Wakeman, P. Doherty and P. A. Hailey, *Journal of Pharmaceutical and Biomedical Analysis*, 1998, **17**, 1285-1309.
52. P. K. Aldridge, C. L. Evans, H. W. Ward, S. T. Colgan, N. Boyer and P. J. Gemperline, *Analytical Chemistry*, 1996, **68**, 997-1002.

53. T. Vankeirsbilck, A. Vercauteren, W. Baeyens, G. Van der Weken, F. Verpoort, G. Vergote and J. P. Remon, *TrAC Trends in Analytical Chemistry*, 2002, **21**, 869-877.
54. <http://www.fda.gov/Cder/OPS/PAT.htm> (accessed 07 Nov 08).
55. D. Hinz, *Analytical and Bioanalytical Chemistry*, 2006, **384**, 1036-1042.
56. R. E. Littleford, P. Matousek, M. Towrie, A. W. Parker, G. Dent, R. J. Lacey and W. E. Smith, *Analyst*, 2004, **129**, 505-506.
57. R. Baker, P. Matousek, K. L. Ronayne, A. W. Parker, K. Rogers and N. Stone, *Analyst*, 2007, **132**, 48-53.
58. T. De Beer, A. Burggraeve, M. Fonteyne, L. Saerens, J. P. Remon and C. Vervaet, *International Journal of Pharmaceutics*, 2011, **417**, 32-47.
59. P. Novak, A. Kišić, T. Hrenar, T. Jednačak, S. Miljanić and G. Verbanec, *Journal of Pharmaceutical and Biomedical Analysis*, 2011, **54**, 660-666.
60. I. M. Clegg, J. Pearce and S. Content, *Appl. Spectrosc.*, 2012, **66**, 151-156.
61. S. Mozharov, A. Nordon, J. M. Girkin and D. Littlejohn, *Lab on a Chip*, 2010, **10**, 2101-2107.
62. G. Févotte, *Chemical Engineering Research and Design*, 2007, **85**, 906-920.
63. E. Merisko-Liversidge and G. G. Liversidge, *Advanced Drug Delivery Reviews*, 2011, **63**, 427-440.
64. J. Huang, G. Kaul, J. Utz, P. Hernandez, V. Wong, D. Bradley, A. Nagi and D. O'Grady, *Journal of Pharmaceutical Sciences*, 2010, **99**, 3205-3212.
65. C. Vervaet and J. P. Remon, *Chemical Engineering Science*, 2005, **60**, 3949-3957.
66. A. Jorgensen, J. Rantanen, M. Karjalainen, L. Khriachtchev, E. Rasanen and J. Yliruusi, *Pharmaceutical Research*, 2002, **19**, 1285-1291.
67. T. R. M. De Beer, C. Bodson, B. Dejaegher, B. Walczak, P. Vercruyse, A. Burggraeve, A. Lemos, L. Delattre, Y. V. Heyden, J. P. Remon, C. Vervaet and W. R. G. Baeyens, *Journal of Pharmaceutical and Biomedical Analysis*, 2008, **48**, 772-779.
68. H. Schmidt, K. Sowoidnich and H.-D. Kronfeldt, *Appl. Spectrosc.*, 2010, **64**, 888-894.
69. D. Yang and Y. Ying, *Applied spectroscopy reviews*, 2011, **46**, 539-560.

70. Y. Ozaki, R. Cho, K. Ikegaya, S. Muraishi and K. Kawauchi, *Applied Spectroscopy*, 1992, **46**, 1503-1507.
71. I. M. Clegg, N. J. Everall, B. King, H. Melvin and C. Norton, *Applied Spectroscopy*, 2001, **55**, 1138-1150.
72. M. M. Reis, P. H. H. Araujo, C. Sayer and R. Giudici, *Polymer*, 2003, **44**, 6123-6128.
73. J. C. Santos, M. M. Reis, R. A. F. Machado, A. Bolzan, C. Sayer, R. Giudici and P. H. H. Araujo, *Industrial & Engineering Chemistry Research*, 2004, **43**, 7282-7289.
74. J. Barron, *BSc Thesis: Characterising pigment polymer processing using in-situ optical spectroscopy*, University of Strathclyde, 2011.
75. A. Dickinson and J. Dunn, *Personal communication: ATR interface effects slides presented at CPACT reserch day Sep 2012*, 2012.
76. S. Kerr, *BSc thesis: The use of spectroscopic methods for monitoring nanoscale polymer-stabilised pigment dispersions*, University of Strathclyde, 2010.
77. A. McIntyre, *PhD Thesis: Extending the scope of mid-infrared spectrometry for in situ process analysis through ATR immersion probes*, University of Strathclyde, 2011.

5. Off-line visible-NIR spectroscopy

The investigation of different optical spectroscopic techniques in chapter 4 showed that NIR was potentially useful for following the particle size reduction of pigment dispersions in-situ. Obtaining the absorption and scattering coefficients for pigment dispersions of different particle size will allow a greater understanding of what causes the change in the reflectance NIR spectra for magenta, yellow and cyan pigment dispersions. Additionally, the effect of number density and the size of particles will be investigated to ascertain which effect is dominant during the milling process where the average particle size is decreased which simultaneously increases the number density of small particles.

The phenomenon of light scattering is not a simple interaction. The wave model of light describes it as a travelling electronic and magnetic wave oscillating at 90° planes to each other and scattering occurs when light interacts with matter. Matter consists of positive and negative charges and the amount of scattering is governed by the polarizability of the molecule which means how easy is it to shift the charges in the molecule (by the incoming source light whether it be ultraviolet, visible or near infrared).

The amount of movement of the charge is governed by the frequency of the wave, and on reaching the particle the light distorts the distribution of charge in the molecule. This movement produces an oscillating dipole or electric oscillator. This oscillation results in most of the light being elastically scattered (Rayleigh scattering) as the light energy is re-emitted at the same wavelength as the incoming source.

Isotropic scattering (where the intensity of scattered light is equal in all directions) occurs when the particle diameter is approximately 10 % of the wavelength of the incoming electromagnetic radiation. However, the picture is not so simple for larger particles. These larger particles have several oscillators dependant on the size, shape and chemical makeup of a particle and these cause a phase difference in the light emitted. This leads to an angular dependence for the intensity of scattered light due to the interference of the emitted light from the different oscillators. This situation is called non-isotropic scattering¹ and is best described using Mie theory².

To simplify where isotropic and non-isotropic scattering occurs the size parameter, a , is used (Equation 5.1). This is calculated using the wavelength of the incident light, λ , and the particle diameter, d .

$$a = \frac{\pi d}{\lambda} \qquad \text{Equation 5.1}$$

Where a is less than 0.3 the scattering of light by the small particles is best characterised by Rayleigh scattering whereas when the size parameter is between 0.3 and 30 the scattering is described by Mie theory. The particle size of the pigment dispersions (circa 150 nm) falls within the Mie scattering domain when the light source used to illuminate the particles is in the near infrared region.

Light incident on a turbid sample will be absorbed and scattered as determined by the physical properties of the sample such as concentration (number density of particles) and particle size. Potentially valuable information can be gained about a process by separating the absorption and scattering coefficient contributions to spectra. This methodology has previously been applied to monitor the growth cycle of bacteria³ using off-line NIR measurements. Bio systems such as fermentation or growths of cell cultures have a number of different chemical and physical features which will affect spectra in the NIR region. Transmission or reflectance spectra will contain both absorption and scattering information. The chemical information relates to the concentration of the product and feedstocks such as glucose and is revealed in changes in the absorption whereas cell size and biomass concentration will contribute to scattering. In this instance it is desirable to be able to separate the two phenomena. This allows the construction of robust calibration models, capable of following the changing chemical and physical properties of the sample.

An understanding of the way absorption and scattering properties behave is important for other consumer products such as sun screen⁴⁻⁶. Products containing nanosize inorganic particles such as titanium dioxide depend on the scattering properties of the small particles to prevent harmful UV radiation reaching the skin and causing cell damage. Agglomeration of inorganic nanoparticles of TiO₂ create a

cosmetic problem where the sun screen appears opaque rather than clear on the end user's skin and, more importantly, the larger particles are less efficient at attenuating the harmful UV-A and UV-B wavelengths (400 to 315 nm and 315 to 280 nm ranges respectively). The particle size of the inorganic pigment determines the scattering properties and how the product performs. To reliably manufacture high quality sun screens, it is crucial that particle size is tightly controlled and the dispersions are stabilised to prevent agglomeration.

The absorption and scattering properties of samples are very important to measurements made in the medical field to achieve non-invasive monitoring of blood oxygen levels. Tseng et al⁷ have described a method for characterising the interrogation region of a diffusing probe on skin tissue, showing that shorter wavelengths of illuminating light (600 nm) captured information from the upper skin layer (epidermis) and longer wavelength (900 nm) captured information from deeper within the tissue (the sub-dermis). From this they deduced that the wavelength of illuminating light was an important factor to consider when measuring the oxygen content of blood and they showed that the oxygenation content for tissue could be reliably measured.

The number of NIR monitoring systems employed for on-line measurement and control is ever increasing and there is a growing need by the pharmaceutical industry to further understand the complex information from the absorption and scattering events that contribute to NIR spectra. A review by Shi and Anderson⁸ provides a good description of the current methods employed to separate absorption and scattering properties for pharmaceutical powders and dispersions (which typically display particle sizes in the μm region). The four main methods to extract μ_a and μ_s are:

1. Spatially resolved spectroscopy
2. Frequency resolved spectroscopy
3. Time resolved spectroscopy
4. Integrating sphere transmission and reflectance spectroscopy

Spatially resolved spectroscopy uses relatively simple equipment where scattered photons are collected (either in transmission or reflectance mode) at set distances from the illuminating source, using a number of detection fibres. This has found use in medical applications where non-invasive measurements of skin, tissue or blood are required. However, there are some difficulties arising from probe contact with the skin as gentle pressure can result in changes to the properties of the sample. Keinle et al⁹ have shown a non-contact methodology which avoids changing the measured sample.

Frequency resolved spectroscopy⁸ is similar to spatially resolved spectroscopy however the illuminating source is modulated. Multiple scattered and attenuated light is collected at several fixed points in the sample. The remaining light collected using optical fibres contains contributions from the attenuation (loss) of photons per distance and the phase shift from the change in modulation of the source.

Time resolved spectroscopy^{10, 11} collects transmission or reflectance spectra using a picosecond laser as the irradiating source. The photons collected at a fixed point from the irradiating source display a band broadening dependant on the chemical and physical properties of the sample under analysis. This temporal broadening can be used to determine the fundamental optical properties.

For the work undertaken, the methodology used was the integrating sphere transmission and reflectance measurements. The radiative transport equation (RTE) (Equation 5.2) is used to rationalise light propagation in biological tissues and dispersions in terms of absorption, scattering and anisotropy.

$$\frac{d\mathbf{I}(\lambda, \mathbf{r}, \mathbf{s})}{ds} = -(\mu_a + \mu_s) + \frac{\mu_s}{4\pi} \int p(\mathbf{s}, \hat{\mathbf{s}}) \cdot \mathbf{I}(\lambda, \mathbf{r}, \hat{\mathbf{s}}) \cdot d\omega \quad \text{Equation 5.2}$$

where $\mathbf{I}(\lambda, \mathbf{r}, \mathbf{s})$ is the specific intensity of light of wavelength λ at point \mathbf{r} with radiation incident along direction \mathbf{s} , μ_s is the bulk scattering coefficient (mm^{-1}), μ_a is the bulk absorption coefficient (mm^{-1}), $p(\hat{\mathbf{s}}, \hat{\mathbf{s}}')$ is the phase function (described by the Henyey-Greenstein equation, Equation 5.3) and $d\omega$ is the solid angle.

$$p(\cos\theta) = 0.5(1 - g^2)(1 - g^2 + 2\cos\theta)^{1.5} \quad \text{Equation 5.3}$$

This is a measure of the angular distribution of scattered light and is usually approximated as a function of the anisotropy factor g and θ is defined as the scattering angle. When the sample scatters equally in all directions g will be 0, when the sample scatters in the backward direction g will be -1 and when the sample scatters in the forward direction g will be 1.

The bulk absorption and scattering parameters are linked to the physical properties of the samples;

$$\mu_a(\lambda) = \sum \rho_i \sigma_{a,i}(\lambda) \quad \text{Equation 5.4}$$

$$\mu_s(\lambda) = \sum \rho_i \sigma_{s,i}(\lambda) \quad \text{Equation 5.5}$$

where bulk absorption and scattering coefficients are functions of the number density (ρ_i) and the absorption and scattering cross sections $\sigma_{a,i}$ and $\sigma_{s,i}$, respectively, of component i present in the sample. These coefficients represent the probability of a photon being scattered or absorbed and the reciprocal of each is the mean free path which is the distance a photon travels between consecutive absorption or scattering events.⁸

By fixing “ g ” it is possible to solve the RTE (Equation 5.2) using two measurements at each wavelength. Solving the equations is performed using the inverse adding and doubling method.¹² As the sample is placed in a quartz cuvette, the reflectance and transmission properties of the cuvette are taken into account in the calculation. The equation is solved in terms of α (albedo *cf.* fraction of reflected radiation) and τ (optical depth) as shown in Equation 5.6 and Equation 5.7, respectively. l is defined as the path length of the cuvette in mm.

$$\alpha = \frac{\mu_s}{(\mu_s + \mu_a)} \quad \text{Equation 5.6}$$

$$\tau = (\mu_s + \mu_a)l \quad \text{Equation 5.7}$$

The RTE has no analytical solution but the scripts used in this work have previously been validated and published in the PhD thesis of Elitsa Dzhongova¹³. Section 3.6 of the thesis deals specifically with how the scripts were validated for a system of latex spheres. The following is an excerpt from that thesis:

Theoretical values for scattering coefficient μ_s (figure 3.8) were calculated from the microsphere radius r and the refractive indices of polystyrene and water using Mie theory in the wavelength region from 350nm up to 2200nm. Experimental values for μ_s were also obtained by calculating them using the inverse adding-doubling method. Figure 3.8 shows the agreement between theoretically calculated and experimentally obtained values for μ_s . From the two curves obtained for the scattering coefficients it can be seen that both have good agreement over most of the wavelength range considered. Some differences occur below 900nm and a small peak appears around 1450nm. In this research, the biological system under consideration is studied only in the region 950-1850nm due to the low quality of the spectroscopic data beyond 1850nm. The truncation of the NIR region is due to the fact that high amount of water is present in the sample and the high water absorption leads to the very low signals beyond 1850nm.

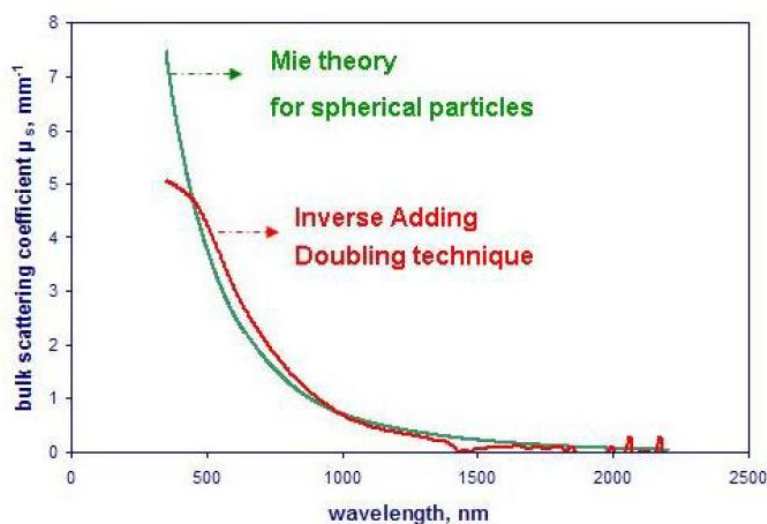


Fig. 3.8 Scattering coefficient μ_s , calculated using inverse adding-doubling techniques and Mie theory for spherical particles.

Additionally, the values from the theoretical scattering coefficients were then used to derive theoretical spectra of the latex sphere system for diffuse transmittance, collimated transmittance and diffuse reflection measurements over the wavelength range 350 – 2200 nm. The calculated spectra showed a good agreement with experimentally measured spectra, indicating that the script was valid up until 1850 nm where there was a significant effect of water on the spectra. This validation by comparison of measured versus theoretical values indicates that the calculations in the script are fit for purpose and are used in the following experimental work to determine the optical properties of pigment dispersions.

5.1 Experimental

This section of work was performed using the magenta pigment dispersions. A number of laboratory scale milling experiments were performed which varied both the pigment and polymer concentrations. Although the primary aim of this work was the investigation of in-situ monitoring using optical spectroscopic techniques, the large number of samples generated presented an opportunity to use pigment samples of different particle size to investigate the fundamental optical properties of the pigment dispersions. The in-situ data will be discussed in chapter 6.

Pigment dispersion mill bases were prepared by dispensing the required weight of dispersing polymer "Acid 46" (Strength 31.5%, FFIC, Grangemouth) and distilled de-ionised water (Table 5.1) in a large beaker and the contents mixed using a Kenwood hand blender. The required weight of 2,9-dimethylquinacridone pigment (provided by FFIC, Grangemouth) was added to the polymer water mixture and stirred by hand before further mixing using the Kenwood hand blender until a smooth dispersion was present.

Milling experiments with varying concentrations of pigment and polymer were undertaken according to a 2 factor 2 level design with a centre point. Pigment concentrations ranged from 15 to 25 % w/w (centre point 20 % w/w) and the polymer loading ranged from 30% to 50 % loading (centre point 40 % loading). Polymer loading is defined as the % of polymer relative to the pigment present.

Table 5.1 - Polymer and pigment concentrations used in the experimental design. Experiments F and G were not used for the off-line spectroscopic investigation of the scattering properties.

Exp	Pigment mass (g)	Polymer mass (g)	Water mass (g)	Pigment dispersion details	
				Pigment strength (% w/w)	Relative polymer conc.
A	105.00	100.00	495.00	15	30
B	140.00	177.78	382.22	20	40
C	175.00	166.67	358.33	25	30
D	140.00	177.78	382.22	20	40
E	140.00	177.78	382.22	20	40
F	105.00	166.67	428.33	15	50
G	175.00	277.78	247.22	25	50

Pigment dispersions were milled using Netzsch minizeta mill for a period of 5 hours. To ensure reliable mixing the sample reservoir was stirred at 400 rpm.

100 mg of pigment dispersion collected at 30, 60, 120, 180, 240 and 300 minutes of the milling experiments were diluted to a volume of 25 mL in a volumetric flask using distilled deionised water. Samples were then measured in transmission and reflectance mode in a 1 mm path length quartz cuvette (Figure 5.1). The operating procedure and instrument parameters are contained within section 3.4.3. The order of analysis was randomised, completing the set of 6 reflectance measurements before reconfiguring the spectrometer for transmission measurement.

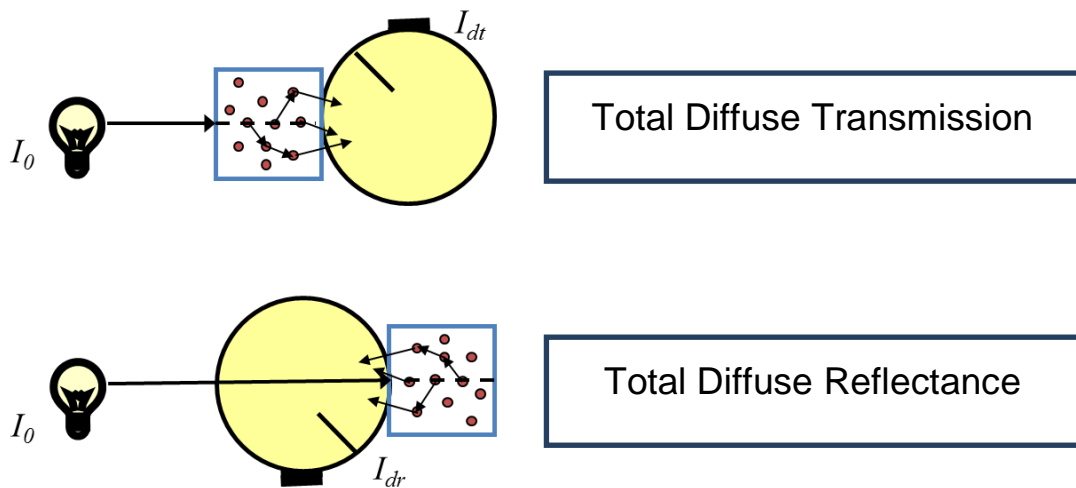


Figure 5.1 – Total diffuse transmission and reflectance measurement using an integrating sphere¹⁴. I_0 , represents the intensity of light from the source when no sample was present and I_{dt} and I_{dr} represent the intensity of light detected in transmission and reflectance measurement modes.

Extraction of μ_a and μ_s was achieved using routines developed by Suresh Thennadil in Matlab and the Optimisation Toolbox (The Mathworks, Natick, Massachusetts, USA). The refractive indices of the quartz cell (1.51), sample (1.34) and air (1.00) are required inputs to the inversion routine in addition to smoothed transmission and reflectance measurements. Smoothing of the data was implemented using the Savitzky-Golay function (filter width 9, order of polynomial 2, order of derivative 0) in PLS_Toolbox (Eigenvector Research, Washington, USA). The anisotropy factor, g , was fixed at 0.8 for all calculations to allow the determination of the μ_a and μ_s using only two measurements. Both, μ_a and μ_s , were extracted at 2 nm intervals for the wavelength range 400 – 1800 nm.

The inversion routine operates by guessing values of α and τ and then calculates the reflectance and transmission spectra from the “guessed” values using the adding-doubling method. These calculated values are then compared with the experimental data and the Optimisation Toolbox program **fmincon** runs until the value of the “guessed” result and experimental results converge. A more detailed description of the mathematics used to extract the absorption and scattering coefficients is given in the papers written by Dzhongova et al³ and Prahl et al.¹²

5.2 Results and Discussion

5.2.1 Magenta pigment dispersions

Spectra of diluted magenta pigment dispersions show subtle differences in the regions where there are no strong absorptions. Figure 5.2 and Figure 5.3 show a set of spectra which were used to solve the radiative transfer equation for μ_a and μ_s (the bulk absorption and scattering coefficients, respectively) for experiment B. Experiment B is shown as it is the first three identical experiments performed with the same pigment and polymer concentrations in the dispersion (20% pigment, 40% polymer loading). Spectra were collected in absorbance and, to calculate the transmission and reflectance values, the spectra were transformed using the relationship given in Equation 5.8.

$$\text{Transmission or Reflectance} = 10^{-\text{Absorbance}}$$

Equation 5.8

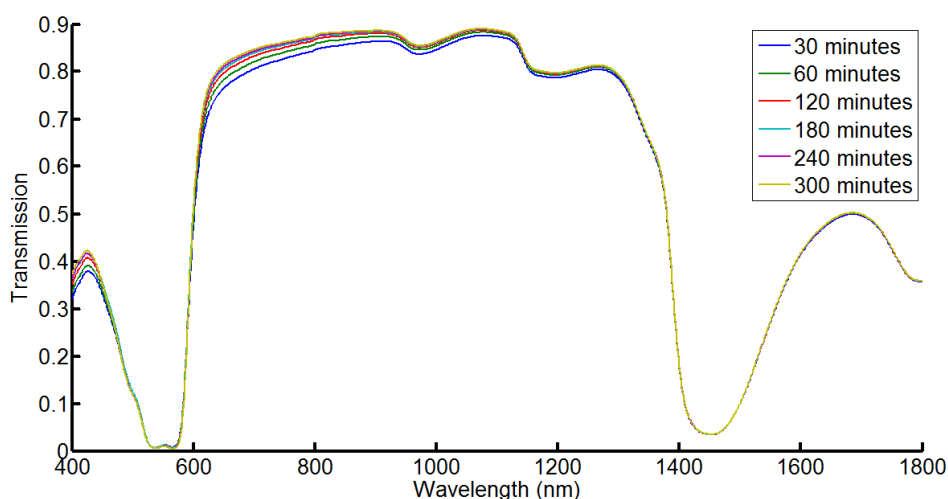


Figure 5.2 – Off-line transmission visible-near infrared spectra of diluted pigment dispersion collected at 30, 60, 120, 180, 240 and 300 minutes during milling of a magenta pigment dispersion (experiment B - 20 % pigment concentration, 40 % polymer loading).

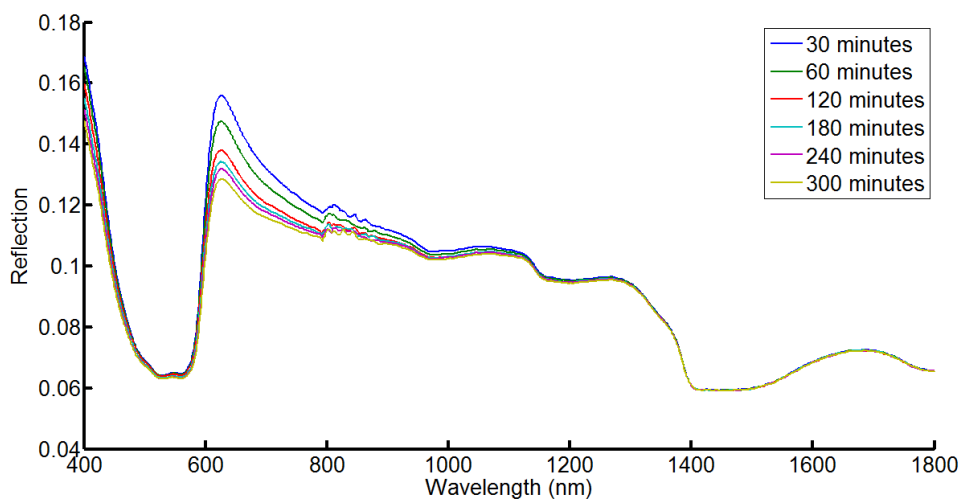


Figure 5.3 – Off-line reflectance visible-near infrared spectra of diluted pigment dispersion collected at 30, 60, 120, 180, 240 and 300 minutes during milling experiment B (20 % pigment concentration, 40 % polymer loading).

In both the transmission and reflectance spectra, there is very little change between spectra exhibiting different particle sizes where there is a strong absorption. Using the methods described earlier, the bulk absorption and scattering coefficients were derived for diluted samples removed at 30, 60, 120, 180, 240 and 300 minutes for milling experiments A to E. Figure 5.4 shows the calculated scattering coefficient over the wavelength range 400 – 1800 nm for experiment B.

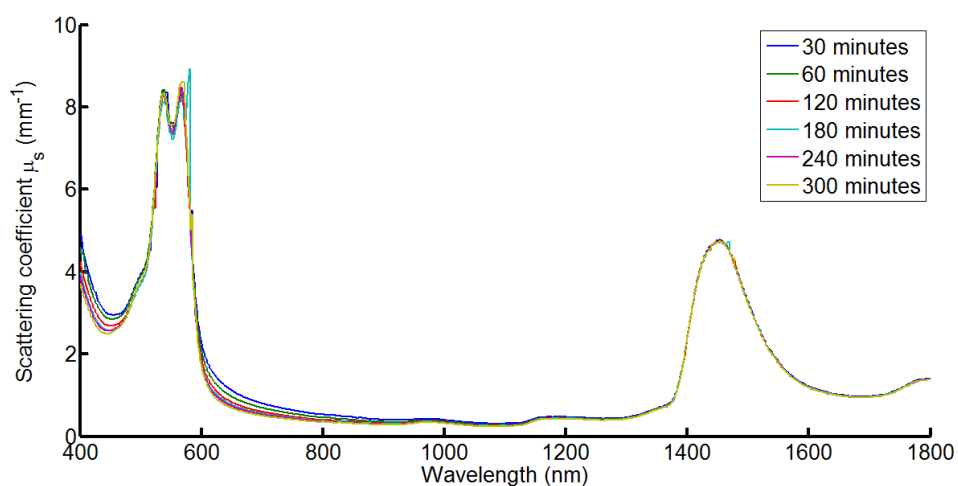


Figure 5.4 – Scattering coefficient values over the wavelength range 400 - 1800 nm for pigment dispersion samples with different particle size values for experiment B.

To ascertain the region where the effect of particle size is greatest (Figure 5.5), the correlation coefficient was calculated of the particle size at each wavelength for experiments A to E (Figure 5.6).

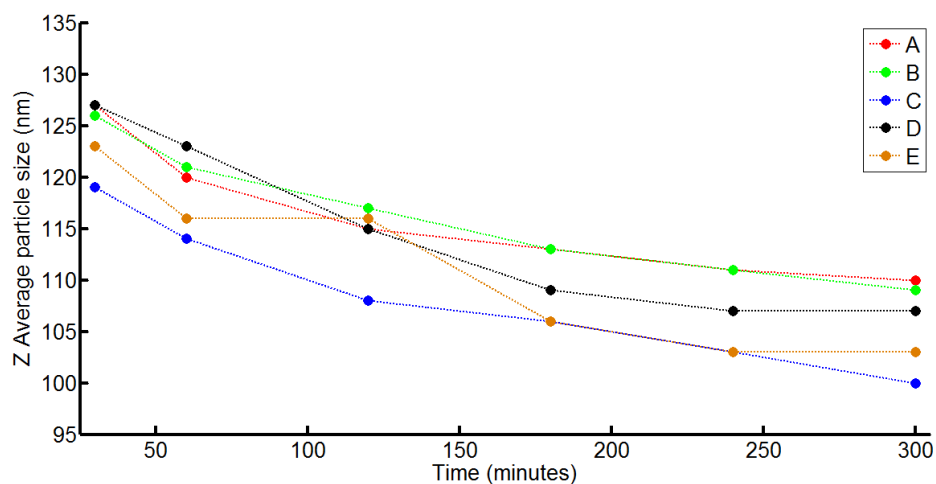


Figure 5.5 – Particle size for magenta pigment dispersions for milling experiments A to E

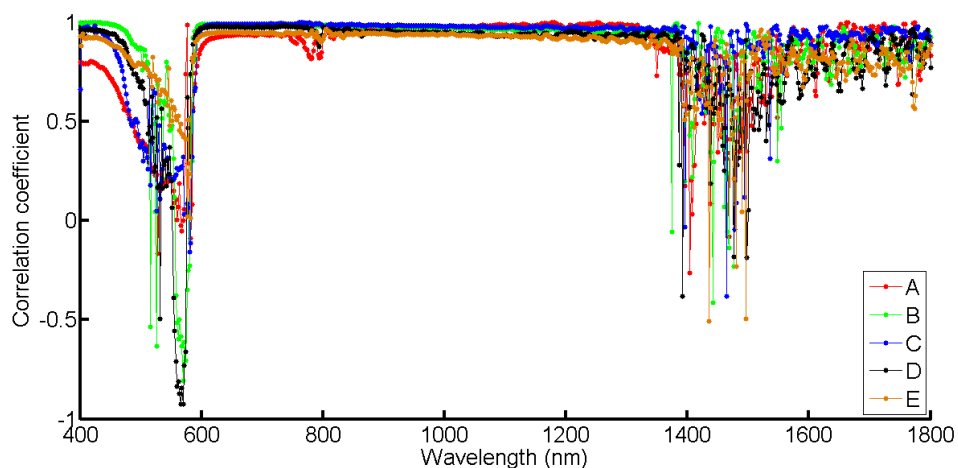


Figure 5.6 – Correlation coefficient relating the scattering coefficient with the particle size for milling experiments A to E.

There is a high correlation between the change in particle size and the calculated scattering coefficient values for experiments A to E over most of the wavelength range examined. The first region where the correlation breaks down (500 – 600 nm) corresponds to the visible absorption band of the magenta pigment and the second

region (1300 – 1600 nm) corresponds to the strong water absorption band in the NIR spectra. Hence, the wavelength range of interest for investigation of the scattering properties of diluted magenta pigment dispersions is between 650 – 1300 nm. Figure 5.7 shows the high correlation of scattering coefficient and particle size for the wavelength region selected. There is still an observable disturbance around 800 nm where the correlation coefficients vary. This is attributed to the detector changeover in the Cary 5000 instrument and the way in which the radiative transfer equation is solved for the absorption and scattering coefficients. The Matlab script calculates each wavelength sequentially, working from high to low wavelength, and uses the previous value as a starting estimate for the next calculation. This also helps explain the slightly more erratic correlation coefficients between 1200 – 1300 nm as calculations performed immediately preceding this region corresponds to the large broad water absorption.

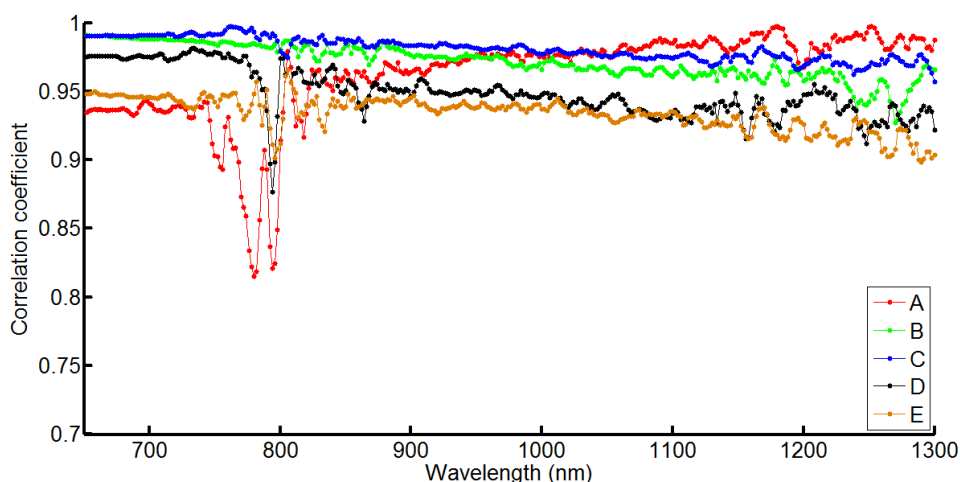


Figure 5.7 – Correlation coefficient for change in the scattering coefficient versus change in the particle size.

Figure 5.8 and Figure 5.9 show the extracted scattering and absorption coefficients, respectively, for the milling of magenta pigment using the conditions given by experiment B in Table 1.

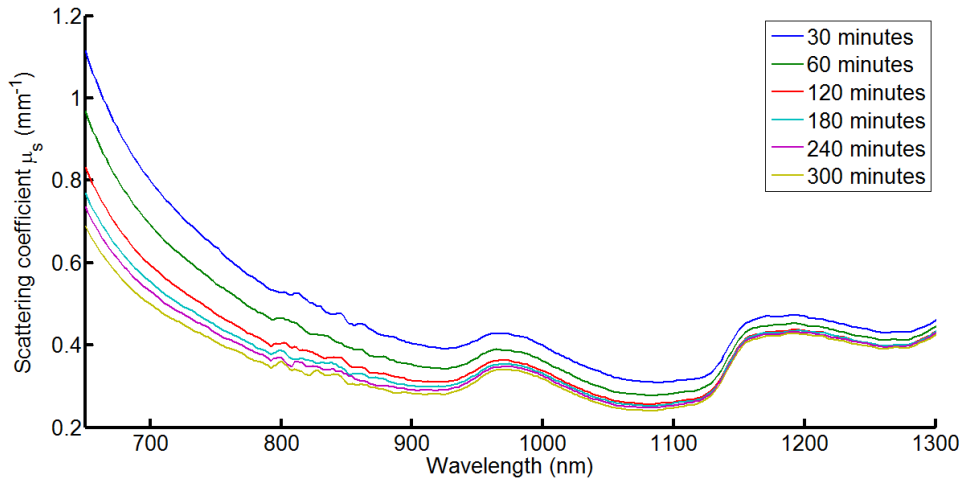


Figure 5.8 – Scattering coefficient from milling experiment B.

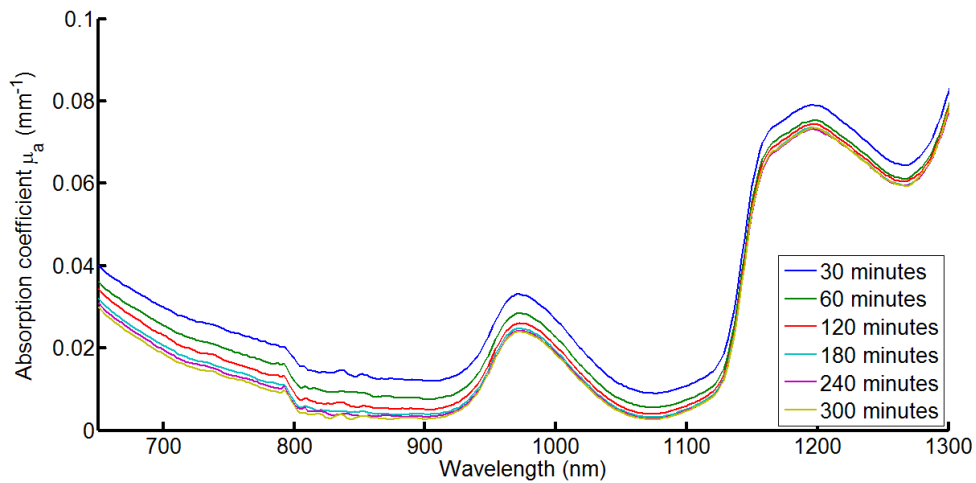


Figure 5.9 – Absorption coefficient from milling experiment B.

Both the absorption and scattering coefficients decrease with reducing particle size and the magnitude of change decreases with decreasing wavelength. The scale of the scattering coefficient is an order of magnitude larger than the scattering coefficient indicating that the physical properties of the pigment dispersion dominate the NIR spectra. Some absorption features in the NIR region at ~970 and ~1150 nm have "leaked" into the scattering coefficient but the general trends are clear. This indicates that observed changes in the on-line reflectance NIR spectra are a result of the changing physical properties of the sample (i.e. particle size) rather than a chemical change in the system. As milling reduces the particle size of the pigment dispersion,

the fundamental optical properties of the sample are changed. Reducing the scattering coefficient means that less light is scattered back towards the collection fibres and hence there is a higher absorption.

Figure 5.10 shows the bulk scattering coefficient for the magenta pigment dispersion sample obtained 30 minutes in to the milling experiment. The scattering coefficients decrease with increasing wavelength. Experiments A and C are separated from the three centre point replicates of the 2 factor, 2 level design of experiments. Experiment A contains 15 % w/w pigment, C 25 % and B, D and E contain 20 % pigment. The separation is a result of the fixed sample preparation step whereby 100 mg of freshly milled magenta samples was diluted to 25 ml in a volumetric flask. No correction for the pigment concentration was used hence there are a higher number of pigment particles in the samples from experiment C and fewer in samples from experiment A.

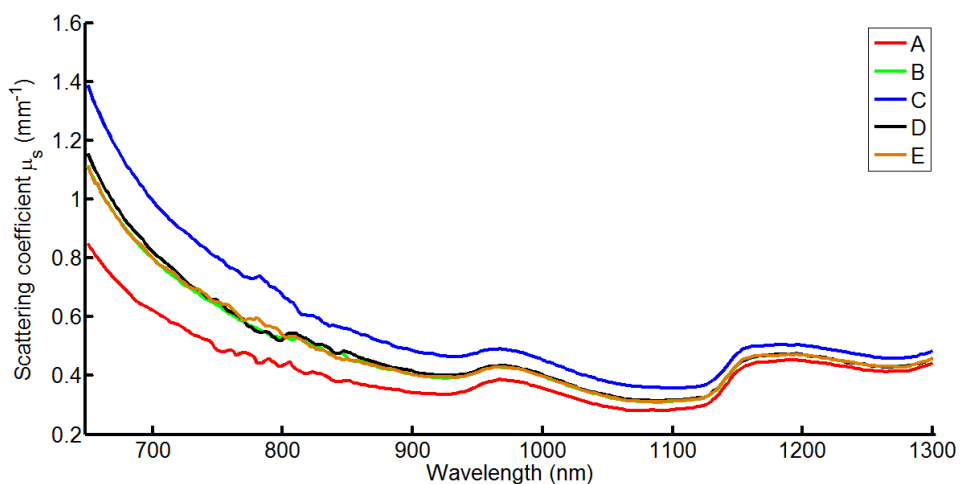


Figure 5.10 – Scattering coefficients for t=30 minute samples collected from magenta pigment dispersion milling experiments A to E.

Figure 5.11 shows the absorption coefficient over the same wavelength range. Again, there is a clear grouping with pigment concentration where lower pigment concentration provides a smaller absorption coefficient and a higher pigment concentration produces a higher absorption coefficient.

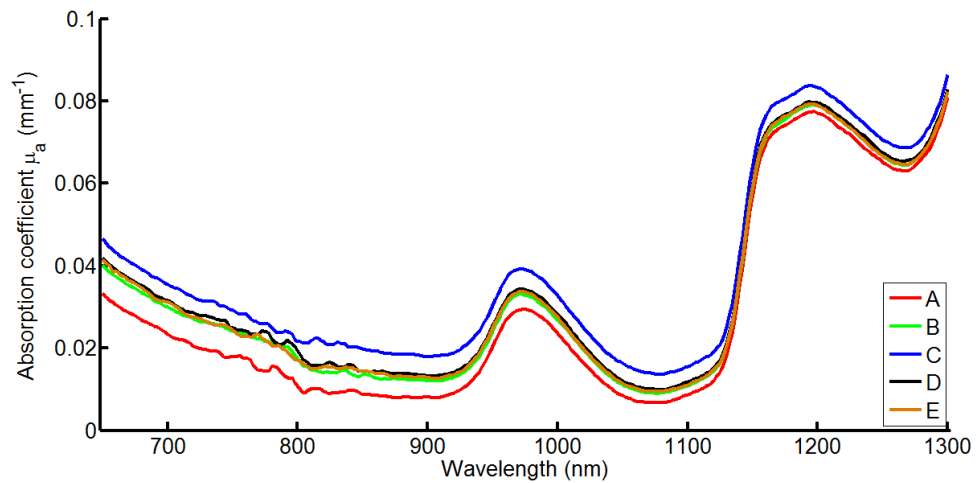


Figure 5.11 – Absorption coefficients for t=30 minute samples collected from milling experiments A to E.

In general, the experimentally derived bulk scattering coefficients for the diluted pigment dispersions decreases with decreasing particle size (Figure 5.12). The wavelength of 900 nm was chosen as this region displayed a large off-set between different particle sizes while the region was relatively flat and free from interfering features. The data from experiment A at 240 minutes has been omitted as the calculation of μ_a and μ_s could not complete. Experiment D shows an increase in the scattering coefficient at 300 minutes which cannot be explained by the particle size reference data.

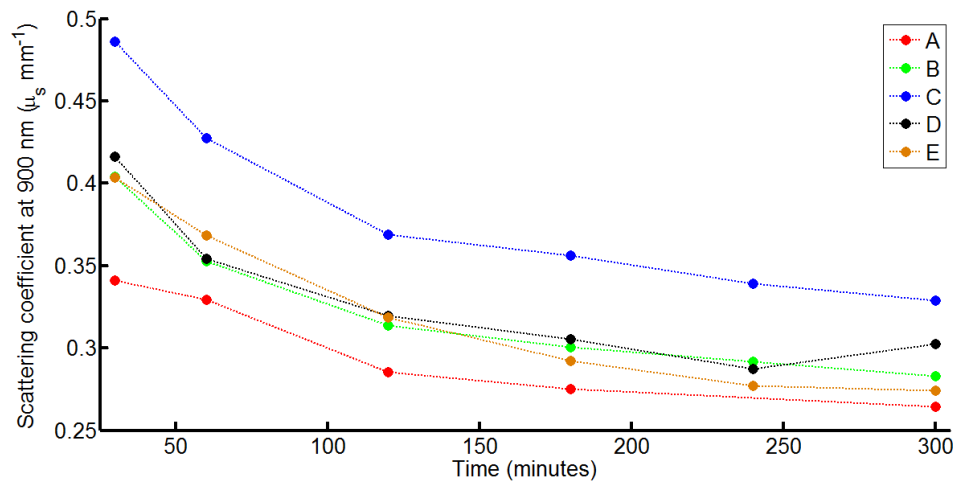


Figure 5.12 – Scattering coefficient values at 900 nm for milling experiments A to E.

Figure 5.13 shows the bulk scattering coefficient at 900 nm versus the measured particle size of each sample. This shows that, generally, the scattering coefficient decreases with decreasing particle size but there are substantial differences between each of the five measured experiments. The identical milling experiments (B, D and E) are clustered whereas the experiment A and C (low and high concentration of pigment) separate either side of experiments B, D and E.

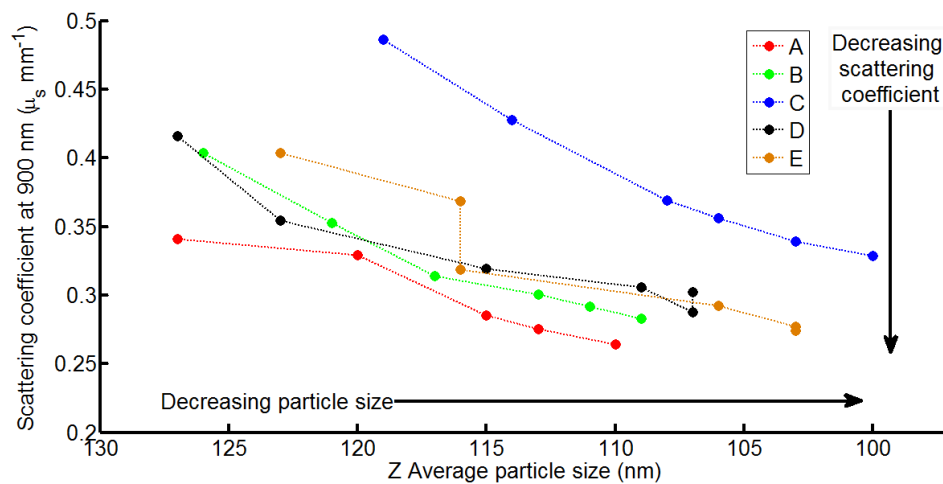


Figure 5.13 – Scattering coefficient values at 900 nm for milling experiments A to E against measured Z-Average particle size.

Normalising the scattering coefficients to show the change in bulk scattering coefficient versus the change in particle size throughout each experiment does not improve the inter experiment variation. Hence, in this instance, building models based on the absorption and scattering coefficients would be very difficult. There are a number of experimental factors to consider such as the fact that each experiment was performed on different days with different environmental conditions in the spectrometer room. Also, the positioning of the cuvette is a potential source of error from sample to sample and experiment to experiment. Nevertheless, the determination that the scattering coefficient decreases with decreasing particle size and decreasing wavelength is valuable to further explain how the on-line diffuse reflectance measurements are effected by changing particle size when measuring concentrated pigment dispersions. Appendix 10.2 contains the separate absorption and scattering plots for magenta pigment dispersion milling experiments A to E.

5.2.1.1 Changing the anisotropy factor g

The anisotropy factor, g , is the measure of the forward direction retained after a single scattering event. Where the g value is -1 , the sample is completely back scattering. When g is 0 , the sample is scattering equally in all directions (isotropic scattering) and the sample is forward scattering the g value is positive between 0 and 1 .

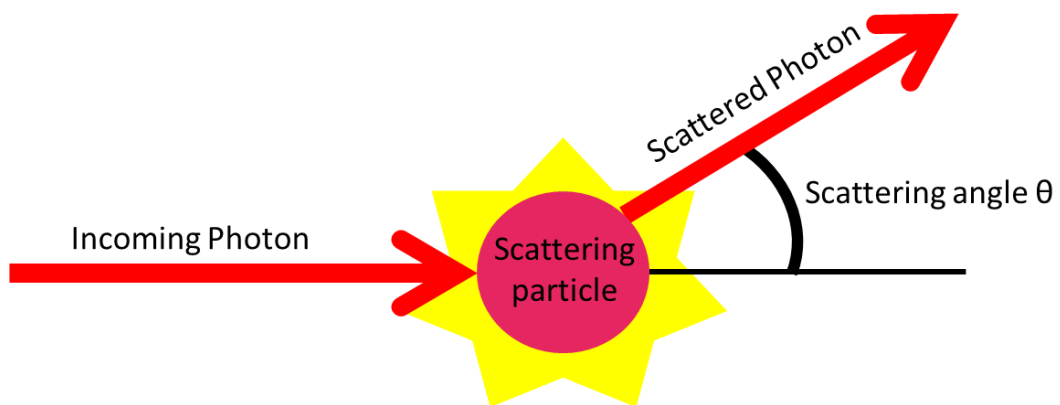


Figure 5.14 –Schematic of light scattering by a small particle.

In the Mie scattering regime, where the particle diameter is approximately the same size as the incoming electromagnetic radiation, the scattering is mostly forward scattering^{3, 15, 16}. The anisotropy factor, g , was fixed at 0.8 for all calculations. In reality the value of g will change in relation to both the particle size and wavelength but in order to solve the radiative transfer equation for μ_a and μ_s and g , measurements of diffuse transmission and reflectance, and collimated transmission would be required. Part of the reason that g can be used as a constant in these experiments is that the change in the particle size is relatively small. Changing the anisotropy factor from 0.8 to 0.9 made little difference to the bulk scattering coefficients determined experimentally. Figure 5.15 shows the calculated scattering coefficient for milling experiment B. Although the scattering coefficient is increased, the qualitative trends between the samples collected at different time points in the experiment (and hence have different particle size properties) remains the same.

Additionally the change in the scattering coefficient between the start and end samples decreases with decreasing wavelength.

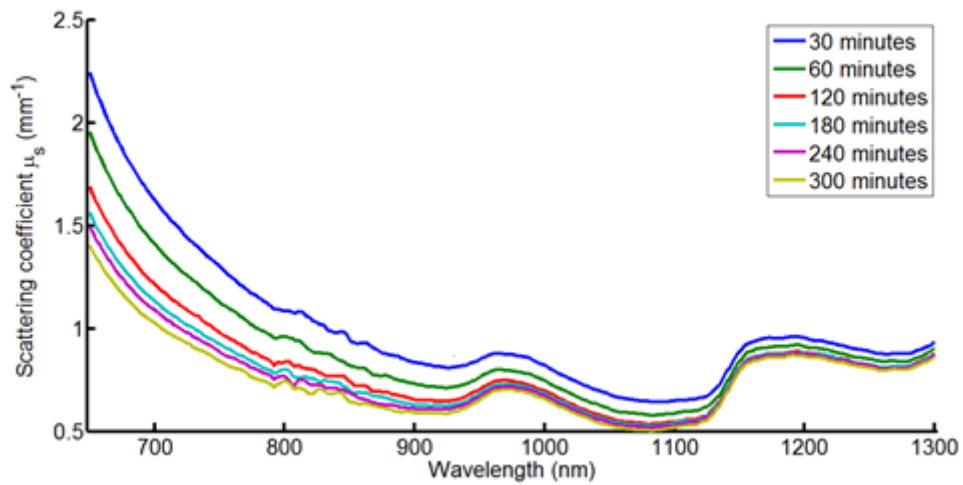


Figure 5.15 – Bulk scattering coefficient values when $g = 0.9$.

This investigation of the absorption and scattering coefficients is purely qualitative, to observe how the fundamental optical properties of the sample change throughout the milling process. It is surmised that fixing the anisotropy factor does not affect the changes in the scattering and absorption constants of each milling sample but if accurate constants were required for quantitative purposes the anisotropy factor g would have to be determined experimentally.

5.2.2 Yellow pigment

Diluted samples of magenta pigment dispersion showed a reduction in the scattering coefficient with wavelength and particle size. On-line reflectance NIR spectra of the concentrated process sample show an increase in absorption (baseline off-set) during the milling of magenta as do yellow milling experiments. The fundamental optical constants were calculated to determine whether yellow pigment dispersion samples followed the same pattern of the magenta pigment fundamental optical constants.

5.2.2.1 Experimental

1.5 kg of 20 % w/w yellow pigment dispersion with 50 % polymer loading of Acid 46 was prepared as per section 3.1 using charges in the table below. The Acid 46 polymer concentration was 31.09 %.

Table 5.2 – Yellow pigment dispersion charge list.

Substance	Weight (g)
PY 74 pigment powder	300.00
Polymer Acid 46	482.47
Water	717.53

The pigment dispersion was milled using the Netzsch minizeta mill for a period of ten hours, collecting samples at 1, 2, 4, 6, 8 and 10 hours. The longer milling time reflected the additional weight of pigment dispersion milled and the increase in volume required the use of a larger sample reservoir. Samples were diluted for off-line NIR analysis (100 mg diluted to volume in a 25 ml volumetric flask using distilled water) and by approximately 4000 for DLS particle size measurements using the Malvern HPPS 5001 particle size instrument. Off-line reflectance and transmission measurements of diluted yellow pigment dispersion samples were performed using the Cary 5000 and extraction of μ_a and μ_s from the transmission and reflectance measurement were performed as described in section 0.

5.2.2.2 Results and discussion

Figure 5.16 and Figure 5.17 show the scattering and absorption coefficients over the wavelength range 650 – 1300 nm. Both calculated μ_a and μ_s show a reduction with wavelength and milling time.

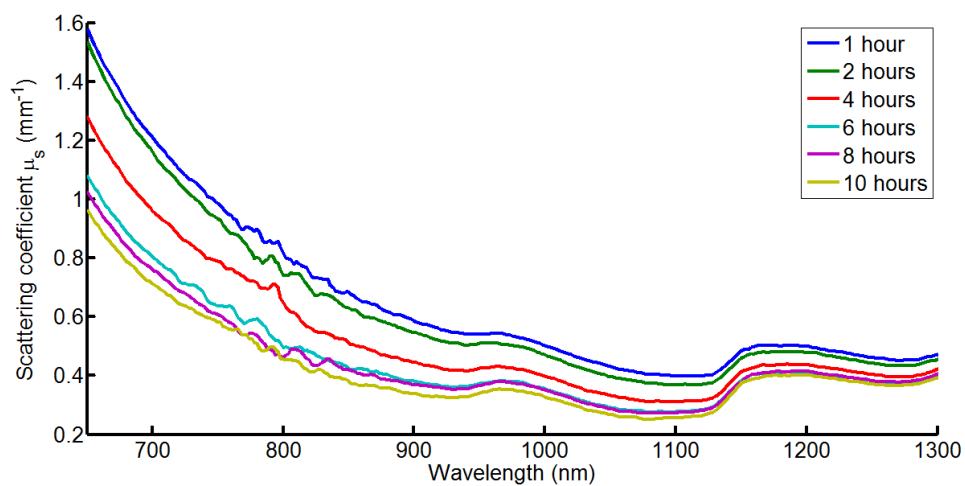


Figure 5.16 – Scattering coefficients for diluted yellow samples generated at different stages of a milling experiment.

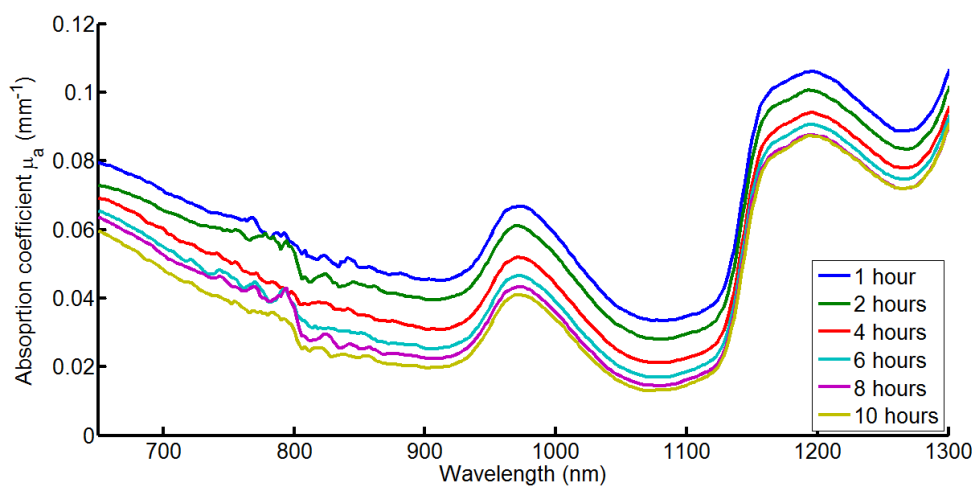


Figure 5.17 – Absorption coefficients for diluted yellow samples generated at different stages of a milling experiment.

Figure 5.18 shows the particle size reference data for the samples extracted at the 7 different times in the milling experiment.

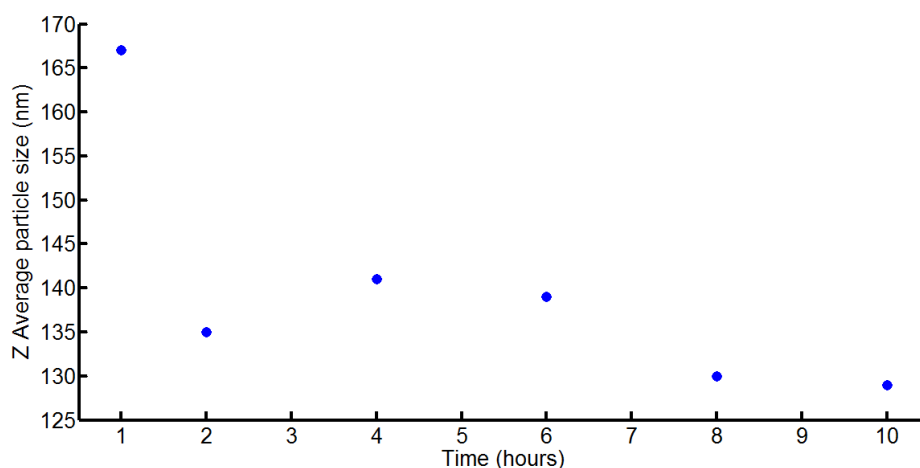


Figure 5.18 – Z Average particle size for the milling of a yellow pigment.

The datapoint at 2 hours does not fit with the general decrease in the particle size with time. Examination of the DLS instrument correlogram and the quality criteria in the software provided no clear reason for this. However, the particle size is shown to decrease and the respective change between the 1 hour sample and 6 hour sample is larger than the drop in particle size between the 6 to 10 hour samples. The rate of change of particle size in a ball mill changes as the experiment progresses. At first the change affected in the pigment dispersion is large, breaking down loose agglomerates and floccules. When the supply of easily broken down material is gone it takes more and more energy to affect further breakdown of the more tightly bound particulates. The fact that the scattering coefficients exhibit this trend further confirms the scattering coefficients relationship with particle size.

5.2.3 Cyan pigment

Both magenta and yellow pigment dispersions were found to have changing optical constants for diluted samples. The optical constants for cyan pigment dispersion were investigated in a similar manner.

5.2.3.1 Experimental

800 g of 20 % w/w cyan pigment dispersion with 60 % polymer loading of Acid 46. The Acid 46 polymer concentration was 31.09 %.

Table 5.3 – Cyan pigment dispersion charge list.

Substance	Weight (g)
PB15:4 pigment powder	160.00
Polymer Acid 46	308.78
Water	331.22

The pigment dispersion was milled using the Netzsch minizeta mill for a period of 5 hours, collecting samples at 30, 60, 90, 120, 180, 240 and 300 minutes. Figure 5.19 and Figure 5.20 show the scattering and absorption coefficients respectively for the milling of a cyan pigment.

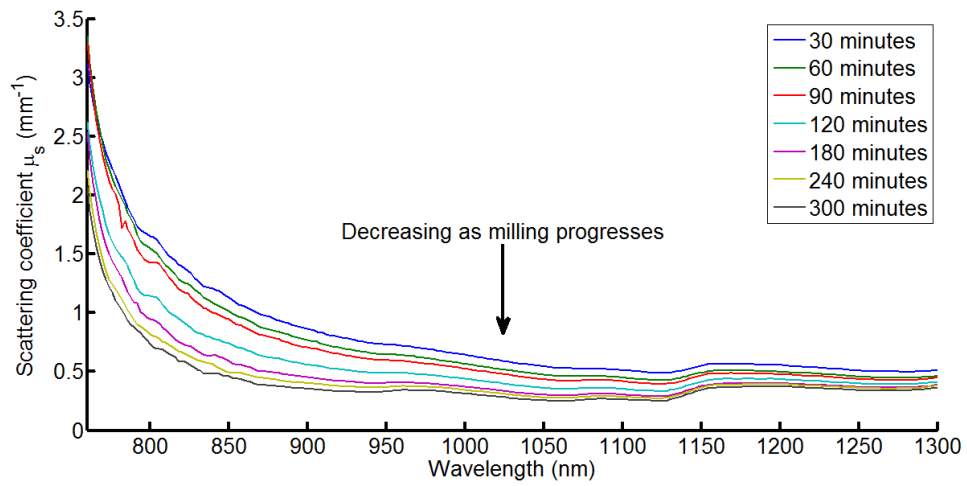


Figure 5.19 – Scattering coefficients for diluted cyan samples generated at different stages of a milling experiment.

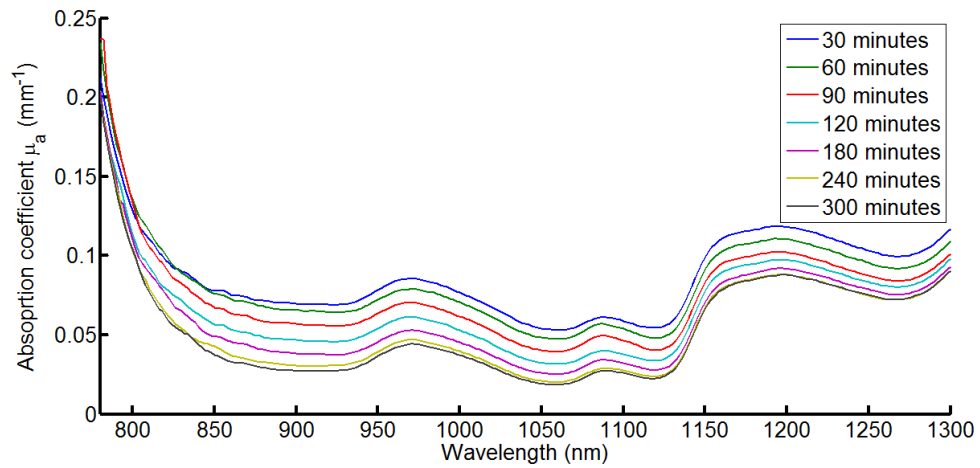


Figure 5.20 – Absorption coefficients for diluted cyan samples generated at different stages of a milling experiment.

Figure 5.21 shows the Z average particle size collected at the different time points of the cyan milling experiment.

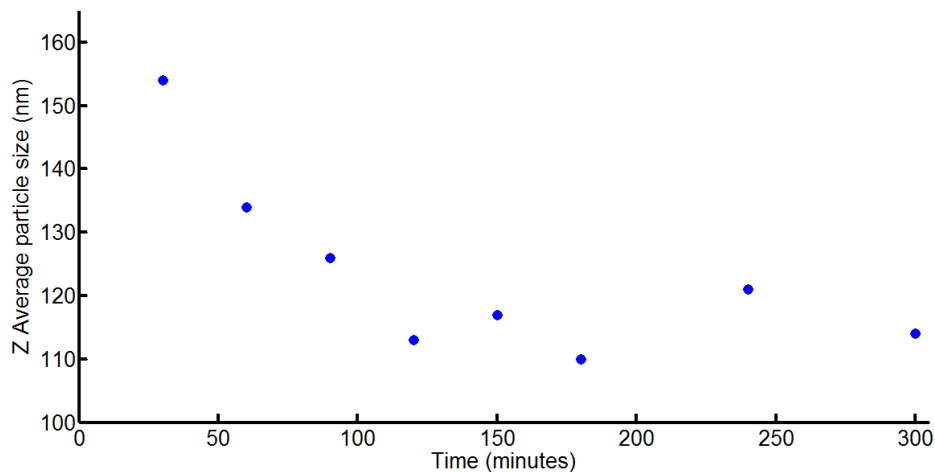


Figure 5.21 – Z-Average particle size for cyan milling experiment

The behavior of the absorption and scattering coefficients throughout the cyan milling experiment mirror those observed in the magenta and yellow milling experiments. Blue pigment dispersions were difficult to characterise by dynamic light scattering measurements, probably due to some absorption of the laser light at 632 nm used in the instrument. However, as before, the particle size decreases as the milling progresses with the greatest change occurring early in the milling experiment. This is repeated in the change observed in the scattering coefficient for the diluted samples.

5.2.4 Particle size and number density

The dominance of the scattering coefficient change with particle size over the corresponding bulk absorption coefficient indicates that the trends observed in the on-line NIR spectra arise from a change in the physical properties of the pigment dispersions during milling. The effect of milling produces not only smaller particles but an increase in the number of particles seen by the NIR reflectance probe. To investigate the effect of particle size and number density of particles, Mie theory was used to calculate the scattering coefficient for monodisperse latex particles in water.

5.2.4.1 Experimental

Using a Mie theory script developed by Suresh Thennadil for use in Matlab, the bulk scattering coefficients for a theoretical system of monodisperse, spherical, latex particulates were calculated. The required inputs for the routine are the particle diameter (varied between 100 – 250 nm), concentration of weight particulates (*cf.* weight fraction varied between 0.05 and 0.30), refractive index of particulates (1.747) and the refractive index of water between 1000 – 1800 nm (1.3217 – 1.3034). The bulk scattering coefficients were calculated at 10 nm intervals over the wavelength range 1000 – 1800 nm.

5.2.4.2 Results and discussion

While the values for the estimated scattering coefficients may be slightly different to those for the pigment samples, qualitatively, the trends will be the same. Figure 5.22 shows a decrease in scattering coefficient when particle size is decreased. Figure 5.23 shows how the number density of particles influences the scattering coefficient. In this case weight fraction has been used as a surrogate to show the effect of number of particles, in dispersion, on the fundamental optical properties. An increase in the number density of particles results in an increase in the scattering coefficient.

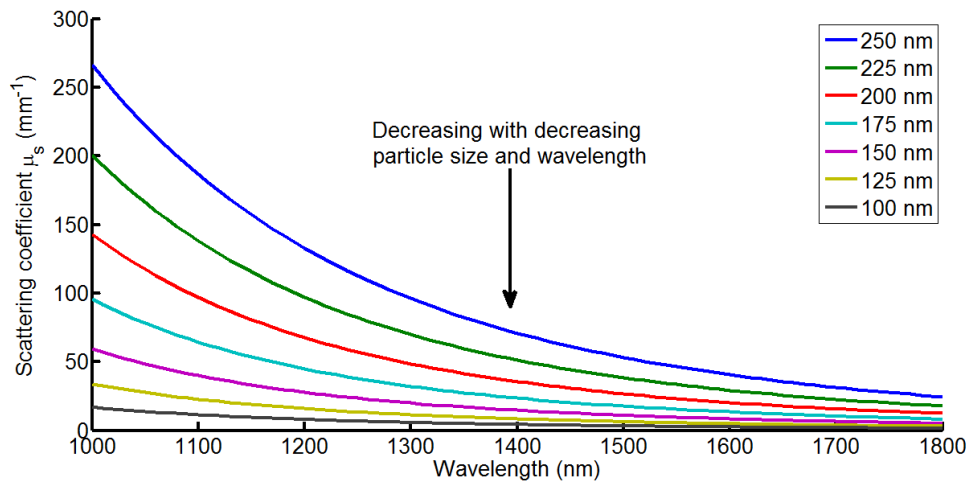


Figure 5.22 – Change in bulk scattering coefficient with decreasing particle diameter at a fixed weight fraction of particles (0.08) .

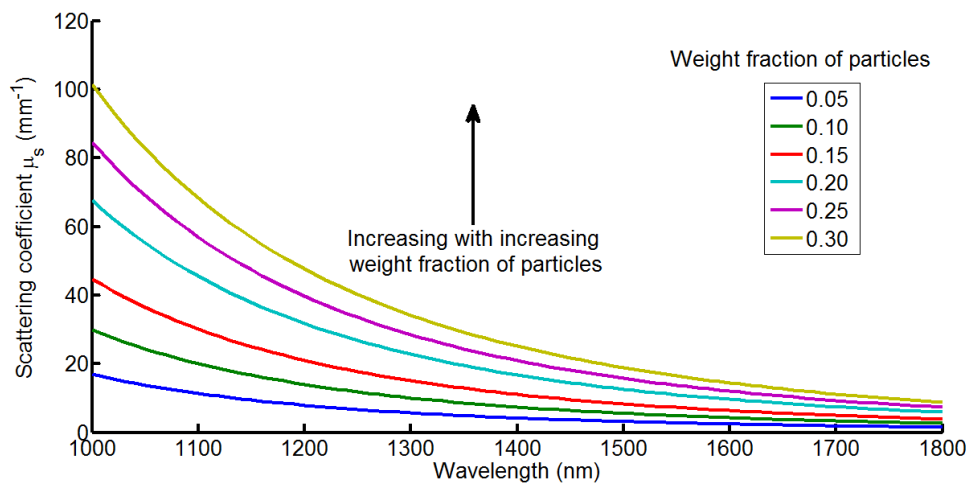


Figure 5.23 – Change in bulk scattering coefficient with increasing number density of particles at fixed particle size (125 nm).

The experimentally derived μ_s (Figure 5.8) decreases as the particle size in the pigment dispersion is reduced. Comparison of these results with the theoretically derived μ_s , as a function of particle size (Figure 5.22) and number of particles (Figure 5.23), indicates that the change in particle size during the milling of the polymer-pigment dispersion is the more dominant factor and consequently the trend observed results from a change in particle size.

5.3 Summary

Milled pigment dispersion samples were generated for magenta, cyan and yellow pigment dispersions and the absorption and scattering coefficients were determined. The milling experiments produce pigments with different particle sizes but keep the concentration of the pigment the same as no additional charges were introduced throughout the milling experiments. For each pigment, it was shown that scattering coefficient decreased with decreasing particle size and with wavelength.

The method of extracting μ_a and μ_s involved fixing a third optical constant in the radiative transfer equation which describes how photons of light propagate through dispersed media. The anisotropy factor, g , was altered for one dataset and the scattering coefficients compared. The result was the scattering coefficients increased slightly, and were off-set in comparison to the lower value of g , but the decrease with decreasing particle size and wavelength was still evident.

The effects of particle size and number density on the scattering coefficient were investigated using a theoretical system of monodisperse latex spheres. This showed that the particle size is the dominant factor over the number density of particles as the experimental scattering coefficients showed a decreasing trend. The trends in the scattering coefficient are useful to describe how changing the scattering properties of the pigment dispersion affect the on-line reflectance measurement of concentrated pigment dispersions in-situ.

5.4 References

1. W. Schärtl, *Light Scattering from Polymer Solutions and Nanoparticle Dispersions*, Springer, 2007.
2. G. Mie, *Annalen der Physik*, 1908, **330**, 377-445.
3. E. Dzhongova, C. R. Harwood and S. N. Thennadil, *Appl. Spectrosc.*, 2009, **63**, 25-32.
4. T. A. Egerton and I. R. Tooley, *International Journal of Cosmetic Science*, 2012, **34**, 117-122.
5. L. M. Kessell, B. J. Naden, I. R. Tooley and T. F. Tadros, in *Colloids in Cosmetics and Personal Care*, Wiley-VCH Verlag GmbH & Co. KGaA, 2008, pp. 61-78.
6. N. J. Lowe, N. A. Shaath and M. A. Pathak, *Sunscreens: development, evaluation, and regulatory aspects*, 1997.
7. S.-H. Tseng, P. Bargo, A. Durkin and N. Kollias, *Opt. Express*, 2009, **17**, 14599-14617.
8. Z. Shi and C. A. Anderson, *Journal of Pharmaceutical Sciences*, 2010, **99**, 4766-4783.
9. A. Kienle, L. Lilge, M. S. Patterson, R. Hibst, R. Steiner and B. C. Wilson, *Appl. Opt.*, 1996, **35**, 2304-2314.
10. C. Abrahamsson, T. Svensson, S. Svanberg, S. Andersson-Engels, J. Johansson and S. Folestad, *Opt. Express*, 2004, **12**, 4103-4112.
11. J. Johansson, S. Folestad, M. Josefson, Spar, A. n, C. Abrahamsson, S. Andersson-Engels and S. Svanberg, *Applied Spectroscopy*, 2002, **56**, 725-731.
12. S. A. Prahl, M. J. C. Vangemert and A. J. Welch, *Applied Optics*, 1993, **32**, 559-568.
13. E. Dzhongova, PhD Thesis: *Monitoring bacterial growth in liquid cultures through the bulk optical parameters in the near-infrared region extracted using the radiative transfer theory*, Newcastle University, 2010.
14. S. N. Thennadil and E. Dzhonova, *Monitoring bacterial culture growth through calibration models built on bulk optical properties - Group meeting* December 2010.
15. M. A. Velazco-Roa and S. N. Thennadil, *Applied Optics*, 2007, **46**, 3730-3735.

16. M. A. Velazco-Roa and S. N. Thennadil, *Appl. Opt.*, 2007, **46**, 8453-8460.

6. On-line NIR measurements

Building on the fundamental understanding developed by examining the effect of particle size on absorption and scattering coefficients, on-line NIR spectroscopy has been investigated as a tool for monitoring the particle size reduction of aqueous based polymer-pigment dispersions. The particle size is a key specification of the product and milling is an important part of the multistep manufacturing process used to produce high quality pigment dispersions for inkjet printing. The milling stage is a bottle neck, limiting plant production capacity. Current methodologies for in process checks of the milling progress involve sampling the process. These samples are then transferred to a centralised lab and are diluted and analysed by a number of different techniques such as laser diffraction or dynamic light scattering. The time losses accrued for each mean that there is a need for a technique capable of providing real-time information throughout development and manufacturing. Although plant versions of laser diffraction and dynamic light scattering instruments are available they require the samples to be diluted, incurring additional expense and increasing the complexity of the plant design. The aim of this work was to:

1. Determine the penetration depth of the NIR reflectance measurement.
2. Develop an NIR method capable of detecting changes in the particle size for magenta, cyan and yellow pigment dispersions.
3. Using a design of experiments approach, investigate whether NIR spectroscopy can monitor a range of different concentrations similar to those used by FFIC.
4. Evaluate whether the process can be modeled by univariate or multivariate techniques.
5. Investigate whether NIR measurement can be applied to similar millings on larger scale ($\times 10$).

6.1 Penetration Depth

The choice of NIR reflectance measurements over transmission or transmittance probes is relatively simple as the alternative probes require very short path lengths because of the high concentration of the pigment dispersion and high absorption from a sample with high water content. Probe fouling is relatively simple to remedy during lab experimentation by removal and cleaning but this can be more problematic when a measurement is employed in plant monitoring or in harsh environments. Technologies have been developed which allow probes to be removed from process streams without interrupting the process for cleaning. Although this is a good way to manage such problems, the more complex sample port required can increase the difficulty of cleaning. This is an important consideration, particularly when plants are not dedicated to manufacture a single product and the potential for cross contamination has to be minimised. This is not to say that reflectance probes are immune to fouling issues, just that they are less likely than the alternative probe designs when high concentration colloidal samples are measured.

Determining the penetration depth of the NIR reflectance probe is necessary to estimate the volume of sample analysed per NIR measurement. On-line measurements in the pharmaceutical industry, such as blending, require each measurement to be a representation of an acceptable portion of the total batch. Measurements in these applications are often described in terms of how many unit doses are measured during the collection of a spectrum or several spectra.

The penetration depth of NIR measurements can be defined in two different ways. The first defines the penetration depth required to provide spectra of an infinitely thick layer whereas the second considers both the depth of the penetration and weighting of the information from each layer. The rationale for this is that the first few layers will contribute more to the encoded information in a spectrum. For the purposes of this thesis, the penetration depth will be defined as the depth of pigment dispersion required to provide constant NIR spectra. Lammertyn et al ¹ have examined the penetration depth of NIR light in apples and have reported penetration depths between 2 – 4 mm, with the penetration depth reducing with increasing wavelength. Haanstra et al² have also investigated the penetration depth of NIR light

for polyethylene films. In this case the information depth was defined as the depth of sample required to reduce the level of light by 50 % from the reference and reports the required depths to be between 0 to 2.5 mm. Again, the penetration depth was found to decrease with increasing wavelength. Clarke et al³ have investigated the penetration depth of NIR radiation in to pharmaceutical materials using FTNIR microscopy. For this study layers of material were placed above a sample and the depth of information defined as the distance of material required to reduce the signal from the sample below to 50% of its original value. This study detailed that the depth of information was between 39 – 61 μm at 1695 cm^{-1} and the depth of information was linked to the wavelength of the NIR photons. When the wavelength was large there a lower information depth and vice-versa for the low wavelength range. Bellamy et al⁴ used non-contact measurements to monitor a convective blender containing a mixture of aspirin and Avicel. The information depth of the sample was estimated at 2.4 mm and there was a relationship observed between the spectra and the particle size of the aspirin in the blender. First derivative spectra of the second C-H overtone of aspirin showed an amount of noise between measurements which was correlated with the particle size of the aspirin (between 100 – 500 μm).

6.1.1 Experimental

The Foss on-line 6500 spectrometer with the interactance reflectance probe was set up as shown in Figure 6.1. A reference scan of the white card in the vial lid was obtained by raising the vial lid so that it was in direct contact with the reflectance probe head. A sample of magenta pigment dispersion (20 % PR122, 45 % polymer loading of Acid 46) which had been milled for 17 hours was used. The Z-Average particle size was 103.5 nm (average of 3 replicates). The depth of pigment dispersion between the probe head and the white card was altered by keeping the probe in a fixed position, which removed any effect from moving the optical fibers, and lowering a jack-stand under the vial lid. The depth of pigment was inferred by measuring the height of the jack-stand after each adjustment using a set of vernier calipers. After introduction of the pigment to the sample vial lid the probe was then pressed the probe head leaving a thin film of pigment dispersion to be measured which was less than 0.1 mm. A set of six measurements was collected and averaged

for 8 different depths of pigment dispersion between < 0.1 and 5.94 mm. The penetration depth was estimated to be where the reflectance spectra no longer changed with increasing pigment depth. At this point, the NIR probe would see a sample as an infinitely thin layer. The average NIR spectrum of 6 scans is reported.

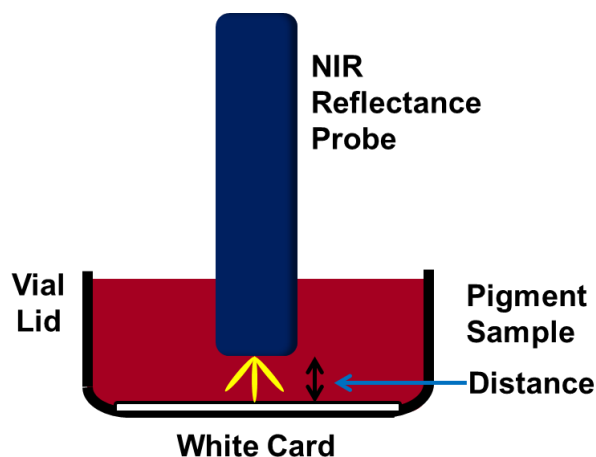


Figure 6.1 – Experimental set up for estimating the penetration depth of NIR photons in concentrated pigment dispersion.

6.1.2 Results and Discussion

Increasing the depth of pigment dispersion between the reference card and the NIR reflectance probe head decreased the number of photons reflected back towards the collection fibres as shown in Figure 6.2. The main region of interest is between approximately 700 and 1300 nm as the strong water absorption at 1400 nm dominated the spectra. For each set of 6 spectra, the standard deviation was very small ($< 0.2\%$) so error bars are not included.

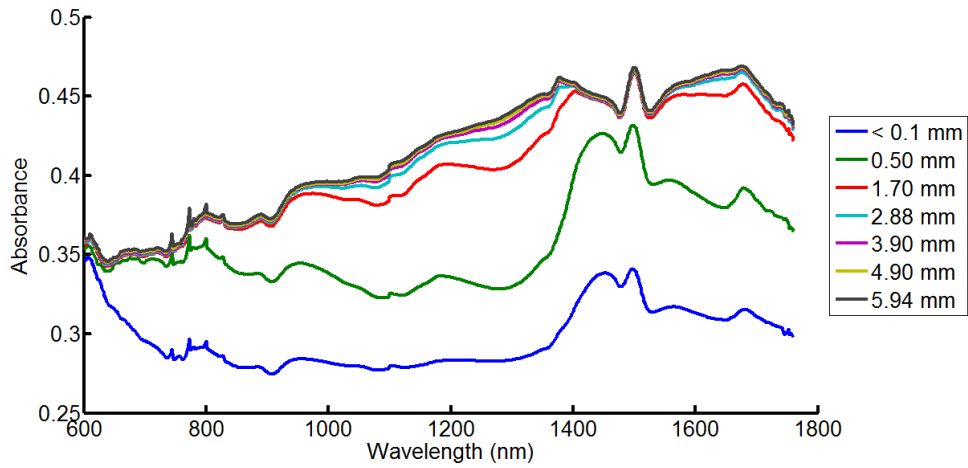


Figure 6.2 –Average (n=6) NIR spectra collected with different depths of pigment dispersion

Figure 6.3 shows the change in absorbance with pigment depth at 150 nm intervals from 700 to 1300 nm. Table 6.1 summarises the effective penetration depth. The NIR spectra appear to still show some change around 1300 nm between 4.90 and 5.94 mm, which indicates that NIR photons are penetrating deeper into the sample than the designed scale of the experiment could capture.

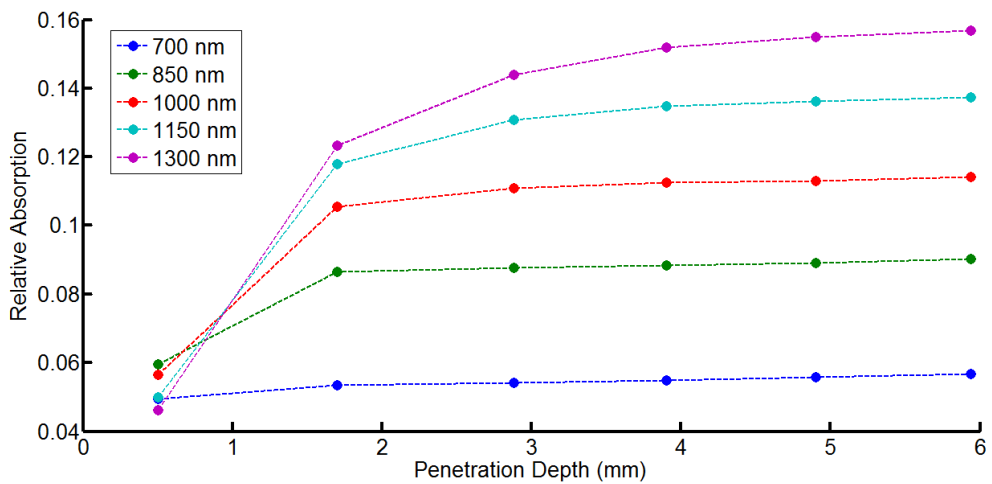


Figure 6.3 – The change in absorption at five different wavelengths with increasing depth of pigment.

There is a measured absorbance when the depth of pigment is zero as there is a very small layer of pigment dispersion trapped between the reflectance probe and the white card.

Table 6.1 – Summary of penetration depths

Wavelength (nm)	Penetration Depth (mm)
700	< 1 mm
850	2 - 3 mm
1000	3 – 4 mm
1150	~ 5
1300	> 6

Interestingly, the penetration depth appears to increase with increasing wavelength until the absorption of the water in the sample dominates. As the wavelength increases, the molecular absorptivity increases, hence why it could be expected that the penetration depth will decrease with wavelength. However, an important point to remember is that the reflectance spectra are a product of both absorption and scattering. If the scattering of the NIR photons is the dominant effect in the spectra, the NIR light will be able to penetrate deeper in to the sample at higher wavelengths when the effect of scattering is lower. Chapter 5 showed that this was the case for real samples and a theoretical investigation for a system of latex spheres showed that the change in particle size dominated the NIR spectra, even when a change in the number density of particles is considered. By contrast, Bellamy et al⁴ showed that penetration depth decreased for increasing wavelength and increased with increasing particle size. This is completely contradictory to the results observed in the pigment dispersions but Bellamy was examining Avicel and Aspirin powders with particle sizes between 38 to 500 μm which is best described by Kubelka-Munk theory. This theory breaks down as the particle size becomes smaller in comparison to the wavelengths of light used to generate the spectra

The penetration depth generated in this experiment will be used later to estimate the volume of pigment dispersion analysed during 200 kg scale milling of pigment

dispersions. The main difficulty in estimating the volume of sample analysed in the laboratory scale is that there is no reliable way of measuring the speed of the sample.

6.2 Small scale milling experiments (~ 1 kg)

Laboratory investigations have shown that reflectance near infrared measurements are capable of measuring a few millimeters into concentrated pigment dispersions and that there is a measurable change in the NIR spectra during the particle size reduction of yellow pigment dispersion (section 5.2.2). Further experiments were performed to investigate whether the effect was consistent across different pigment colours.

6.2.1 Magenta

6.2.1.1 Experimental

Three milling experiments using a 14 % w/w dispersion of PR122 with 30 % loading of acid 46 were performed to assess the repeatability of the small scale milling process. Each independently prepared 800 g batch pigment was milled for approximately five hours using the Netzsch minizeta mill and near infrared spectra collected using the FOSS online 6500 spectrometer. The reflectance probe was placed in the stirred sample pot. Each spectrum was an average of 32 scans and spectra were collected at 2 minute intervals. Samples were analysed by dynamic light scattering using the instrument Malvern HPPS5001 NIBS particle sizer.

6.2.1.2 Results and Discussion

The NIR spectra were examined qualitatively by examining the univariate trends in the data as described for the yellow milling experiment detailed earlier. Figure 6.4 shows the change in absorbance at 1220 nm for the three experiments. Differences in the positioning of the NIR probe fibres caused slight offsets between each of the experiments which were performed on different days.

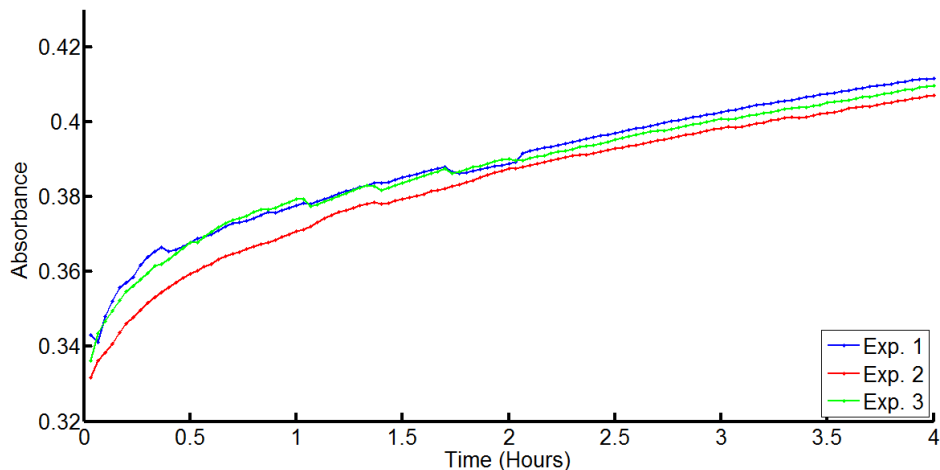


Figure 6.4 – Absorbance at 1220 nm for 3 milling experiments of magenta pigment dispersion.

The particle size reference data from dynamic light scattering measurements of samples taken throughout are presented in Figure 6.5.

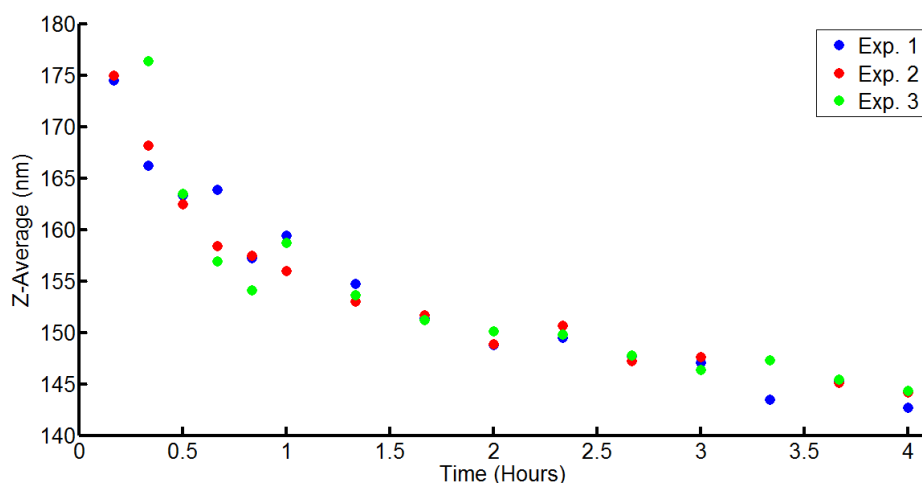


Figure 6.5 – Z-Average particle size for 3 milling experiments of magenta pigment dispersion.

The particle size reduction profiles are consistent across the three milling experiments. Most of the change in the particle size occurs early in the milling experiment and the rate of change of particle size gradually decreases with time. This trend is mirrored in the on-line near infrared spectra whereby the rate of change in the absorption at 1220 nm gradually decreases as the milling experiment continues. Figure 6.6 shows the trends between the absorbance at 1220 nm and the z-average

particle size data. The absorbance and particle size data show an anti-correlation, particularly at smaller particle sizes when the experiments are closer to completion.

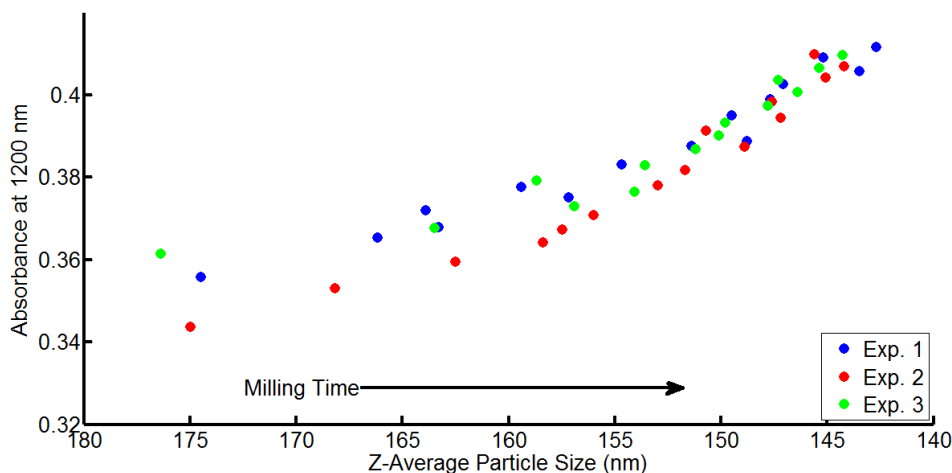


Figure 6.6 – Absorbance and particle size data for three milling experiments conducted with magenta pigment dispersions

6.2.2 Summary

Magenta milling experiments were monitored by on-line NIR reflectance measurements. The spectra were collected with the reflectance probe positioned in the small sample reservoir of the Netzsch minizeta mill. The NIR spectra were sensitive to movement of the fibres and/or the probe, which could be improved by using a more robust set up. For both experiments carried out with the yellow (section 4.4.2) and magenta pigments, the on-line NIR spectra show a change as particle size decreases. The NIR spectra display a baseline offset which increases with increasing wavelength from 600 to around 1350 nm before the spectra is dominated by the strong and broad water absorption at 1400 nm. The spectra still show a change in the baseline offset above 1400 nm but the magnitude decreases slightly.

Three replicate milling experiments using magenta pigment dispersions showed good reproducibility and a strong correlation between the particle size and absorption at 1220 nm. This indicated that NIR measurements of concentrated pigment dispersions are sensitive to particle size and may be used to monitor the milling process.

6.3 Milling Reservoir Temperature

Vibrational spectra reflect the chemical structure and functional groups present in a molecule and this includes contributions from inter and intra-molecular forces such as hydrogen bonding⁵. Changes in temperature alter the intermolecular forces and this is manifest as a change in the vibrational mode, hence a change can be observed in the spectra⁶. To show that the changes in the milling experiments are a function of the particle size, and not a change brought about by changes in the temperature of the pigment dispersion, the temperature profile in the sample pot of the Netzsch was monitored throughout three typical milling experiments.

6.3.1 Experimental

Three milling experiments of a 20 % w/w PV 19 magenta dispersion (acid 10, 30% polymer loading) were performed. In each case the total charge of pigment dispersion was 600 g. The temperature was monitored using a PTFE coated temperature probe and the data logged every 20 seconds using reactor control software, WinISO (HEL, Hertfordshire, UK).

6.3.2 Results and Discussion

The milling chamber and the first section of pipework from the mill is water jacketed to remove the heat generated in the high energy bead mill. Figure 6.7 shows the temperature profiles of the sample reservoir of the Netzsch minizeta mill. For each of the three experiments there is a general trend where the temperature increases dramatically from room temperature at the start and then reaches an equilibrium state where the heat generated in the sample is equal to the heat lost via the cooling jackets and the surrounding environment. Experiment 3 shows a decrease in the temperature where the milling was paused for a few minutes. The water jackets are fed from the mains water supply which is not temperature or pressure controlled. Both properties vary from day to day; hence, there are differences between the temperatures during each milling experiment.

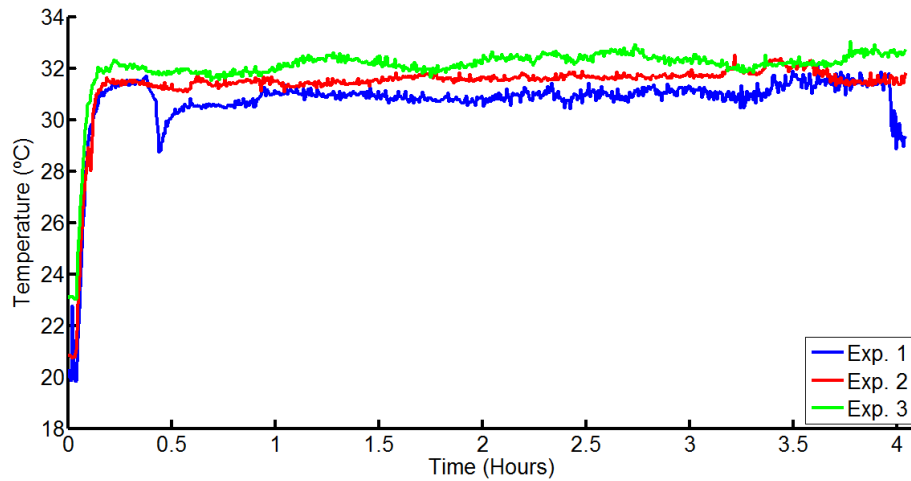


Figure 6.7 – Milling reservoir temperature for milling experiments (n=3)

The stability of the temperature in the mill sample reservoir allows it to be concluded that the changes observed in the NIR spectra are not a product of the temperature of the sample. Comparing the temperature profile (Figure 6.7) with the NIR spectra (Figure 6.4 shown earlier) shows that the temperature reaches a steady state much sooner than the time taken for the particle size reduction to level off.

6.4 DoE matrix of milling experiments for magenta pigment PR122

A design of experiments (DoE) matrix of milling experiments were monitored using on-line NIR measurements. The range of concentrations of pigment and polymer were selected to encompass those used by FFIC in Grangemouth. The NIR spectra were analysed using univariate and multivariate techniques to extract information relating to the particle size as it changes throughout the milling process. Additionally, the spectra were interrogated using chemometrics to assess the possibility of measuring the concentration of the stabilising polymer.

6.4.1 Experimental

The same experiments used to generate pigment dispersion samples for the determination of the absorption and scattering coefficients were monitored using in-situ NIR spectroscopy. See section 5.1 for details. Table 6.2 is included again as a reference guide to the different milling experiments undertaken.

Table 6.2 - Polymer and pigment concentrations used in the experimental design.

Exp	Pigment mass (g)	Polymer solution mass (g)	Water mass (g)	Pigment dispersion details		Overall polymer content (%w/w)
				Pigment strength (% w/w)	Relative polymer conc.	
A	105.00	100.00	495.00	15	30	5.2
B	140.00	177.78	382.22	20	40	9.2
C	175.00	166.67	358.33	25	30	8.6
D	140.00	177.78	382.22	20	40	9.2
E	140.00	177.78	382.22	20	40	9.2
F	105.00	166.67	428.33	15	50	8.6
G	175.00	277.78	247.22	25	50	14.4

Pigment dispersions were milled using a Minizeta mill (Netzsch, Germany) with 200 mL ceramic mill beads (0.6 – 0.8 mm diameter) for a period of 5 hours. To ensure reliable mixing the sample reservoir was stirred at 400 rpm.

Samples of pigment dispersion were extracted from the return line of the mill at 15 minute intervals for the first 60 minutes then every 20 minutes for the remaining 4 hours. The pigment samples were then immediately diluted by a factor of 4000 and stored in cuvettes for analysis using the Malvern HPPS5001 NIBS particle sizer.

6.4.2 Results and Discussion

The mean Z-average particle size (Figure 6.8), determined by off-line DLS, for three milling experiments (B, D and E – 20 % pigment, 40 % polymer loading) show milling profiles that are consistent. The percentage relative standard deviation (% RSD) of particle size for each time point of the three separate experiments generally decreases as the experiment reaches the end of the milling process. At the beginning of the milling process there is a large distribution of particle sizes in the samples. Oversize particles tend to sediment and cause wider variations in the reported Z-average.

For the three centre point experiments the RSD of the Z-average particle size for samples taken at 30 and 300 minutes are 7.0 and 1.5 % respectively. The typical % RSD for a single sample measured 3 times is 0.5 %.

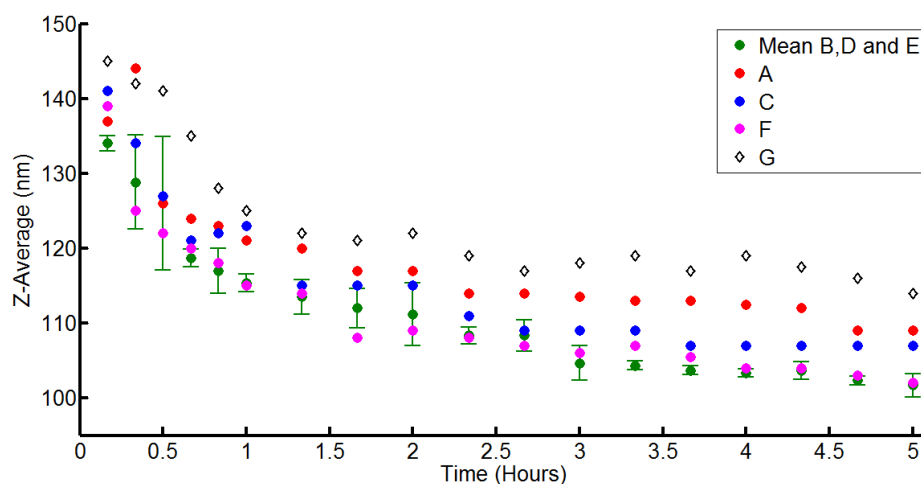


Figure 6.8 - Particle size data for milling experiments A to G. The mean of the three milling experiments B, D & E (centre point in the experimental design) is plotted \pm one standard deviation (n=3).

The milling profiles for C and F (25% pigment, 30 % polymer loading and 15% pigment, 50% polymer loading, respectively) are comparable to the centre point milling profile but A and G are different. Milling experiments A and G (15% pigment, 30% polymer loading and 25% pigment, 50% polymer loading, respectively) are the extreme low and high of the 2 factor, 2 level experimental matrix and the physical properties of the mill base effect how efficiently the particle size of the dispersion is reduced in the mill chamber. In experiments C and F the viscosity of the resulting mill base was visually similar to that of the centre point experiments B, D and E but experiment A exhibited a lower overall viscosity as more water was present in the mill base. Conversely, for G, there was less water in the mill base and the viscosity was higher than that of the centre point mill bases. Ultimately, the viscosity of the mill base controls how efficiently the pigment particulates are broken up in the milling chamber. When the viscosity of the mill base is too low or too high the kinetic energy from the rapidly agitated beads in the chamber is not efficiently transferred to break up the particulates, hence, slower milling profiles can be observed for experiments A and G.

6.4.2.1 Univariate Analysis

Near infrared spectra collected throughout the milling process show a steady increase in absorption which appears as a baseline offset. Spectra collected during milling experiment B are shown in Figure 6.9. The magnitude of the baseline offset increases until the water absorption dominates the spectra at 1400 nm.

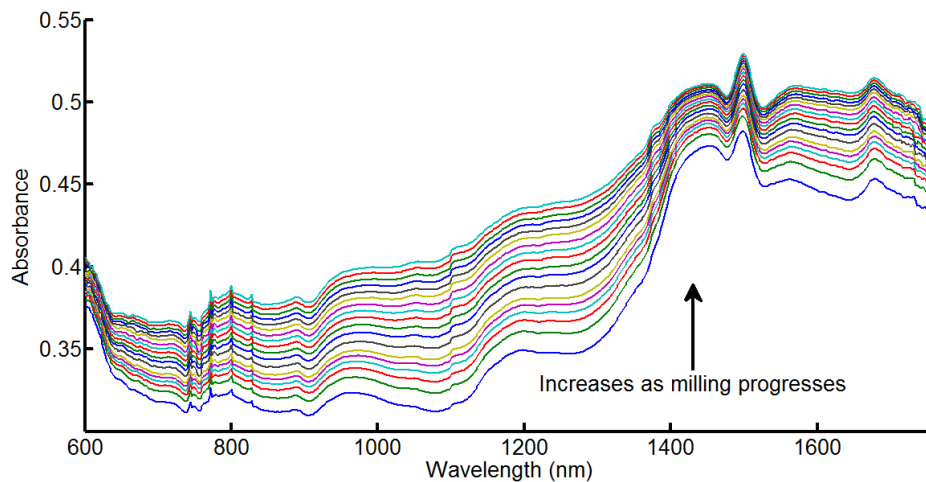


Figure 6.9 – Spectra collected during experiment B. The spectra shown correspond to each of the sampling points where an aliquot of sample was removed for particle size analysis.

The choice then has to be made how to use this data. As discussed previously, extensive pre-processing of the data may remove some of the valuable particle size information. Chapter 5 shows that the change in the particle size which cause a change in the scattering coefficient. This change in the scattering coefficient is the cause of the baseline off-set, the magnitude of which increases with wavelength. The changing physical properties of the sample are manifest in the spectra as the base line offsets but the spectra seem to show slight variations between experiments. The between experiment variations can be explained in the difficulties in setting up seven identical experiments. Changes in the fibre orientation and the probe positioning will affect the spectra despite the best efforts being made to replicate the experiments exactly. This is less of an issue when the probe and fibres are fixed in position. Figure 6.10 shows the change in absorption at 1220 nm where the baseline offset is largest.

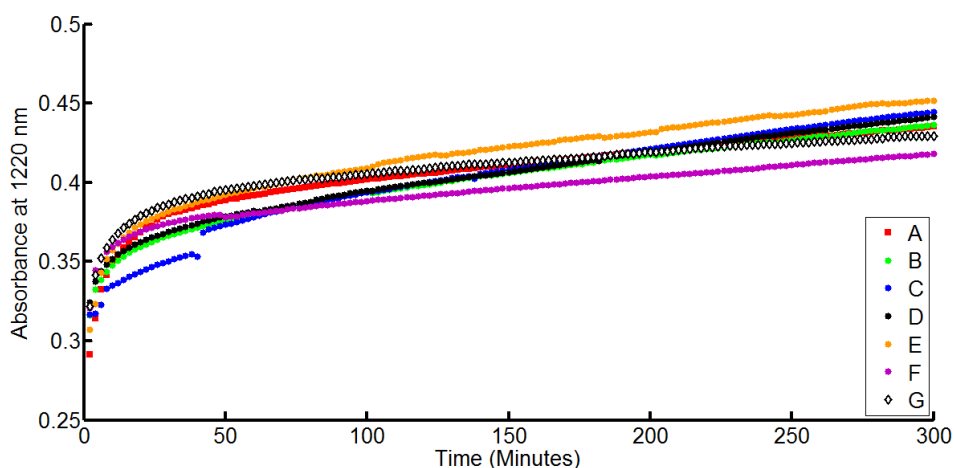


Figure 6.10 – Absorbance at 1220 nm for milling experiments A – G (Table 6.2)

Figure 6.11 shows the absorbance at 1220 nm against the particle size for milling experiments A to G and there is a considerable spread in the data. The difficulty in setting up the experiment, such as repeatable probe positioning and the different pigment concentration may affect the spectra in ways that are not captured by simple univariate modelling of the baseline offset at 1220 nm.

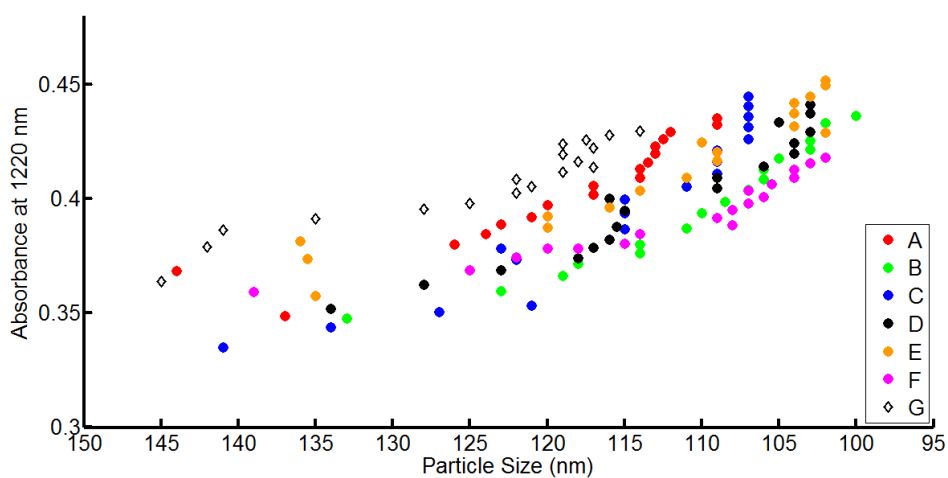


Figure 6.11 – Absorbance at 1220 nm and corresponding Z-Average particle size for milling experiments A to G.

Hence, the spectra were analysed using multivariate techniques principal PCA and PLS (principal component analysis and partial least squares regression, respectively).

6.4.2.2 Principal Component Analysis

PCA was carried out on the mean centered NIR spectra collected during the 7 milling experiments (600 – 1698 nm). Three principal components encompass 99.45 % of the variance in the spectra which occurs as a result of the physical properties (particle size and distribution) and chemical makeup (constituent concentrations) of the sample. For the PCA investigation, extensive pre-processing using algorithms such as SNV, MSC, orthogonal signal correction (OSC), normalisation etc. were not used as these remove particle size effects from the spectra. Figure 6.12 represents a 3 dimensional score plot of all 7 milling experiments. The points corresponding to measurements at the start of the experiment are highlighted in Figure 6.12. Samples at the start of the experiment have a larger and more variable particle size owing to flocculation and aggregation of the pigment. The data collected during Experiment C shows a discontinuity due to a probe readjustment.

Data from experiments B to F lie within a plane (shaded blue in Figure 6.12) and congregate at a similar point near the end of the experiment. Experiment A (low pigment and polymer concentration) is quite close to the plane although the PC3 score values are slightly lower. Experiment G (high pigment and polymer concentration) shows a similar trend in the 3 dimensional scores plot but is separated from the plane described by experiments B to F. Both experiments A and G also display slower particle size reduction profiles (Figure 6.8) from the off-line measurement of particle size. The reasons for which have been discussed previously.

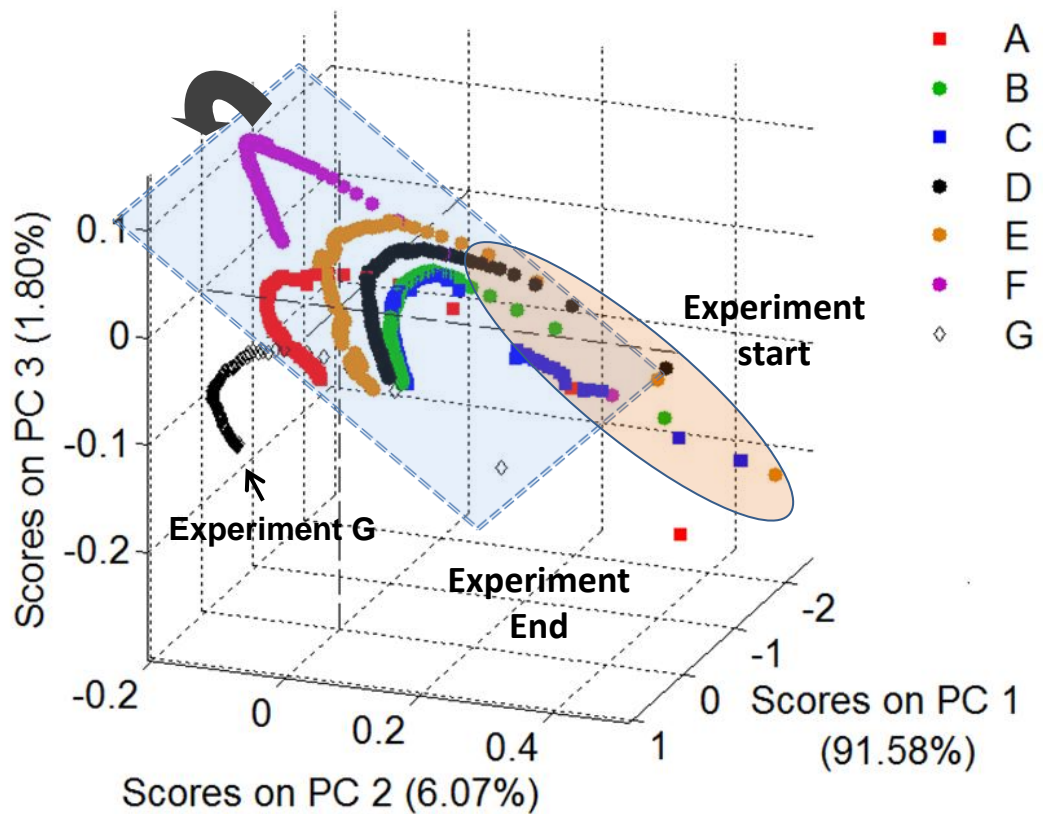


Figure 6.12 – PC1 v PC2 v PC3 scores plot from PCA of mean centred NIR spectra in the range 600 – 1760 nm collected during seven milling experiments (A to G).

Figure 6.13 shows that the PC1 loadings increase with increasing wavelength up to approximately 1400 nm. NIR spectra from experiments show that at low wavelength the effect of changing the particle size is small and an increase in the baseline offset increases with increasing wavelength until ~1300 nm where contributions from the C-H 2nd and 1st overtones begin to contribute to the NIR spectra. The magnitude of the base line offset declines further as the wavelength range approaches the OH absorption at 1400 nm which dominates the spectra. Hence, PC 1 is predominantly describing changes in the particle size and accounts for 91.58 % of the variance in the data .The PC1 score (-ve to +ve) is indicating an increasing baseline off-set (from loadings - Figure 6.13)

PC 2 loadings decrease from the visible to NIR region at around 1150 nm and then the loading values becomes anti-correlated with changes in the system. PC3 loadings

show high contributions from the tail edge of the visible absorption (~600 nm) and shows a distinct contribution from the water absorption band (>1400 nm).

Scores values in the 3 dimensional plot (Figure 6.12) show some differences for the three centre point replicate experiments (B, D and E). Experiment E is slightly off-set from experiments B and D. One explanation for this can be the slight variations in experimental set up when running batches on different days.

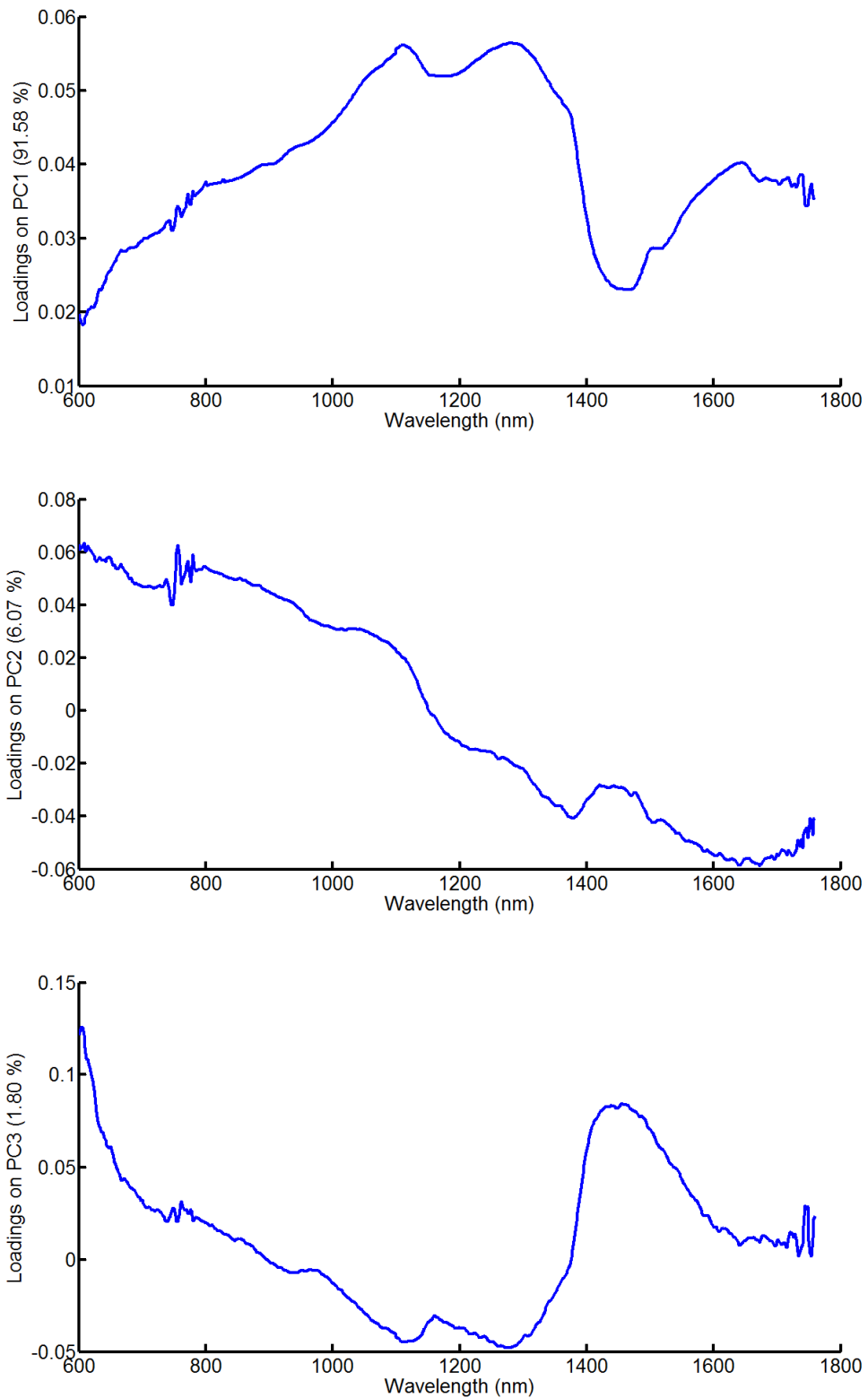


Figure 6.13 - Loadings plot for PCs 1, 2 and 3 from PCA of mean centred NIR spectra in the range 600 – 1760 nm collected during seven milling experiments (A to G).

Subtracting NIR spectra collected near the start and end of experiment B (Figure 6.14) shows that the difference between the two spectra (Figure 6.15) closely approximate the baseline offset. This is the largest change observed in the NIR spectra during milling and it is effectively captured in the first principal component (Figure 6.13).

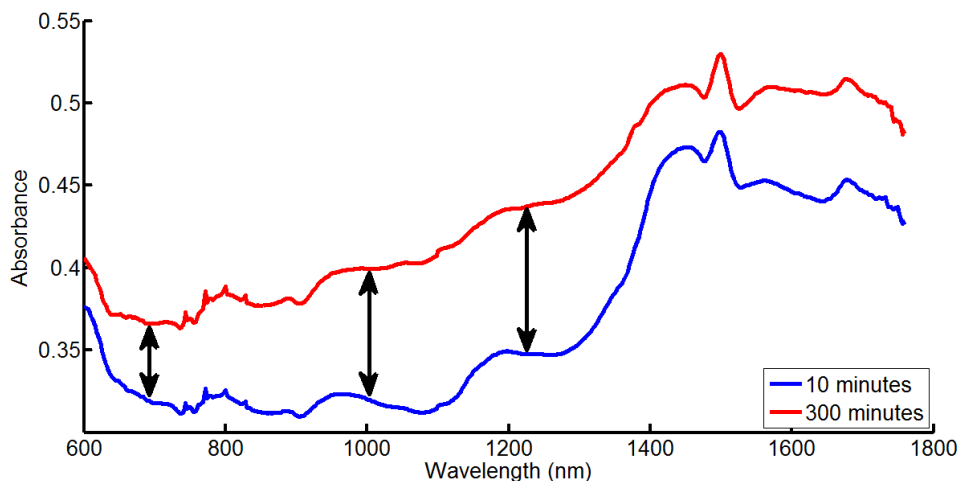


Figure 6.14 – Spectra collected 10 and 300 minutes in to milling experiment B.

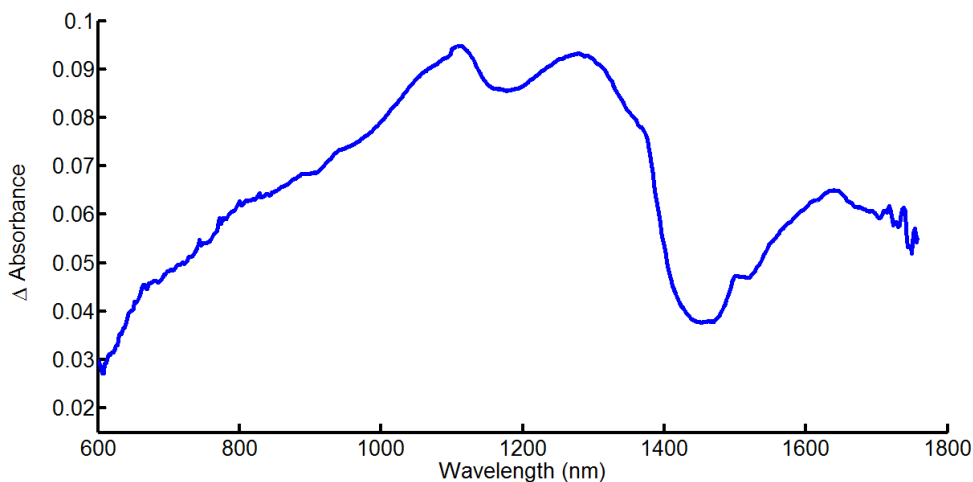


Figure 6.15 – resultant difference between the 300 minute and 10 minute spectra collected during milling experiment B.

6.5 PLS

To further explore the data, PLS models were created for the DoE matrix of magenta milling experiments. The models were created by sequentially omitting one of the seven experiments from the calibration set and using it as a prediction set. Table 6.3 shows the data sets used to construct the models and the root mean square error of prediction (RMSEP) for the omitted dataset when compared to the measured particle size. The same model building process was repeated using 1st derivative data which was used to investigate whether data pre-treatments would improve the predictive ability of the model.

Table 6.3 - Calibration model parameters and root mean square error of prediction (RMSEP) for particle size during milling.

Calibration set	Prediction set	Untreated data		1 st derivative data	
		Latent variables	RMSEP (nm)	Latent variables	RMSEP (nm)
A-F	G	3	8.59	1	19.39
A-E,G	F	3	7.92	3	13.67
A-D,F-G	E	1	5.18	3	5.06
A-C, E-G	D	3	2.36	3	3.38
A-B, D-G	C	1	4.51	4	4.54
A, C-G	B	2	5.75	3	4.55
B-G	A	2	3.73	1	7.39

The predictions from models constructed using the untreated data have generally lower RMSEP values and require fewer latent variables. As the untreated data models are better only those will be discussed in the remainder of the results interpretation. The reason for including the first derivative models was understand whether all the particle size information was removed. From the understanding developed in section 5 the untreated data will contain most of the particle size information in the form of the baseline off-set. However, practical experiments are never identical and differences in the positioning of the NIR probe fibres can cause off-sets between experiments. It is apparent that in this sequence of experiments the

models are improved by not applying the first derivative which will correct for the off-set at the expense of the baseline offset information.

Figure 6.16 shows the predicted versus measured particle size for 4 of the 7 experiments. Predictions for experiment G are poor, whereas, predictions for experiment A are good and this can be rationalised by considering the PCA plot in Figure 6.12 as experiment A is in the centre of the space defined by a PCA model built on experiments B to G. A model built on the data from experiments A to F does not predict the particle size of experiment G well as experiment G is out with the area defined by the model. Predictions for experiment F are also poor for the same reason. Predictions for experiment C show a deviation from the off-line data at low particle size. Even although the reference technique showed the same particle size the NIR spectra continued to change, as would the particle size throughout milling.

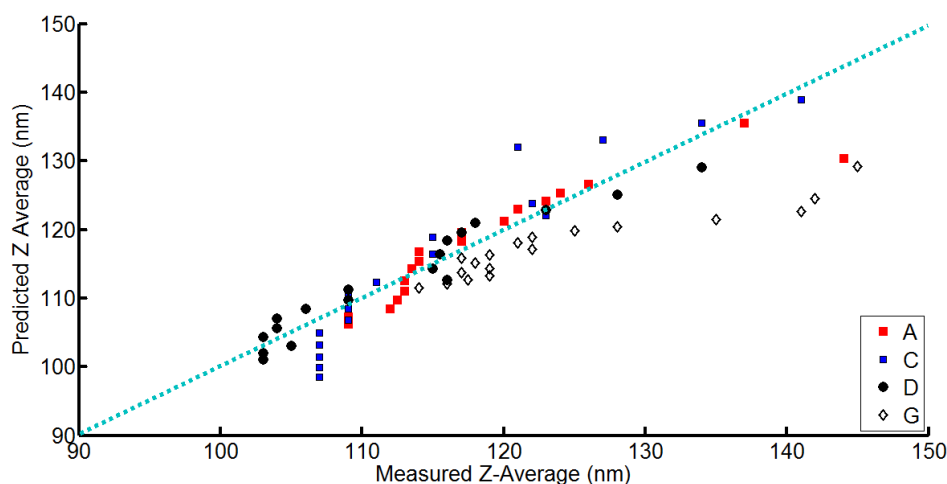


Figure 6.16 – Predicted v actual (from DLS) particle size for experiments A, B, C and G.

This work shows the suitability of using near infrared as a measure of particle size in the nanometre size domain in concentrated pigment dispersions but there are complicating experimental issues which will affect how well the prediction of particle size performs. One thing to consider is the day to day experimental variability. Before each experiment a scan of a white spectralon® disc is required for use as the external reference for that day's experiment. Great care is taken to ensure that the probe and fibres are maintained in a similar orientation and position to those used in the experiment but small differences will invariably arise. This may account

for some of the variation seen in different experiments. This will be less of an issue when the measurement is implemented on plant as the fibres and reflectance probe head would be fixed into semi-permanent fixings for the duration of plant trials. Similarly, the probe positioning in the sample reservoir will be altered from experiment to experiment but in larger scale experimentation the interface containing the probe would be able to maintain a more reproducible position between experiments.

6.6 Chemical Information

Although the primary purpose of the in-situ NIR measurement is to follow the particle size reduction process, there is information relating to the concentration of pigment and polymer encoded into each spectra. It was beneficial to use minimal spectral preprocessing when looking at the changing physical properties (ie the scattering coefficients discussed in chapter 5 which produce baseline off-sets in the in-situ spectra collected during milling experiments) of the sample but removing some of this information may reveal some of the chemical information. An indication of the polymer concentration could potentially avoid costly and time consuming mistakes on plant and add an extra level of confidence in the production process.

6.6.1 Data selection and processing

Spectra from the 7 milling experiments were selected at 30, 60, 120, 180 and 240 minutes and preprocessed using PLS toolbox algorithms before performing PCA on the transformed data set. The NIR dataset was trimmed, using the data points between 898 – 1598 nm. To remove some of the particle size information the spectra were processed to their derivative form using the savgol function with a filter window of 11 data points, a second order polynomial and the first derivative.

6.6.2 Results and discussion

A PCA model was constructed using the derivative NIR spectra (an example of which are contained within Figure 6.17). Preprocessing the spectra using the first derivative transformation does remove a significant amount of the variation between the spectra, although some differences remain. Principal components 1 and 2 represent 82.67 and 10.17 % variance in the dataset. The trends in the first principal component scores values are comparable to those observed in the PCA models constructed in section 6.4.2.2 and it is therefore reasonable to assume that the particle size information is the largest contributor. The second principal component cannot be easily assigned to a specific property of the pigment dispersion. However, the third principal component correlated well with the polymer concentration in the pigment dispersion.

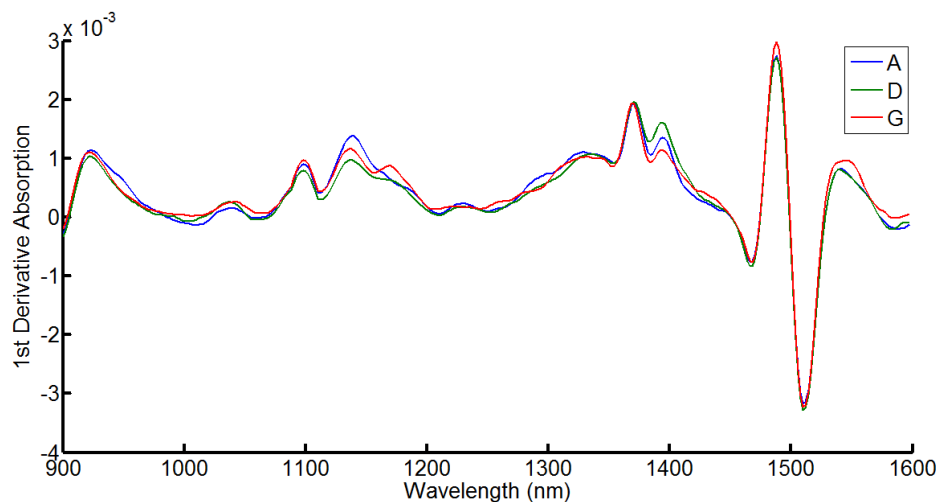


Figure 6.17 – 1st Derivative spectra collected at 240 minutes in milling experiments A, D and G.

The pigment dispersions were prepared with a polymer concentration which was relative to the weight of pigment present (see Table 6.2). Figure 6.18 show the scores values of the selected spectra from each of the 7 experiments in the design. The separation of experiments A and G from the other five experiments with mid concentration polymer is shown. In each case the scores value show consistent trends, decreasing as the milling time decreases. This is the residual of the particle size information which cannot be completely eliminated using simple first derivative pre-processing.

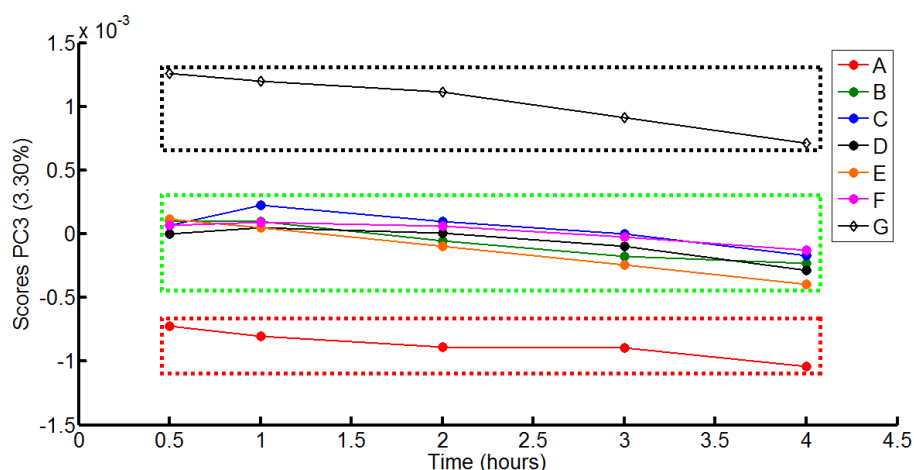


Figure 6.18 – PCA of first derivative spectra. Principal component 3 scores values for 5 time points during each of the 7 milling experiments. The high, medium and low polymer concentration experiments are encompassed by the red, green black dashed boxes respectively.

Figure 6.19 shows the loadings plot for the third principal component. The amount of variance captured is small and comparatively noisy in comparison to the first two principal components loading plots (not shown) but some strong features which contribute can be observed at approximately 900 – 1000 and 1100 - 1200 nm. In these regions the contributions from C-H and O-H overtones will contribute. The polymer contains a lot of these groups and the polymer itself is dissolved in dipropylene glycol so it is difficult to determine whether the major contribution is solely due to the polymer or more likely a combination of the polymer and the components of the matrix it is prepared in.

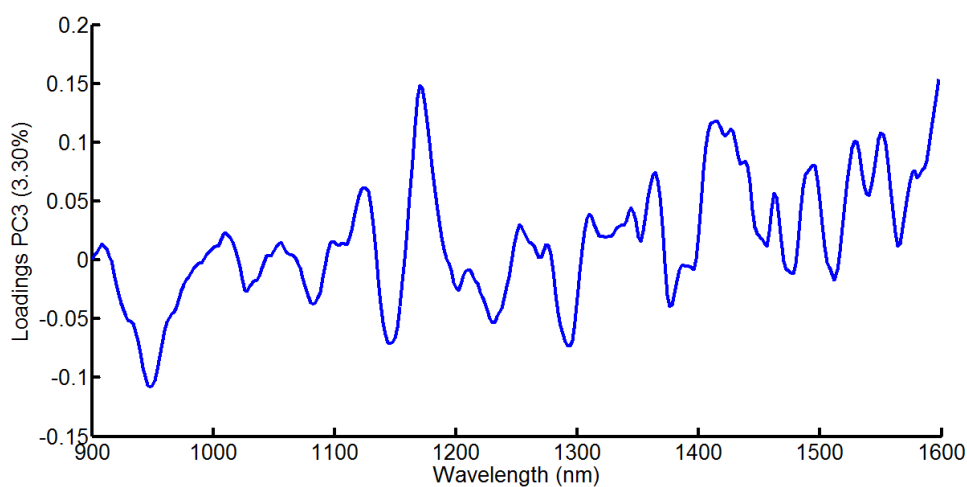


Figure 6.19 – Loadings for principal component 3

6.7 Larger scale milling experiments (10 kg)

Milling experiments with approximately 10 kg pigment dispersions were monitored by NIR reflectance spectroscopy to assess whether the same processes could be observed on a larger scale for cyan, magenta and yellow.

6.7.1 Experimental

Milling experiments were performed at FFIC in Grangemouth. Pigment dispersions were prepared using the detailed weights and batches of materials contained in Table 6.4. The order of addition and method of preparation was the same as that used for smaller scale experimentation. Before the samples were introduced to the mill all samples were mixed at high speed for 1 hour using a Silverson high shear mixer.

Milling was performed in the Netzsch labstar mill and NIR spectra recorded using the FOSS online 6500 NIR spectrometer. DLS and laser diffraction particle size measurements were performed as per sections 3.5.1 and 3.5.2 for the Malvern ZS90 zetasizer and the Malvern mastersizer 2000, respectively. For each of the experiments only the Z-average is reported.

Table 6.4 – Pigment dispersion details for 10 kg milling experiments

Experiment	Inhouse Batch No.	Pigment	Batch No	% Pigment concentration	Polymer	Batch	% Polymer loading	Milling time (hours)
1	1589	PB15:3	307-195A1	20	Acid 45	NBZ6477/02D	45	10
2	1591	PY74	90188FWO	20	Acid 46	D03R053	50	31
3	1609	PR122	39R-317Q0	20	Acid 45	NBZ6477/01D	30	12
4	1622	PR122	003372H6	20	Acid 45	NBZ6477/01D	30	14

6.7.2 Cyan pigment dispersion milling - Results and Discussion.

The cyan pigment was milled for a total of 10 hours and the spectra were collected throughout. The spectra showed a strong change in the baseline offset as milling progressed, as shown in Figure 6.20. With the magenta (section 6.2) and yellow experiments (to be discussed in section 6.7.2), there is an increase in the baseline offset with increasing wavelength until the water peak dominates. However, the copper (II) phthalocyanine also exhibits two strong absorptions in the NIR region at approximately 800 and 1100 nm.

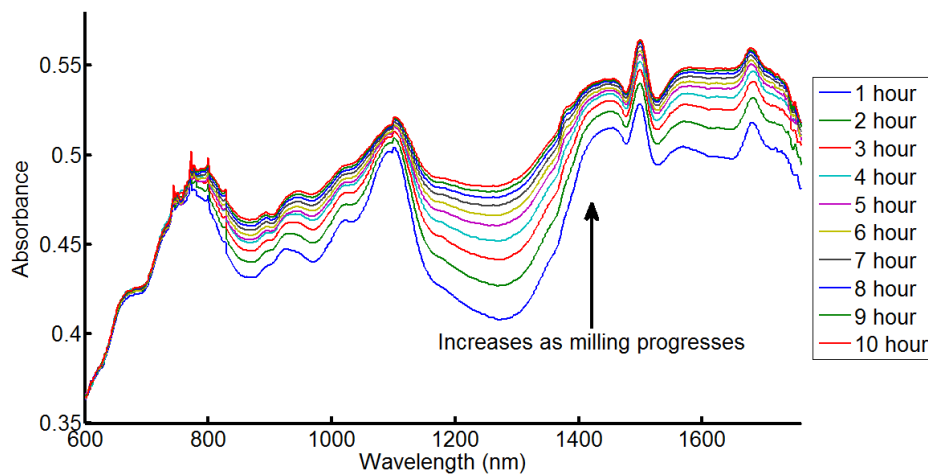


Figure 6.20 – Reflectance NIR spectra collected during the milling of cyan.

Figure 6.21 shows an increase in absorption with time and the corresponding z-average particle size. The milling experiment was completed over two days, the first milling period lasted 4 hours 15 minutes and the second period 5 hours 45 minutes. Interestingly, the near infrared spectra do not show a discontinuity between the two days. When the mill is in operation a significant amount of heat is generated in the milling chamber. Whilst most of the heat is removed by water jackets surrounding the milling chamber there is still a measurable rise in the temperature of the sample in the reservoir. This was measured each hour along with various other parameters such as the mill power draw. What was observed was that the mill sample reservoir quickly reached 32 °C and remained there while the experiment progressed.

The milling equipment was allowed to cool overnight to room temperature before recommencing and the same temperature trend was observed. The fact that the NIR spectra do not change significantly with this small temperature variation between the two days experimentation is significant and confirms that the change in the NIR spectra are not a result of temperature cycling but a physical change in the sample (decreasing particle size).

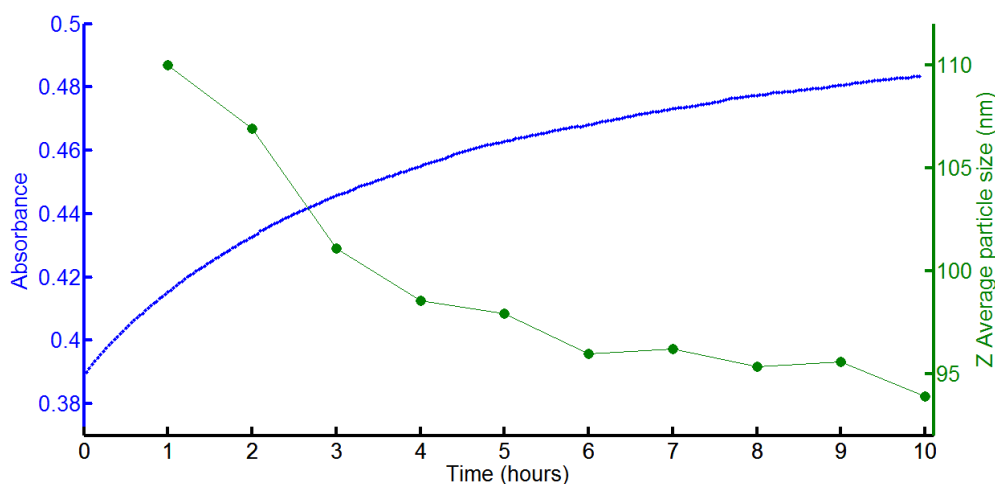


Figure 6.21 – NIR Absorption at 1220 nm and Z-average particle size data collected during the milling of cyan pigment dispersion.

6.7.3 Yellow pigment dispersion milling- Results and Discussion

A yellow pigment dispersion (experiment 2 in Table 6.4) was milled and monitored using NIR spectroscopy. The milling experiment was substantially longer than any other that had previously been monitored. FFIC note that the milling of yellow pigment dispersions requires substantially more time and energy to reduce the particle size to their target specification in comparison to cyan and magenta pigment dispersions. Figure 6.22 shows selected spectra collected during the milling experiment.

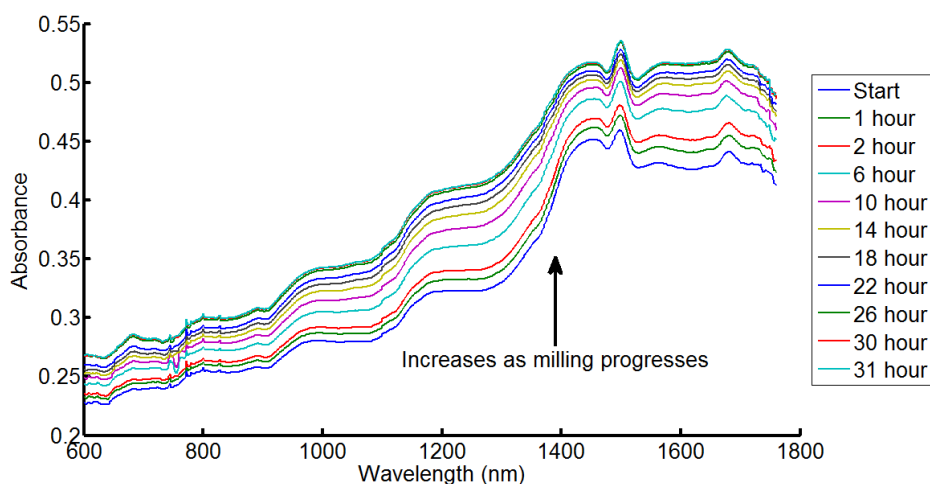


Figure 6.22 – Selected NIR spectra collected during the milling of yellow pigment dispersion (Table 6.4, experiment 2).

The NIR spectra are closer to those observed during the milling of magenta pigment dispersions. The baseline offset increases with increasing wavelength from 600 to 1400 nm until the strong water absorption begins to dominate the spectra. The spectra differ subtly from the magenta spectra as there is still a visible baseline offset at low wavelength (~600 nm). This is because, unlike the magenta pigment, the yellow does not contain a strong absorption in this region. Figure 6.23 show the change in absorption and z average particle size.

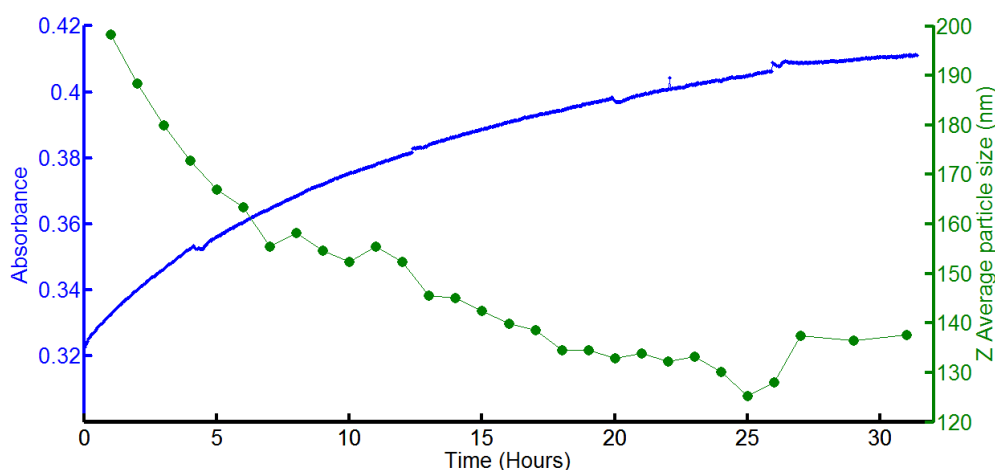


Figure 6.23 – Absorption at 1220 nm and Z average particle size versus time for the yellow pigment milling experiment (Table 6.4, experiment 2)

The milling experiment was completed over five days and slight disturbances can be observed in the trends in the data at 5, 13, 20 and 27 hours. This corresponds to removal and cleaning of the NIR reflectance probe head from the sample reservoir. In all the experiments undertaken, there were no instances of probe fouling. Removal and washing of the probe window was performed to confirm this during the extended experiment. After 27 hours there was an increase in the Z-average particle size and despite continued milling the particle size could not be reduced further. This appears to correspond with the NIR spectra as they show very little change in the last 4 hours of milling.

6.7.4 Transferability of a PLS model developed on < 1 kg magenta milling experiments

Two magenta milling experiments were performed on different days (experiments 3 and 4 in Table 6.4). From here on in these two experiments are referred to as magenta 1 and magenta 2, respectively. Each experiment was monitored using NIR spectroscopy as per section 3.4.1. The particle size of each of the two experiments is shown in Figure 6.24.

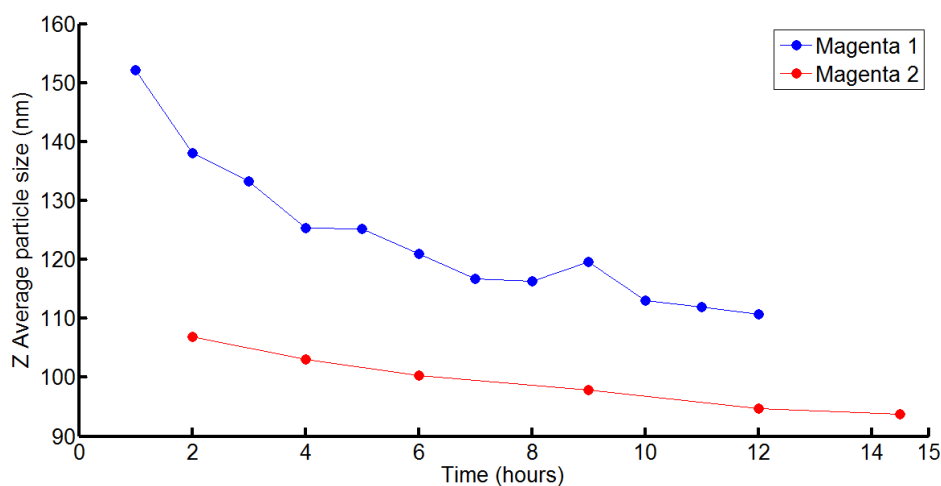


Figure 6.24 – Z Average particle size data versus time for two magenta milling experiments detailed in Table 6.4.

The particle size reference data for each of the two experiments is quite different and it follows that the NIR spectra should reflect this. Figure 6.25 shows the NIR spectra collected in-situ. The magnitude of the change in particle size is much larger in magenta 1 than magenta 2 and the change in the baseline offset experiment "magenta 1" is much larger than the change in the experiment "magenta 2".

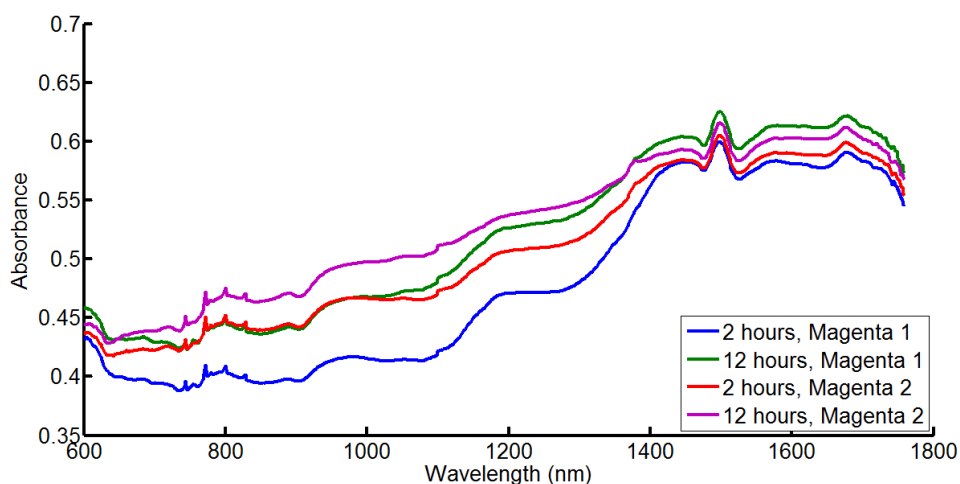


Figure 6.25 – NIR spectra collected near the beginning and end of two magenta pigment dispersion milling experiments.

The red (magenta experiment 2, beginning) and green (magenta experiment 1, end) spectra appear to be quite similar up to 1050 nm despite their significantly different particle size. Milling experiments Magenta 1 and Magenta 2 were similar to those performed in the DoE experiments in section 6.4. The polymer used in the larger scale experiments (acid 45) is chemically similar to the acid 46 polymer which was used in the DoE experiments, differing only in the ratios of the monomers used in the polymerisation. This allowed a direct comparison between the smaller sub 1kg DoE milling experiments and the larger 10 kg milling experiment and testing whether a multivariate model could be applied across the different scales.

6.7.4.1 PCA

The NIR spectra (600 nm – 1798 nm) collected for the magenta two milling experiments were examined using PCA for absorbance and first derivative spectra (Figure 6.26 and Figure 6.27, respectively) along with the spectra collected during

the DoE experiments in section 6.4. The aim was to use a PLS model constructed using the smaller sub 1 kg magenta milling experiments to predict the 2 larger scale, 10 kg, magenta milling experiments. To assess whether untreated or first derivative data would provide the best model, the PCA scores of a model created using the smaller scale DoE experiments and experiments Magenta 1 and Magenta 2 were plotted. Figure 6.26 shows the PC1 scores for the model created using the untreated spectra. There is a large offset between the DoE experiments and the larger scale milling experiments.

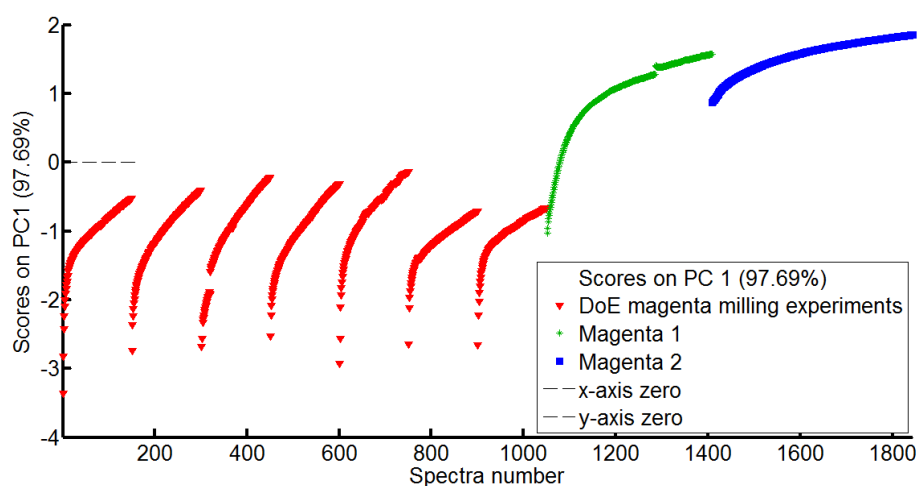


Figure 6.26 – PCA scores of untreated NIR spectra used to create a qualitative model. The red markers represent the 7 DoE magenta milling experiments detailed in section 6.4 and the green and blue markers represent the milling experiments Magenta 1 and Magenta 2 which were performed in the 10 kg scale.

To investigate whether 1st derivatives improved the data a PCA model was created as above but with 1st derivative transformed data. Figure 6.27 shows the corresponding scores values for each of the spectra.

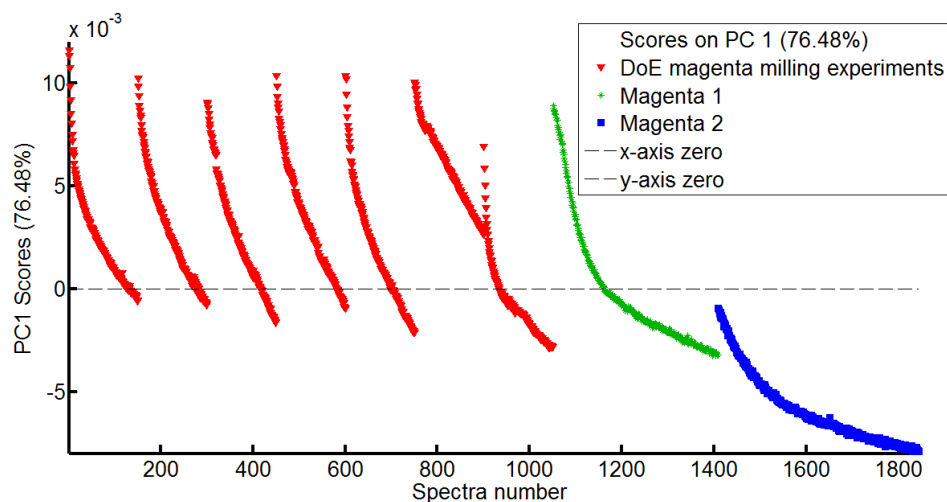


Figure 6.27 - PCA scores of 1st derivative (Savitzky-Golay, filter width 11, polynomial order 2) transformed NIR spectra used to create a qualitative model. The red markers represent the 7 DoE magenta milling experiments detailed in section 6.4 and the green and blue markers represent the milling experiments Magenta 1 and Magenta 2 which were performed in the 10 kg scale.

A first derivative transform removed off-sets between the different data sets showing that the experiment Magenta 1 was now within the range observed for the DoE experiments and Magenta 2 started within the range of the DoE experiments but then moved away from this range.

6.7.4.2 PLS models

PLS models were created using spectra and particle size information generated for smaller scale laboratory milling experiments detailed in section 6.4 and used to predict the two magenta milling experiments in Table 6.4

PLS models constructed using the first derivative NIR spectra show a significant improvement in predictions in comparison to the models with only mean centering (Table 6.5). PLS models constructed using the underivited NIR spectra predict the trend observed from the reduction of particle size but there is a large offset between the predicted and actual particle sizes. This off-set has been removed by using the 1st derivative which is effectively removing some of the particle size information that is

encoded in the spectral data. In this case, more significantly, the differences between experimental set ups and optical fibre positioning are removed, leaving variation due to the sample properties.

Table 6.5 – PLS model information. Calibration set = DoE experiments detailed in section 6.4. Prediction set = spectra collected from experiments Magenta 1 and Magenta 2.

Model	Latent Variables	Preprocessing	RMSEC	RMSECV	RMSEP
1	2	Mean centering	4.89	7.70	62.40
2	4	1 st derivative then mean centering	4.49	4.85	4.55

Figure 6.28 shows the predicted and measured particle size data using the trimmed 1st derivative NIR spectra as the calibration set. From this it is easy to see that the PLS model predicted the particle size well for experiment magenta 1. The PLS model predicts well for the largest particle size but predictions are of poorer quality as the particle size moves below the range covered in the calibration set.

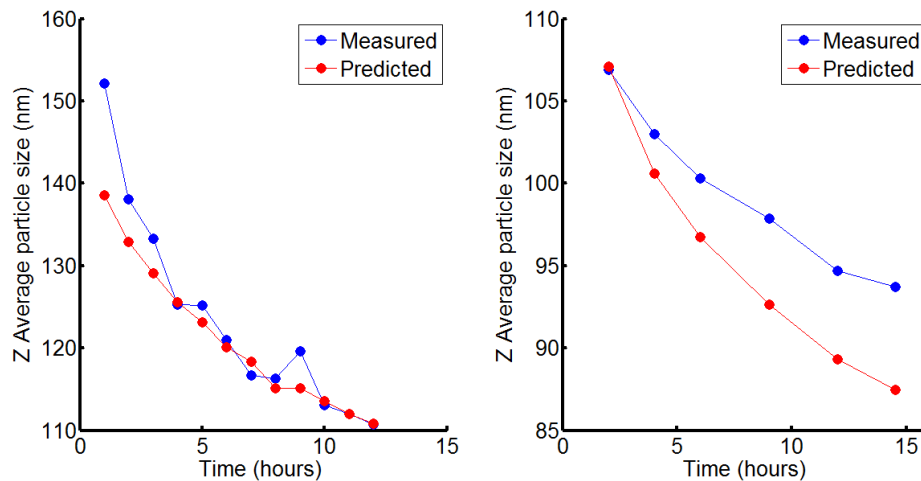


Figure 6.28 – Measured and predicted particle size from PLS models constructed using 1st derivative NIR spectra between 898 and 1598 nm. The left plot show the prediction versus actual for experiment "magenta 1" whereas the right plot shows the predicted versus actual for experiment "magenta 2".

This echoes the scores plots from the PCA analysis. The reason for the bad prediction of Magenta 2 is that the calibration set does not cover the smaller particle sizes obtained in this experiment.

The performance of the NIR model shows that it is possible to build models of milling experiments on one scale and apply them to another. This is especially useful as validating a model at smaller scale reduces waste and avoids calibrating the measurement on plant which can be costly and time consuming.

6.8 Summary

It has been show that there is substantial information gained from up to approximately 6 mm in to the sample from the NIR reflectance probe head and that NIR spectra are affected by particle size for concentrated cyan, magenta and yellow pigment dispersions.

During milling experiments there is a substantial amount of heat generated in the pigment dispersion from the energetic collisions with the milling media in the mill chamber. It has been shown that temperature of the pigment dispersions can be

considered constant during milling. Showing the observed change in NIR spectra collected during milling is a result of the changing physical properties of the sample and not a temperature effect. The NIR spectra, collected in-situ during milling experiments, consistently showed an increasing baseline offset which increased as particle size decreased. This offset increases with wavelength until strong absorptions such as the water absorption around 1400 nm dominate the NIR spectra.

The pigment dispersion stability was estimated for concentrated and diluted samples. This revealed that the best method of preparation was to dilute samples immediately on extraction from the mill and samples could be analysed up to 5 days after preparation.

A wide range of pigment and polymer concentrations were monitored for small scale (~ 1 kg) magenta experiments. PCA revealed experimental process to be robust and PLS models were constructed which predicted the particle size with good accuracy. Additionally, PCA revealed some correlation between derivative NIR spectra and the polymer concentration for the magenta experiments on the smaller laboratory scale.

10 kg scale milling experiments revealed similar effects on the NIR spectra to those observed on the smaller experimental scale for magenta and yellow. The blue dispersions showed a similar trend with some stronger absorptions in the NIR region.

PLS models constructed using the smaller scale magenta experiments (600 g) were applied to two larger scale (10 kg) experiments. 1st derivative pre-treatment allowed enough particle size information to be retained for good predictive ability. The PLS model performs well over the range of particle sizes used to construct the model

6.9 References

1. *Biology and Technology*, 2000, **18**, 121-132. , *Postharvest*
2. W. G. Haanstra, W. Hansen, M. J. G. Huys, B. J. Kip, P. Palmen, J. Roumen, M. Snieder, T. V. D. Weerdhof, S. Wiedemann and V. A. L. Wortel, *Applied Spectroscopy*, 1998, **52**, 863-868.
3. F. C. Clarke, S. V. Hammond, R. D. Jee and A. C. Moffat, *Applied Spectroscopy*, 2002, **56**, 1475-1483.
4. L. J. Bellamy, A. Nordon and D. Littlejohn, *Analyst*, 2008, **133**, 58-64.
5. F. Wülfert, W. T. Kok and A. K. Smilde, *Analytical Chemistry*, 1998, **70**, 1761-1767.
6. F. O. Libnau, O. M. Kvalheim, A. A. Christy and J. Toft, *Vibrational spectroscopy*, 1994, **7**, 243-254.

7. NIR for 200 kg scale milling experiments.

Small scale experimentation has shown that there is a measurable change in NIR spectra as the particle size of magenta, cyan and yellow pigment dispersions are reduced. Experiments performed on 2 different scales (< 1 kg and 10 kg) showed that multivariate calibration models could be developed on the smaller scale and then applied to the larger process, accounting for issues involved when changing the positioning of the spectrometer, fibres and reflectance probe head. This chapter aims to apply this learning to large scale monitoring for either qualitative or quantitative. The specific aims of this section are to:

1. Estimate the volume of sample analysed per NIR spectra.
2. Assess the effect of switching from monitoring the sample reservoir to monitoring the return flow of the mill.
3. Demonstrate that the 200 kg scale milling process can be monitored for the cyan, magenta and yellow pigment dispersions.
4. Investigate whether the NIR technique is suitable for monitoring the milling of a highly absorbing pigment such as carbon black.

7.1 Experimental

NIR spectra were collected using the FOSS on-line instrument (section 3.4.2) integrated into the return stream of the 200 kg scale milling equipment, detailed in section 3.3. Several large scale experiments were monitored for cyan, magenta, yellow and black pigment dispersions. The premixing of the pigment dispersion is analogous to the procedure used for the preparation of pigment dispersions for small experiments but it is performed at a much larger scale to produce total dispersion weights of around 200 kg. Premixing is undertaken in a large vessel equipped with a high shear mixing blade before the dispersion is transferred to the mill.

For all of the experimental data presented herein, "Acid 45" was used as the dispersing polymer. The polymer concentration was 31% w/w. The formulation of the pigment dispersions was the same as described in section 3.2 whereby, polymer was added relative to the concentration of pigment. Table 7.1 details a complete list of pigment dispersion experiments monitored on the 200 kg scale using NIR spectroscopy. The pigments used were PR122 for magenta, PY74 for yellow, PB15:4 for cyan and carbon black for the black dispersions.

Table 7.1 – 200 kg scale dispersion milling experiments which were monitored on-line using the FOSS on-line 6500 spectrometer.

Experiment	Reference number	Pigment Concentration (% w/w)	Polymer Loading (%)	Milling time (hours)
Cyan 1	10109	18.70	30	48.2
Cyan 2	10110	19.16	30	31.4
Cyan 3	10112	17.21	30	29.2
Cyan 4	10117	19.80	30	26.0
Cyan 5	10118	19.14	30	60.1
Cyan 6	10119	19.08	30	45.0
Magenta 1	10033	26.11	30	26.1
Magenta 2	10034	27.18	30	19.5
Magenta 3	10035	27.94	30	19.5
Magenta 4	10069	21.84	30	26.3
Magenta 5	10070	21.83	30	15.6
Magenta 6	10071	21.84	30	16.2
Magenta 7	10073	21.83	30	18.9
Yellow 1	10075	21.58	50	69.8
Yellow 2	10076	21.58	50	80.1
Yellow 3	10078	21.59	50	82.3
Yellow 4	10079	21.58	50	79.8
Yellow 5	10081	21.59	50	93.6
Yellow 6	10108	21.59	50	63.2
Black 1	10114	15.44	40	17.1
Black 2	10115	17.42	40	17.7
Black 3	10121	17.99	40	16.4
Black 4	10122	19.15	40	16.8

7.2 Results and discussion

7.2.1 Sample volume

The sample volume of pigment dispersion was estimated for the FOSS reflectance probe for the milling of pigment dispersions during large scale experiments. Assuming a standard batch volume 200 L, the volume of pigment dispersion sampled was calculated at 700, 850, 1000, 1150 and 1300 nm. The NIR penetration depth increases with increasing wavelength (as detailed in section 6.1) and the following penetration depths were used to determine the samples volume (Table 7.2).

Table 7.2 – NIR penetration depths from section 6.1 and the approximate values used to calculate the volume of pigment dispersion samples per NIR spectrum

Wavelength (nm)	Experimentally determined penetration depth (mm)	Penetration depth used for calculations (mm)
700	< 1 mm	0.75
850	2 - 3 mm	2.5
1000	3 – 4 mm	3.5
1150	~ 5	5.0
1300	> 6	6.0

Pigment dispersion is recirculated at a fixed rate of 3.53 m³ per hour from the milling chamber to the sample reservoir, passing along the probe port containing a 2 inch (5.08 cm) internal diameter circular pipe at the section where the NIR reflectance probe is placed.

$$\text{Area of the probe port cross section} = \pi \cdot r^2 = \pi \times \left(\frac{0.0508 \text{ m}}{2}\right)^2 = 2.03 \times 10^{-3} \text{ m}^2$$

$$\text{Sample speed} = \frac{\text{vol. per hour}}{\text{cross section area}} = \frac{3.53 \text{ m}^3 \text{ h}^{-1}}{2.03 \times 10^{-3} \text{ m}^2} = 1741.64 \text{ m h}^{-1}$$

$$\therefore \text{Sample speed} = 0.48 \text{ m s}^{-1}$$

Each spectrum is a collection of 32 scans which takes 51 seconds to acquire and the probe reflectance window is 0.80 cm in diameter. For the calculation of the volume of sample analysed, the shape of the propagation of light in the sample is approximated as a cylinder although, in reality, the sample area is more likely to be a widening cylindrical shape (Figure 7.1).

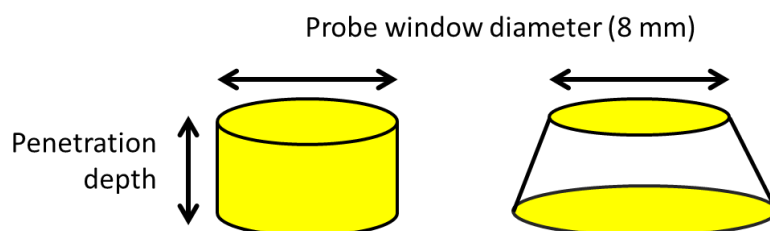


Figure 7.1 – Schematic representations of sampling geometry of the NIR reflectance probe.

For each NIR spectrum, the sampled volume will correspond to the volume of the cylinder and rectangle in Figure 7.2. The pigment will be moving like a conveyer belt of sample and at the start and finish of the measurement there will be a half cylinder following the shape of the NIR reflectance probe window. These are summed to simplify the picture. The FOSS Online 6500 is a scanning grating instrument which collects 650 data points at 2 nm intervals. 32 scans take 51 seconds, hence:

$$\begin{aligned} \text{Acquisition time at each data point} &= \frac{\text{Aquisition time}}{\text{Number of datapoints in 1 spectrum}} \\ &= \frac{51}{650} = 2.446 \times 10^{-3} \text{ Seconds per data point} \end{aligned}$$

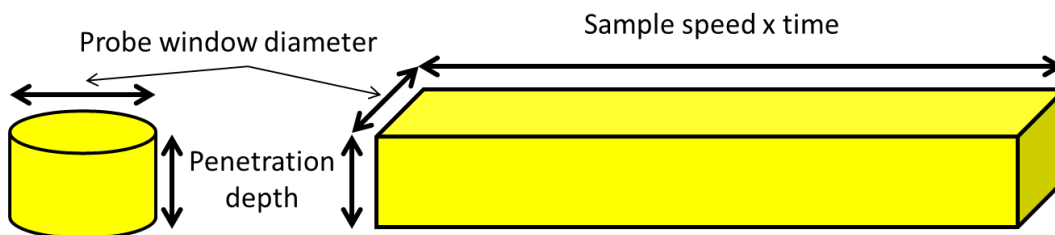


Figure 7.2 – Schematic diagram detailing the volume of pigment dispersion samples per NIR spectrum

An example calculation for the penetration depth at 1150 nm is shown below:

$$\text{Volume of the cylinder} = \pi \cdot r^2 \cdot l = \pi \times (0.004)^2 \times 0.005 = 2.51 \times 10^{-7} \text{ m}^3$$

$$\text{Volume of the cuboid} = l \cdot b \cdot h = \left(0.48 \times \frac{51}{650}\right) \times 0.008 \times 0.005 = 1.51 \times 10^{-6} \text{ m}^3$$

$$\therefore \text{The volume sampled at 1150 nm} = 1.76 \times 10^{-6} \text{ m}^3 \Rightarrow 1.76 \text{ ml}$$

Table 7.3 – Sampled volume per NIR spectra for varying wavelengths and penetration depths.

Wavelength (nm)	Penetration depth (mm)	Analysed volume of dispersion (ml)	Percentage of the total batch (10^{-5} %)
700	0.75	0.26	1.13
850	2.5	0.88	3.77
1000	3.5	1.23	5.27
1150	5.0	1.76	7.53
1300	6.0	2.11	9.04

The wavelength range 700 to 1300 nm encompasses 300 individual data points. Figure 7.3 shows the volume of pigment contributing to one spectrum at each of the 300 data points over 700 – 1300 nm.

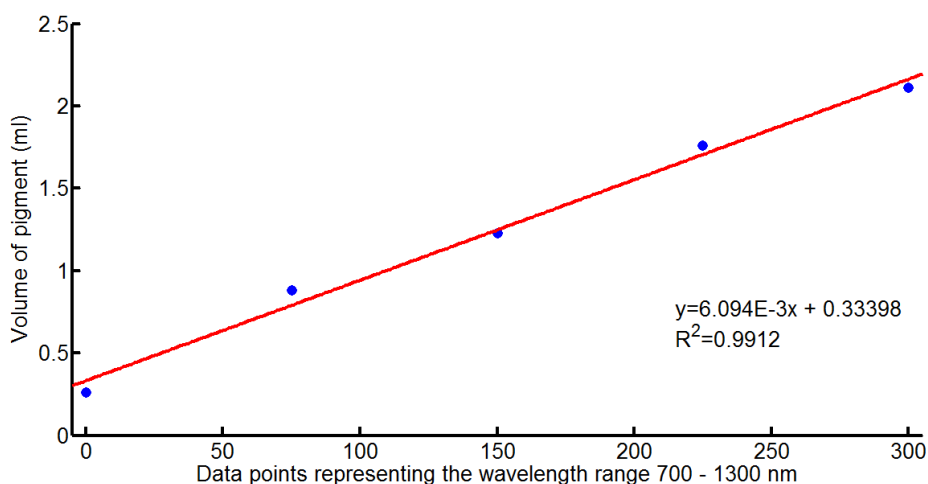


Figure 7.3 – Volume of pigment dispersion contributing to each NIR spectrum at each data point representing the range 700 – 1300 nm.

Using the equation of the line in Figure 7.3, the volume of sample that contributes to an NIR spectrum, between 700 and 1300 nm, can be found as the area under the graph. The sum total volume of sample which is measured over the wavelength range 700 – 1300 nm is 374 ml. This corresponds to approximately 0.19 % of the total batch volume.

The calculations shown here are a simplified picture of the interaction of the NIR light with the sample. To improve the estimated volume of sample contributing to each spectrum, the contribution from sequential layers of the pigment would have to be taken in to account. Material nearest the probe window will contribute more information to a spectrum than the material below it and to account for this, a weighting factor could be calculated from the decaying change in the NIR spectra observed at different depths (the penetration depth experiment) but this greatly increases the complexity of the calculations. It may be desirable to do this in some instances but in this case an estimate of the sampled volume is sufficient.

7.2.2 Milling temperature

Small scale milling experiments (~1 and 10 kg) showed that the temperature of the milled dispersion milling was above room temperature (by approximately 10 °C) but it remained constant throughout most of the experimentation, The temperature was dependent on the temperature and flow rates of the cooling water used in the jackets of the small scale mills. On the large scale, NIR spectra of the pigment dispersions were collected after the pigment had travelled through a heat exchanger and as a result, the temperature of the pigment dispersion as it passed the NIR probe head was consistent. The temperature was manually recorded for a number of millings performed on the large scale which showed that once the temperature had risen from room temperature and reached a certain level, it remained consistent ($\pm 2-3$ °C) throughout the remainder of the milling. Figure 7.4 shows an example for each colour of pigment dispersion.

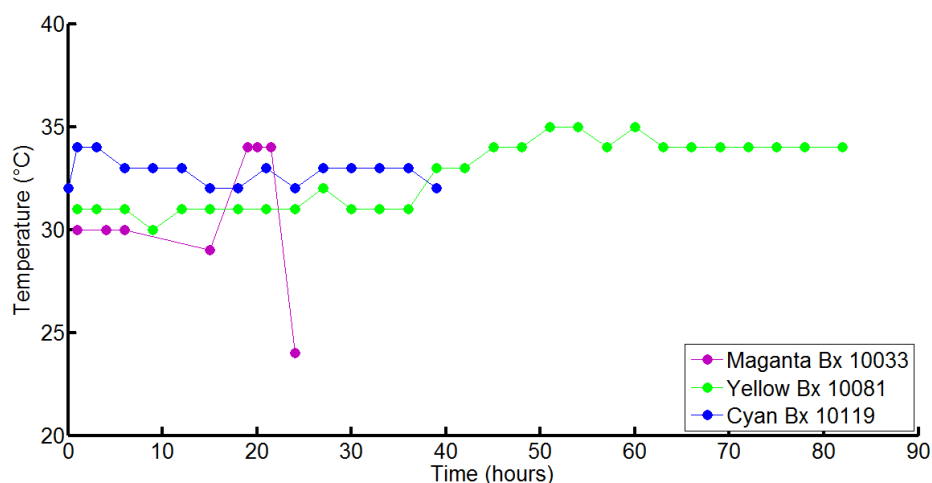


Figure 7.4 – Temperature of pigment post mill for magenta, yellow and cyan pigment dispersions.

Several magenta pigment dispersions, including experiment 10033, were milled over different days. This introduced a cool down time before restarting the milling process. NIR spectra showed a small disturbance as the milling restarted but the trends continued from where they left off the previous day. Indicating that reduction

of particle size is the dominant effect on the NIR spectra. The temperature is comparable to those observed during milling experiments on the smaller scale.

7.2.3 200 kg scale milling data

The milling of cyan, magenta, yellow and black pigment dispersions (Table 7.1) was monitored on-line using the FOSS on-line 6500 (section 3.4) using the NIR probe integrated in to the pipework as per section 3.4.1.2 . Figure 7.5 shows NIR spectra for the four colours near the end point of each milling. The blue pigment displays a characteristic absorption circa 1100 nm that was observed when monitoring smaller scale milling experiments and the black pigment has a relatively high absorbance compared to the other colours (as would be expected). The magenta and yellow pigment dispersions produce similar spectra over the NIR wavelength range. A common feature to all is the noise observed from the detector at 800 nm and the data sets were trimmed to exclude this.

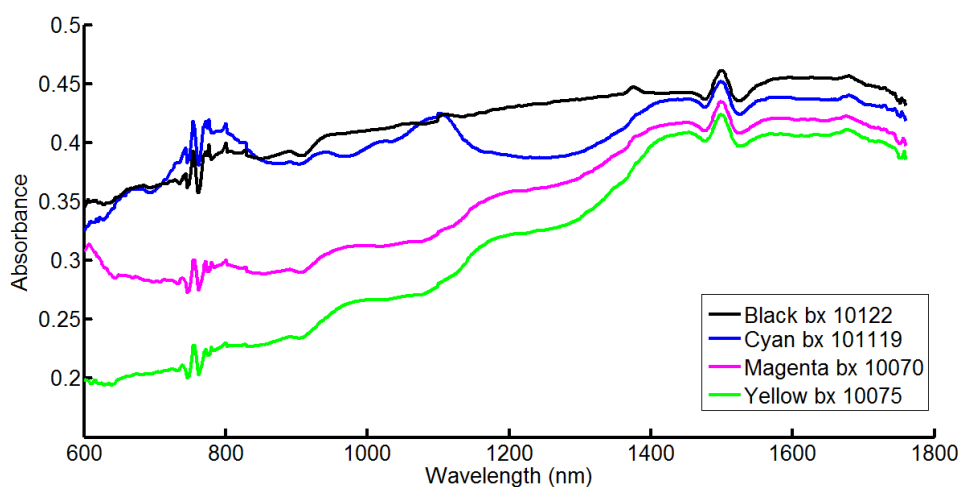


Figure 7.5 – Example NIR spectra collected at the end large scale pigment dispersion milling.

7.2.3.1 Multivariate or Univariate

Spectra collected from laboratory milling experiments, performed at 2 scales, used a combination of univariate and multivariate techniques for extracting useful information from NIR spectra. Multivariate techniques were used as an investigative tool to visualise complex datasets (PCA) and to build a calibration model for a DoE matrix of magenta milling experiments with different concentrations (PLS). Simple univariate techniques were used to observe the change in the NIR spectra by following the change in the absorption at 1220 nm which showed a significant change in baseline offset with particle size. Multivariate techniques were assessed alongside simpler univariate data analysis.

7.2.3.1.1 Method

PCA was performed for NIR data collected during large scale milling of pigment dispersions over wavelength range 898 – 1598 nm in Matlab. The omitted region below 898 nm shows some detector noise and the region above 1598 nm was omitted as there is consistently less change than is present between 898 – 1598 nm during particle size reduction. Noise in the NIR spectra below 898 nm was observed during small scale experimentation but the effect was much smaller as the operating times for the spectrometer were much shorter. The matrix of spectra were mean centred.

The way in which the probe was integrated into the large scale milling equipment meant that a reference scan of the white spectralon disc could not be collected between experiments. Instead, a reference was taken at the start of each a sequence of experiments where the probe could not be removed. Performance checks were carried out in the Vision software to ensure the spectrometer was operating within normal parameters.

7.2.3.1.2 Results

Figure 7.6 shows the PC1 scores from the model constructed using all the NIR spectra collected during the milling of cyan, magenta, yellow and black pigment dispersions detailed in Table 7.1. Each experiment is represented by an arc where the

scores values increase (rapidly at the start of each milling followed by a decrease in the rate of change – echoing the particle size reduction process). The x axis represents the sample number and is, in effect, a time axis. Each experiment is presented in the scores plot in the same order as Table 7.1, i.e. the first 6 arcs represent the milling of cyan pigment experiments 1-6 in ascending order. One striking feature from the black pigment dispersions is that there is relatively little change in the NIR spectra in comparison to cyan, magenta and yellow pigment dispersion but there is still some measureable change in the spectra observed.

PC1 describes 93.59 % of the variation in the data and Figure 7.7 shows PC1 versus PC2 (5.74 %). The NIR spectra of magenta and yellow pigment dispersions are similar and show an offset from each other whereas the spectra from the cyan and black pigment are quite different, thus, the spectra collected during the milling of cyan and black are easily distinguishable from the magenta and yellow milling experiments represented in Figure 7.7.

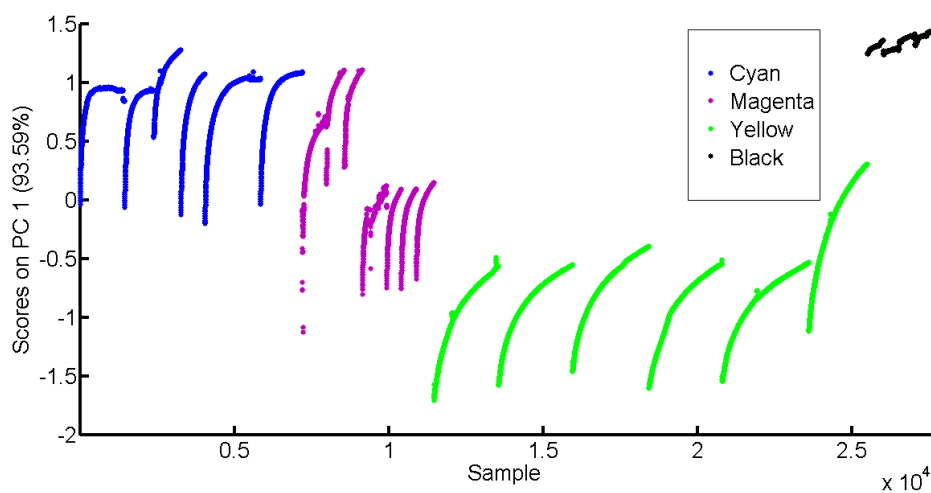


Figure 7.6 – PCA scores values for trimmed NIR spectra collected during all milled pigment experiments detailed in Table 7.1. The x axis is retained as sample number and can be converted to time in minutes by multiplying the values by two.

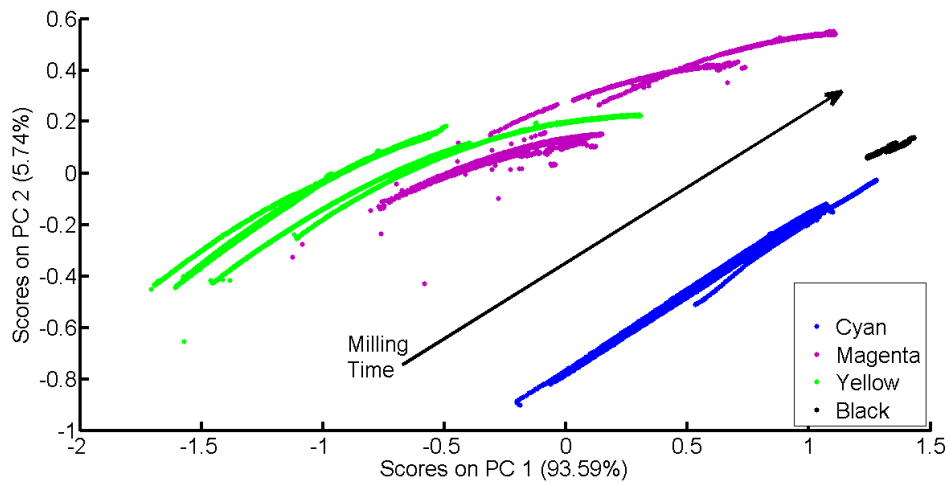


Figure 7.7 – PC1 scores versus PC2 scores for all NIR spectra collected throughout 200 kg scale pigment dispersion milling.

Figure 7.8 represents the loadings plots for each of the two principal components selected which cumulatively represent 99.33 % of the dataset variation. The loadings plot are constructed from the data matrix that contains different colours of pigment dispersions and hence, they look quite different to loadings plots created for single colours where the largest source of variation in the dataset is the baseline offset caused by the reducing particle size.

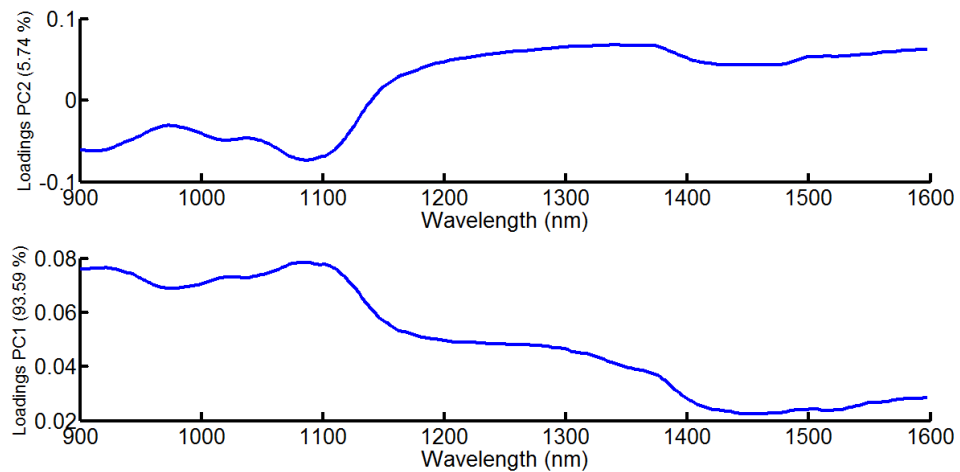


Figure 7.8 – PCA loading plots for PC1 and PC2 calculated from NIR spectra (898 – 1598 nm) collected during the milling of pigment experiments in Table 7.1.

Figure 7.9 shows the scores values for PC1 from the PCA in blue and the green data points represents the absorption at 1220 nm for the same 200 kg scale millings of cyan pigment dispersions. This shows that PC1 effectively captures the same variance in the spectra as can be represented by simply observing the change in the base line offset at 1220 nm. The PCA model is constructed using the complete dataset with all 4 different pigment colours.

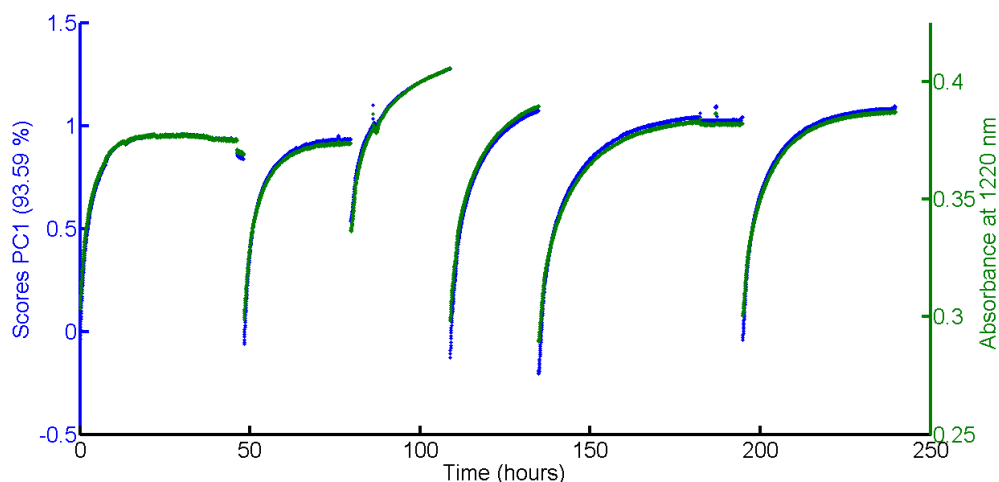


Figure 7.9 – PCA PC1 Scores values and absorbance at 1220 nm for cyan milling experiments 1 to 6.

Figure 7.10 shows the PC1 scores and absorbance at 1220 nm versus time for magenta, yellow and black pigment dispersion milling. The particle size reduction can be followed using univariate methods (at 1220 nm) just as well as multivariate techniques although some difficulties arise when the probe is removed and replaced. The different orientation of the fibres alters the path of the illuminating and collected photons as they travel through the fibre run. This can result in an offset of the NIR spectra which can be observed between similar milling processes with similar operating conditions.

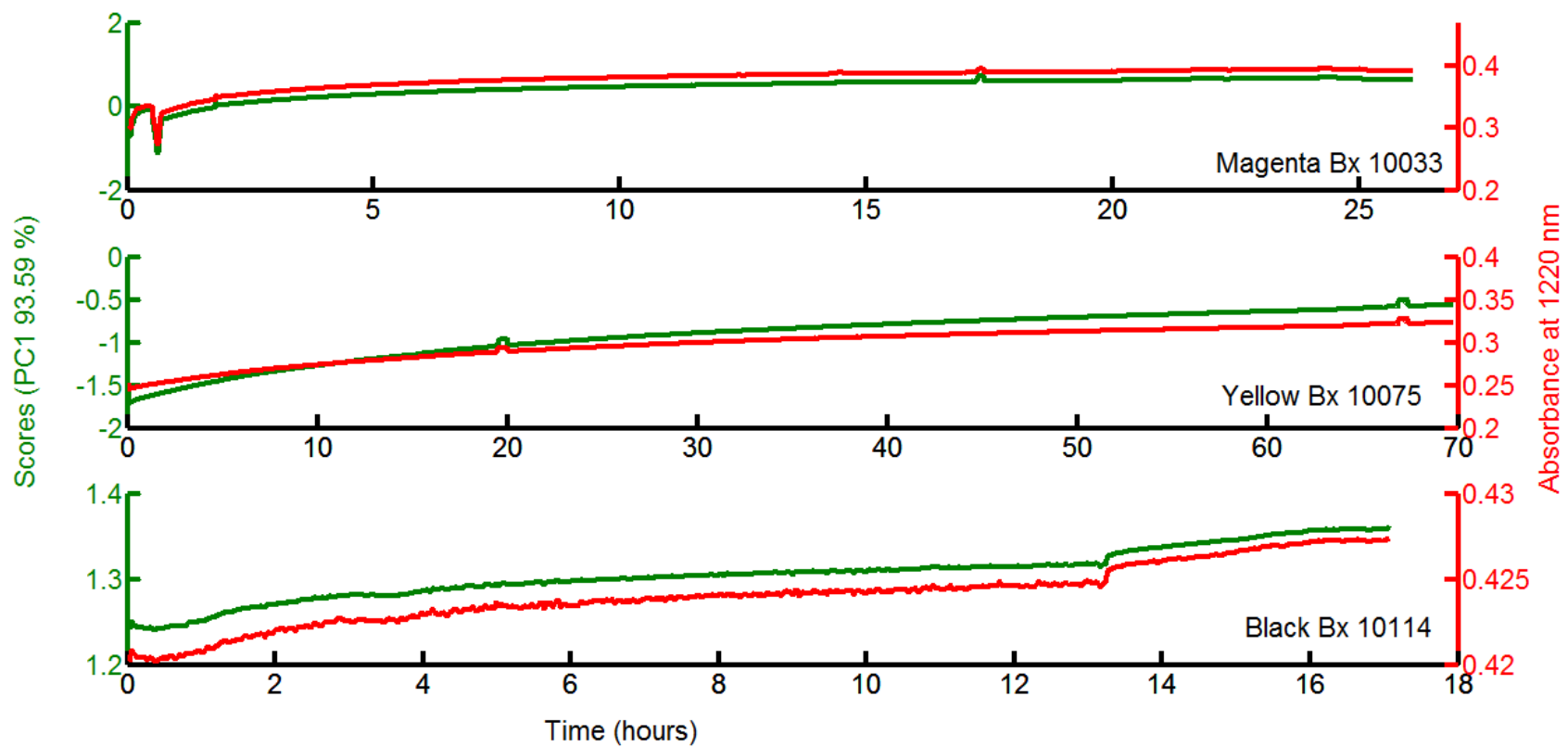


Figure 7.10 –PC1 scores and absorbance at 1220 nm for magenta experiment 1 (number 10033), yellow experiment 1 (number 10075) and black experiment 1 (number 10114).

7.2.3.2 Magenta milling data - part I

The milling of seven magenta pigment dispersions, performed over two campaigns, was monitored using on-line NIR spectroscopy. The 1st campaign consisted of three experiments (numbers 10033 to 10035) which were high concentration pigment dispersions of approximately 26 % w/w pigment dispersion. Figure 7.11 shows the absorption at 1220 nm which follows the baseline offset in the NIR spectra and there is a clear offset between experiment 10033 and experiments 10034 and 10035.

Table 7.4 – Magenta pigment dispersions milled on the 200 kg scale –part I.

Experiment	Reference number	Pigment Concentration (% w/w)	Polymer Loading (%)	Milling time (hours)
Magenta 1	10033	26.11	30	26
Magenta 2	10034	27.18	30	19.5
Magenta 3	10035	27.94	30	19.5

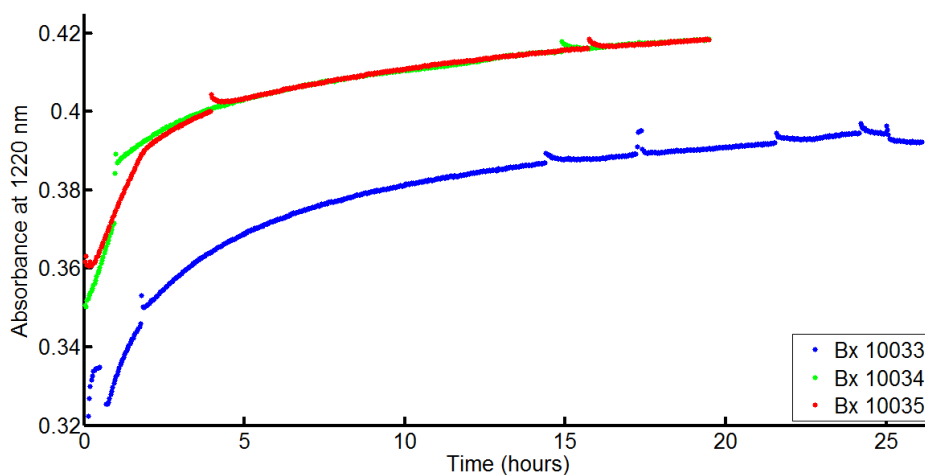


Figure 7.11 – NIR absorbance at 1220 nm, collected during the milling of three high concentration magenta pigment dispersions.

Experiment 10033 was the first to be monitored using the NIR reflectance probe integrated in to the recirculation line which moved sample from the milling chamber, through a heat exchanger before passing through the probe port on the route back to the holding tank. After each milling, the pipework and mill were flushed with water to remove excess pigment dispersion. To check whether the flushing routine was adequate to clean the NIR reflectance probe head, the probe was extracted and inspected. The flushing procedure had removed any trace of the pigment dispersion on the flat end of the probe containing the window.

The probe port was positioned horizontally at a level of about 5 feet above ground level and the removal and inspection of the probe caused the fibres to be disturbed. Additionally, a fresh reference scan of a white spectralon disc was collected and applied as the reference before the probe was replaced.

To ascertain whether the offset was a result of the two different reference scans, the absorbance values at 1220 nm were recalculated for experiment 10033 using the reference scan collected prior to the milling of experiments 10034 and 10035. On inspection, the reference scan values were close with a small offset and changing the reference scan did not reduce the offset observed between experiment 10033 and the following two magenta pigment dispersion experiments 10034 and 10035. This indicates that there is a substantial source of error when the probe and fibres are repositioned. The NIR probe was marked with levels corresponding to the top of the sealing PTFE coupler to ensure that the probe was repositioned consistently and the probe protruded in to the flow of the pigment dispersion at the same depth. Hence, it is more likely that the orientation of the fibre bundle was the cause of the offset between the three magenta pigment dispersion milling experiments.

To remove this potential source of error, a decision was made to reduce disturbances to the fibres and probe position, by leaving the probe and fibres in position during each milling campaign. The NIR absorbance values at 1220 nm show no such offsets between the two millings (experiments 10034 and 10035)

Each of the three experiments shows some discontinuity in the absorbance trends at 1220 nm whilst the pigment is charged from a mixing vessel (Figure 7.11), through the mill (this process is called the "first pass") but all of the trends are consistent after

two hours. This can be attributed to the different rates at which the pigments are fed from the holding vessel but when the loop is closed and the recirculation milling is underway, the trends are more consistent.

Figure 7.12 shows a magnified portion of which shows a portion of the absorption trends for magenta pigment dispersion experiments 10034 and 10035 in more detail. The trends appear to be identical approaching the endpoint.

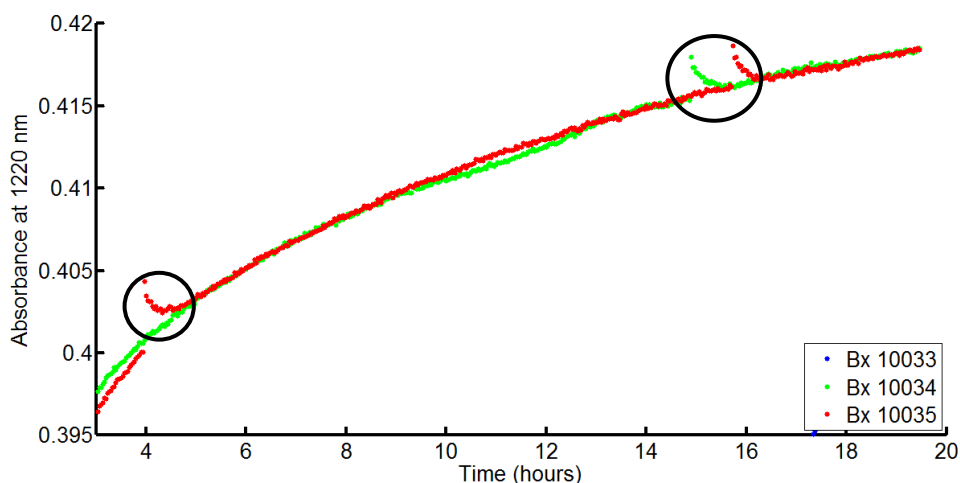


Figure 7.12 – NIR absorbance values at 1220 nm from 4.5 to 20 hours collected during the milling of magenta pigment dispersions (experiment numbers 10034 and 10035).

Key features of the figure are highlighted in the circled areas. These correspond to the mill being restarted after a shutdown period (i.e. overnight or awaiting analytical results) and always display an increase in absorption before resuming the trend from earlier. Apart from providing a useful indicator of milling times when analysing the NIR spectra, the fact the trends resume add to the confidence that the particle size is really the cause of the change in the NIR spectra. Also, the millings of the two experiments in Figure 7.11 were collected with no movement of the probe and optical fibres which shows that good quality, consistent measurements of pigment dispersions can be made on the larger scale.

Unfortunately, experiments 10033 – 10035 have relatively little characterisation data (Table 7.5) but, at a first glance, measuring the particle size change of milling

pigment dispersions on large scale milling experiments using on-line NIR spectroscopy is a real possibility. Additionally, identification of problems such as moving the fibres and probe is valuable information and allowed informed decisions to be made for monitoring future experiments. The particle size data also shows that experiments 10034 and 10035 have very similar particle sizes and that the particle size reduction of experiment number 10033 was more problematic with a Z-average particle size 10 nm larger than the following two experiments. This could contribute to the offset NIR spectral trends at 1220 nm but the removal of the probe does not allow a direct comparison of the NIR spectra with any confidence.

Table 7.5 – Off-line particle characterisation data for magenta pigment dispersions. Experiment numbers 10033, 10034 and 10035.

Reference number	Time (hours)	Z-Average particle size (nm)
10033	15	128.4
	20	126.6
	25	126.0
	26	126.0
10034	16	114.1
10035	18	115.5

7.2.3.3 Magenta milling data – part II

A number of additional magenta pigment dispersions were monitored using on-line NIR measurements. The experiments consisted of 4 identical formulation pigment dispersions (Table 7.6). Drawing on conclusions from earlier work, the probe and fibres were not removed or disturbed.

Table 7.6 – Magenta pigment dispersions milled on the 200 kg scale – part II.

Experiment	Reference number	Pigment Concentration (% w/w)	Polymer Loading (%)	Milling time (hours)
Magenta 4	10069	21.84	30	26.3
Magenta 5	10070	21.83	30	15.6
Magenta 6	10071	21.84	30	16.2
Magenta 7	10073	21.83	30	18.9

Figure 7.13 shows the absorbance at 1220 nm for each of the four experiments. It is clear that the milling of experiment 10069 does not proceed as smoothly the following three experiments. Importantly, the absorbance values at the start of the milling process are lower and returns to a value of approximately 0.3, showing that the measured change in the NIR spectra is not a consequence of instrumental drift.

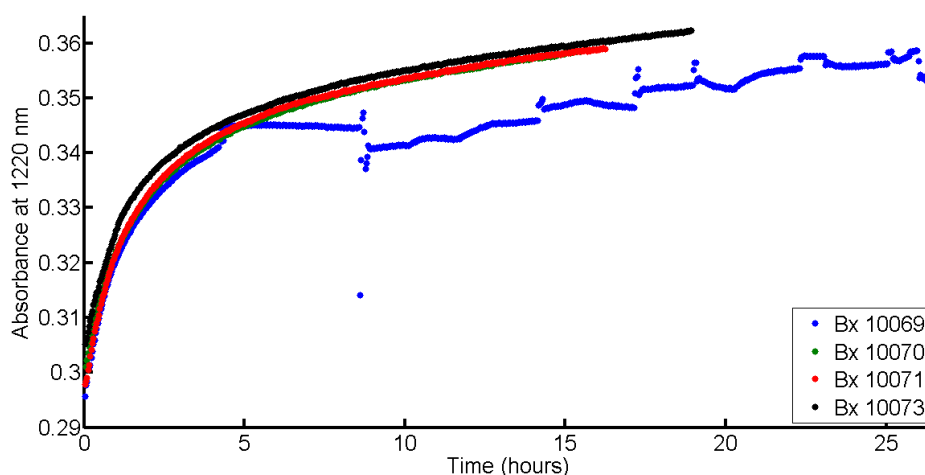


Figure 7.13 – NIR absorbance at 1220 nm for magenta pigment dispersions - experiment numbers (10069, 10070, 10071 and 10073).

Experiment 10069 shows several discontinuities along the 26 hours of milling which correspond to repeated attempts to restart the milling process. In this instance, a blocked heat exchanger obstructed the flow of the pigment dispersion causing a

lower recirculation rate of pigment dispersion (usually held at a constant rate of 3.53 m³ per hour). This shows the possibility of using an on-line measurement, not only for particle size determination, but to indicate when the process has a fault.

Relatively few samples were removed for particle size analysis throughout the four magenta milling experiments but samples removed near the end of the milling process were analysed by dynamic light scattering and laser diffraction. Using the DoE matrix of lab magenta milling experiments as a calibration set, univariate and multivariate models were created and applied to the large scale milling data. The calibration experiments were PR122 pigment dispersions with polymer acid 46 and

7.2.3.3.1 Univariate data analysis

A univariate model was created (Figure 7.14) to predict particle size using the NIR absorbance at 1220 nm versus particle size from lab scale magenta milling experiments detailed in section 6.4. The DoE 2 level, 2 factor design covers a range of pigment (15 % w/w to 25 % w/w) and polymer loading (30 to 50 % loading).

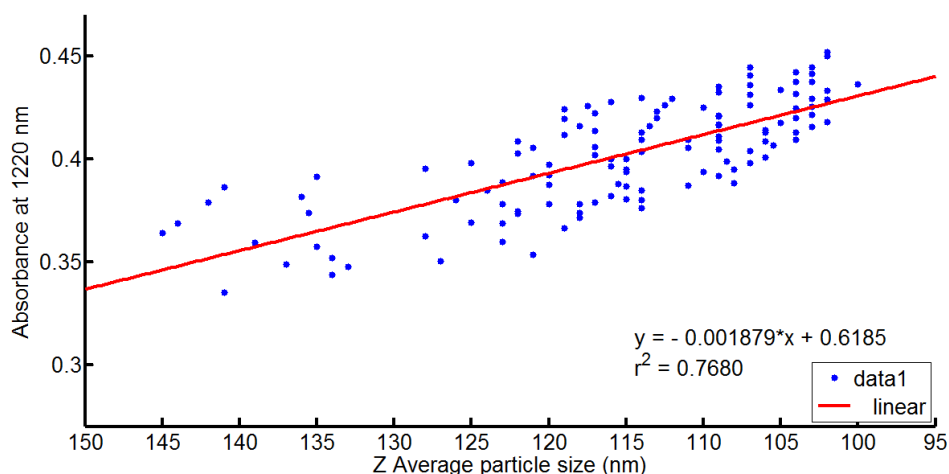


Figure 7.14 – Univariate model showing Z-average particle size versus absorbance at 1220 nm for all 7 lab scale magenta milling experiments performed in section 6.2.

Figure 7.15 show the predictions for all of the spectra accumulated during large scale monitoring of 7 200 kg scale magenta pigment dispersion milling experiments. Considering the first three experiments, where the concentration of pigment dispersion is around 27 % w/w, there is a large offset for experiment 10033 (blue line) in comparison to the green and red trends (experiments 10034 and 10035, respectively), mirroring the untreated NIR spectral data. It is suggested that the removal and replacement of the NIR probe and the resulting disturbance to the optical fibres contributed to an offset between the NIR spectra acquired for experiment 10033 in comparison to the milling pigment dispersion experiments of similar formulation (experiments 10034 and 10035). Predictions for experiments 10034 and 10035 are closer to the measured particle size than experiment 10033 although caution must be used when interpreting the results as the calibration data set does not cover the same range of concentrations as the large scale milling data.

Pigment dispersion experiments 10069 – 10073 contain around 22 % w/w pigment dispersion for all. Experiment 10069 has an erratic particle size trend owing to the problems encountered through the milling process (inconsistent flow rates due to blockages before the dispersion reaches the probe port). However, experiments 10070 to 10073 display very similar particle size reduction trends although it is noted that the predicted particle size is much higher than the measured particle size information.

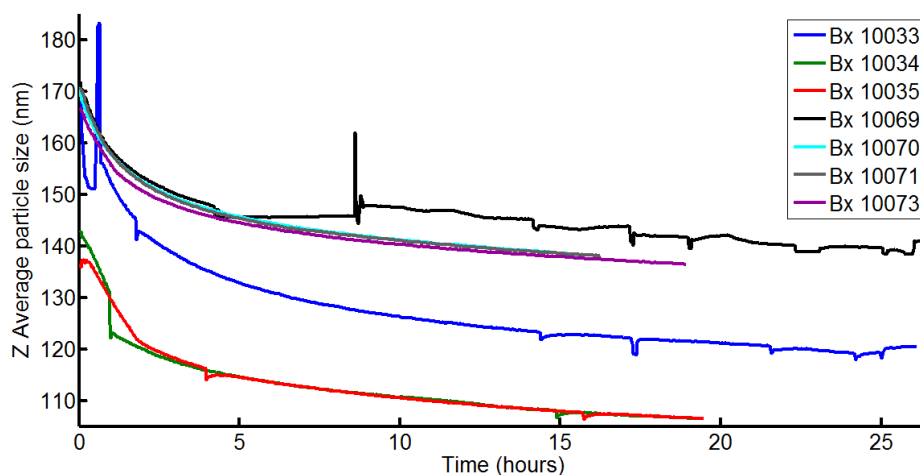


Figure 7.15 – Univariate prediction of particle size versus milling time for magenta pigment dispersions which were milled on the 200 kg scale.

Table 7.7 shows the actual particle size (measured by DLS) and the predicted particle size.

Table 7.7 – Measured and predicted pigment dispersion particle size data from large scale milling experiments. The predictive univariate model was constructed using ~1 kg milling experiments of magenta pigment dispersions (section 6.4).

Experiment	Time (hours)	Measured Z-average particle size (nm)	Predicted Z-average particle size (nm)
10033	15	128.4	122.7
	20	126.6	121.1
	25	126.0	118.2
	26	126.0	120.4
10034	15.6	114.1	107.7
10035	18	115.5	107.8
10069	N/A	N/A	N/A
10070	15	114.9	138.6
10071	16	114.2	138.1
10073	18	113.1	136.8
	18.9	111.1	136.4

The root mean square error of prediction (RMSEP) for the univariate model is 16.1 nm. Predicted particle sizes for experiments 10033, 10034 and 10035 are reasonably close to the measured particle size although there is an offset of approximately 7 nm. For the latter 2 experiments, the predicted particle size is shown to be reducing as milling progresses. The measured particle size at the two different time points for experiments 10034 and 10035 are very similar and the predicted values reflect this although there is still an offset between the predicted and actual particle sizes.

No particle size information was available for experiment 10069 but comparison of the actual versus predicted particle size information for experiments 10071, 10071 and 10073 shows that the univariate model overestimates the z-average particle size. Interestingly, the offset between the predicted and actual particle size is consistent between the 3 magenta pigment dispersion milling experiments. This may allow the use of trend analysis whereby the rate of change in the spectra could be used to determine the length of a milling rather than using a model to predict an absolute particle size. Both methods are potentially valid ways of controlling manufacturing

processes and providing information to either closed loop control systems or plant operators in control rooms.

7.2.3.3.2 Multivariate qualitative analysis

PLS models were constructed using the NIR spectra and corresponding particle size from each of the 7 milling experiments detailed in section 6.4. The construction of the PLS models was done as per section 6.5. The NIR dataset was trimmed, using the data points between 898 – 1598 nm. The effect of preprocessing the spectra was assessed by constructing models using first derivative spectra and untreated spectra. In each instance the x and y blocks were mean centred. The first derivative transformation was executed using the savgol function with a filter window of 11 data points, a second order polynomial. Cross validation of the PLS models was performed using random samples subset with 10 splits and 20 iterations.

Table 7.8 shows the predicted versus measured particle size information for each two PLS models constructed. The RMSEP (root mean square error of prediction) for a simple absorbance univariate model of particle size is 16.1 nm and a multivariate PLS model using untreated NIR spectra has an RMSEP of 41.1 nm. The best predictions are obtained using the PLS model constructed with 1st derivative NIR spectra, where the RMSEP is 7.9 nm. For the 1st derivative PLS model, the particle size is underestimated at higher concentration and overestimated at lower concentration.

Table 7.8 – Measured particle size data from large milling of pigment dispersions and the corresponding predictions of particle size using 2 multivariate calibration models.

Reference number	Time (hours)	Measured Z-average particle size (nm)	PLS prediction Z-average (nm) no pre-processing	PLS prediction Z-average (nm) 1st derivative
10033	15	128.4	151.6	125.5
	20	126.6	150.7	124.6
	25	126.0	148.0	121.5
	26	126.0	151.7	122.6
10034	15.6	114.1	131.8	118.0
10035	18	115.5	130.9	117.2
10069	N/A	N/A	N/A	N/A
10070	15	114.9	173.6	126.3
10071	16	114.2	173.5	125.7
10073	18	113.1	171.8	124.2
	18.9	111.1	171.5	124.1

The first derivative removes baseline offsets, which has both positive and negative effects that need to be kept in mind when constructing predictive models. Removal of baseline offsets can reduce the inter experiment variability caused by moving fibres and probes but the change in particle size is also manifested in the NIR spectra by a changing baseline offset. For pigment dispersion spectra, the magnitude of the baseline offset increases with increasing wavelength until absorption effects dominate the NIR spectra. Preprocessing the NIR spectra may improve the predictive ability of a model but over processing, by using techniques such as the second derivative may remove too much particle size information. A second derivative transform will remove a sloping baseline offset which may further remove the particle size information encoded in the NIR spectra.

7.2.3.4 Large scale cyan milling data

NIR reflectance spectra were collected at 2 minute intervals for the milling of 6 cyan pigment dispersion experiments (Table 7.9). For some of the experiments, the milling process did not reduce the particle size which provided an interesting opportunity to investigate whether on-line NIR measurements could be used to determine when millings had effectively "stalled".

Table 7.9 – Pigment concentration, polymer loading and milling time for 6 large scale milling experiments monitored using in-situ NIR reflectance measurements.

Experiment	Reference Number	Pigment Concentration (% w/w)	Polymer Loading (%)	Milling time (hours)
Cyan 1	10109	18.70	30	48.2
Cyan 2	10110	19.16	30	31.4
Cyan 3	10112	17.21	30	29.2
Cyan 4	10117	19.80	30	26.0
Cyan 5	10118	19.14	30	60.1
Cyan 6	10119	19.08	30	45.0

7.2.3.4.1 Cyan millings I

Samples of cyan pigment dispersion experiments 10109 and 10110 were removed at different stages of the milling process and analysed using off-line by dynamic light scattering and accuser. The accuser data is used to monitor the number of oversized particles and returns the number of particles above 500 μm in diameter at 1 % w/w concentration of pigment dispersion. Figure 7.16 shows the NIR absorbance value at 1220 nm, Z-average particle size and accuser results for cyan pigment dispersion, Experiment number 10109.

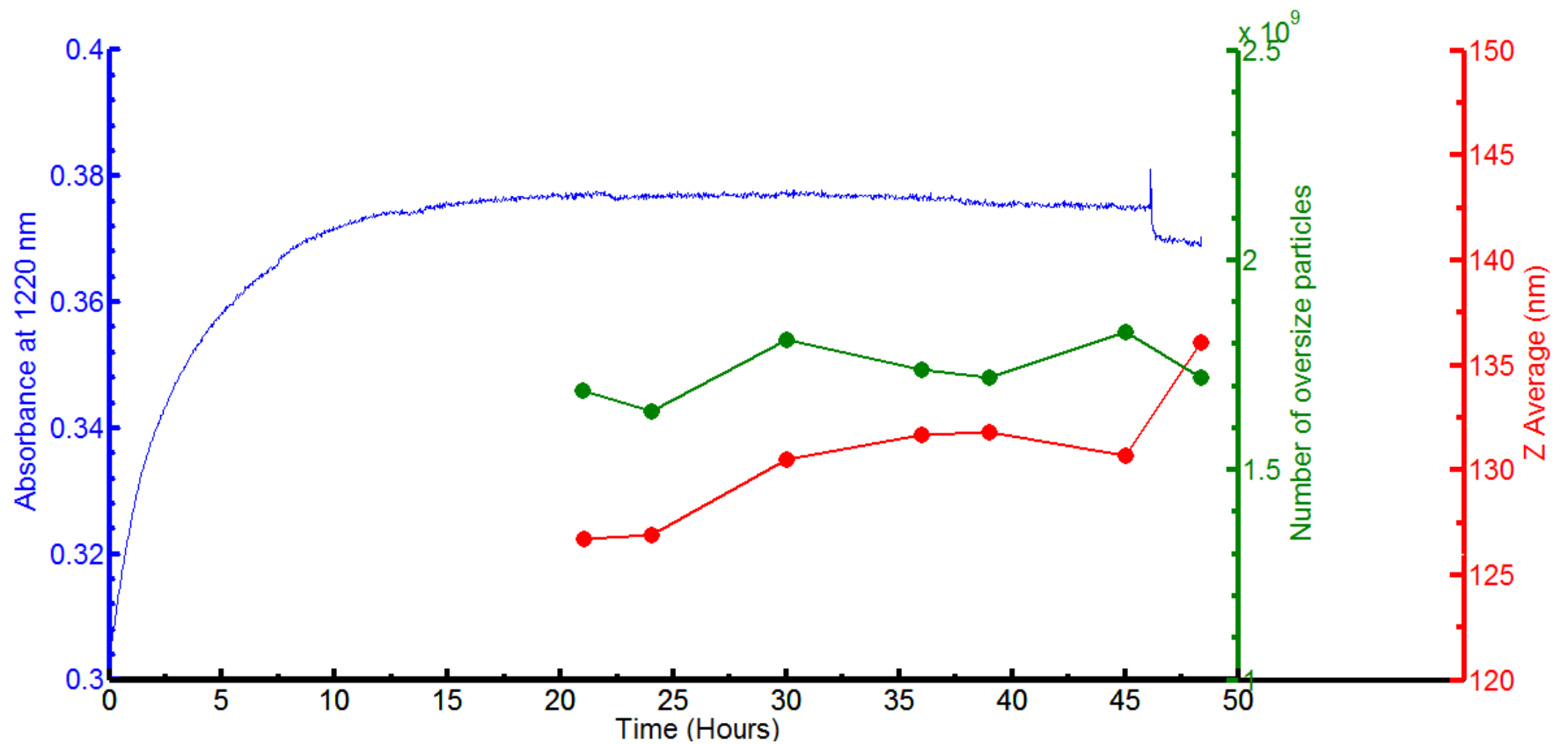


Figure 7.16 – Bx10109 milling data showing the NIR absorbance at 1220 nm, Z-average particle size (measured by DLS) and number of oversize particles measured by accuser.

For experiment 10109, the milling has stalled after 20 hours. The term stalled means that despite continued milling the particle size has stopped decreasing. There are a number of possibilities which may cause this to happen. Firstly, the high concentration of stabilised pigment dispersion is sterically jammed, causing smaller particles to aggregate and producing loosely bound floccules of pigment. Another possibility relates to the sample's viscosity. The sample's viscosity may have changed during the initial particle size reduction, such that, the kinetic energy from rapidly agitated beads in the milling chamber is not efficiently transferred to the dispersion, which provides the force to break up the pigment particulates. Another possibility is that the beads in the milling chamber may have degraded through heavy use which will cause the beads to fracture. Determining the root cause of stalled millings is not the primary focus of the work presented here but the ability to detect when such an instance has occurred during is potentially valuable.

Previous work has shown that the absorbance, across all of the NIR spectra, increases with decreasing particle size and no small scale experiment is able to mimic the reverse process of particle growth for the pigment dispersions. The Z-average for experiment 10109 shows the particle size effectively increases between 20 and 45 hours and the NIR trend changes direction, showing a small decrease in absorption over the same period. The step change in the NIR absorbance after 45 hours is caused by the dilution of the pigment dispersion by water. Ignoring the step change, the absorbance continues to drop with additional milling and the Z average particle size further increases. The milling process is expensive and a measurement that can tell operators that milling has reached a limit would allow more informed decision making for the subsequent processing steps. For example, instead of continued milling when the process has plateaued, a filtration step could be used to remove some of the larger pigment particles before passing to the next phase of processing. This would free additional time on the equipment and reduce energy costs.

Figure 7.17 shows the following experiment (reference number 10110) which had the same formulation and was processed in the same way. For this experiment, samples were removed earlier in the milling cycle to avoid lengthy and unnecessary milling.

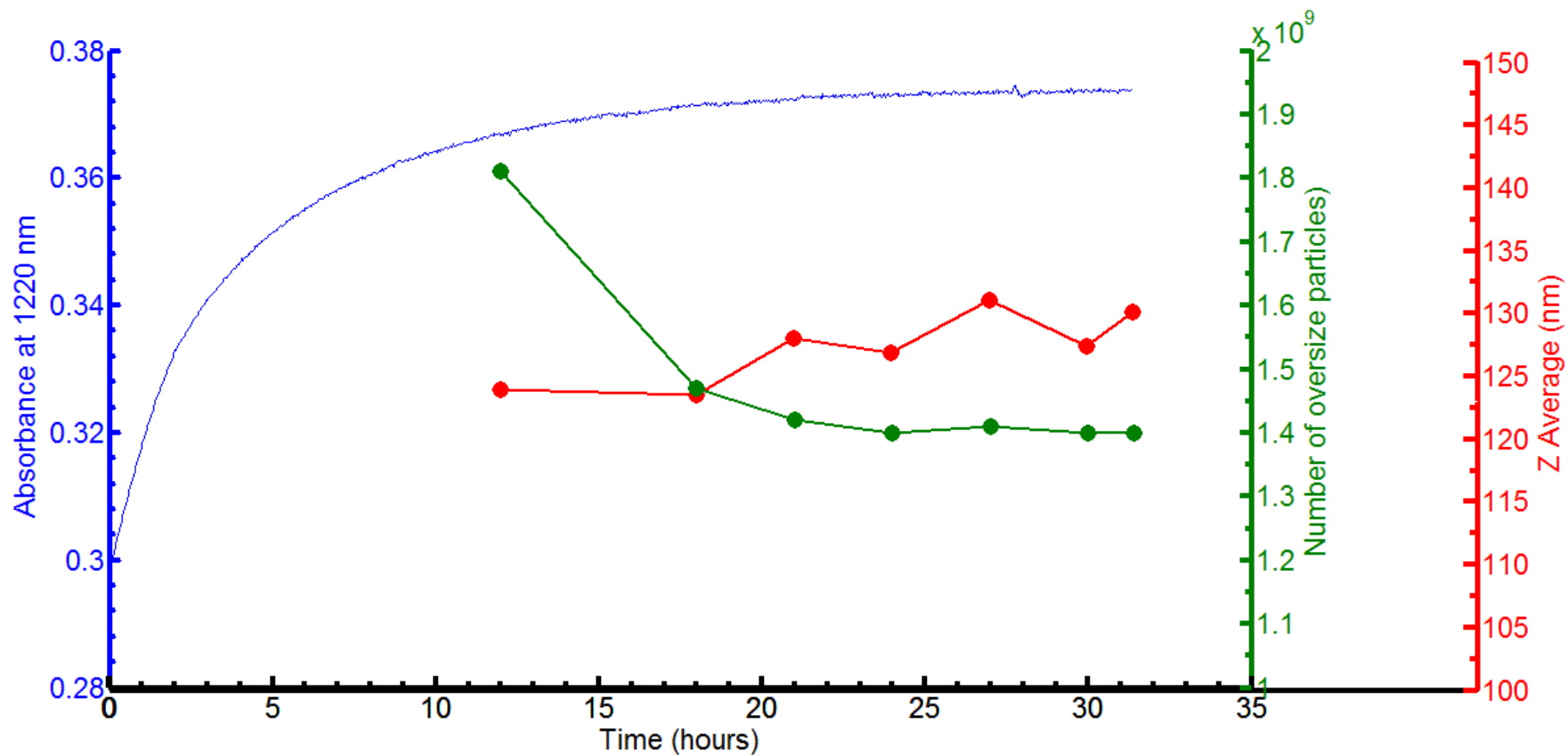


Figure 7.17 – Experiment reference no. 10110 milling data showing the NIR absorbance at 1220 nm, Z-average particle size (measured by DLS) and number of oversized particles measured by accuser.

The rate of change of the absorbance at 1220 nm decreases with time and the off-line z-average particle size appears to increase although there is a larger spread of particle sizes. By approximately 30 hours the absorbance of the pigment dispersion is no longer changing, indicating that further milling will not be effective to reduce the particle size. From this it is concluded that visually comparing absorbance trends at 1220 nm will allow an operator to see when milling is no longer effective at reducing the particle size of the cyan pigment dispersion.

7.2.3.4.2 Cyan millings II

A further four cyan pigment dispersion experiments were monitored using NIR during the milling process. Figure 7.18 shows the absorbance trend at 1220 nm for cyan pigment dispersion experiments 10112, 10117, 10118 and 10119 and the end point particle size data for 3 of the four experiments. No reference data was available for experiment 10117.

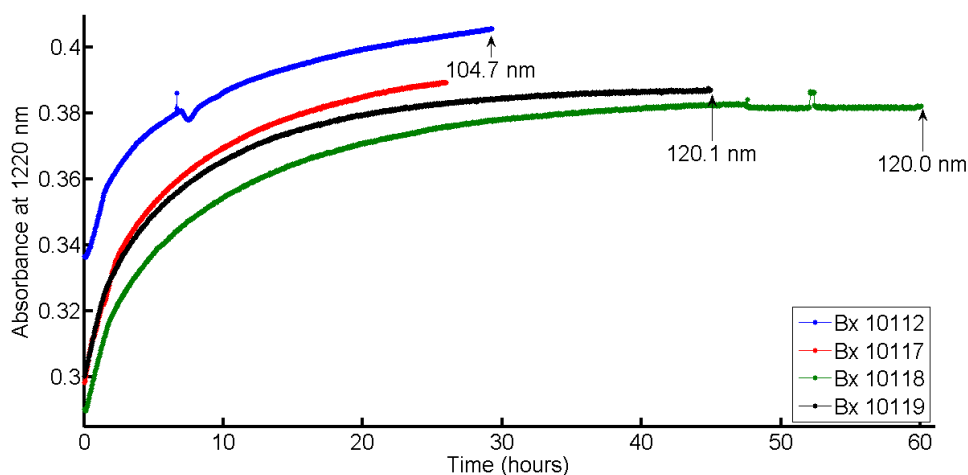


Figure 7.18 – Absorbance at 1220 nm versus milling time for 4 experiments of cyan pigment dispersion milled on the 200 kg scale.

The blue trend in Figure 7.18 (experiment 10112) was collected during the milling of a 17% w/w cyan pigment in dispersion whereas the other three experiments were

approximately 19 % w/w pigment in dispersion. The NIR data contains a discontinuity at around 9 hours that cannot be easily assigned to any specific event.

NIR absorbance decreases with decreasing concentration but the resulting particle size of the dispersion is smaller than the other experiments. The starting point of the blue trend is higher than the higher concentration experiments and this may be attributed to the pre-mix before the pigment dispersion is introduced to the mill. It is surmised that high shear mixing of a lower concentration (hence, viscosity) pigment dispersion has resulted in a more efficient breakup of the particulates in the premix step which has left less work for the mill to do. Figure 7.19 shows the relative change in absorbance at 1220 nm from the commencement of milling for the same four pigment dispersions. The blue trend shows that there is less change observed during the course of milling experiment 10112.

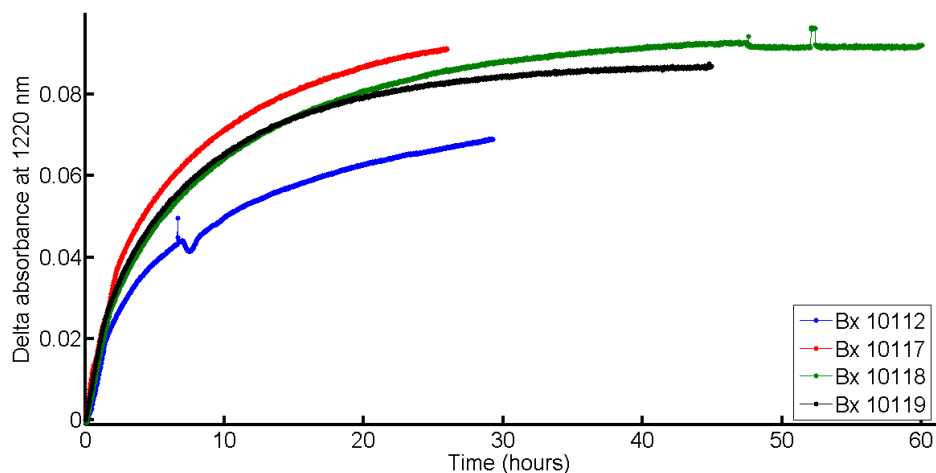


Figure 7.19 – Relative change in absorption at 1220 nm for 4 experiments of cyan pigment dispersion milled on the 200 kg scale.

Experiment 10118 shows an interesting trend after some water was added to the mill contents. The NIR data shows that the pigment dispersion is no longer changing with continued milling. Offline particle size measurements of in-process samples show that the Z-average particle size is no longer affected by continued milling. Figure 7.20 show the particle size and NIR absorbance at 1220 nm for the last 18 hours of milling for experiment 10118. The figure shows a step change in the NIR data

around 47 hours which corresponds to the addition of water to the pigment dispersion. The experiment is then milled with no decrease in the Z average particle size over the following 6 hours. The discontinuity in the NIR data at 52 hours is a result of the mill being restarted. The pigment dispersion was milled for a further 6 hours after the last sampling point and no significant change was observed in the NIR spectra. It is noted that the number of particles larger than 0.5 μm measured by accuser mirrored the DLS measurement of Z-average particle size.

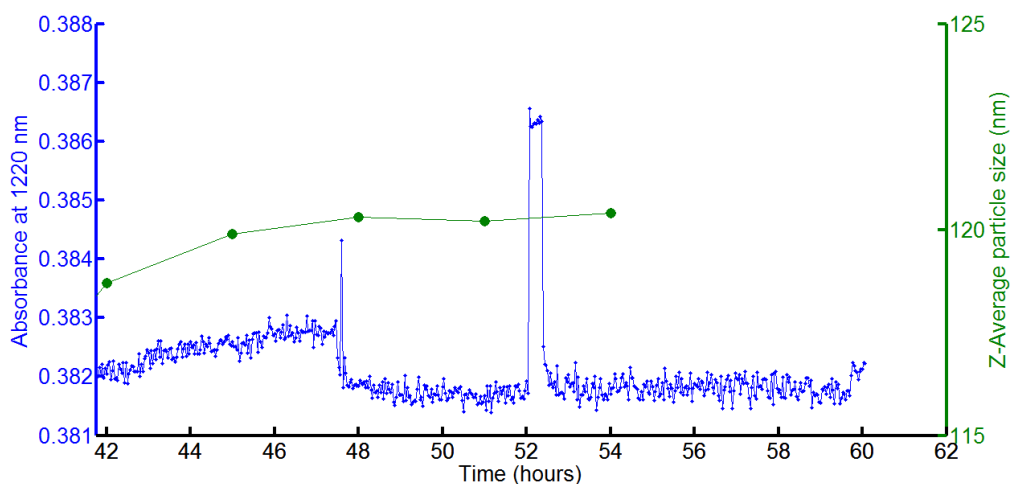


Figure 7.20 – NIR absorbance at 1220 nm and Z-average particle size for the milling of cyan pigment dispersion experiment 10118.

7.2.3.5 Yellow milling data

Six, 200 kg scale, yellow pigment dispersion milling experiments were monitored using NIR measurements as per the magenta and cyan experiments discussed previously. Table 7.10 contains the experimental information.

Table 7.10 - Pigment concentration, polymer loading and milling time for 6 yellow pigment dispersions milled on the 200 kg scale and monitored using in situ NIR reflectance measurements.

Experiment	Reference number	Pigment Concentration (% w/w)	Polymer Loading (%)	Milling time (hours)
Yellow 1	10075	21.58	50	69.8
Yellow 2	10076	21.58	50	80.1
Yellow 3	10078	21.59	50	82.3
Yellow 4	10079	21.58	50	79.8
Yellow 5	10081	21.59	50	93.6
Yellow 6	10108	21.59	50	63.2

Figure 7.22 shows the changing absorbance at 1220 nm for each experiment. From experience, the milling of yellow pigment dispersions takes the longest of all pigments used. The first 5 yellow pigment dispersion experiments were milled consecutively and the last experiment was milled a few weeks later. The particle size information (Figure 7.21) shows the last experiment (number 10108) has a significantly smaller particle size than the other 5 experiments and this is reflected in a higher absorbance.

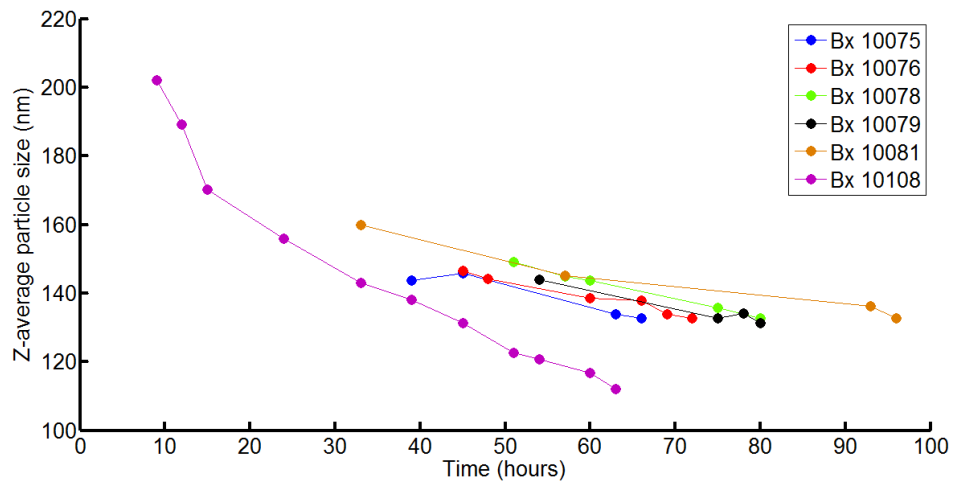


Figure 7.21 – Z-average particle size data collected by DLS for large scale yellow pigment dispersion millings.

It is not clear what changes experimental conditions have altered the particle size reduction profile but altering the premix stage may be responsible. The fact that the NIR measurements show that the experiment is significantly different from the other 5 milling experiments and the absorbance reflects a much smaller particle size reinforces the belief that NIR measurements are a good indicator of particle size. To remove the offset between the 6 data sets, change in absorption at 1220 nm was calculated using the fifth spectrum collected in each experiment as the reference point (Figure 7.23). The fifth spectrum was chosen as the first few spectra collected during each milling experiment showed a characteristic rise and drop as the flow of dispersion stabilises when milling begins.

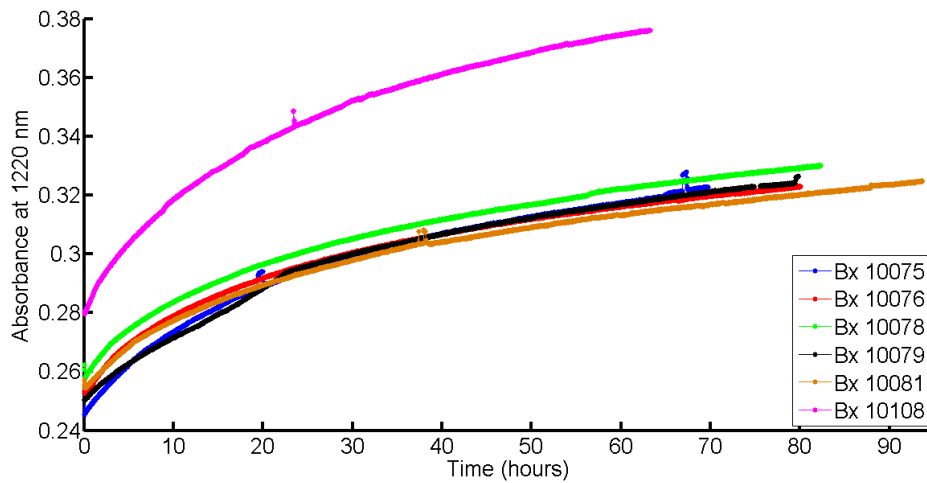


Figure 7.22 - Absorbance at 1220 nm versus milling time for 6 yellow pigment dispersion experiments milled on the 200 kg scale.

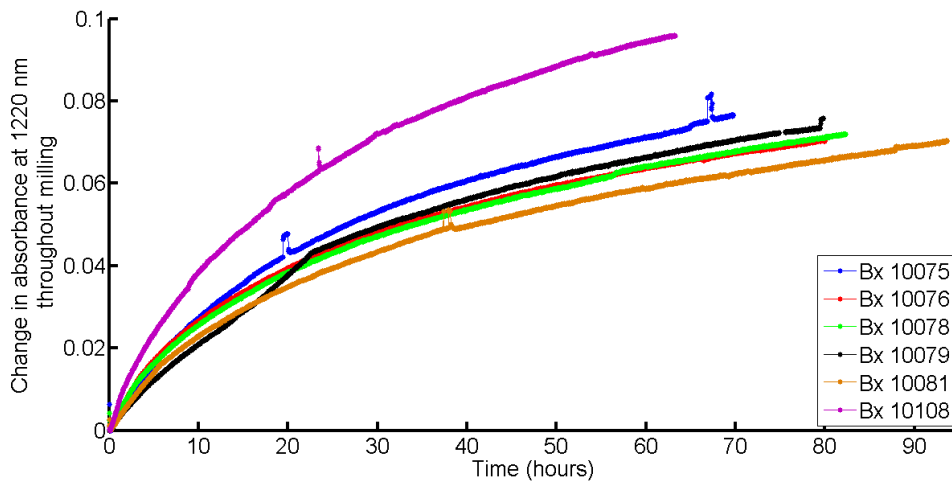


Figure 7.23 – Relative change in the absorption at 1220 nm observed for 6 yellow milling experiments

The 6 experiments were well characterised at various stages of the milling process. Figure 7.24 shows the particle size versus change in absorbance for all 6 experiments. There is a general trend whereby, as the particle size decreases, the absorbance increases.

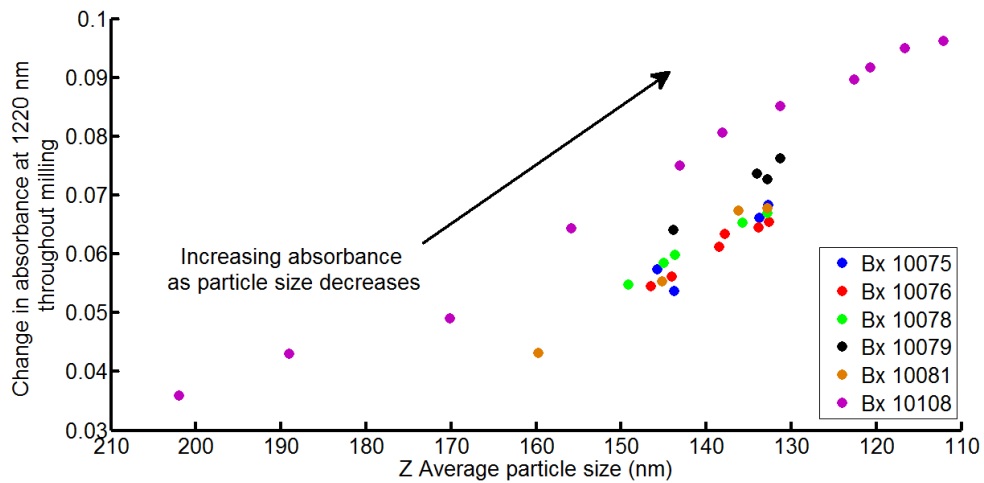


Figure 7.24 – Change in absorbance versus particle size for the milling of 6 yellow pigment dispersions.

The changing absorbance at 1220 nm is a good indicator of particle size and millings which were performed consecutively show a high level of consistency in the NIR data. The offset observed in the NIR spectra of the last experiment of yellow pigment dispersion may be a result of different processing before the dispersion is introduced to the mill or a result of the optical fibres being moved. By removing the offset, it is observed that the NIR spectra change at a faster rate and the higher absorbance indicates that the particle size is significantly smaller in experiment 10108 in comparison to the other 5 experiments. This is confirmed by the off-line particle size information.

7.2.3.6 Black milling data

The milling of four black pigment dispersions was monitored as the NIR was semi-permanently installed on the large scale milling equipment and set to collect spectra every 2 minutes. Table 7.11 details the pigment and polymer concentrations. The pigment used for the black colour is called carbon black. It is an amorphous form of carbon and is typically generated in a furnace which produces a fluffy black powder that is difficult to handle.

Table 7.11 - Pigment concentration, polymer loading and milling time for 4 black pigment dispersions milled on the 200 kg scale and monitored using in situ NIR reflectance measurements.

Experiment	Reference number	Pigment Concentration (% w/w)	Polymer Loading (%)	Milling time (hours)
Black 1	10114	15.44	40	17.1
Black 2	10115	17.42	40	17.7
Black 3	10121	17.99	40	16.4
Black 4	10122	19.15	40	16.8

The black pigment absorbs all of the NIR radiation but as the probe is contained in a sleeve there is some reflection at the boundary of the sapphire window whilst the remaining portion of the light penetrated in to the sample. The NIR spectra do not show the typical absorption features, arising from C-H and O-H groups, as were observed with the cyan, magenta and yellow pigments.

Figure 7.26 shows the change in absorption at 1220 nm for each of the four cyan pigment dispersion experiments. The change in the spectra is much smaller than the change observed for the other pigments analysed.

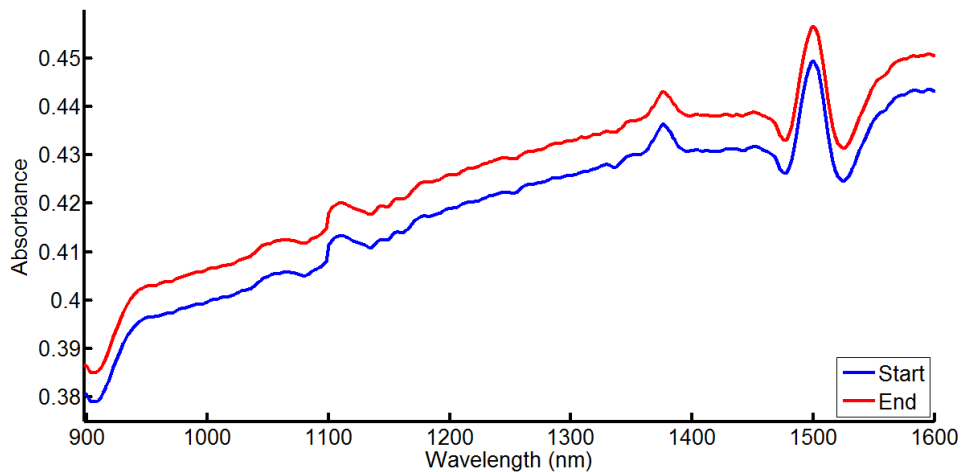


Figure 7.25 – NIR spectra captured at the start and end of black pigment dispersion milling (experiment number 10114).

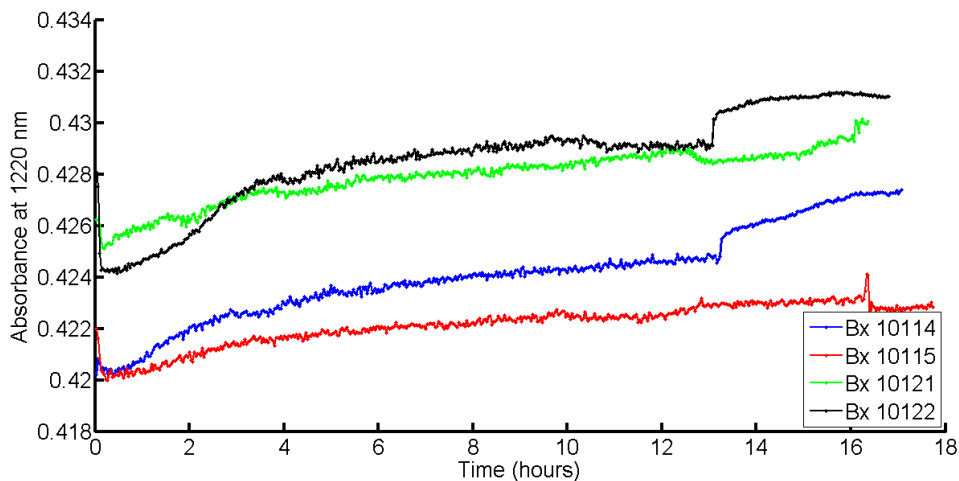


Figure 7.26 – Absorbance at 1220 nm throughout the large scale milling of 4 black pigment dispersions.

Step changes in that absorbance at 1220 nm are observed for experiment 10114 and experiment 10122 is observed at 13 hours which correspond to dilution of the dispersion. Comparison of the temperature and end point particle size showed no clear correlation with absorbance. NIR is not a suitable method for following the particle size reduction of black pigment dispersions because of the high absorption across the NIR region. It would be possible to use the NIR spectra as a confirmatory check to determine the colour of pigment being milled due to the characteristic

featureless spectrum. This would only be useful if the process was controlled remotely and visual inspection of the pigment was not possible.

7.3 Conclusions

The milling of cyan, magenta, yellow and black pigment dispersions has been monitored on the 200 kg scale and the spectra obtained can be used to follow the particle size reduction for all except the black pigment. The NIR spectrometer is a post dispersive scanning grating monochromator which scans the wavelength range sequentially and it is estimated that the wavelength range 700 – 1300 nm represents approximately 374 mL (approximately 0.19 % of the total experiment volume).

Milling can be monitored quantitatively by building multivariate or univariate models. For quantitative analysis, univariate and multivariate models were developed from <1 kg scale magenta milling experiments. Predictions from the models showed that the best predictions were obtained with a multivariate PLS model where the NIR spectra were transformed to the first derivative. The first derivative transform removed some of the baseline offsets between experimental data which showed some variability due to the different alignment of the optical fibres between days.

For qualitative analysis, the change in absorbance at 1220 nm is a good indicator of milling progress for cyan, magenta and yellow pigment dispersions. Stalled millings, where the particle size stopped decreasing or increased, were monitored for the cyan pigment dispersion. The absorbance trends showed no increase where the particle size reduction was "stalled". The absorbance profiles at 1220 nm could also be used to indicate when there is a fault in the mill. In one instance, the heat exchanger blocked which affected the recirculation around the mill. The trend in the absorbance at 1220 nm shows several step changes throughout the milling and the data does not exhibit a smooth, gradual change in.

The temperature effect on NIR spectra was assumed to be negligible. Milling of pigment dispersions which were performed over different days meant that the dispersion cooled down overnight or over the weekend. On resumption of the milling, the NIR trends at 1220 nm continued uninterrupted. Large scale milling

showed very little change in the temperature of the pigment dispersion at the NIR probe.

To rule out spectrometer drift, several experiments were monitored consecutively with no intervention to the NIR instrument or probe. In each case, the NIR spectra showed a sharp change to lower absorption when un-milled material was introduced.

NIR has been shown as a suitable method for measuring the milling process of high concentration aqueous based pigment dispersions. Both quantitative and qualitative information can be used to observe the milling process. The benefits of using either methodology are that timely measurement of the particle size or change in the particle size will:

- Reduce labour intensive off-line testing required.
- Enable real-time feedback for trouble shooting.
- Reduce the energy costs associated with particle size reduction.
- Increased capacity.
- Avoid over -processing, resulting in less scrappage.

8. Raman spectroscopy

A preliminary investigation into the suitability of Raman spectroscopy for monitoring pigment dispersion milling in chapter 4 showed there was a correlation between the milling time (and particle size reduction) and a change in the Raman spectra for yellow pigment dispersions. The application of Raman spectroscopy for in-situ measurements of pigment dispersions is not an obvious one because of the likelihood of sample fluorescence although several papers detail the elucidation of pigments present in ancient artifacts and paintings using Raman¹⁻⁴. Common problems encountered include localised sample heating, leading to sample damage, and fluorescence from either the analyte or impurities which may be more intense than the Raman scattered photons. The increased specificity of Raman spectrometry and the low sensitivity to water means that well resolved spectra of complex aqueous mixtures can be obtained. Building on the investigation in chapter 4, this chapter aims to:

1. Explore options for overcoming the fluorescence problem for the magenta pigment.
2. Estimate the penetration depth of the Raman PhAT probe system.
3. Assess the non-contact PhAT probe Raman instrument for monitoring the milling process for pigment dispersions in the lab scale.

8.1 Individual component spectra

Raman spectra of all the components in the pigment dispersions (pigment powders, stabilising polymer and dipropylene glycol) were obtained to identify which parts of the Raman spectra of pigment dispersions were attributed to the dispersed pigment particles.

8.1.1 785 nm Excitation

Raman spectra were collected using the Kaiser Rxn 1 spectrometer and PhAT probe as detailed in section 3.4.2. The collection time and number of accumulations were optimised for each sample analysed and the details are given in the table below. A sample of dipropylene glycol (DPG) was analysed at a later date using the University of Strathclyde Kaiser Rxn 1 Raman spectrometer complete with the Mark II probe head with non-contact optic as the PhAT probe Raman system was returned to Clairat Scientific. Both spectrometers use a 785 nm source and thermoelectrically cooled CCD detectors. The non-contact Mark II probe has a smaller spot size (approximately 80 μm) than the PhAT probe (6 mm).

Table 8.1 – Raman probe, acquisition time and number of accumulations used to collect spectra of neat components present in pigment dispersions

Material	Raman Probe	Acquisition time (seconds)	Accumulations	Figure
Yellow pigment powder	PhAT	16	2	Figure 8.1
Cyan pigment powder	PhAT	60	2	Figure 8.1
Acid 46 polymer	PhAT	15	4	Figure 8.2
DPG	Mark II with non-contact optic	20	1	Figure 8.2

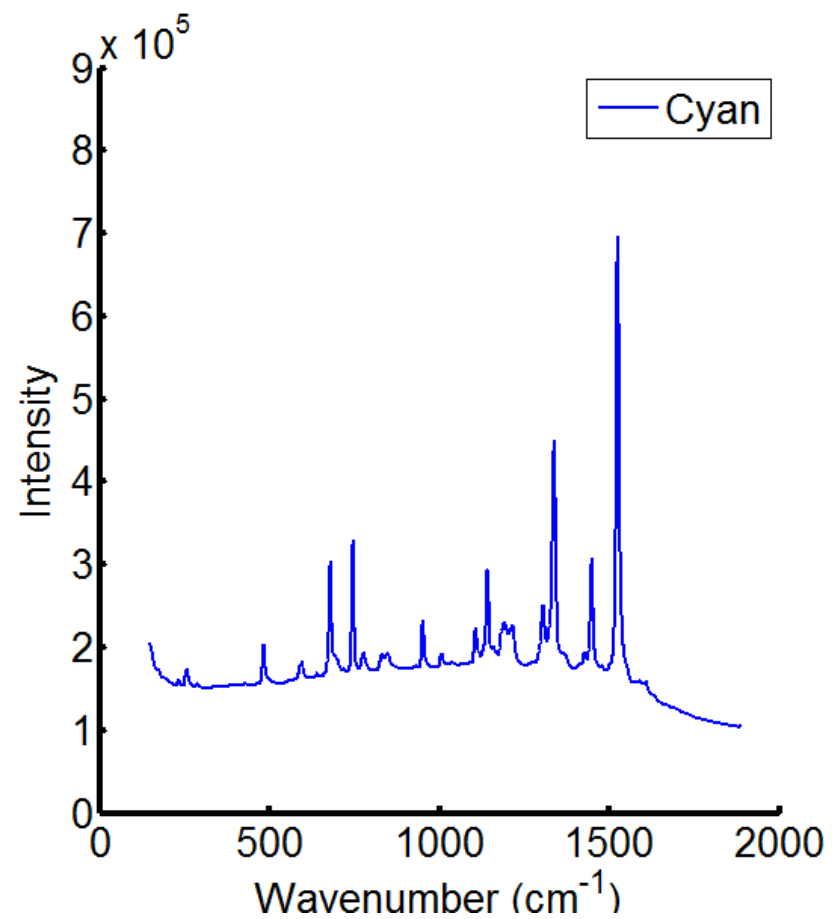
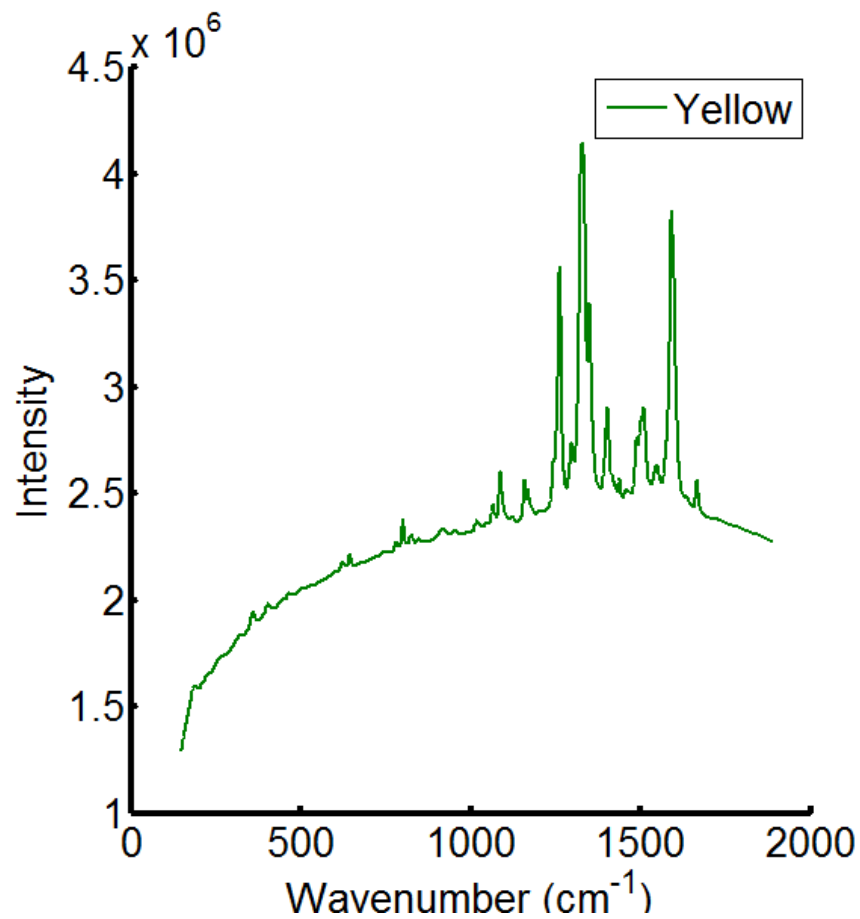


Figure 8.1 – 785 nm Raman PhAT probe spectra of yellow and cyan pigment powder (as detailed in Table 8.1).

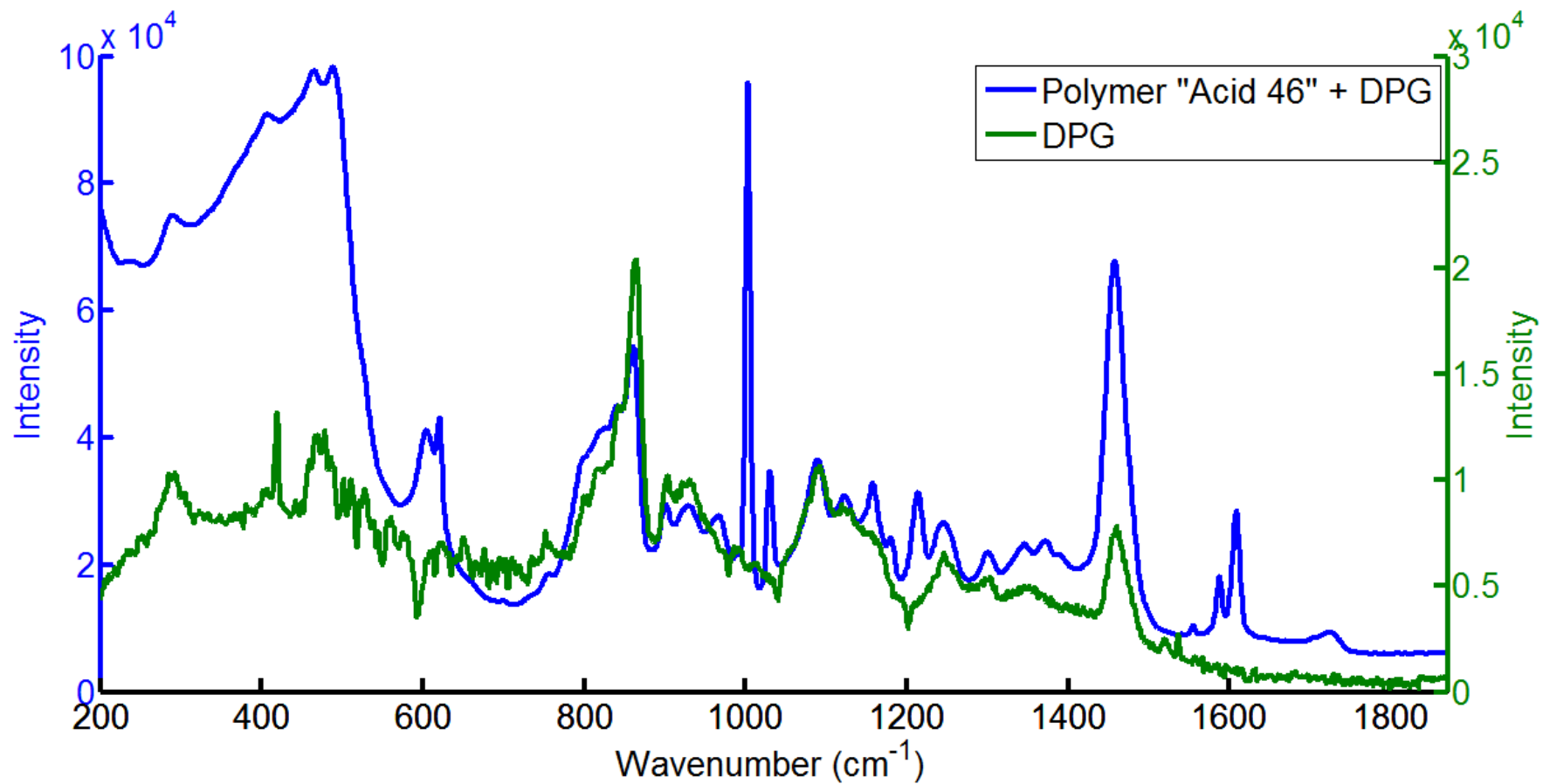


Figure 8.2 – 785 nm Raman spectra of polymer "Acid 46" and dipropylene glycol collected using the Raman PhAT probe system and Mark II non-contact probe head respectively.

Table 8.2 details the major band assignments for the raw materials used to prepare the cyan and yellow pigment dispersions.

Table 8.2 – Raman band assignments

Material	Wavenumber (cm⁻¹)	Assignment
Yellow (PY74 aka Irgallite yellow)	1667 (w)	Amide
	1592 (s)	Aromatic ring vibration
	1403 (m)	CH ₃
	1351 (s)	Aromatic azo
	1330 (vs)	Aromatic nitro
	1263 (s)	Amide
Cyan (PB15:4 aka Copper II phthalocyanine)	1525 (vs)	See Below
	1449 (s)	
	1338 (s)	
	1140 (m)	
	952 (m)	
	747 (s)	
Dipropylene glycol	1470 (m)	CH ₂ , CH ₃
	860 (m)	C-C aliphatic chains
Acid 46 polymer + DPG	1603 (w)	Aromatic C-C
	1003 (vs)	Monosubstituted benzene

Empirical band assignments for the copper phthalocyanine are somewhat less useful. At 785 nm resonance Raman is achieved as the energy of the incoming excitation wavelength is absorbed, promoting an electron from the highest occupied molecular orbital to the lowest unoccupied molecular orbital and in to one of a number of higher vibronic bands. Resonance Raman provides selective band enhancements, increasing the number of Raman scattered photons which allows detection and quantification at lower concentrations. Because copper phthalocyanine is a large structure, the spectra are very complex. The vibrational spectra arise from the multitude of C-C, C-H and C-N bonds present in the species and Basova et al⁵ and Tackley et al^{6, 7} have published an experimental and theoretical investigation which assigned the significant bands of the Raman spectra.

Raman spectra provide sharper, well defined peaks which are easily assignable to the functional groups present in an analyte and it was suspected that the pigment and polymer could be followed separately throughout milling. There is a distinct peak

from the monosubstituted benzene group present in the Acid 46 polymer that can be observed in the Raman spectrum of the polymer but at the concentrations used to prepare pigment dispersions the peak is no longer visible. The formulations of the pigment dispersions prepared in this chapter follow guidance from FFIC on what polymer loading provide the most stable dispersions. An attempt was made to observe the polymer peak by increasing the polymer loading to 100% for one yellow pigment dispersion. This made the polymer difficult to prepare and mill due to an increase in the sample viscosity. The high polymer loading also affected the sample stability. A 10 hour milling experiment was split over 2 days and measured using the PhAT probe. The spectra collected show that the trend did not pick up from the last point of the previous days milling, instead resetting to the first value observed on day one and repeating the trend. It is suspected that at high polymer loading the pigment particles agglomerate to form floccules over time. These floccules are loosely bound and can be broken up by vigorous agitation or further milling. The particle size did not show any increase in the particle size from the end of milling on day one to the commencement of milling on day 2 but the flocculates are loosely bound together and the dilution step for DLS measurement may have shocked the floccules apart again. Hence, for the polymer Acid 46, Raman spectroscopy is not a suitable tool for characterisation during the development of pigment dispersions or on-line monitoring.

8.1.2 998 nm Excitation

Magenta pigment powder fluoresced when exposed to the 785 nm laser which meant that Raman spectrometry at this wavelength would not be a suitable technique for in process monitoring. An opportunity was provided by Clairet scientific (Northampton, UK) to analyse cyan, magenta and yellow pigment dispersions using a 998 nm excitation Kaiser Raman spectrometer RXN 2. Samples of pigment dispersions, generated from lab milling experiments and stored in glass vials, were analysed. In each case, the pigment dispersions selected were close to the end of milling. Table 8.3 contains the sample information of the pigment dispersions analysed using the longer wavelength of excitation and Figure 8.3 shows each of the spectra.

Table 8.3 – Pigment dispersions analysed using a 998 nm excitation Raman spectrometer.

Sample	Details	Acquisition time (seconds)	Accumulations
Magenta pigment dispersion	20 % w/w Magenta PR122 with 40 % loading acid 46 polymer. Sample milled for 5 hours.	10	5
Cyan pigment dispersion	20 % w/w Cyan with 60% loading acid 46 polymer. Sample milled for 1 hour.	1	20
Yellow pigment dispersion	14 % w/w yellow with 50 % loading acid 46 polymer. Sample milled for 5 hours.	10	2

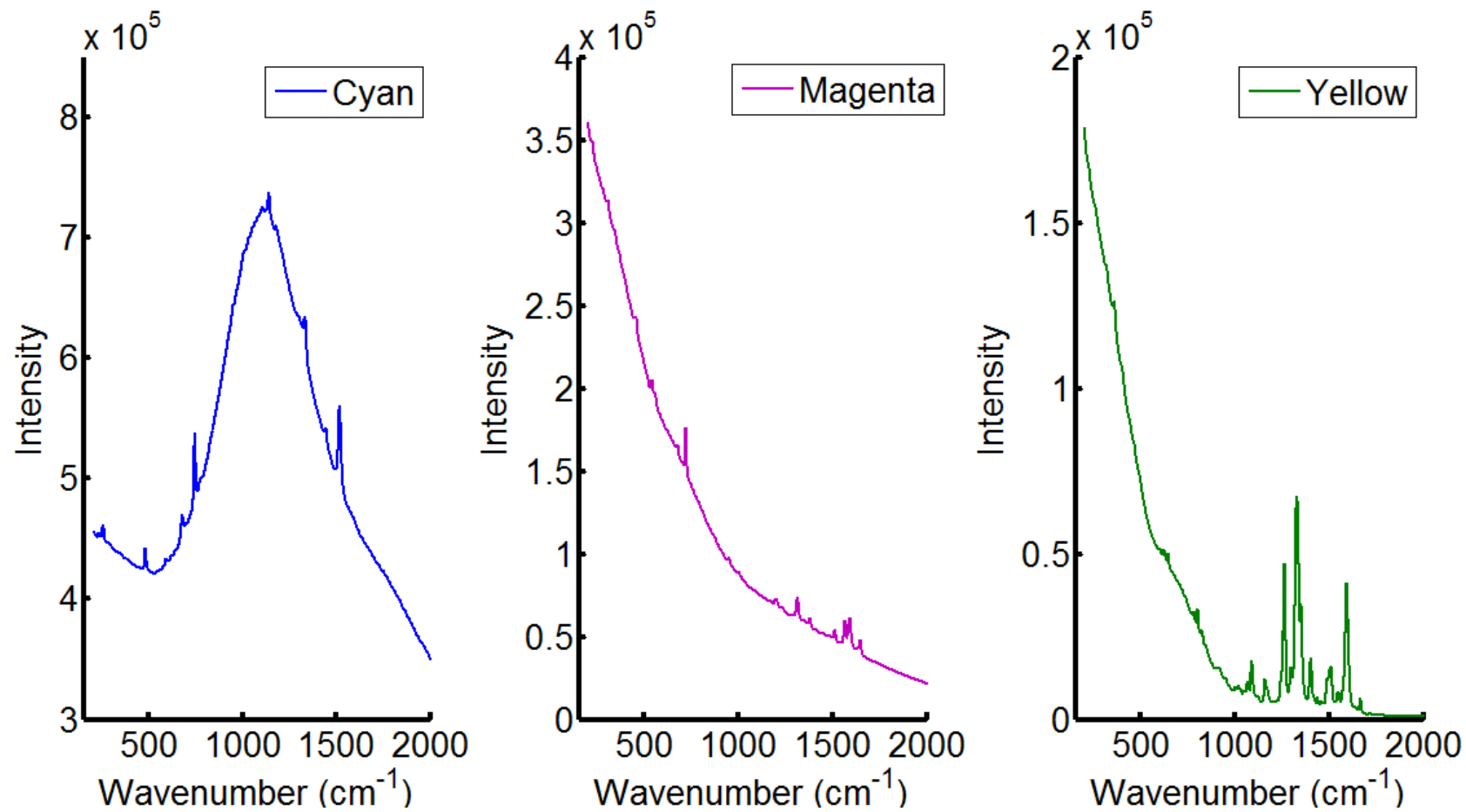


Figure 8.3 – 998 nm Excitation Raman spectra of magenta, cyan and yellow pigment dispersions.

The cyan pigment dispersion sample does not provide good Raman spectra in this instance. This may be attributed to combination of the reduced Raman scattering efficiency at higher wavelengths and the sample was not stirred. Presentation of the sample to the Raman probe is important and will be discussed later.

Somewhat surprisingly, the PR122 pigment dispersion does contain some small bands which are clearly observed by transforming the spectra to the 1st derivative form. This was achieved using the Savitzky-Golay function in the PLS toolbox add in to Matlab. The transform used a filter width of 11 and a second order polynomial.

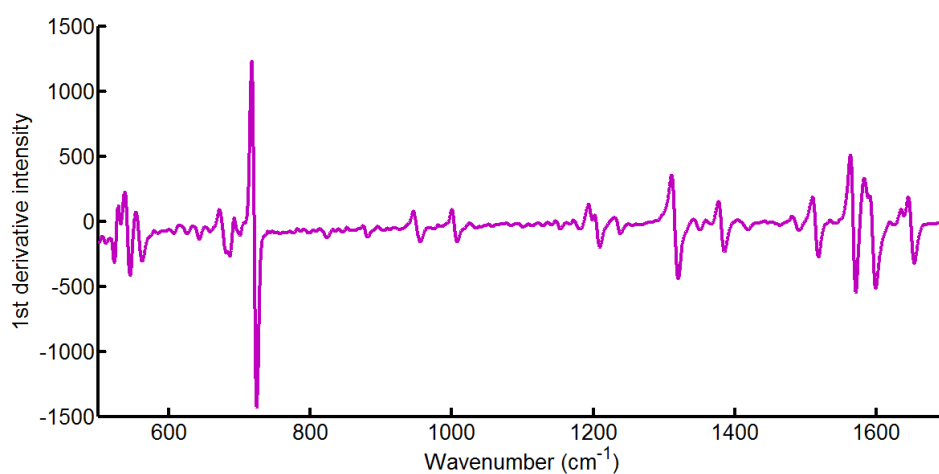


Figure 8.4 – 998 nm excitation, 1st derivative, Raman spectrum of magenta pigment dispersion.

The spectrum shows a large band that cannot be easily assigned at 720 cm^{-1} which is usually where C-S, C-Cl, or C-F bands would appear in the Raman spectrum. At $\sim 1330\text{ cm}^{-1}$ there are contributions from the methyl group and above 1500 cm^{-1} there are bands originating from the aromatic rings. This suggests that long wavelength Raman spectroscopy is a suitable technique for process monitoring of magenta pigment dispersions during development and manufacturing whereas 785 nm excitation Raman is not.

8.2 Penetration depth at 785 nm

The penetration depth of Raman scattering was assessed for the Kaiser Raman PhAT probe system. The larger spot size means more is measured for each Raman spectrum than conventional Raman probes which have spot diameters of around 80 μm . The larger area is especially useful in pharmaceutical applications such as powder blending where measuring a larger proportion of the batch allows greater confidence in determining when the powder blend has reach uniformity.

8.2.1 Experimental

An experiment was devised using a flower of sulphur disc which is a good Raman scatterer and contains a strong band at approximately 218 cm^{-1} which does not overlap with the Raman spectrum of yellow pigment dispersion.

A pigment dispersion containing 20 % w/w yellow with 50 % polymer loading of polymer Acid 46 was prepared and milled to generate fresh pigment samples of different particle size. Aliquots of dispersion were analysed extracted from 15 minutes, 30 minutes, 1 hour, 2 hours 4 hours and 6 hours in to the milling experiment and characterised using the Malvern HPPS5001 NIBS particle sizer. An additional sample of pre-milled pigment was retained and analysed by DLS and used in the Raman penetration depth experiment.

Each of the neat pigment samples generated from the milling was measured using the setup in Figure 8.5. The Raman PhAT probe was positioned 3 cm above a foiled surface in the sample compartment. A 10 mm diameter disc of compressed flowers of sulphur was immobilised on the foil surface directly under the beam from the Raman probe. A small flat bottomed glass container was filled with depths of pigment dispersion between 0.5, 1, 1.5, 2, 3 and 4 mm for each of the 6 samples generated from milling and the one sample of pre-milled material. The pigment depth was estimated by placing a dip stick in to the dispersion and measuring the length of the yellow stained area using a magnifying glass and a small steel rule. All measurements were performed in a darkened laboratory and the measurements were collected in the sample compartment accessory. Raman spectra were collected using 6 accumulations of 5 seconds.

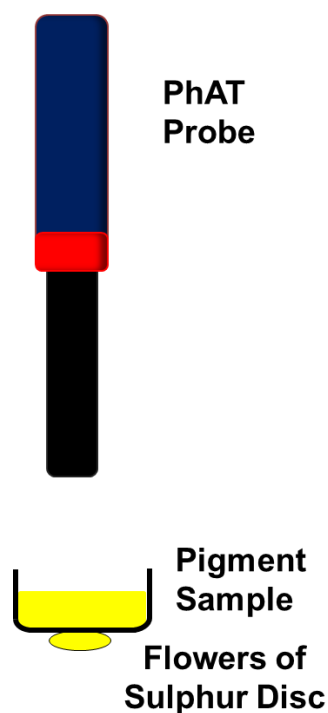


Figure 8.5- 785 nm excitation Raman photon penetration depth experimental set-up.

8.2.2 Results and discussion

The Raman spectra were transformed to the 1st derivative form using the Savitzky-Golay function in the PLS toolbox in Matlab. The transform used a filter width of 11 and a second order polynomial. Figure 8.6 shows the flower of sulphur disc collected with 0.5 mm pigment dispersion placed between the Raman probe and the sulphur disc for samples generated during by milling. The pre-milling sample is omitted as the DLS measurements were unable to define the particle size of the sample. Although the pigment dispersion is well mixed before being introduced to the mill, the sample retains a large number of oversize particles. These oversize particles tend to sediment in the diluted solution and DLS measurements are only possible when Brownian motion causes the movement of the pigment particulates. At smaller particle size the intensity of the Raman band from the sulphur disc is higher. Smaller particle have smaller scattering coefficients (as was discussed in the fundamental optical properties), hence, more of the Raman scattered light is available for

collection. In this instance the term scattering refers to the fundamental optical properties of the sample and not the phenomenon of Raman scattering.

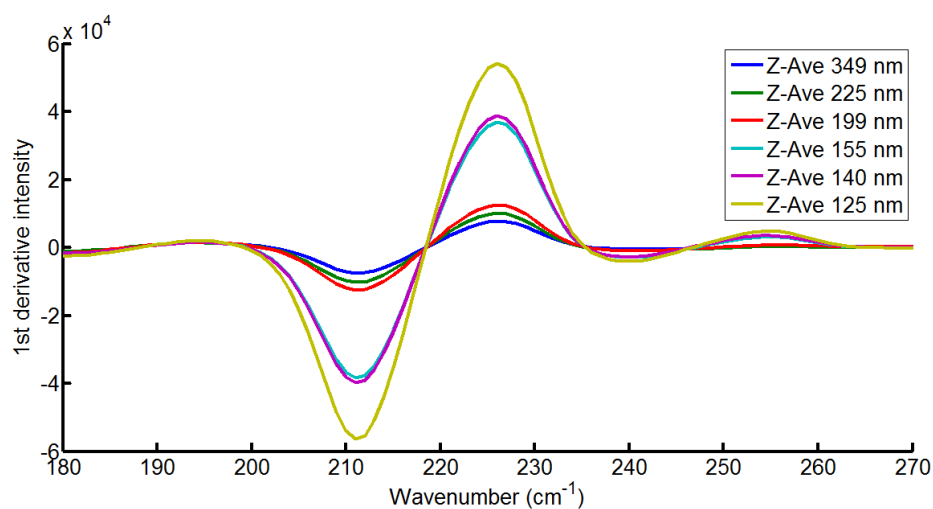


Figure 8.6 – 785 nm excitation, 1st derivative, flowers of sulphur disc signal obtained with 0.5 mm depth of yellow pigment dispersion placed between the Raman probe and sulphur disc. Each spectrum represents a different particle size of pigment dispersion.

Figure 8.7 shows the 1st derivative intensity of the sulphur signal for changing particle size and depths of pigment dispersion. The premix sample is included and the data point for 0.5 mm pigment dispersion depth is masked behind the data point showing the derivative intensity of the 199 nm sample at 0.5 mm depth. The particle size of the dispersion before milling covers a very broad range and contains some larger particulates that prevented the characterisation of the sample by DLS measurement.

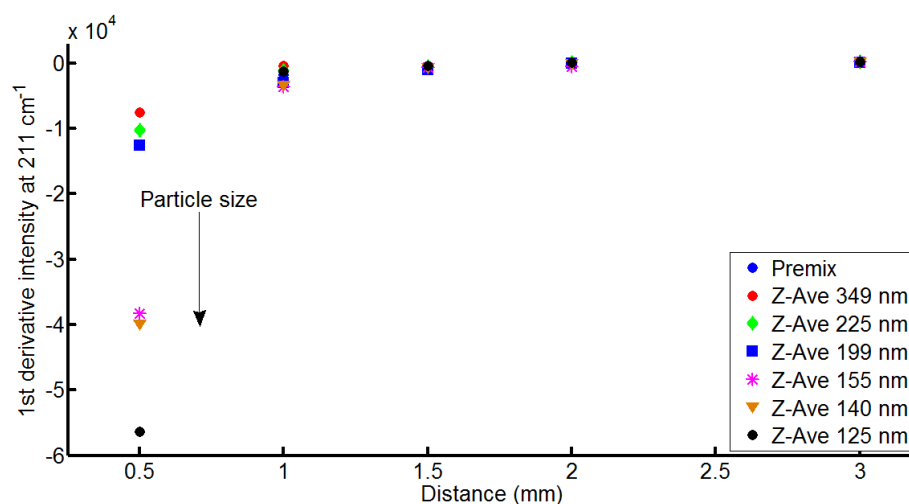


Figure 8.7 – 785 nm Raman excitation, 1st derivative intensity at 211 cm⁻¹ for the flowers of sulphur disc signal with different particle size pigment dispersion and differing depths of dispersion.

The signal stops changing where there is approximately 2 mm of pigment between the Raman PhAT probe and the sulphur disc and this is consistent for all the particle sizes of yellow pigment dispersion generated by milling experiments. The Raman signal travels better through smaller particles but, overall, the effective penetration depth of the Raman laser light does not change significantly over the course of an experiment. Exploiting the effect of particle size on Raman spectroscopy is not new. Choi et al⁸ have shown that different size nanoparticles of TiO₂ yield different spectra. The Raman bands broadened and shifted with decreasing particle size. Decreasing the particle size changed the force constants and vibrational amplitudes of the neighbouring bonds.

8.3 Interfering effects

8.3.1 Stirring

Through some initial experiments it was found that the spectrum of cyan pigment dispersion displayed increasing fluorescence when the laser light impinged on to a static sample. To remove this effect the sample needs to be well agitated so a simple experiment was devised to show how the stir rate of cyan pigment dispersion in the sample reservoir of the Netzsch minizeta mill affected the Raman spectra.

8.3.1.1 Experimental

800 g of 20% w/w cyan pigment with 60 % loading polymer of polymer "Acid 46" was prepared as per section 3.2 and milled for 6 hours using the Netzsch minizeta mill. The mill was stopped and the stir rate in the sample reservoir of the mill altered by adjusting an overhead stirrer with a digital rpm display. The agitator was a small 4 cm diameter turbine type stirrer shaft and three spectra were collected at agitation rates of 100, 200 and 300 rpm. Only 2 spectra were recorded of the static pigment dispersion as fluorescence increased with each measurement causing the third spectrum to overload the detector.

Raman spectra were acquired using the Kaiser Rxn 1 Raman spectrometer with PhAT probe (Kaiser Optical systems, Ann Arbor, USA) and recorded using IC Raman software (Mettler-Toledo, Columbus, USA). Each spectrum was the product of 3 acquisitions of 20 seconds. The 8 inch probe spacer was positioned at the lip of the sample reservoir.

8.3.1.2 Results and discussion

Figure 8.8 shows the Raman spectra collected at different stir rates. There is a large increasing fluorescence signal at 400 cm^{-1} when the sample is static which prevented the collection of three spectra. This fluorescence decreased when the sample was stirred but the spectra still showed some variation in the lower wavenumber region. Prolonged exposure to a high intensity laser source may induce photo-degradation

but one of the main advantages of pigment dispersions over conventional soluble inks is that the photo stability is good. At 100 rpm stirring, the sample appeared to be static at the surface and higher stir rates caused the pigment dispersion to flow across the top of the sample reservoir.

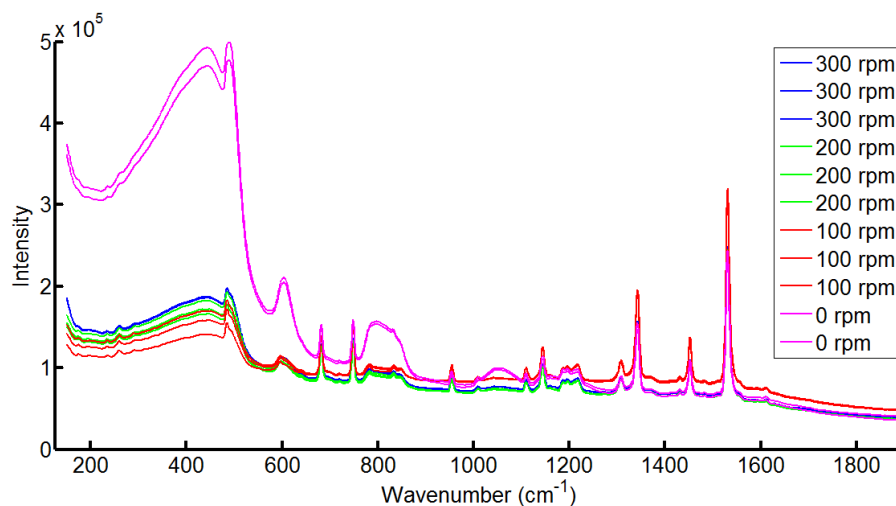


Figure 8.8 – 785 nm excitation Raman spectra of cyan pigment dispersion collected at different stir rates.

The Raman spectra appear more consistent at stir rates between 200 to 300 rpm in the region above 900 cm⁻¹. The Raman band at 1530 cm⁻¹ has an RSD value of 0.92 % which indicates that if the sample is adequately stirred between 200 – 300 rpm, the Raman spectra will be consistent and suitable for process monitoring. A stir rate of 240 rpm was selected for all future experiments to provide adequate agitation without causing the dispersion to trap air bubbles or overflow at the edge of the reservoir.

8.3.2 Sample distance

The level of the pigment dispersion dropped slightly during milling because of the removal of sample for off-line characterisation by DLS. Adjusting the probe set up after each sample removal is impractical so an experiment was devised to quantify how the distance between the probe and the sample affected Raman spectra. An experiment was set up to examine the effect of changing the sample distance from the probe head and assess the magnitude of effect.

8.3.2.1 Experimental

The pigment dispersion and milling procedure was as per section 8.2.1 The positioning of the Raman probe was adjusted between sets of three measurements to cover a range of distances between the PhAT probe spacer and the pigment dispersion.

8.3.2.2 Results and discussion

Figure 8.9 shows the change in Raman intensity for 5 main bands present in the cyan pigment dispersion where the distance from the probe to sample was varied from 17 to 80 mm. When monitoring milling experiments the Raman probe and spacer are placed 30 mm from the sample and the level drops by a maximum of 10 mm over an extended milling experiment of approximately 10 hours.

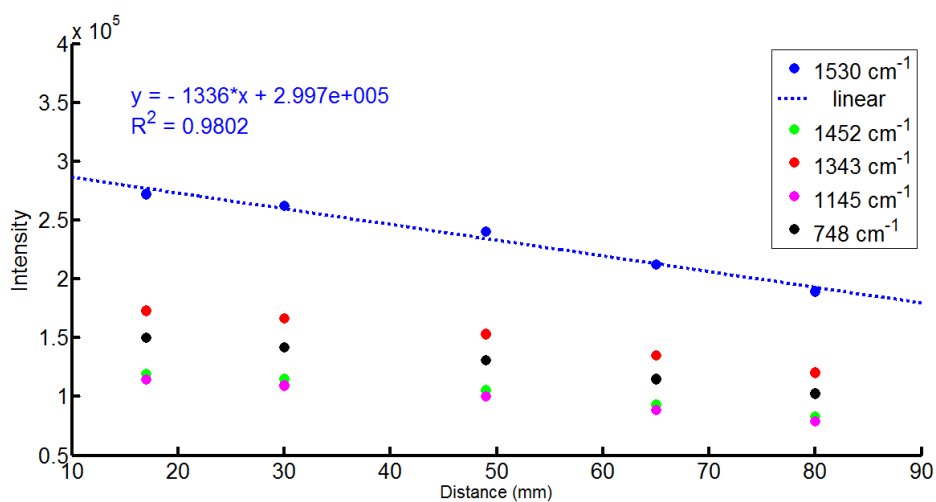


Figure 8.9 – Intensity of Raman spectra bands (785 nm excitation) versus distance from the end of the PhAT probe spacer to the stirred pigment sample.

The relationship between untreated Raman spectral band intensity and the distance of the probe is linear over the range analysed. Between 30 and 40 mm the intensity of the band drops 5.14 %. This drop is over the whole experiment and is considerably less than the total change observed during the milling of either cyan or yellow pigment dispersions which are discussed in the sections to follow.

8.4 Milling of yellow pigment dispersion

Three milling experiments of yellow pigment dispersion were monitored using on-line Raman spectrometry.

8.4.1 Experimental

Three 800 g 20% w/w yellow pigment with 50 % loading polymer of polymer "Acid 46" were prepared as per section 3.2 and milled for approximately 11 hours using the Netzsch minizeta mill. The sample reservoir was stirred at 240 rpm using an overhead stirrer. The agitator was a small 4 cm diameter turbine type stirrer shaft.

Raman spectra were acquired using the Kaiser Rxn 1 Raman spectrometer with a PhAT probe (Kaiser Optical systems, Ann Arbor, USA) and recorded using IC Raman software (Metler-Toledo, Columbus, USA). Each spectrum was the product of 6 acquisitions of 5 seconds and repeated every 60 seconds. The Raman PhAT probe and spacer were situated 30 mm from the level of the pigment dispersion in the stirred sample reservoir (Figure 8.10).

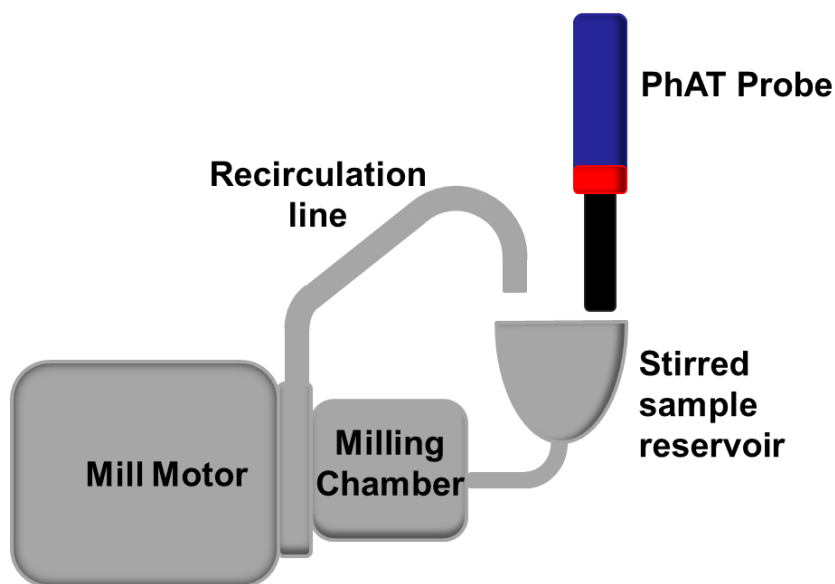


Figure 8.10 – Raman PhAT probe experimental set up used to monitor the milling of pigment dispersions.

8.4.2 Results and discussion

The Raman spectra of the yellow pigment dispersion decreased as the particle size reduced (Figure 8.11). Both the intensity of the strong Raman bands and the baseline offset decreased with decreasing particle size. On-line NIR and an off-line investigation of the fundamental optical constants for diluted pigment dispersion have shown that the optical scattering coefficient decreases with decreasing particle size. Although the range of the reported optical constants does not extend to 785 nm it is reasonable to assume that the scattering coefficient will reduce with reducing particle size at the wavelengths of light encountered in 785 nm excitation Raman spectroscopy.

The fundamental optical constants are not to be confused with Raman scattering. A sample's efficiency of Raman scattering will remain consistent for the wavelength of excitation but the distance of travel of the Raman scattered photon will be affected by the fundamental optical properties of the sample. When the scattering coefficient is higher, the greater the probability of the Raman scattered photon being able to escape the pigment dispersion and be collected by the PhAT probe. As the optical scattering coefficient decreases, the less likely this becomes and this is manifest in the spectra as a drop in the baseline and in the intensity of the Raman active bands.

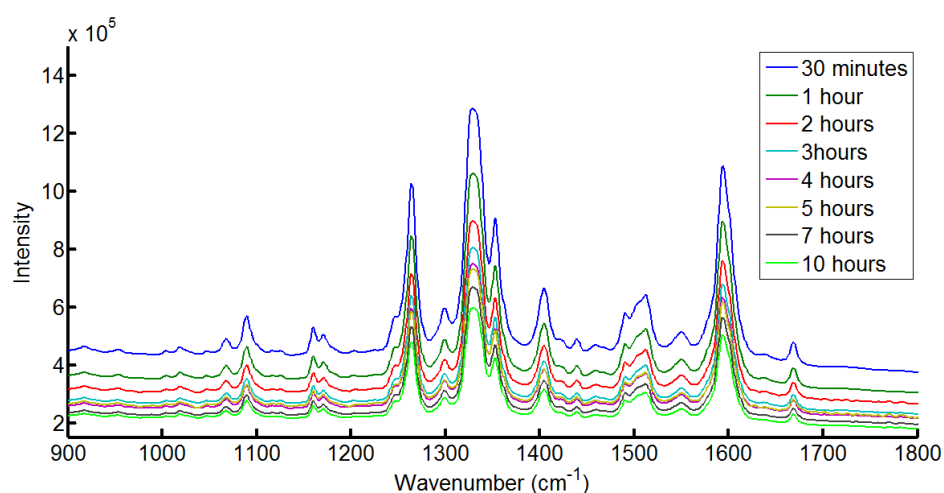


Figure 8.11 – 785 nm excitation Raman PhAT probe spectra collected during the milling of yellow pigment dispersion experiment 1.

Figure 8.12 shows the off-line particle size information for three milling experiments of yellow pigment dispersion. In each instance the particle size decreases substantially over a 12 hour milling cycle and the third experiment displays a larger particle size than experiments 1 and 2.

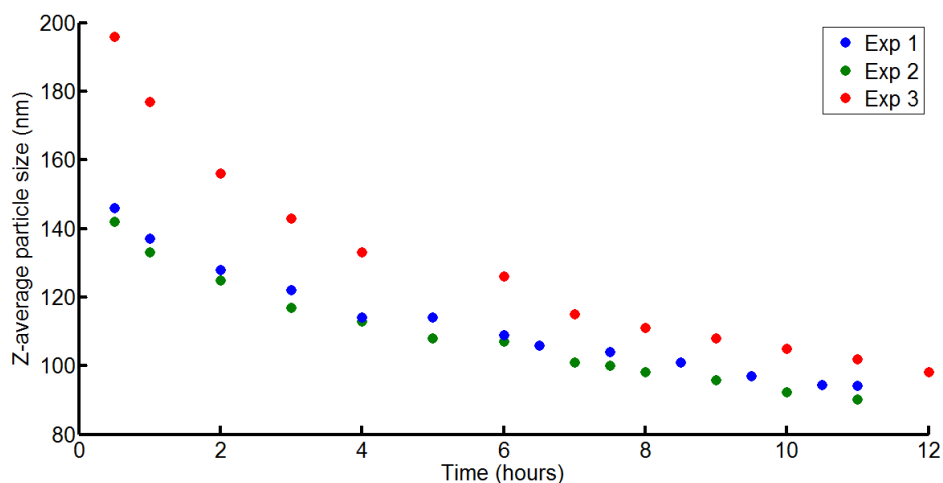


Figure 8.12 – Z-average particle size for three milling experiments of yellow pigment dispersion.

Figure 8.13 shows the correlation coefficient for particle size and Raman intensity across a complete spectral range. For experiments 1 and 2 the correlation of Raman intensity and particle size is consistently high over the range from 600 to 1890 cm^{-1} . Experiment 2 shows a lesser correlation with particle size and examination of the spectra show that there were significant disturbances each time the milling was disrupted to extract a sample. At each sampling point the collection of Raman spectra was paused and the foil which prevented stray light from being collected by the PhAT probe was removed. Sampling the return stream of the mill required the return pipe of the mill to be lifted from underneath the surface of the pigment dispersion. The return flow was placed under the level of the pigment dispersion to avoid introducing air bubbles into the dispersion which may affect the quality of the Raman spectra and could introduce an air block in the mill. The intensive sampling regime meant that there were numerous disturbances as a result of working within a tight space at the sample reservoir.

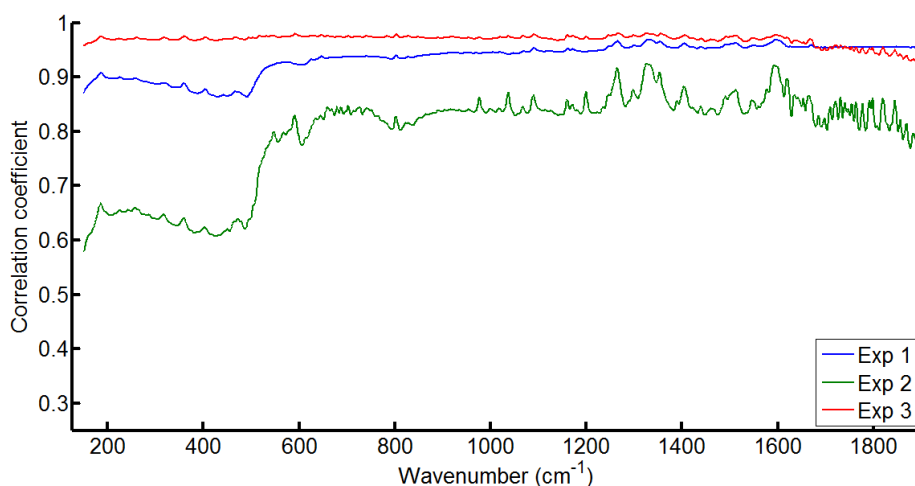


Figure 8.13 – Correlation coefficients for yellow milling experiments 1 to 3. The correlation shown is calculated for the Z-average particle size and the 785 nm excitation Raman spectra intensity over the range 150 to 1890 cm^{-1} .

Figure 8.14 shows the changing intensity of the Raman band at 1353 cm^{-1} for each of the three milling experiments. Over the course of the milling the milling experiments the largest Raman band drops to around 30% of the original value at the start of the milling process. The drop of the level of pigment dispersion form sampling does not account for this significant change. Additionally, the spectral trend shows a consistent decrease between sampling intervals where the distance of the probe to the sample is a constant.

Experiment 2 shows the lowest correlation of particle size with the Raman spectra across all of the wavenumber range collected using the PhAT probe and the trend in intensity at 1353 cm^{-1} shows that the spectra have step changes at sampling times when the probe was susceptible to slight movement.

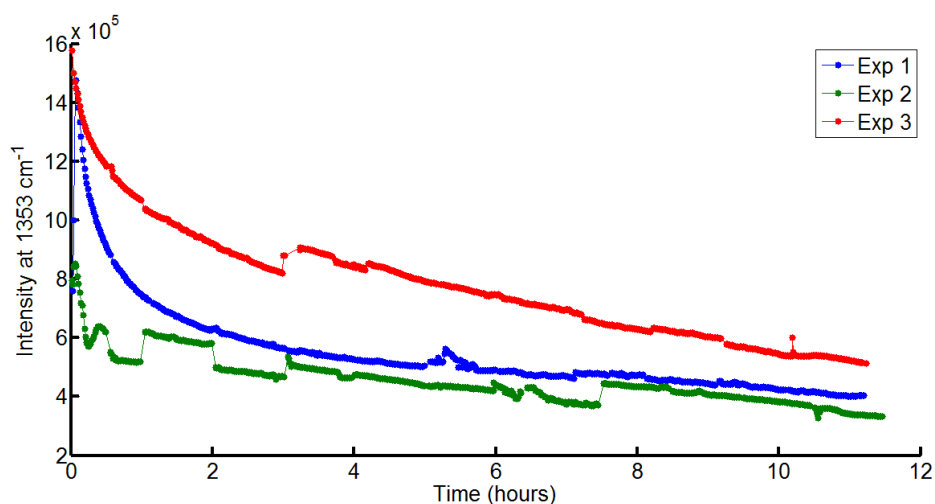


Figure 8.14 – 785 nm excitation Raman intensity at 1353 cm^{-1} for three milling experiments of yellow pigment dispersion.

Spectral pre-treatments such as derivatives (1st and 2nd order) and base line corrections do not remove the periodic step changes that are incurred by altering the position of the Raman PhAT probe. To increase the robustness of the measurement in future experiments a glass window could be incorporated in the mills sample reservoir although this may introduce further complications such as window fouling.

The particle size data shows that the largest particle size at 11 hours belongs to experiment 3 which also displays a higher Raman signal at 1353 cm^{-1} . The particle size data also shows that the particle size results for experiments 1 and 2 are very similar and this is mirrored in the trend observed in the Raman spectra. The purpose of the experiments undertaken was to investigate whether good quality Raman spectra can be obtained using a non-contact PhAT probe and show that there is a measurable effect from changing the particle size of the pigment dispersion. It has been shown that the particle size influences the Raman spectra collected during the milling experiments of yellow pigment dispersions but the laboratory set up requires refinement.

The Raman spectra show both a decrease in band intensity and decrease in baseline off-set with decreasing particle size during the milling of high concentration pigment dispersions. Unfortunately, few published examples deal with regimes where the particles are smaller than the excitation wavelength of the Raman laser which makes

it difficult for direct comparisons with my results. However, Allan et al have observed the effect of particle size while monitoring powder blending with wide area illumination Raman spectroscopy. The second derivative Raman signals for three blend components (aspirin, sodium nitrate and Avicel) increase with particle size at smaller particles but then decrease with increasing particle size for larger particles. In this example the particle size range is from ~50 to 650 μm , which is much larger than those for the milled pigment dispersions. Chen et al¹⁰ have developed a mathematical approach of correcting the effect of particle size and powder compactness on Raman spectra which enhanced the accuracy of predictive models for mixtures of barium nitrate and potassium chromate. This is again in the μm domain of particle sizes.

Reis et al¹¹ have used Raman to develop a PAT technique for closed loop control of an emulsion polymerisation reaction where the particle size can be monitored using in-situ Raman. The change particle size was around 50 – 150 nm and it was observed that the region between 400 – 500 cm^{-1} showed some correlation with particle size. As the particle size increased, the intensity in the chosen region increased, which is concomitant with observations in the pigment dispersions although this is observed over the whole spectra for the pigment milling. One key difference to remember is that the polymerisation reaction was monitored using narrow spot confocal Raman with very short collection times whereas the pigment dispersion monitoring used a wide field illumination PhAT probe.

8.5 Summary

Good quality Raman spectra can be obtained with the 785 nm Kaiser RXN1 Raman spectrometer and PhAT probe for blue pigment powder (PB15:4) and (PY74) as well as the stabilising polymer (Acid 46) and dipropylene glycol. Magenta pigment powder (PR122) and milled pigment dispersions containing the pigment show a large fluorescence signal which dwarf any contribution from the Raman scattering at 785 nm. The opportunity arose to examine milled pigment dispersions using a longer wavelength (998 nm) laser excitation Raman spectrometer and it was shown that although there was still some fluorescence, there were clear features present in the spectra which could be observed in the first derivative of the spectra. At the longer excitation wavelength the yellow pigment dispersion displayed good quality Raman spectra whereas the blue pigment dispersion showed a building fluorescence signal with each measurement. This was probably due to the sample being stationary as it was shown, for the 785 nm Raman spectrometer, that good quality Raman spectra were obtained when the sample was well mixed. The mixing prevented the laser spot repeatedly striking the same sample which may cause the dispersion to degrade. Low stir rates caused an increase in a broad signal around 400 cm^{-1} which overloaded the Raman spectrometer CCD detector.

The penetration depth of the Raman PhAT probe system at 785 nm was assessed by placing different depths of yellow pigment dispersion between the probe and a flower of sulphur disc which is a strong Raman scatterer. By following the decay in the sulphur signal it was observed that the Raman spectra contain information from approximately 2 mm in to the concentrated pigment dispersion for all particle sizes between 349 to 125 nm. The smaller particles have a smaller scattering coefficient which means more of the photons were able to reach the sulphur disc than when the particle size was large.

Milling of the pigment dispersion required that samples were removed for off-line analysis by DLS (the reference technique). A simple investigation showed that distance of the probe from the pigment dispersion would have a small effect on the Raman spectra (a reduction in signal of 5 % at 1530 cm^{-1} over the distance 30 – 40

mm) but over the course of milling experiments the reduction in intensity of the Raman signal was much greater than the effect of sample distance.

On-line monitoring of yellow and cyan pigment dispersion milling showed that the spectra reduced in both band intensity and baseline during particle size reduction. The laboratory experimental set up meant that the PhAT probe was susceptible to movement which affected the quality of the Raman spectra but overall there was a clear correlation between particle size and the Raman spectra. This shows the potential of Raman spectrometry for on-line monitoring of cyan and yellow pigment dispersions using a 785 nm wavelength excitation laser and the Kaiser Raman PhAT probe with a wide illumination spot. Although not included in this section, some experimental studies were performed using a conventional immersion optic Raman probe which had a very small focal point. Unfortunately the spectra showed very little change during the milling of cyan and yellow pigment dispersions and it is concluded that the wide illumination PhAT probe is the most suitable method of acquiring good quality Raman spectra for the dispersions under study. The PhAT probe offers another advantage as the measurement requires no physical contact with the sample. Any opportunity to remove operator interaction with high concentration pigments is desirable as handling can be difficult and messy.

Overall, Raman spectroscopy is a useful tool for monitoring the particle size reduction. In comparison to NIR, the main drawback is that 785 nm excitation cannot be used to monitor magenta pigments due to fluorescence. Additionally, the capital costs of process Raman spectrometers is generally higher than the cost of a plant ready NIR spectrometer. Both NIR and Raman can be coupled to probes using optical fibres but there are safety concerns that are specific to Raman spectrometers. Firstly, the probe must be housed somewhere where there is no external light and secondly, there are safety implications associated with high power collimated laser beams - particularly in areas where there are a lot of reflective surfaces. Raman does offer the possibility of a completely non-contact measurement (as can NIR) of the pigment dispersions. Although Raman spectroscopy provides more detailed spectra than NIR, there is no additional information in the Raman spectra of the particle size that cannot be seen by using an NIR reflectance measurement.

8.6 References

1. C. Binant and A. Lautie, *Applied Spectroscopy*, 1989, **43**, 851-855.
2. C. Frausto-Reyes, M. Ortiz-Morales, J. M. Bujdud-Pérez, G. E. Magaña-Cota and R. Mejía-Falcón, *Spectrochimica Acta Part A: Molecular and Biomolecular Spectroscopy*, 2009, **74**, 1275-1279.
3. T. R. Ravindran, A. K. Arora, S. Ramya, R. V. Subba Rao and B. Raj, *Journal of Raman Spectroscopy*, 2011, **42**, 803-807.
4. F. Schulte, K.-W. Brzezinka, K. Lutzenberger, H. Stege and U. Panne, *Journal of Raman Spectroscopy*, 2008, **39**, 1455-1463.
5. T. V. Basova, V. G. Kiselev, B.-E. Schuster, H. Peisert and T. Chassé, *Journal of Raman Spectroscopy*, 2009, **40**, 2080-2087.
6. D. R. Tackley, G. Dent and W. Ewen Smith, *Physical Chemistry Chemical Physics*, 2000, **2**, 3949-3955.
7. D. R. Tackley, G. Dent and W. Ewen Smith, *Physical Chemistry Chemical Physics*, 2001, **3**, 1419-1426.
8. H. C. Choi, Y. M. Jung and S. B. Kim, *Vibrational Spectroscopy*, 2005, **37**, 33-38.
9. P. Allan, L. J. Bellamy, A. Nordon, D. Littlejohn, J. Andrews and P. Dallin, *Journal of Pharmaceutical and Biomedical Analysis*, 2013, **76**, 28-35.
10. Z.-P. Chen, L.-M. Li, J.-W. Jin, A. Nordon, D. Littlejohn, J. Yang, J. Zhang and R.-Q. Yu, *Analytical Chemistry*, 2012, **84**, 4088-4094.
11. M. M. Reis, P. H. H. Araujo, C. Sayer and R. Giudici, *Polymer*, 2003, **44**, 6123-6128.

9. Conclusions and Future Work

The aims of the work presented were to detail an optical spectroscopic method capable of measuring the particle size reduction of pigment dispersions through in-situ measurements. UV-visible, mid infrared, near infrared (NIR) and Raman spectrometry were investigated as potential techniques for the measurement of particle size.

Building on previous work by FFIC, Grangemouth, UV-visible spectroscopy using an ATR probe was investigated. Extensive experimentation revealed that the technique could not provide repeatable spectra that could be used to model the particle size of pigment dispersions. An investigation showed a strong dependence of the UV-visible absorption on the sample speed. Off-line measurements using static sample also showed variability. It was concluded that ATR measurements were subject to complex boundary issues between the pigment dispersion and the ATR crystal and the technique was discarded.

Similarly, MIR ATR spectroscopy was assessed as a potential tool for monitoring changes in the particle size of pigment dispersions. The MIR spectra showed no coherent change that could be related to the reduction of the pigment dispersion particle size. It is assumed that as the wavelength of light in the MIR region is much larger, the evanescent wave of the ATR probe extends much deeper in to that sample than UV-visible wavelengths. This effectively blinded the measurements to the effect of particle size.

NIR reflectance spectra, collected on-line, exhibited a change during pigment dispersion milling experiments. To understand what caused the change in the NIR spectra, the fundamental optical constants were calculated using the radiative transfer equation. Experimentally derived absorption and scattering coefficients (μ_a and μ_s respectively) showed that the scattering coefficient was the dominant change observed between diluted pigment dispersions of different particle sizes.

The milling of pigment dispersion is effectively a locked chemical system which meant that milling effectively produced a larger number of smaller particles with time. The number density of particles exposed to the NIR probe light increased as

milling experiments progressed. An attempt was made to understand the effect of the number density of particles and the particle size individually on the scattering coefficient. For a theoretical system of latex spheres, the scattering coefficient was shown to be dominated by the effect of particle size. The calculated absorption and scattering coefficients for cyan, magenta and yellow pigment dispersions all exhibited a reducing scattering coefficient with particle size and wavelength

The change observed in the scattering coefficient with reducing particle size were used to rationalise the observations from the on-line NIR data. On-line NIR spectra showed an increase in the baseline offset between 700 – 1400 nm. The region above 1400 still showed some offset but the strong water absorption dominated the NIR spectra. The absorbance of the on-line spectra increased with decreasing particle size and the scattering coefficient decreases with decreasing particle size. It fits that the reduction in scattering coefficient of the pigment dispersion as the pigment is milled results in less light being scattered back to the collection fibres of the on-line NIR probe, hence the absorption increases. A 2 level, 2 factor DoE where the magenta pigment and polymer concentrations were varied showed the NIR measurement of the milling process to be robust.

NIR pigment milling experiments were monitored on three scales (< 1kg, 10 kg and 200 kg) between the laboratory and large scale development for all three pigment colours (cyan, magenta and yellow). Multivariate models for the prediction of particle size which were constructed using magenta milling experiments on the <1 kg scale showed a good predictive ability for the larger scale magenta pigment dispersion milling (both 10 kg and 200 kg scales). The most accurate predictions were obtained by using the first derivative form of the NIR spectra. This was necessary to remove some of the variation accrued as a result of moving the NIR spectrometer and probe. Ideally, models without the use of derivatives should be used as the particle size data is encoded in the baseline offset of the NIR spectra.

200 kg scale milling experiments of cyan, magenta yellow and black pigment dispersions were monitored using on-line NIR. The good predictive ability of PLS models constructed on <1 kg milling experiments demonstrated the potential for applying the on-line NIR measurement as a means of following the particle size

reduction on a larger scale. Large scale experiment monitoring also revealed the potential value of real time NIR measurements as a troubleshooting tool. Real time measurements obtained in-situ would allow better decision making regarding whether to continue milling or advance to other processing steps. One 200 kg milling experiment was monitored, by NIR, which showed that the particle size was no longer reducing despite continued milling. The benefits of real time measurement would be a reduction in energy costs as the milling step could have been ended much sooner.

Raman spectroscopy was explored as an alternative to NIR spectroscopy. A Raman PhAT probe which had a 6 mm wide illumination spot provided high quality Raman spectra that changed with particle size.

The penetration depth of the Raman PhAT probe was determined experimentally to be around 2 mm in to a high concentration yellow pigment dispersion. Raman spectroscopy at 785 nm is a useful tool for monitoring the particle size reduction of cyan and yellow pigment dispersions but the magenta fluoresced. Raman spectra collected using a 998 nm system removed some of the fluorescence of the magenta pigment. Small scale (< 1 kg) milling experiments showed that it was possible to follow the reduction of particle size for cyan and yellow pigment dispersions. The increased specificity of the Raman spectra was not enough to obtain a clear signal from the dispersing polymer molecule because of the low concentration in the dispersion. Although Raman spectroscopy provides more detailed spectra than NIR, NIR measurements are easier (requiring less protection from external light sources) and can be used on all three coloured pigment dispersions.

It is suggested that any future work would solely focus on NIR reflectance measurements as a means of monitoring the particle size reduction of pigment dispersions. The NIR measurements could either be used to determine the particle size from models or could simply display the trend in absorption which could be used to show when the rate of change has plateaued or the system has a fault.

The next steps to deploy a NIR reflectance measurement for real time control would be:

- 1 Assess the types of interface and control systems that FFIC require. For example, whether a NIR measurement was used for closed loop feedback control or whether the information was provided to an operator. Additionally the type of information given to the operator would have to be discussed. The output from an on-line measurement could be a simple GO/STOP instruction or could be a prediction of the particle size number.
- 2 Once that has been decided the next step would be to decide how to integrate the output from the spectrometer to the existing control software used to control the plant.
- 3 Decide what type of modeling will be required as this would affect the choice of spectrometer. Potentially, a simpler univariate method could be monitored to follow the change in the baseline off-set over a narrow wavelength range. This has the advantage of using a simpler, less expensive spectrometer which has a narrower range of measurement than the one used in the experimental work presented earlier.
- 4 A new spectrometer system and probe system would have to be trialed in place and a more detailed investigation of the effect of flow rate and temperature on the NIR spectra. Additionally, a method of referencing the spectrometer would have to be devised that did not involve removing the probe from the installation in the process stream. A number of clean and reference in place probe systems could be investigated for this purpose.
- 5 For the new spectrometer system a new calibration model would have to be constructed or methods of calibration model transfer between instruments investigated if a particle size readout measurement is required.

After these steps the robustness of the on-line particle size measurement system would have to be assessed before a trialed handover to plant operators. Additionally, a system of keeping the calibration models up to data would have to be devised such as using the new data gathered throughout the operation of the plant to continually update and improve the model.

The application of on-line spectroscopic methods for monitoring milling can be applied across a variety of challenging applications where there a high concentrations

of suspended solids such as cosmetic and consumer product manufacturing. The work undertaken was for a process where the particle size was reduced but the learning outcomes can be applied equally to processes where particles are grown. This may be of particular interest for crystallisations where particles are grown from the nanometer domain to the micrometer domain. Additionally, the ability to monitor particle size in slurries remotely may be beneficial for pharmaceutical manufacturing processes which are hazardous to sample or in biopharmaceutical applications where sterility is a key concern. The nuclear industry also processes waste slurries and manual handling of nuclear waste materials is not an option. Non-contact measurement using either NIR or Raman spectrometry removes the need for probes to be in direct contact with dangerous materials and more importantly the systems can be set up to allow operators to be situated away from the process in safe zones.

10. Appendices

10.1 Spectrometer specifications

Table 10.1 - Zeiss MCS 522 UV-Visible spectrometer

Wavelength Range	200 – 730 nm
Source	Xenon flash lamp
Pixel Spacing	2.2 nm
Wavelength resolution	> 7 nm (Rayleigh criterion)
Wavelength Accuracy	± 0.5 nm
Ordinate range	± 0.02 AU
Detector	Hamamatsu photodiode array
Noise	< 0.0002 AU rms

Table 10.2 – ABB MB3000 FTIR spectrometer with AgX ATR probe

Spectral range	485 – 8500 cm ⁻¹
Detector	DTGS
Max S/N	50000:1 at 4 cm ⁻¹ resolution
Resolution	Better than 0.7 cm ⁻¹
Probe Fibre	1.5m Silver halide
Probe type	12.7 mm diameter Hastelloy probe with 3 bounce diamond ATR sample

Table 10.3 – FOSS On-line 6500 NIR spectrometer

Wavelength Range	600 – 1800 nm
Source	Halogen lamp
Spectrometer type	Post dispersive
Grating type	Scanning grating monochromator type F2
Scan rate	1.8 scans per second
Slit width	20 mm
Detector	Thermoelectrically cooled InGaAs
Fibres type	Low hydroxy content silica
Fibre bundle	3 m length

Table 10.4 – Cary 5000 spectrophotometer with diffuse reflectance accessory

Wavelength Range	175 – 3300 nm
Source	175 – 350 nm Deuterium lamp 350 – 3300 nm Halogen lamp
Grating	UV-Vis – Dual sided 70 – 45 mm, 1200 lines/mm, blazed at 250 nm NIR – 300 lines/mm, blazed at 1192 nm
Wavelength resolution	UV-Vis - < 0.05 NIR < 0.2 nm
Wavelength Accuracy	UV-Vis - ± 0.1 nm NIR - ± 0.4 nm
Detector	UV-Vis – Photomultiplier tube NIR – PbS

Table 10.5 – Kaiser RXN 1 PhAT probe system

Source	785 nm 400 mW Invictus diode laser
Range	150 – 1890 cm^{-1}
Detector	1024 x 256 Array thermoelectrically cooled CCD
Grating	f/1.8 Holographic transmissive spectrograph
Resolution	5 cm^{-1}
Fibre bundle length	3 m
PhAT probe spot size	6 mm diameter
PhAT probe focal distance	~ 25 cm
Laser power at sample	> 20 mW

10.2 Absorption and scattering coefficients

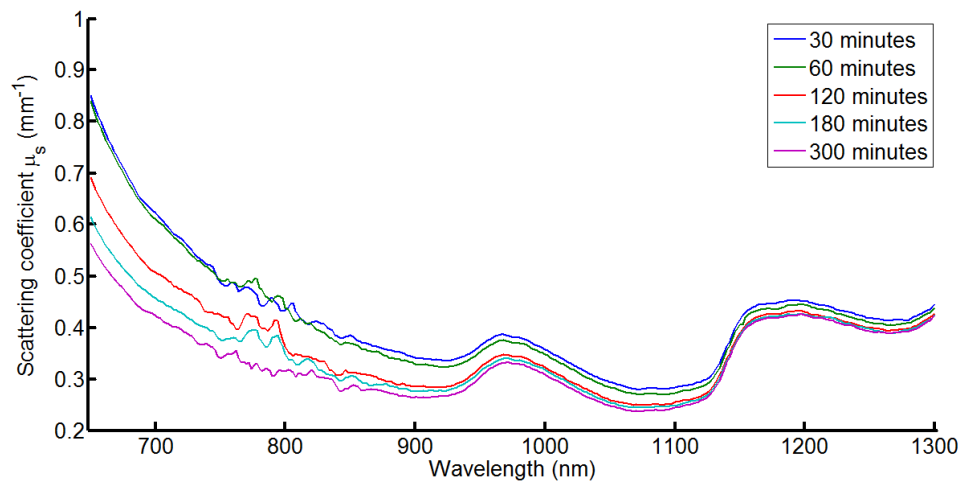


Figure 10.1 – Scattering coefficients for magenta milling experiment A.

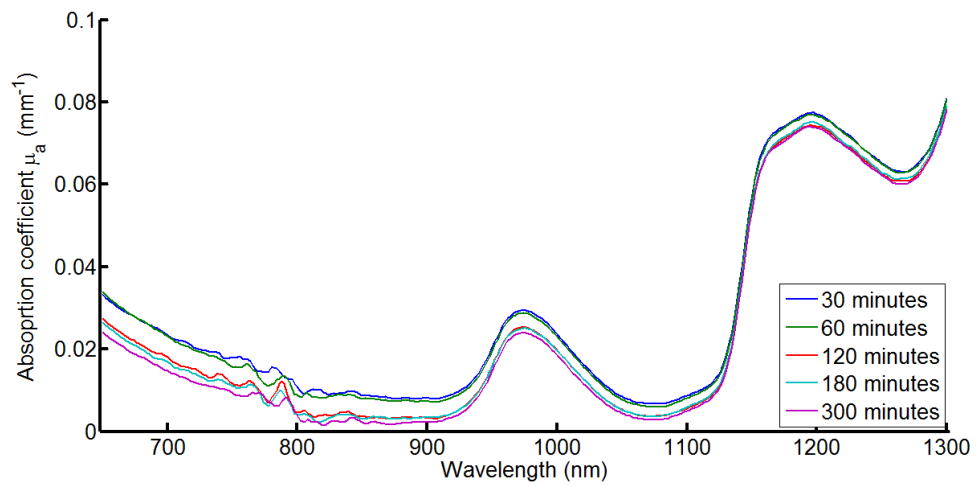


Figure 10.2 – Absorption coefficients for magenta milling experiment A.

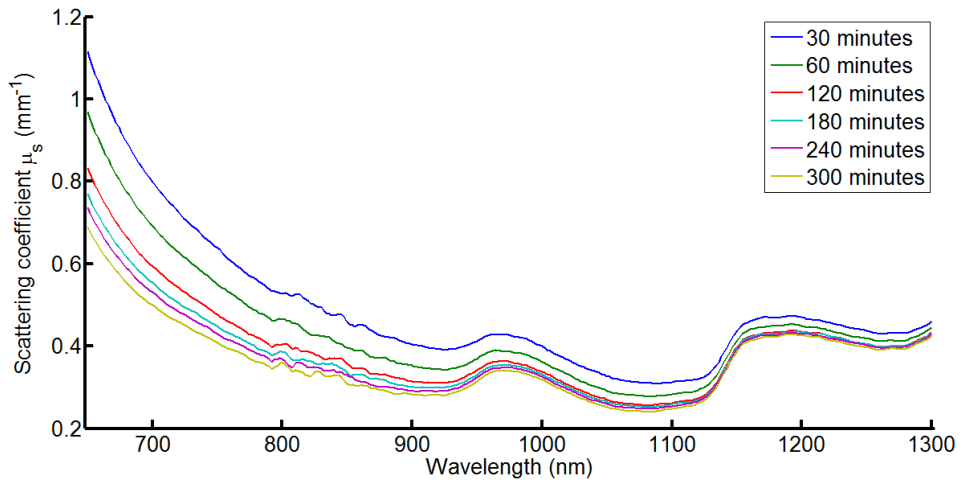


Figure 10.3 – Scattering coefficients for magenta milling experiment B.

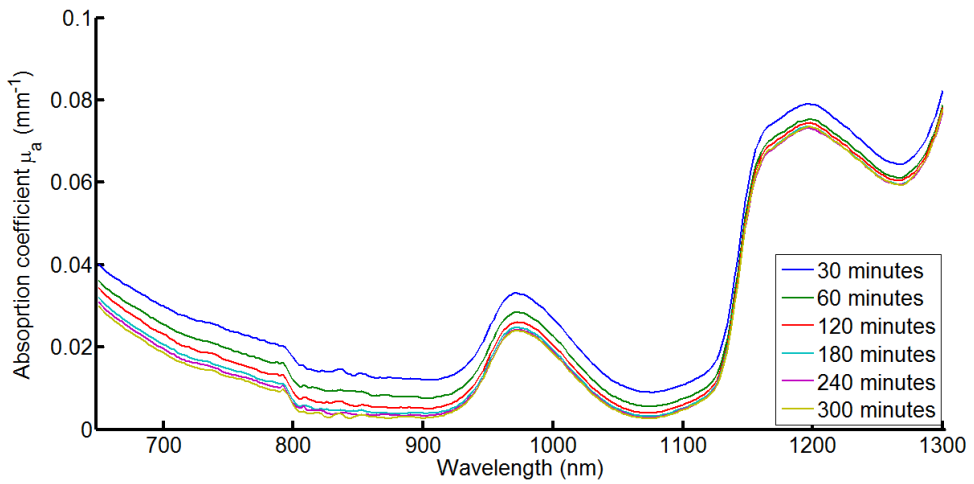


Figure 10.4 – Absorption coefficients for magenta milling experiment B.

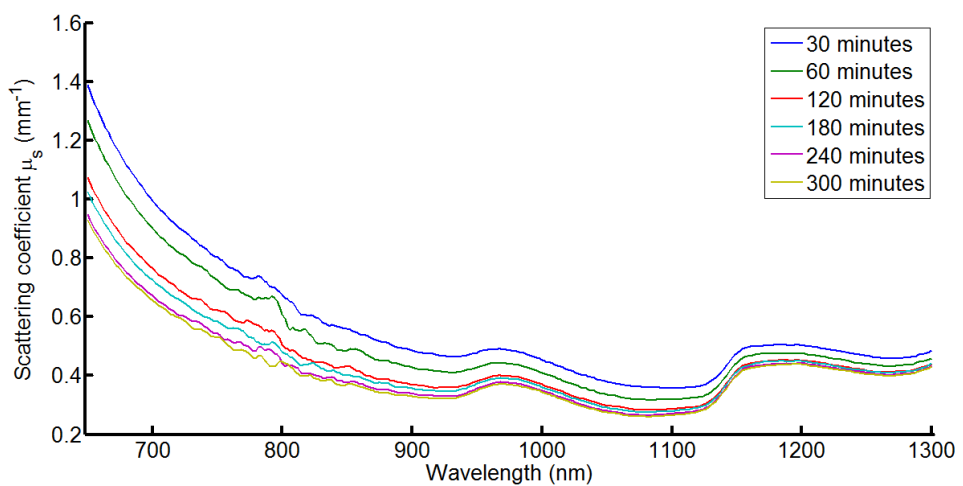


Figure 10.5 – Scattering coefficients for magenta milling experiment C.

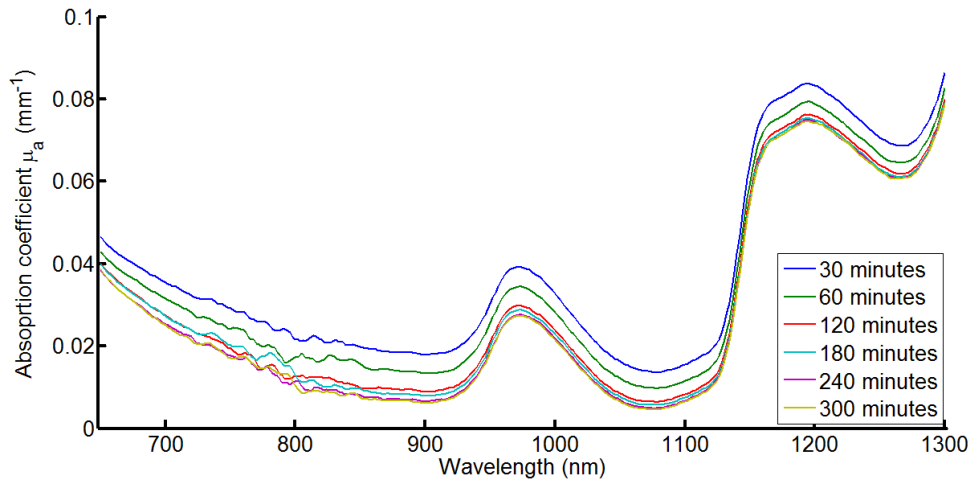


Figure 10.6 – Absorption coefficients for magenta milling experiment C.

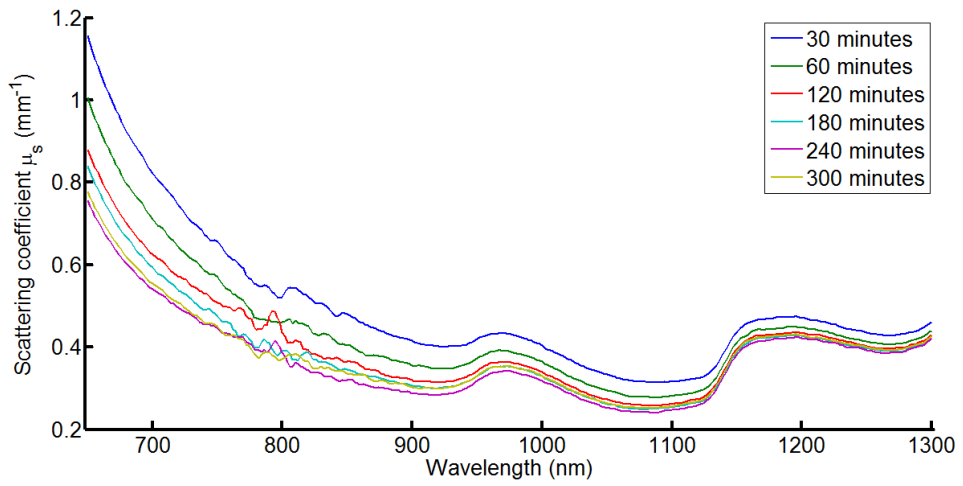


Figure 10.7 – Scattering D

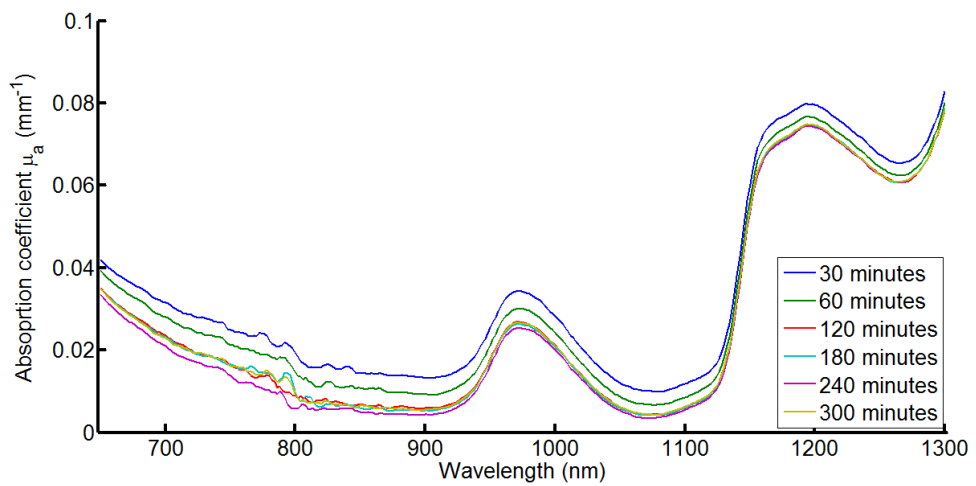


Figure 10.8 – Absorption coefficients for magenta milling experiment D.

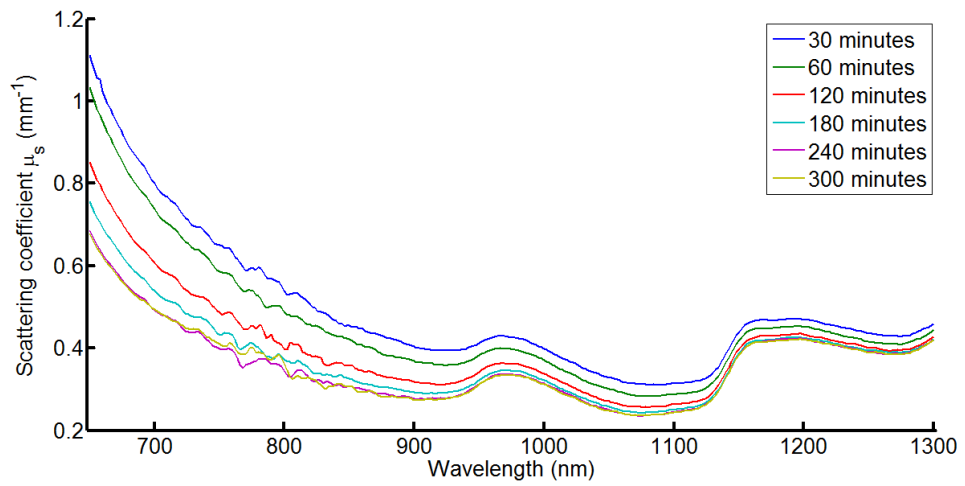


Figure 10.9 – Scattering coefficients for magenta milling experiment E.

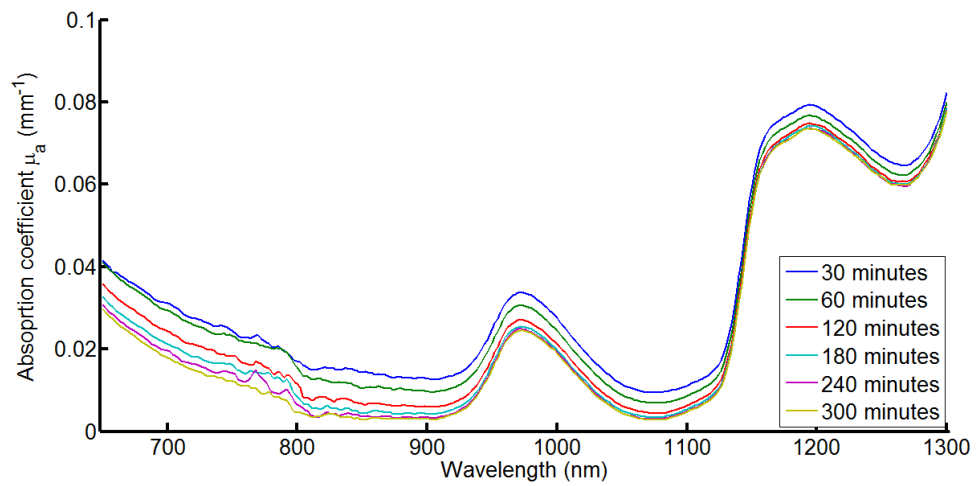


Figure 10.10 – Absorption coefficients for magenta milling experiment E.